UNIVERSITÉ DU QUÉBEC À TROIS-RIVIÈRES

SURVEILLANCE NON-BINAIRE DU SOL SAISONNIÈREMENT GELÉ: DES CAPTEURS IN SITU AUX RESTITUTIONS CONTINENTALES PAR MICRO-ONDES PASSIVES

NON-BINARY MONITORING OF SEASONALLY FROZEN GROUND: FROM IN SITU SENSORS TO CONTINENTAL PASSIVE MICROWAVE RETRIEVALS

THÈSE PRÉSENTÉE
COMME EXIGENCE PARTIELLE DU
DOCTORAT EN SCIENCES DE L'ENVIRONNEMENT

OFFERT PAR L'UNIVERSITÉ DU QUÉBEC À MONTRÉAL
EN ASSOCIATION AVEC
L'UNIVERSITÉ DU QUÉBEC À TROIS-RIVIÈRES

PAR

HESAM SALMABADI

AOÛT 2026

UNIVERSITÉ DU QUÉBEC

DOCTORAT EN SCIENCES DE L'ENVIRONNEMENT (PH. D.)

Programme offert par l'Université du Québec à Montréal (UQAM)

en association avec

l'Université du Québec à Chicoutimi (UQAC)

l'Université du Québec à Rimouski (UQAR)

l'Université du Québec en Abitibi-Témiscamingue (UQAT)

et l'Université du Québec à Trois-Rivières (UQTR)

Direction de recherche :

Alexandre Roy, Ph. D. — Université du Québec à Trois-Rivières

Directeur de recherche

Aaron Berg, Ph. D. — University of Guelph

Codirecteur de recherche

Jury d'évaluation :

Alexandre Roy, Ph. D. — Université du Québec à Trois-Rivières

Directeur de recherche

Aaron Berg, Ph. D. — University of Guelph

Codirecteur de recherche

Vincent Maire, Ph. D. — Université du Québec à Trois-Rivières

Président de jury

Xiaolan Xu, Ph. D. — NASA Jet Propulsion Laboratory

Évaluateur externe

Nicolas R. Leroux, Ph. D. — Environment and Climate Change Canada

Évaluateur externe

Thèse soutenue le 16 juin 2026

Université du Québec à Trois-Rivières

Service de la bibliothèque

Avertissement

L'auteur de ce mémoire, de cette thèse ou de cet essai a autorisé l'Université du Québec à Trois-Rivières à diffuser, à des fins non lucratives, une copie de son mémoire, de sa thèse ou de son essai.

Cette diffusion n'entraîne pas une renonciation de la part de l'auteur à ses droits de propriété intellectuelle, incluant le droit d'auteur, sur ce mémoire, cette thèse ou cet essai. Notamment, la reproduction ou la publication de la totalité ou d'une partie importante de ce mémoire, de cette thèse et de son essai requiert son autorisation.

In memory of my friend, Dr. Iman Aghabali (1991–2020),
one of the 176 lives lost on Flight PS752, 8 January 2020.

Résumé

Le sol saisonnièrement gelé (SSG) est une composante importante de la cryosphère terrestre sensible aux changements climatiques, exerçant des contrôles de premier ordre sur le partitionnement hydrologique, les émissions de carbone du sol et l'échange d'énergie à la surface terrestre à travers les vastes régions boréales, subarctiques et de toundra de l'hémisphère Nord. La télédétection micro-ondes passive est un outil privilégié pour surveiller les cycles gel–dégel (GD) du sol à des échelles continentales, en exploitant le fort contraste de permittivité diélectrique entre l'eau liquide et la glace. Pourtant, une tension fondamentale persiste entre la réalité physique du processus de gel et la manière dont il est représenté tant dans les algorithmes satellitaires que dans les jeux de données *in situ* utilisés pour les entraîner et les évaluer. Le sol ne gèle pas instantanément à 0 °C ; il passe plutôt par un état de transition thermodynamiquement prolongé—la *phase de rideau zéro*—dans lequel l'eau liquide et la glace coexistent dans l'espace poral, gouvernées par la texture du sol, la teneur en matière organique et l'humidité antécédente. Cet état partiellement gelé est biogéochimiquement actif et hydrologiquement distinct du sol complètement gelé, mais les produits satellitaires opérationnels et les mesures *in situ* terrain utilisées pour les calibrer s'appuient massivement sur des seuils de température binaires à 0 °C qui efface entièrement la phase de rideau zéro. Résoudre cet état de transition à partir de mesures de terrain nécessite de construire une courbe caractéristique de gel du sol (CCGS)—le cadre standard qui quantifie l'épuisement progressif de l'eau liquide avec la baisse de température et constitue la seule approche *in situ* capable de résoudre la période de rideau zéro. Cependant, la CCGS conventionnelle repose sur la conversion de la permittivité diélectrique volumique en teneur en eau liquide, une conversion qui introduit de fortes incertitudes dans les sols riches en matière organique, argileux ou à humidité variable—précisément les types de biomes où les dynamiques de transition sont les plus prononcées et les plus importantes sur le plan écologique. Il en résulte une représentation systématique du moment et de la durée du gel–dégel, qui se propage du capteur de terrain au produit satellitaire jusqu'aux modèles écosystémiques.

L'objectif central de cette thèse est de résoudre cette représentation simpliste en construisant, évaluant et appliquant un cadre physiquement fondé, de bout en bout, qui capture le continuum complet GD du sol—du signal diélectrique d'un capteur *in situ* à l'empreinte continentale des

satellites micro-ondes passifs—et quantifie les conséquences écologiques de la représentation explicite de l'état de transition. Cet objectif est abordé à travers trois chapitres de recherche séquentiels et mutuellement complémentaires, chacun résolvant une couche distincte du problème : en établissant d'abord une méthodologie de référence *in situ* robuste qui contourne les défis d'étalonnage inhérents aux sols gelés, puis en exploitant ce cadre pour entraîner et valider une restitution satellitaire probabiliste multi-fréquence, et enfin en déployant la base de données résultante pour attribuer les patrons spatiotemporels du sol gelé et relier l'état cryosphérique directement au flux de carbone en saison froide.

Le premier chapitre propose une reformulation de la CCGS théorique directement dans l'espace permittivité–température. En opérant entièrement dans le domaine diélectrique, l'approche contourne la conversion à forte incertitude de la permittivité volumique en teneur en eau liquide—une conversion qui nécessite la connaissance de la teneur en glace, de la porosité du sol et de la permittivité minérale, difficile à obtenir de manière fiable dans des environnements de terrain dynamiques. Le modèle CCGS est ajusté aux mesures de 87 sites répartis sur huit réseaux de surveillance canadiens couvrant les forêts boréales de l'est et de l'ouest, les prairies et la toundra, en utilisant un regroupement partiel hiérarchique bayésien pour dériver des estimations fiables de la gamme de la température d'apparition du gel (T_f : 0,15–0,44 °C) et de la netteté de la transition (b : 0,92–3,47 °C^{-1}). L'analyse démontre empiriquement que l'état de transition n'est pas un cas limite mais une caractéristique saisonnière significative : il peut persister pendant plus de 100 jours dans les environnements boréaux de l'Est caractérisés par de fortes humidités du sol et par d'épais horizons organiques, pendant 30–60 jours dans les réseaux boréaux de l'ouest et des prairies plus sèches, et pendant plus de 40 jours même dans les sites de toundra sous des conditions de froid extrême. Ces résultats établissent que l'isolation de surface—liée à la neige et à la végétation—et l'humidité du sol—et non la seule température de l'air—gouvernent le régime du sol gelé à travers les écozones canadiennes, et produisent les paramètres CCGS spécifiques au biome qui servent d'étiquettes d'entraînement physiquement fondées dans le 2^e chapitre.

S'appuyant directement sur cette caractérisation *in situ*, le deuxième chapitre développe un modèle probabiliste de détection GD non binaire piloté par des observations micro-ondes passives multi-fréquences. Un modèle de régression logistique stratifié par biome intègre le rapport de polarisation normalisé L-band SMAP (Z_{NPR}) avec l'indice de différence normalisée V-Pol Ka/Ku-band AMSR2 (Z_{NDV})—une combinaison parcimonieuse à deux caractéristiques sélectionnée par analyse d'information mutuelle et ablation de caractéristiques comme l'équilibre optimal entre la sensibilité diélectrique dans les biomes ouverts et la sensibilité à la diffusion par la canopée dans les environnements forestiers. Les états du sol utilisés pour l'entraînement sont dérivés en utilisant les paramètres CCGS spécifiques au biome établis au Chapitre 1, qui isolent les sols gelés et non gelés avec une forte précision par rapport aux données de saison intermédiaire

intrinsèquement ambiguës, plutôt qu'en appliquant les seuils universels de 0 °C qui confondent les jeux de données d'entraînement existants. Évalué par rapport à trois produits existants (FT-SMAP, FT-ESDR et FT-SMOS) sur un échantillon spatial aléatoire, la méthode proposée atteint des taux de concordance de 78,8–98,2 % et des valeurs de Kappa de Cohen de 0,44–0,87 sur cinq biomes nord-américains, avec des performances suivant un gradient physiquement interprétable allant de la toundra ouverte aux forêts mixtes à canopée dense. La validation thermodynamique confirme que la classe de transition mathématiquement dérivée s'ancre à la chaleur latente de fusion dans tous les biomes, et non à un artefact radiométrique. Le chapitre introduit l'indice continu de gel (*Frozenness Index*, D)—une distance géométrique standardisée par rapport à la frontière de décision logistique qui suit l'épuisement progressif de l'eau liquide du sol pendant la congélation et s'adapte de manière cohérente au domaine continental—qui constitue la variable diagnostique principale du dernier chapitre.

Le troisième chapitre applique ce nouveau jeu de données de gel du sol non binaire sur neuf ans (2015–2024), corroboré par le produit FT-SMOS indépendant, afin de poursuivre deux objectifs scientifiques interconnectés : quantifier les patrons spatiotemporels et les moteurs environnementaux des jours de gel et de rideau zéro à travers les biomes nord-américains, et établir un lien mécaniste entre l'indice de gel et la respiration de l'écosystème en saison froide. L'analyse spatiale révèle un patron contre-intuitif et non latitudinal : la durée du rideau zéro atteint un pic dans les forêts mixtes de latitude moyenne (57,4 jours) et atteint son minimum dans la toundra de l'Arctique élevé (13,7 jours)—un patron que la température de l'air seule ne peut expliquer. L'analyse de co-variation à l'échelle du biome identifie la densité de végétation automnale (NDVI) comme présentant la correspondance la plus claire avec la durée du rideau zéro à travers les cinq biomes nord-américains, ce qui est cohérent avec le rôle des canopées denses dans l'interception du rayonnement infrarouge sortant et le tamponnement des dynamiques thermiques du sol à travers son impact sur la neige. Un cadre d'attribution XGBoost avec décomposition SHAP confirme que les températures atmosphériques printanières et automnales constituent les contrôleurs primaires de la fréquence totale du sol gelé. Enfin, la régression segmentée de la respiration de l'écosystème AmeriFlux (R_{eco}) par rapport à l'indice de gel (D) démontre que le seuil d'arrêt métabolique s'aligne précisément avec l'apparition dérivée par satellite de la phase de rideau zéro, et l'analyse de ligne limite révèle une décroissance exponentielle du potentiel respiratoire maximal à mesure que la teneur en eau liquide du sol est progressivement épuisée par le gel—confirmant empiriquement que c'est la teneur en eau liquide, et non la température, qui gouverne le flux de carbone en saison froide une fois que le sol entre dans l'état de transition.

Pris ensemble, ces trois chapitres font progresser les sciences de l'environnement selon deux axes complémentaires. Sur le plan méthodologique, ils livrent une progression cohérente—d'un cadre de surveillance *in situ* agnostique aux capteurs et sans étalonnage à une restitution satellitaire

multi-fréquence physiquement validée—qui peut être opérationalise dans les cadres existants de restitution de GD micro-ondes passives. Sur le plan conceptuel, les résultats intégrés recadrent l'état de transition du sol d'un artefact de classification à une quantité écologiquement nécessaire : son apparition constitue une limite thermodynamique ferme sur le flux de carbone en saison froide que les modèles binaires sont structurellement incapables de détecter, et sa durée est gouvernée par les propriétés du paysage davantage que par la seule température de l'air. Alors que le réchauffement accéléré de l'Arctique continue de remodeler le moment, la durée et l'étendue spatiale du SSG, la méthodologie et l'enregistrement de restitution développés ici fournissent les outils diagnostiques nécessaires pour réduire l'incertitude dans les estimations du cycle global du carbone et améliorer la manière dont les modèles de surface terrestre et du système terrestre simulent les flux de carbone en saison froide et la phénologie du gel–dégel à travers le domaine saisonnièrement gelé.

Abstract

Seasonally frozen ground (SFG) is an important climatically sensitive component of the terrestrial cryosphere, exerting first-order controls on hydrological partitioning, soil carbon emissions, and land-surface energy exchange across the vast boreal, sub-arctic, and tundra regions of the Northern Hemisphere. Passive microwave remote sensing has emerged as one of the preeminent tools for monitoring soil freeze–thaw (FT) dynamics at continental scales, exploiting the stark contrast in dielectric permittivity between liquid water and ice. Yet a fundamental misrepresentation persists in how the physical reality of the freezing process is captured both in satellite algorithms and in the *in situ* datasets used to train and evaluate them. Soil does not freeze instantaneously at 0°C; rather, it passes through a thermodynamically prolonged transitional state—the *zero-curtain phase*—in which liquid water and ice coexist within the pore space, governed by soil texture, organic content, and antecedent moisture. This partially frozen state is biogeochemically active and hydrologically distinct from fully frozen ground, yet operational satellite products and the ground-truth records used to calibrate them largely rely on binary 0°C temperature thresholds that erase it entirely. Resolving this transitional state from field measurements requires constructing a Soil Freezing Characteristic Curve (SFCC)—the standard framework that quantifies the progressive depletion of liquid water with declining temperature and is the only *in situ* approach capable of resolving the zero-curtain period. However, the conventional SFCC relies on converting bulk dielectric permittivity to liquid water content, a conversion that introduces high uncertainties in organic-rich, clay-heavy, or moisture-variable soils—precisely the biome types where transitional dynamics are most pronounced and most ecologically consequential. The result is a systematic misrepresentation of freeze–thaw timing and duration that propagates from field sensor to satellite product to Earth System Model.

The central objective of this dissertation is to resolve this misrepresentation by building, evaluating, and applying a physically grounded, end-to-end framework that captures the full soil FT continuum—from the dielectric signal of an *in situ* sensor to the continental footprint of passive microwave satellites—and quantifies the ecological consequences of explicitly representing the transitional state. This objective is addressed through three sequential and mutually reinforcing research chapters, each resolving a distinct layer of the problem: first establishing a robust *in situ*

reference methodology that circumvents the calibration challenges inherent to frozen soils, then leveraging that framework to train and validate a probabilistic multi-frequency satellite retrieval, and finally deploying the resulting data record to attribute the spatiotemporal patterns of frozen ground to their environmental drivers and link the cryospheric state directly to cold-season carbon flux.

The first chapter proposes a reformulation of theorotical SFCC directly in permittivity–temperature space. By operating entirely within the dielectric domain, the approach bypasses the high-uncertainty conversion from bulk permittivity to liquid water content—a conversion that requires knowledge of ice content, soil porosity, and mineral permittivity that is difficult to obtain reliably in dynamic field environments. The SFCC model is fitted to measurements from 87 sites across eight Canadian monitoring networks spanning eastern and western boreal forests, prairies, and tundra, using Bayesian hierarchical partial pooling to derive stabilized network-level estimates of the freezing onset temperature (T_f: 0.15–0.44 °C) and transition sharpness (b: 0.92–3.47 °C^{-1}). The analysis empirically demonstrates that the transitional state is not an edge case but a significant seasonal feature: it persists for over 100 days in moisture-rich eastern boreal networks insulated by thick organic horizons, for 30–60 days in drier western boreal and prairie networks, and for over 40 days even in tundra sites under extreme cold. These results establish that surface insulation—from litter, moss, vegetation cover, and snow—and soil moisture—not air temperature alone—govern the frozen ground regime across Canadian ecozones and that the analysis produces the biome-specific SFCC parameters that serve as physically grounded training labels in the chapter that follows.

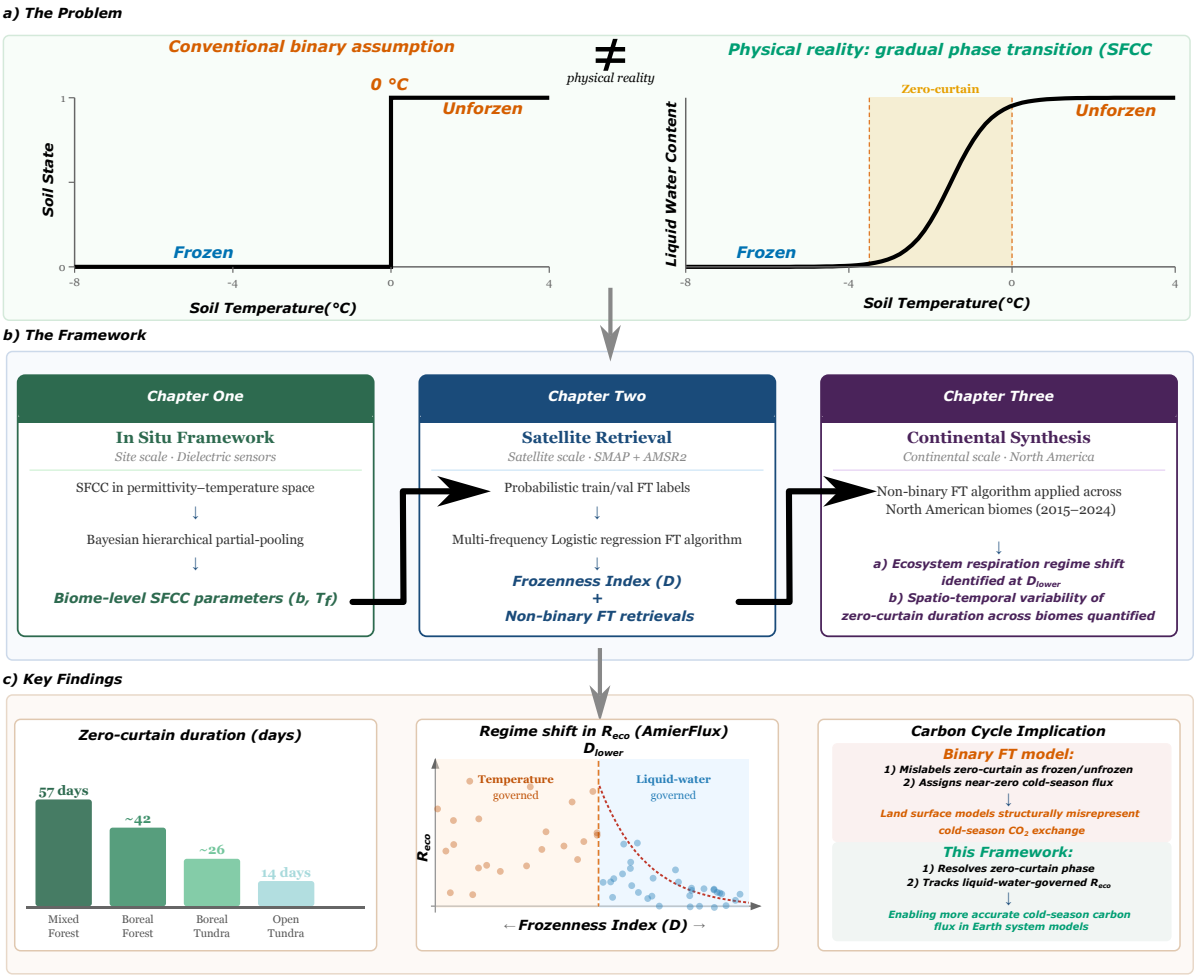
Building directly on this *in situ* characterisation, the second chapter develops a probabilistic, non-binary FT detection model driven by multi-frequency passive microwave observations. A biome-stratified logistic regression model integrates the SMAP L-band Normalized Polarization Ratio (Z_{NPR}) with the AMSR2 Ka/Ku-band Normalized Difference V-Pol index (Z_{NDV})—a parsimonious two-feature combination selected through mutual information analysis and feature ablation as the optimal balance between dielectric sensitivity in open biomes and canopy-scattering sensitivity in forested environments. Critically, ground-state training labels are derived using the biome-specific SFCC parameters established in Chapter 1, which isolate high-confidence frozen and unfrozen end-members from the inherently ambiguous shoulder-season data, rather than applying the universal 0°C thresholds that confound existing training datasets. Evaluated against a three-product consensus of FT-SMAP, FT-ESDR, and FT-SMOS across a randomized spatial sample, the framework achieves match rates of 78.8–98.2% and Cohen's Kappa values of 0.44–0.87 across five North American biomes, with performance following a physically interpretable gradient from open tundra to canopy-dense mixed forests. Thermodynamic validation confirms that the mathematically derived transitional class anchors to the latent heat of fusion across all

biomes, not to radiometric artefacts. The chapter introduces the continuous Frozenness Index (D)—a standardized geometric distance from the logistic decision boundary that tracks the progressive depletion of soil liquid water during the phase change and scales coherently to the continental domain—which constitutes the primary diagnostic variable for the final chapter.

The third chapter applies this nine-year non-binary retrieval record (2015–2024), corroborated by the independent FT-SMOS product, to pursue two interconnected scientific objectives: quantifying the spatiotemporal patterns and environmental drivers of frozen and zero-curtain days across North American biomes, and establishing a mechanistic linkage between the Frozenness Index and cold-season ecosystem respiration. Spatial analysis reveals a counter-intuitive, non-latitudinal pattern: zero-curtain duration peaks in mid-latitude mixed forests (57.4 days) and reaches its minimum in the high-Arctic tundra (13.7 days)—a pattern that atmospheric temperature alone cannot explain. Biome-level co-variation analysis identifies fall vegetation density (NDVI) as showing the clearest and most monotonic correspondence with zero-curtain duration across the five North American biomes, consistent with the role of dense canopies in intercepting outgoing longwave radiation and buffering soil thermal dynamics. An XGBoost attribution framework with SHAP decomposition confirms that while spring and fall atmospheric temperatures constitute the primary global controllers of total frozen ground frequency, dense forest canopies trigger a structural regime shift in which sub-canopy snowpack supersedes direct thermal forcing as the dominant driver of frozen ground duration. Finally, piecewise regression of AmeriFlux ecosystem respiration (R_{eco}) against the Frozenness Index (D) demonstrates that the metabolic shutdown threshold aligns precisely with the satellite-derived onset of the zero-curtain phase, and boundary line analysis reveals an exponential decay in maximum respiratory potential as soil liquid water content is progressively depleted by freezing—empirically confirming that liquid water content, not temperature, governs cold-season carbon flux once the soil enters the transitional state.

Taken together, these three chapters advance environmental science along two complementary axes. Methodologically, they deliver a coherent, end-to-end progression—from a sensor-agnostic, calibration-free *in situ* monitoring framework to a physically validated multi-frequency satellite retrieval—that can be operationalized within existing passive microwave FT retrieval frameworks. Conceptually, the integrated findings reframe the transitional soil state from a classification artefact into an ecologically necessary quantity: its onset constitutes a hard thermodynamic boundary on cold-season carbon flux that binary models are structurally incapable of detecting, and its duration is governed by landscape properties more than air temperature alone. As accelerating Arctic warming continues to reshape the timing, duration, and spatial extent of SFG, the methodology and retrieval record developed here provide the diagnostic tools needed to reduce uncertainty in global carbon cycle estimates and improve how land surface and Earth System Models simulate cold-season carbon fluxes and freeze–thaw phenology across the seasonally frozen domain.

Graphical Abstract



Acknowledgements

To Negar — you never asked me to be anywhere other than where I needed to be, even when that meant late nights, missed weekends, and years of a partner who was always half somewhere else. You carried us through it without ever once making me feel guilty for it. We met when I was a master's student and you have still never met a version of me that was not a student; thank you for waiting so patiently to find out who that person is. You are the quietest and most complete kind of love I know, and none of this exists without you.

To my parents — you wanted to be in the room for the defence, and the distance made that impossible, but you were never absent from any of it. Everything I know about patience and stubbornness in the face of a hard problem I learned from the two of you, and it is on every page of this work.

To my supervisor, Alexandre — first of all, you were never only a supervisor. I am glad I made it to this step, not because it means the PhD is finished, but because it means I managed to follow the first rule of the lab (those who know the first rule will know). Thank you for the hours on the road to the field, for trusting me with the work, and for the fact that every trip left us closer and left me with another story worth keeping. A few months into this PhD I already knew I was in the good old days, rather than realising it only once they were gone,[1] and that was entirely because of you. That you are a husband and a father of three and still made time whenever anyone needed you says more than I can fit here. You are an exceptional scientist with an even bigger personality, and I was very lucky to do this with you.

To my co-supervisor, Aaron — being in different cities never made you any less present, and the fieldwork, workshops, and conferences we shared in person were a genuine pleasure on top of that. Thank you for the freedom you gave me, and for the room to explore on my own terms, but also for the questions you asked when I brought the results back. Your instinct for what the numbers were and were not saying shaped how I think about data far more than you probably realise, and it was an honour to have you as a supervisor.

To Esteban and Alex G., aka Galex — I came out of this PhD with two real friends. I regret the days I could not be on campus at UQTR (and who knows, you may yet talk me into moving to

[1] Bernard, A. (2013). *Finale.* The Office, Season 9, Episode 23. NBC.

Trois-Rivières), and I know what I was missing, because I could tell from every field trip and every beer we shared. Thank you for your kindness and for how easily you made room for me. You are both warm, sharp, and genuinely lovely people, and I have no doubt we will still be calling each other friends a long time from now.

To my labmates Azza, Camille, and Rémi — thank you for your help through the hardest of the fieldwork. It simply would not have been possible without you.

Finally, my thanks to the members of the jury for their time and their feedback, and to Xiaolan Xu in particular for making the trip from Pasadena to Trois-Rivières.

Contents

Résumé **iv**

Abstract **viii**

Graphical Abstract **xi**

Acknowledgements **xii**

1 General Introduction **1**

1.1 Context and Background 1
1.2 Problem Statement 6
1.3 Research Objectives 8
1.4 Thesis Structure 9
1.5 References 11

2 *In situ* Monitoring of Seasonally Frozen Ground **18**

2.1 Introduction 22
2.2 Materials and Methods 24
2.2.1 Data Collection 24
2.2.2 Data Preprocessing 26
2.2.3 Data Processing 27
2.2.4 Data Postprocessing 30
2.3 Results 31
2.3.1 Evaluation of SFCC Fits and Parameter Analysis 31
2.3.2 Model Application to Field Data 33
2.4 Discussion 35
2.5 Conclusions 41
2.A Appendix 44
2.A.1 CS616 (Campbell Scientific) 44

2.A.2 HydraProbe (Stevens Water) . . . 45
2.A.3 Instrumentation Setup . . . 46
2.A.4 Derivation of Bai et al.'s Model in Permittivity-Temperature Space . . . 46
Supplementary Material . . . 49
S1 Extended Context on Soil Freezing Theory and Measurement . . . 49
S2 Extended Context on Technical Challenges in Estimating Unfrozen Water Content from Dielectric Measurements . . . 50
S3 Modeled Soil Data . . . 51
S4 Extended SFCC Parameter Data . . . 51
S5 Biome-Level Parameter Estimation . . . 52
S6 Supplementary Figures . . . 52
2.7 References . . . 52

3 Non-Binary Passive Microwave Freeze–Thaw Retrievals 65
3.1 Introduction . . . 69
3.2 Data and Methods . . . 71
3.2.1 Ground Reference Data . . . 71
3.2.2 Passive Microwave Satellite Observations . . . 73
3.2.3 Data Preparation and Exploratory Analysis . . . 75
3.2.4 Model Training and Evaluation . . . 78
3.2.5 Evaluation and Benchmarking . . . 81
3.2.6 Physical Validation and Thermodynamic Consistency . . . 82
3.3 Results . . . 83
3.3.1 Feature Selection and Physical Validation . . . 83
3.3.2 Preprocessing Validation and Training Representativeness . . . 84
3.3.3 Physical Interpretation of Regional Model Dynamics . . . 86
3.3.4 Comparative Classification Accuracy . . . 88
3.3.5 Thermodynamic Validation of the Transition Zone . . . 90
3.4 Discussion and Conclusion . . . 92
Supplementary Material . . . 100
S1 Microwave Indices and Reference Baselines . . . 100
S2 Feature Discriminability and Physical Validation . . . 101
S3 Preprocessing Validation and Training Representativeness . . . 104
S3.1 Validation of Local Radiometric Scaling . . . 104
S3.2 Domain Representativeness of the Training Subset . . . 105
S4 Extended Algorithmic Evaluation and Inter-Mission Benchmarking . . . 107

S4.1 Inter-Mission Pairwise Agreement and Baseline Variance 107
S4.2 Localized Benchmarking Against *in situ* Soil Temperature Networks . . 108
S5 Thermodynamic Validation of the Transition Zone 110
3.6 References 111

4 Frozen Ground Dynamics and Ecosystem Respiration 121
4.1 Nomenclature 125
4.2 Introduction 126
4.3 Data and Methods 128
4.3.1 Study Domain and Spatial Stratification 128
4.3.2 Passive Microwave Freeze–Thaw Data Records 128
4.3.3 Phenology Extraction and Frequency Metrics 129
4.3.4 Spatiotemporal Trend Analysis 130
4.3.5 Environmental Predictors of Frozen Ground 130
4.3.6 Machine Learning Attribution and SHAP Analysis 131
4.3.7 AmeriFlux Data and Frozenness Index Definition 131
4.3.8 Piecewise Regression and Boundary Line Analysis 132
4.4 Results and Discussion 132
4.4.1 Baseline Spatial Patterns of the Freeze–Thaw Regime 132
4.4.2 Machine Learning Attribution of Frozen Ground Frequency 136
4.4.3 Mechanistic Linkage Between the Frozenness Index and Ecosystem Respiration 140
4.5 Conclusion 143
Supplementary Material 146
S1 Extended Results 146
S1.1 Feature Selection and Correlation Analysis 146
S1.2 Baseline Spatial Patterns of the Freeze–Thaw Regime 148
S1.3 Interannual Trends and Variability 149
S1.4 Within-Biome Pixel-Level Regression of Fall Zero-Curtain Duration . . 153
S2 FT-SMOS product performance 153
4.3 References 154

5 General Discussion and Conclusion 159
5.1 Opening Synthesis 159
5.2 Bridging Observational Scales: From Soil Sensor to Satellite 160
5.3 Biogeochemical Coupling and Earth System Implications 161
5.4 Limitations 162

5.5 Broader Impacts and Future Directions 164

Scientific Contributions **166**

List of Figures

1.1 Principal hydrological and ecological fluxes regulated by the soil freeze–thaw cycle. Hydrologically, soil freezing impedes infiltration and percolation, redirecting precipitation and snowmelt into surface runoff and suppressing groundwater recharge. Biologically, the cycle governs both above- and below-ground activity: while frozen conditions suppress plant evapotranspiration, the spring thaw reactivates root water uptake to initiate the growing season. Concurrently, below ground, the microbial community sustains the emission of greenhouse gases—CO_2, CH_4, and N_2O—throughout the cold season, linking the soil cryospheric state directly to the atmospheric trace-gas budget. Adapted from Ala-Aho et al. [2021]. . . . 2

1.2 Soil pore water fractions and their correspondence to zones of the Soil Freezing Characteristic Curve (SFCC). Pore water is partitioned into gravitational (unbound, large-pore), capillary, and hygroscopic (bound, surface-adsorbed) fractions, each retained at progressively higher energetic states. The SFCC traces the sequential freezing of these fractions: gravitational water freezes first near T_f, driving the steep liquid-water decline of Zone 2; capillary water freezes progressively; and hygroscopic bound water persists as liquid into Zone 3, constituting the residual water content W_r. W_0 denotes the initial (saturation-level) water content; T_s marks the temperature below which liquid water content stabilises at W_r. Adapted from Beach and Flood [2017] and Zhang et al. [2019]. 4

1.3 Conceptual framework of the freeze–thaw process and its dual regulation of soil water content and soil respiration, adapted from Du et al. [2013] and Mikan et al. [2002]. Both quantities share a common soil temperature axis: soil respiration (green line) and water content derived from the Soil Freezing Characteristic Curve (blue). The co-plotted curves make explicit the mechanistic link between the two variables across three thermodynamically distinct zones. In Zone 3 (below the freeze–thaw critical point T_s), liquid water is stable at its residual value, substrate availability is severely constrained, and temperature sensitivity is low ($Q_{10} \approx 3.5$; Du et al. 2013). In Zone 2 (between T_s and the bulk freezing point $T_f \approx 0\,^{\circ}C$), small temperature increases release disproportionate liquid water via the steep SFCC slope, rapidly expanding the substrate pool accessible to microorganisms and producing a strongly elevated apparent temperature sensitivity ($Q_{10} \approx 16$; Du et al. 2013). In Zone 1 (above T_f), liquid water is at its maximum and no longer limits microbial activity; temperature sensitivity returns to a moderate level ($Q_{10} \approx 7.8$; Mikan et al. 2002). The non-monotonic arc — low, then very high, then moderate — reflects the overriding control of liquid water availability on sub-zero respiration dynamics. 5

2.1 A typical Soil Freezing/Thawing Characteristic Curve (SFCC/STCC), adapted from Zhang et al. [2019]. T_f marks the temperature at which soil begins to freeze, while T_{res} indicates the temperature at which the liquid water content stabilizes near the residual water content. 23

2.2 Geographic distribution of monitoring networks across Canadian landscapes. The land cover map is adapted from Latifovic [2019]. 26

2.3 Comparison of observed and fitted effective permittivity values for freezing cycles. 32

2.4 CDFs of residuals across networks (**a**), showing most residuals are small with steep slopes near zero, indicating minimal bias. Residuals as a function of soil temperature (**b**), with random subsampling of an equal number of samples per network for balanced representation. 33

2.5 Forest plots showing the distribution of model parameters across networks: freezing point T_f **(a)** and shape factor b **(b)**. Squares indicate network means, and circles represent individual freezing cycles with vertical bars showing 95% confidence intervals. 34

2.6 Fitted SFCC **(a)** and corresponding time series of soil temperature, air temperature, snow cover, and freezing probability **(b)** for the EC17 site in the Kenaston network (prairie). The site location is available via the interactive map on GitHub: Soil-Temperature-Permittivity-Monitoring-Sites. 36

2.7 Similar to Fig. 2.6, but for the BT17 site in the Candle Lake network (western boreal forest). 37
2.8 Similar to Fig. 2.6, but for the BJ01 site in the Baie-James network (eastern boreal forest). 38
2.9 Similar to Fig. 2.6, but for the GR01 site in the George River network (tundra). 39
2.10 Monthly mean freezing probability for each network. Numbers within cells indicate monthly mean soil and air temperatures (T_s, T_a; °C), while the semi-transparent black fill of each cell represents the monthly mean snow cover (%). 40
A1 Instrumentation setup for soil moisture probes (CS616, HydraProbe, and TEROS12), with a schematic and corresponding probe images. 46
S1 Histogram of electrical conductivity (EC) values measured at Trail Valley Creek (TV), James Bay (BJ), La Romaine (LR), and Montmorency Forest (FM) sites. 53
S2 Soil Freezing Characteristic Curve (SFCC) visualized in both sensor raw output–temperature space and permittivity–temperature space. These representations highlight the freezing transition as captured directly by the sensor output and after conversion to effective permittivity. 53

3.1 Spatial distribution of the *in situ* validation stations overlaid on the study domain's land cover classification map. Sites assigned to the same DBSCAN-derived spatial block are represented in the same color. 77
3.2 Global feature importance ranking based on Mutual Information (MI) scores. The bar chart quantifies the non-linear dependency between each feature and the binary targets. 83
3.3 Time series of standardized radiometric anomalies for the Normalized Polarization Ratio (Z_{NPR}) and the Normalized Spectral Difference (Z_{NDV}) overlaid with *in situ* soil temperatures for five representative sites across distinct biomes. The top horizontal color bar, denoted as $P(F)$, represents the continuous probability of the frozen state calculated with the normalized SFCC. Within this probability bar, dark red indicates a high-confidence unfrozen classification, dark blue indicates a high-confidence frozen classification. 85
3.4 Two-dimensional KDE contour maps illustrating the joint multivariate feature space (Z_{NPR} versus Z_{NDV}) across five biomes. The plots display the spatial representativeness of the *in situ* training subset (red contours) overlaid on the primary density nodes of the broader environment background (blue shaded regions). 86

3.5 Two-dimensional physical feature space of the Normalized Polarization Ratio (Z_{NPR}) versus the Normalized Spectral Difference (Z_{NDV}) illustrating the logistic model decision boundaries across five distinct biomes. Blue and red points represent *in situ* high-confidence frozen and unfrozen observations respectively. The background gradient indicates the standardized physical distance (D, frozenness) from the decision boundary (dashed black line), with the yellow band representing the probabilistic transition zone. 87
3.6 Temporal evolution of the continuous physical distance D (Frozenness index), plotted alongside *in situ* soil and ERA5 air temperatures at a representative station. The top categorical ribbons compare the proposed logistic model's classification against the binary FT-SMAP, FT-ESDR, and FT-SMOS products. 90
3.7 Distribution of the 10-day rolling mean air temperature (ERA5) across model-derived unfrozen, transitional, and frozen states. Central black lines represent the median temperatures, with outliers omitted for visual clarity. The distinct staircase progression of medians supports the large ε^2 effect sizes reported in Table 3.6 and confirms the monotonic thermal ordering validated by the Jonckheere-Terpstra test. 92
3.8 Distribution of *in situ* soil temperature measurements (5 cm) categorized by model state. The transitional class (gold) is effectively pinned to the 0°C isotherm across all biomes, with the Tundra showing exceptional alignment to the latent heat plateau. This provides robust empirical evidence that the model accurately isolates the zero-curtain effect. 92
3.9 Phase change trajectories illustrating the shift in physical state across the two-dimensional microwave feature space (Normalized Polarization Ratio, Z_{NPR}, vs. Normalized Difference V-Pol, Z_{NDV}). Markers represent the bivariate centroids (mean feature values) for unfrozen, transitional, and frozen classifications within each biome. The connecting dashed lines trace the passive microwave phase-state trajectory through the bivariate feature space from the unfrozen to the frozen end-member. 94
3.10 Domain-wide application of the logistic model across the Northern Hemisphere during the autumn freeze-up (October to December 2016). The left column illustrates the continuous physical distance (D, Frozenness), capturing the thermodynamic intensity of the phase state. The right column displays the corresponding categorical classifications, highlighting the southward migration of the transitional phase boundary as the freezing front advances. 97

3.11 Same as Fig. 3.10, but for the spring thaw period (January to March 2017). The continuous distance maps capture the gradual retreat of the frozen state, while the categorical maps illustrate the northward migration of the transitional boundary as the thaw progresses. 98
S1 Spatial distribution of reference statistics used for index normalization. 100
S2 Pearson correlation matrix of all candidate input features computed across the double-balanced training set. 101
S3 Global distributional separability of frozen and unfrozen samples for candidate features. Box plots display the median and interquartile range. 102
S4 Distributional separability of frozen and unfrozen samples for candidate features, stratified by biome. Box plots display the median and interquartile range within each specific biome. 103
S5 Scatter plots of Z_{NPR} against Z_{NDV} for a randomly selected subset of observations, stratified by land cover class: (a) Tundra, (b) Boreal Tundra, (c) Boreal Forest, (d) Mixed Forest, and (e) Cropland. 104
S6 A/B preprocessing ablation study for Z_{NPR}. Kernel Density Estimation (KDE) distributions compare the *in situ* training pixels (red) against the broader environmental background samples (blue) across five biomes. The top row displays the raw, unscaled distributions, while the bottom row displays the locally scaled anomalies. The Two-Sample Kolmogorov-Smirnov D-statistic is provided to quantify the distributional alignment between the two samples. 105
S7 Same as Fig. S6, but for the vertical Normalized Difference Spectral Index (Z_{NDV}). 105
S8 One-dimensional Kernel Density Estimation (KDE) histograms evaluating the spatial representativeness of the *in situ* training subset. The distributions compare the selected training pixels (red) against the broader environment samples (blue) across five biomes. The top row displays the marginal distributions for the scaled polarization ratio (Z_{NPR}), and the bottom row displays the marginal distributions for the scaled spectral index (Z_{NDV}). 106
S9 Spearman's rank correlation (ρ) between the continuous index of frozenness (D) and the 10-day rolling mean air temperature. Points are color-coded by temperature and anchored at -2.5°C (gold) to highlight the transition zone. . . 110
S10 Scatter plot of index D versus *in situ* soil temperature. The concentration of observations at 0°C across the $D = 0$ decision boundary demonstrates the model's ability to capture the thermodynamic transition between zero-curtain and fully frozen states. 110

4.1 These maps display the mean spatial distribution of the freeze–thaw regime across North America (2015–2024) derived from the FT-CUSTOM product. They illustrate the multi-year mean accumulation of (a) strictly frozen days and (b) zero-curtain days. The lower panels display the corresponding mean phenological timing for the (c) end of growing season (EOS) and (d) start of growing season (SOS). 134

4.2 Biome-level co-variation between fall zero-curtain duration and six environmental predictors across five North American ecosystems. Each point represents a biome mean; error bars indicate ±1 standard deviation of pixel-level values within each biome. Panels show fall zero-curtain duration against: (a) mean fall NDVI, (b) mean fall soil moisture, (c) mean fall SWE, (d) mean fall air temperature, (e) clay fraction, and (f) soil organic carbon. The figure documents biome-level descriptive patterns rather than pixel-scale mechanistic relationships. 136

4.3 A SHAP summary beeswarm plot visualizes the primary global machine learning model (trained on the FT-CUSTOM target). Predictors are ranked on the y-axis by their mean absolute SHAP value, representing their average impact on the predicted total frozen duration (annotated in brackets). The x-axis illustrates the specific impact of individual pixel observations on the model output, measured in days. Dot color represents the raw feature value from low (blue) to high (red). . 138

4.4 A heatmap depicts the shifting mean absolute SHAP values (impact in days), stratified by distinct structural landcover classes. Color intensity indicates the magnitude of each environmental predictor's influence on the total frozen ground duration. The visualization highlights a critical regime shift: while atmospheric temperatures strictly dominate the freeze–thaw dynamics in open biomes like the tundra, the relative influence of structural modifiers such as snow water equivalent (SWE) and vegetation density increases significantly in complex forested environments. 140

4.5 Scatter plots demonstrate the relationship between ecosystem respiration (R_{eco}) and the passive microwave Frozenness Index (D) across four biomes: (a) cropland, (b) mixed forest, (c) boreal forest, and (d) boreal tundra. The optimal threshold identified by piecewise regression (red dashed line) aligns closely with the lower boundary (D_{lower}, left dotted line), marking the onset of the zero-curtain phase. Data points are color-coded by ground-measured soil temperature (T_{soil}), illustrating that the zero-curtain zone anchors strictly to near-0°C conditions. The green line represents the maximum flux limit (75th percentile envelope) mapping the exponential decay of respiratory potential. 142

4.6 Distributional box plots illustrate ecosystem respiration (R_{eco}) categorized by soil phases (strictly frozen, zero-curtain, and unfrozen) across the four evaluated biomes. The distributions display a clear, step-wise down-regulation of biological activity as the landscape progresses through the freezing phase change, culminating in a deeply dormant phase with minimal flux variance during the strictly frozen period. 143

S1 Pearson correlation matrix evaluating multicollinearity among the features. The analysis utilizes the balanced dataset across the targeted landcover classes. Note that the seasonal snow fraction predictors indicate the total number of days with snow cover per season, based on IMS data [Center, 2004]. Detailed descriptions of all remaining features and their original data sources are outlined in the methodology Sect. 4.3.5. 146

S2 Mutual Information (MI) scores of the selected features relative to the target variable. The dataset was balanced across landcover classes to prevent class imbalance from skewing the information gain. The snow fraction variables represent the number of days per season with snow cover, derived from IMS data [Center, 2004]. Detailed descriptions of all remaining features and their original data sources are outlined in the methodology Sect. 4.3.5. 147

S3 These maps present the mean spatial distribution of the freeze–thaw regime across North America (2015–2024) derived from the FT-SMOS product. They illustrate the multi-year mean accumulation of (a) strictly frozen days and (b) zero-curtain days. The lower panels display the corresponding mean phenological timing for the (c) end of growing season (EOS) and (d) start of growing season (SOS). . . 148

S4 Annual Mann-Kendall trends indicate the frozen, zero-curtain, and total frozen ground duration in days. Both products capture highly dynamic interannual fluctuations, with predominantly non-significant long-term linear trends across most land covers. 149

S5 Fall season Mann-Kendall trends indicate the frozen, zero-curtain, and total frozen ground duration in days. The results demonstrate consistent tracking between the CUSTOM and SMOS products alongside high interannual variance. Tundra region exhibits a localized trend in frozen days. 150

S6 Spring season Mann-Kendall trends replicate the analysis of Fig. S5 for the spring season. The data demonstrate consistent tracking between the CUSTOM and SMOS products alongside high interannual variance, with no significant trends observed. 150

S7 This plot illustrates the interannual variability in the EOS timing (2015–2023). The CUSTOM and SMOS trajectories show excellent agreement in capturing early versus late freeze years, with no significant trends observed. 151
S8 This plot illustrates the interannual variability in the SOS timing (2015–2023), mirroring Fig. S7. The timing of the spring thaw exhibits fluctuations with non-significant linear trends over the observational period. Both products track each other closely. 151
S9 Interannual variability in the cold-season duration — defined here as the continuous phenological interval between the end of growing season (EOS) and the start of growing season (SOS) — from 2015 to 2023. Unlike the frequency metrics reported in Fig. S4–S6, which represent aggregate counts of daily soil-state labels, this metric capture the total elapsed time between the onset of sustained freezing and the onset of sustained thawing. Both products exhibit highly dynamic interannual variability with no statistically significant directional trend over the observational period. 152
S10 Within-biome coefficient of determination (R^2) for ordinary least-squares regressions of fall zero-curtain duration against six environmental predictors, computed independently for each of the five North American biomes using pixel-level observations averaged across the 2015–2024 record. Asterisks denote raw OLS significance (* $p < 0.05$, ** $p < 0.01$, *** $p < 0.001$), which should be interpreted cautiously given spatial autocorrelation between adjacent 9 km pixels. The uniformly low R^2 values across all predictor–biome combinations indicate that none of the seasonal variables employed here explains a meaningful fraction of spatial variance in zero-curtain duration within any individual biome. 153

List of Tables

2.1 Summary of soil moisture sensor deployment across our networks 25
2.2 Performance of SFCC curve fitting by network. Relative RMSE and MAE (shown in parentheses) were normalized by the per-network dynamic range. "Overall (balanced)" represents random subsampling with an equal number of samples per network to mitigate overrepresentation effects. 31
2.3 Posterior means and 95% credible intervals of b and T_f from hierarchical partial pooling across networks. 35
S1 Modeled soil physical properties and organic carbon across networks. 51
S2 Soil Freezing Characteristic Curve (SFCC) parameters by network. 51
S3 Biome-level b parameters with 95% Highest Density Intervals (HDI). 52
S4 Biome-level T_f (°C) parameters with 95% Highest Density Intervals (HDI). . . 52

3.1 Biome stratification and UMD land cover aggregation. 75
3.2 Mutual information (MI) scores stratified by biome. 84
3.3 Production logistic regression parameters and cross-validation evaluation metrics, stratified by biome. Model coefficients (β_0, β_1, β_2) and the EER-optimized threshold (τ_{opt}) are from the final production model trained on all available data (script 06). The transition bounds ($[D_{\text{lower}}, D_{\text{upper}}]$) denote the standardized 10% and 90% probability distances from the decision boundary, scaled by 0.5. PR AUC (mean ± std) is reported from spatially independent cross-validation (script 05) and represents the honest out-of-sample performance estimate. . . . 87
3.4 Cross-validation classification metrics aggregated across all spatially independent test folds, stratified by biome. N denotes the total number of test observations pooled across unique (non-padding) folds. Sensitivity and specificity are computed with respect to the frozen class. Balanced accuracy is the arithmetic mean of sensitivity and specificity. 88

3.5 Performance of the optimized logistic model evaluated against a 3-way unanimous consensus pseudo-truth (FT-SMAP, FT-ESDR, and FT-SMOS). The evaluation was conducted over a randomized spatial sample across North America during non-summer months. The Consensus Ratio indicates the percentage of non-summer days where all three reference datasets unanimously agreed on the physical ground state. 89

3.6 Physical validation statistics for model-derived freeze–thaw states across diverse biomes. Columns report the in-band temperature fraction (%) for each class, Spearman's rank correlation (ρ), rank-based epsilon-squared effect size (ε^2), and the Jonckheere-Terpstra standardized statistic (Z). 91

S1 Comparative feature ablation study across five major biomes. Values represent the change in Precision–Recall Area Under Curve (ΔPR AUC) when altering the baseline parsimonious model (Z_{NPR} + Z_{NDV}). Negative values indicate performance degradation relative to the baseline configuration. 103

S2 Quantitative assessment of spatial representativeness comparing the *in situ* training subset to the broader environmental background. The 1D marginal distributions are evaluated using the Two-Sample Kolmogorov-Smirnov D-statistic and Wasserstein Distance (in standard deviations). The 2D joint feature space (Z_{NPR} and Z_{NDV}) is evaluated using the Maximum Mean Discrepancy (MMD). 107

S3 Pairwise agreement analysis quantifying inter-mission consistency across the study domain. Metrics represent the raw Agreement Percentage (%) and Cohen's Kappa (κ) between the proposed logistic model and the operational satellite products during non-summer months. This evaluation highlights the baseline variance expected between independent operational retrievals. 108

S4 Comparative accuracy assessment strictly isolating the non-summer period. Metrics evaluate the proposed logistic model against operational AMSR, SMAP, and SMOS products using spatially harmonized *in situ* soil temperature data. Summer months were masked using processing mask to prevent trivial classifications from inflating performance metrics. 109

4.1 Mean annual strictly frozen, zero-curtain, and total frozen ground days, alongside climatological freeze and thaw timing by biome, derived from the primary FT-CUSTOM product (2015–2024). Values in parentheses denote the number of zero-curtain days specifically occurring during the fall freeze-up phase. The corresponding FT-SMOS corroboration dataset is provided in Table S1. 134

4.2 Cross-validated predictive performance of the XGBoost model trained on the primary FT-CUSTOM target, reported across global and biome-specific domains. R^2 and MAE values represent means ± standard deviation across leave-P-years-out cross-validation folds. The corresponding FT-SMOS product performance is provided in Table S2. 137

S1 Mean annual strictly frozen, zero-curtain, and total frozen ground days, alongside climatological freeze and thaw timing by biome, derived from the independent FT-SMOS product (2015–2024). Values in parentheses denote the number of zero-curtain days specifically occurring during the fall freeze-up phase. This table is provided as a corroboration of the primary FT-CUSTOM results (Table 4.1); the two products are algorithm-independent and differ in sensor, retrieval architecture, and spatial footprint, so absolute offsets are expected. Interannual directional agreement between the products is discussed in Sect. 3.3. 148

S2 Cross-validated predictive performance of the XGBoost model trained on the independent FT-SMOS target, reported across global and biome-specific domains. R^2 and MAE values represent means ± standard deviation across leave-P-years-out cross-validation folds. This table is provided as a corroboration Table 4.2; near-equivalent performance across both targets indicates that the attribution results are not an artefact of the FT-CUSTOM retrieval. 153

Chapter 1

General Introduction

1.1 Context and Background

The global climate system is warming at an accelerating rate, with the Arctic and subarctic regions experiencing temperature increases that consistently exceed the global mean—a phenomenon known as Arctic amplification [Rantanen et al., 2022]. This warming trend is driving the widespread degradation of the terrestrial cryosphere [Meredith et al., 2019]. A geophysically significant components of this changing cryosphere is *seasonally frozen ground* (SFG), which affects most land areas above 45°N latitude [Zhang, 2003] and regulates a suite of critical land-surface processes with direct implications for hydrology, biogeochemistry, and ecology in cold regions. Under ongoing warming, the duration and spatial extent of SFG across the Northern Hemisphere have been declining at measurable rates [Li et al., 2021, Yang et al., 2025a], highlighting the need to understand and monitor its dynamics.

SFG is defined as the condition in which soil pore water turns to ice during the cold season [Williams and Smith, 1989, Zhao et al., 2026]. It plays a fundamental role in the land-surface energy and water balance, influencing ecological, hydrological, and biological processes across vast boreal, subarctic, and Arctic landscapes [Ala-Aho et al., 2021, Hayashi, 2013, Zhao et al., 2026]. Hydrologically, the freeze–thaw (FT) cycle of the soil exerts first-order control on infiltration capacity, groundwater recharge, and streamflow generation [Chang et al., 2012]. When soil water freezes, hydraulic conductivity drops by several orders of magnitude, impeding vertical drainage and redirecting precipitation and snowmelt into surface runoff [Hayashi, 2013]. Conversely, the spring thaw releases this hydraulic constraint, enabling recharge of groundwater stores and sustaining baseflow in snowmelt-dominated river systems throughout the warm season [Zhao et al., 2026]. The timing of the FT cycle also governs the onset and duration of biological activity across cold-region ecosystems. Above ground, the spring thaw initiates plant root water uptake, coupling the soil cryospheric state directly to growing season length and broader

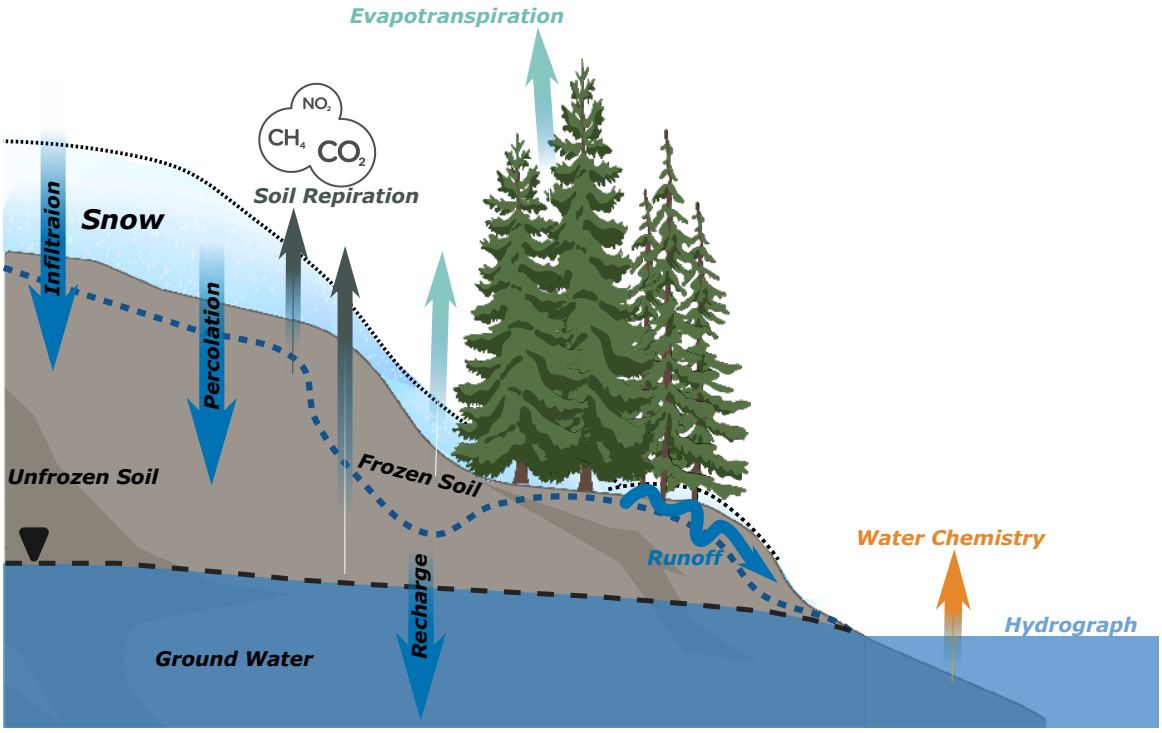


Figure 1.1: Principal hydrological and ecological fluxes regulated by the soil freeze–thaw cycle. Hydrologically, soil freezing impedes infiltration and percolation, redirecting precipitation and snowmelt into surface runoff and suppressing groundwater recharge. Biologically, the cycle governs both above- and below-ground activity: while frozen conditions suppress plant evapotranspiration, the spring thaw reactivates root water uptake to initiate the growing season. Concurrently, below ground, the microbial community sustains the emission of greenhouse gases—CO_2, CH_4, and N_2O—throughout the cold season, linking the soil cryospheric state directly to the atmospheric trace-gas budget. Adapted from Ala-Aho et al. [2021].

ecosystem functioning [Kim et al., 2012]. Below ground, the physical state of the soil acts as a master switch for biogeochemical cycling [Natali et al., 2019, Arndt et al., 2023, Schuur et al., 2015]. By dictating the timing of microbial reactivation and respiration, the duration of frozen ground becomes a critical determinant of the annual carbon balance of northern ecosystems. The principal hydrological and ecological fluxes regulated by the soil FT cycle are summarised in Fig. 1.1.

A thermodynamically distinct and ecologically pivotal feature of the SFG cycle is the *zero-curtain effect*: a period during which latent heat exchanged at the liquid-to-ice phase boundary stabilises soil temperatures near 0 °C, allowing liquid water and ice to coexist simultaneously within soil pores [Outcalt et al., 1990]. During this transitional period, the soil occupies an intermediate physical state—neither fully frozen nor fully unfrozen—with thermal and hydrological properties [Hayashi, 2013] and biogeochemical properties [Mikan et al., 2002, Mavrovic et al., 2023, Du et al., 2013] that are fundamentally distinct from both the frozen and unfrozen end-members.

The progression through these three states is described quantitatively by the Soil Freezing Characteristic Curve (SFCC). The SFCC (Fig. 1.2) describes the relationship between soil liquid water content (θ_{lw}) and sub-zero temperature [Koopmans and Miller, 1966, Spaans and Baker, 1996]: as temperature decreases below the freezing onset point (T_f), liquid water is progressively expelled from soil pores and replaced by ice, following an exponential decay characterised by the transition sharpness parameter b [Bai et al., 2018]. This process defines three thermodynamically distinct zones—the unfrozen zone (above T_f, Zone 1), the transitional zone (the zero-curtain period where liquid water and ice coexist, Zone 2), and the residual zone (where liquid water is largely depleted, Zone 3)—each with distinct thermal, hydrological, and biogeochemical properties. The progressive, rather than abrupt, nature of the SFCC reflects the thermodynamic heterogeneity of pore water within the soil matrix. Soil water exists in three energetically distinct fractions: gravitational (free) water, held loosely in large inter-particle pores and draining readily under gravity; capillary water, retained within smaller pores by cohesive surface-tension forces; and hygroscopic (bound) water, tightly adsorbed to mineral particle surfaces at high tension [Beach and Flood, 2017, Osman, 2012, Zhang and Pei, 2021]. These fractions freeze in a strict energetic sequence: gravitational water freezes first, at temperatures just below T_f, driving the steep initial decline in liquid water content that characterises Zone 2; capillary water freezes progressively as temperature continues to fall; and hygroscopic bound water—held at the highest adsorption energies—remains largely unfrozen throughout Zone 2 and constitutes nearly all of the residual liquid water content W_r in Zone 3 [Chen et al., 2021, Tian et al., 2014] (Fig. 1.2). It is precisely this energetic hierarchy that sustains a film of liquid water on mineral surfaces at temperatures well below T_f, maintaining the substrate availability on which sub-zero microbial activity depends [Hu et al., 2020, Watanabe and Osada, 2017].

The fall zero-curtain period can extend for weeks, depending on soil organic content, antecedent moisture, and the insulating properties of the snowpack and overlying vegetation [Davesne et al., 2022, Prince et al., 2019]. This extended duration carries profound biogeochemical consequences. Because microbial respiration in cold soils is regulated critically by the availability of liquid water rather than temperature alone [Mikan et al., 2002, Harrysson Drotz et al., 2010], the zero-curtain sustains heterotrophic activity well into the winter. As long as the energetic hierarchy of the SFCC maintains an unfrozen water film, microbes can metabolise soil organic matter and release CO_2 at sub-zero temperatures. CO_2 emissions accumulated during this phase can equal or exceed those of the entire remaining winter, and are large enough to convert high-latitude landscapes from net growing-season carbon sinks into net annual sources [Arndt et al., 2023, Natali et al., 2019]. The temperature sensitivity of this microbial activity is itself governed by the SFCC (Fig. 1.3). Du et al. [2013] demonstrated that sub-zero soil respiration follows two thermodynamically distinct regimes separated by the *freeze–thaw critical point*—the temperature

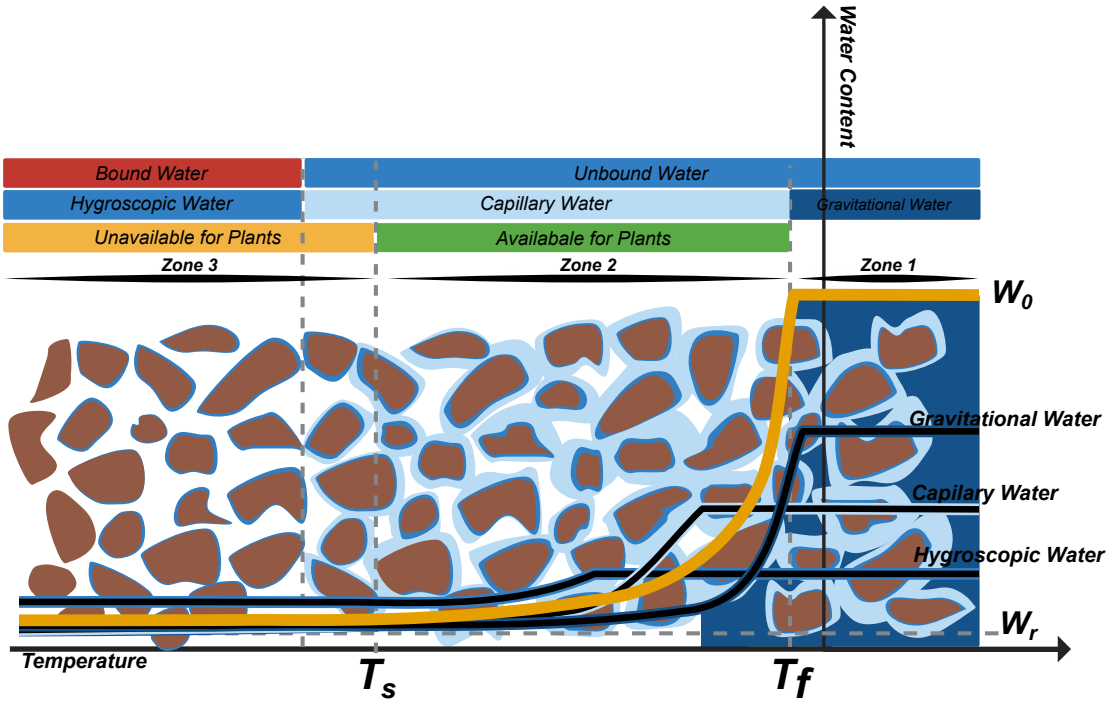


Figure 1.2: Soil pore water fractions and their correspondence to zones of the Soil Freezing Characteristic Curve (SFCC). Pore water is partitioned into gravitational (unbound, large-pore), capillary, and hygroscopic (bound, surface-adsorbed) fractions, each retained at progressively higher energetic states. The SFCC traces the sequential freezing of these fractions: gravitational water freezes first near T_f, driving the steep liquid-water decline of Zone 2; capillary water freezes progressively; and hygroscopic bound water persists as liquid into Zone 3, constituting the residual water content W_r. W_0 denotes the initial (saturation-level) water content; T_s marks the temperature below which liquid water content stabilises at W_r. Adapted from Beach and Flood [2017] and Zhang et al. [2019].

at which liquid water stabilises at its residual value W_r, corresponding to the base of Zone 3 on the SFCC. In the transitional zone above this critical point, where pore water is still declining steeply along the SFCC curve, the apparent Q_{10} value (the factor by which respiration increases per 10 °C rise in temperature) is approximately 16, because small temperature increases release disproportionate amounts of liquid water from pore ice, rapidly expanding microbial substrate availability; below the critical point, in Zone 3 where only tightly bound water remains, Q_{10} drops to approximately 3.5 [Du et al., 2013, Wang et al., 2014]. In permafrost-affected tundra and boreal ecosystems, the transitional shoulder seasons—spanning both the fall zero-curtain and the spring thaw—contribute approximately 27% of total annual soil respiration, while winter months account for a further 15% [Watts et al., 2021].

Recent modelling work has demonstrated that improving the representation of latent heat exchange in the phase-change scheme of a land surface model — which better reproduced

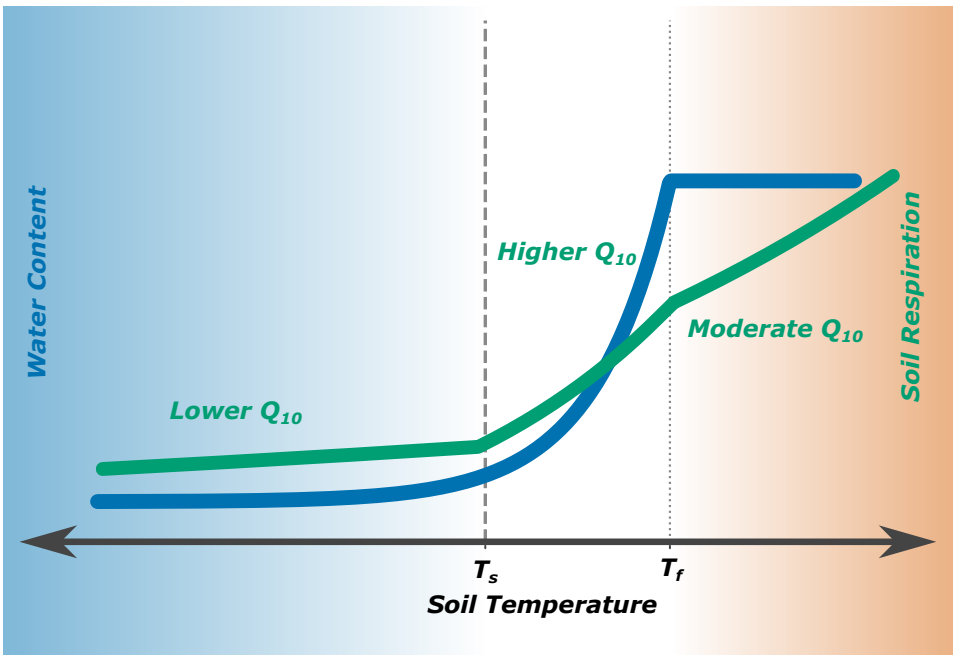


Figure 1.3: Conceptual framework of the freeze–thaw process and its dual regulation of soil water content and soil respiration, adapted from Du et al. [2013] and Mikan et al. [2002]. Both quantities share a common soil temperature axis: soil respiration (green line) and water content derived from the Soil Freezing Characteristic Curve (blue). The co-plotted curves make explicit the mechanistic link between the two variables across three thermodynamically distinct zones. In Zone 3 (below the freeze–thaw critical point T_s), liquid water is stable at its residual value, substrate availability is severely constrained, and temperature sensitivity is low ($Q_{10} \approx 3.5$; Du et al. 2013). In Zone 2 (between T_s and the bulk freezing point $T_f \approx 0\,^{\circ}\mathrm{C}$), small temperature increases release disproportionate liquid water via the steep SFCC slope, rapidly expanding the substrate pool accessible to microorganisms and producing a strongly elevated apparent temperature sensitivity ($Q_{10} \approx 16$; Du et al. 2013). In Zone 1 (above T_f), liquid water is at its maximum and no longer limits microbial activity; temperature sensitivity returns to a moderate level ($Q_{10} \approx 7.8$; Mikan et al. 2002). The non-monotonic arc — low, then very high, then moderate — reflects the overriding control of liquid water availability on sub-zero respiration dynamics.

zero-curtain duration and soil thermal conditions — reduced simulation errors in cold-season CO_2 emissions by approximately 70% [Tao et al., 2021]. As climate change continues to compress the strictly frozen period and extend the seasonal freeze–thaw transition across northern landscapes [Tao et al., 2021, Li et al., 2021], the need for physically consistent, spatially resolved observations of zero-curtain dynamics has become increasingly pressing for global carbon cycle science.

To track land surface FT processes across vast and inaccessible northern landscapes, we require observational approaches that operate at broader spatial and temporal scales than point-based ground networks can provide. Passive microwave remote sensing from satellite platforms provides the primary operational approach for delivering daily observations of land surface FT state at

continental to global extents [Zuerndorfer et al., 1990, Kim et al., 2011, Xu et al., 2023, Derksen et al., 2017, Rautiainen et al., 2025]. The physical basis for this capability lies in the large contrast in dielectric permittivity between liquid water and ice: as soil water freezes, the microwave emissivity of the land surface increases sharply, producing a distinctive brightness temperature signature detectable from orbit [Rautiainen et al., 2014]. Different microwave frequencies provide complementary information. L-band observations at 1.4 GHz, provided by satellites including the Soil Moisture Active Passive (SMAP) and Soil Moisture and Ocean Salinity (SMOS) missions, among others, maximise the dielectric contrast associated with the liquid-to-ice phase transition and penetrate more deeply through vegetation canopies, offering direct sensitivity to near-surface soil permittivity [Roy et al., 2015, Rautiainen et al., 2014]. Higher-frequency Ka-band (36.5 GHz) and Ku-band (18.7 GHz) observations from the Advanced Microwave Scanning Radiometer 2 (AMSR2) have shallower sensing depths but are highly sensitive to scattering from snow microstructure and near-surface conditions, serving also as strong proxies for land surface temperature [Kim et al., 2011]. Together, these sensors observe the land surface at daily to sub-daily temporal resolution with global coverage, making them well-suited for tracking the progression of seasonal FT cycles across the entire Northern Hemisphere.

1.2 Problem Statement

Despite the recognised importance of SFG dynamics, limitations at each observational scale—both in ground-based monitoring and in satellite remote sensing—impede a physically coherent, multi-scale understanding of the FT cycle and its role in the Earth system.

Limitation at the site scale: the binary 0 °C threshold and SFCC parameterisation. A common approach to characterising SFG state in ground-based monitoring networks relies on a binary temperature threshold of 0 °C to distinguish frozen from unfrozen soil. This classification fundamentally misrepresents the physics of soil freezing, which is not a step function but a gradual, continuous process governed by the Soil Freezing Characteristic Curve (SFCC). By collapsing this continuous process into a binary classification, the 0 °C threshold systematically misidentifies soils in the transitional state, which can persist for weeks to months and sustain significant biogeochemical activity. This misclassification not only distorts our understanding of SFG dynamics at the site scale but also propagates errors into the development and validation of satellite FT products that rely on *in situ* data as reference. The SFCC provides a physically grounded alternative, but deriving it consistently from standard *in situ* sensor data presents a fundamental challenge. Common dielectric sensors measure bulk effective permittivity (ε_{eff}) rather than liquid water content directly; converting permittivity to θ_{lw} in partially frozen soils

requires accurate knowledge of the ice fraction—a quantity that is difficult to obtain under dynamic field conditions [Amankwah et al., 2022]. Empirical permittivity–moisture calibrations developed for unfrozen soils do not account for the dielectric contribution of ice and introduce uncertainty when applied in the partially frozen state [Yoshikawa and Overduin, 2005, Zhou et al., 2014]. This calibration challenge has prevented the consistent derivation of SFCC parameters—particularly T_f and b—across the diversity of soil types and sensor configurations present in large-scale monitoring networks. Compounding this, long-term *in situ* monitoring of SFG across diverse biomes using SFCC-based approaches remains sparse [Pardo Lara et al., 2021], limiting the availability of standardised, physically grounded reference data for satellite algorithm development and evaluation, and constraining our broader understanding of how soil freezing behaviour varies across soil types, biomes, and climate regimes.

Limitation at the satellite scale: binary FT products cannot resolve the zero-curtain. Existing passive microwave FT products—including the FT-SMAP product [Xu et al., 2023], the FT-ESDR long-term record [Kim et al., 2011], and many recently developed algorithms [Donahue et al., 2023]—classify the land surface into two discrete states: frozen or unfrozen. This binary output cannot capture the zero-curtain period during which the soil occupies an intermediate physical state for potentially weeks to months. By design, binary algorithms must assign transitional soils to one of two incorrect classes, introducing systematic misclassification errors precisely during the zero-curtain period. Although the operational FT-SMOS product has recently introduced a partially frozen transitional class [Rautiainen et al., 2025], the broader challenge of retrieving non-binary FT states in a physically transparent, spatially generalizable, and multi-frequency framework has not been fully addressed. Multi-frequency passive microwave approaches that integrate L-band and higher-frequency observations have demonstrated improved FT classification accuracy over single-frequency baselines [Donahue et al., 2023, Muzalevskiy and Ruzicka, 2020, Yang et al., 2025b], but a physically grounded multi-frequency retrieval framework for non-binary FT states has not been developed. Beyond discrete classification, representing soil cryospheric state as a continuous variable — rather than a set of labelled classes — would better reflect the gradual nature of the freeze-thaw transition and provide a spatially consistent metric for tracking its progression across landscapes.

Limitation at the continental scale: environmental controls and carbon flux coupling. The factors that influence soil freezing processes—including antecedent soil moisture, vegetation cover, soil organic content, snow depth, and air temperature—are well established [MacKinney, 1929, Fu et al., 2018, Zhang, 2005, Decker et al., 2003, Kersten, 1949, Lei et al., 2020]; however, the relative importance of these factors in governing the duration of both the fully frozen period and

the transitional zero-curtain phase across diverse biomes has not been systematically quantified at the continental scale using three-state, satellite-derived FT metrics. Equally important, the mechanistic linkage between the continuous trajectory of soil freezing and the decline of cold-season ecosystem respiration has not been rigorously established across a diversity of northern biomes. While the theoretical basis for this linkage—the suppression of microbial activity as liquid water is depleted by freezing—is well understood at the process level [Mikan et al., 2002, Mavrovic et al., 2023], rigorously quantifying this linkage across diverse northern biomes by integrating satellite-derived FT state metrics with eddy covariance flux tower measurements requires approaches that have not previously been applied at this scale. The absence of such a framework leaves a critical gap between remote sensing retrievals of soil physical state and ecosystem-scale carbon flux observations, limiting our ability to use satellite data to constrain cold-season carbon budget estimates.

Together, these three limitations—at the site, satellite, and continental scales—collectively impede a physically coherent understanding of SFG and its role in the Earth system under a changing climate. They motivate the multi-scale observational framework developed in this thesis.

1.3 Research Objectives

This thesis pursues three specific and interconnected objectives:

1. **Objective 1** (Chapter 2): To characterise soil freezing dynamics across 87 sites in eight Canadian long-term monitoring networks spanning boreal, prairie, and tundra ecozones by applying the Soil Freezing Characteristic Curve (SFCC) in permittivity–temperature space—enabling three-state (unfrozen, transitional, frozen) classification from standard *in situ* dielectric sensors without soil-specific liquid water content calibrations—and to estimate SFCC parameters (T_f and b) using a Bayesian hierarchical partial-pooling model, yielding biome-consistent parameter priors that extend frozen ground state inference to sites where only soil temperature observations are available.

2. **Objective 2** (Chapter 3): To develop a probabilistic, non-binary freeze–thaw retrieval algorithm using multi-frequency passive microwave observations—fusing the SMAP L-band Normalised Polarisation Ratio (Z_{NPR}, 1.4 GHz) with the AMSR2 Normalised Difference V-pol index (Z_{NDV}, 18.7 and 36.5 GHz)—that maps the land surface into unfrozen, transitional, and frozen states across five North American biome types, and to derive a continuous Frozenness Index (D) from the logistic regression decision boundary as a spatially consistent, physically grounded metric of soil cryospheric state.

3. **Objective 3** (Chapter 4): To characterise the spatiotemporal patterns of zero-curtain duration and strictly frozen ground frequency across North American biomes, to identify and rank their dominant environmental drivers using biome-level co-variation analysis and pixel-level XGBoost with SHAP attribution, and to establish a mechanistic, quantitative linkage between the satellite-derived Frozenness Index (D) and cold-season ecosystem respiration (R_{eco}) from AmeriFlux eddy covariance towers using piecewise regression and boundary line analysis.

1.4 Thesis Structure

This thesis is structured as a manuscript-based (article-based) thesis and comprises three original scientific articles, framed by a general introduction and a general conclusion. Each article is presented as a self-contained chapter with its own introduction, methods, results, and discussion. A brief description of each chapter is provided below.

Chapter 2 — Article 1 addresses Objective 1. Under the title *In Situ Monitoring of Seasonally Frozen Ground Using Soil Freezing Characteristic Curve in Permittivity–Temperature Space* (published in *The Cryosphere*), this article recasts a theoretical SFCC directly into permittivity–temperature space, demonstrating that physically meaningful three-state (unfrozen, transitional, frozen) soil classification can be achieved from standard dielectric sensors without converting permittivity to liquid water content—bypassing the ice-content calibrations that are problematic in field conditions. The SFCC model is fitted to measurements from 87 sites across eight Canadian monitoring networks spanning boreal forest, prairie, and tundra ecozones. A Bayesian hierarchical partial-pooling model is applied to derive stabilised, network- and biome-consistent estimates of T_f (range: 0.15–0.44 °C) and b (range: 0.92–3.47 $^{\circ}\mathrm{C}^{-1}$) across networks. Results reveal that the transitional freeze–thaw state is a significant seasonal feature: in high-moisture eastern boreal forest environments, it persists for more than 100 days; in western boreal and prairie environments, for 30 to 60 days; and in Arctic tundra, for over 40 days. These findings confirm that surface insulation and antecedent soil moisture—not air temperature alone—govern the SFG regime, and provide a reproducible, physically based reference framework for satellite freeze–thaw product development and validation.

Chapter 3 — Article 2 addresses Objective 2. Under the title *Non-Binary Retrievals of Soil Freeze–Thaw Dynamics Using Multi-Frequency Passive Microwave Data* (under review in *Remote Sensing of Environment*), this article introduces a probabilistic logistic regression framework that fuses the SMAP L-band Normalised Polarisation Ratio (Z_{NPR}) with the AMSR2 Normalised Difference V-pol index (Z_{NDV}) to map the full FT continuum—unfrozen, transitional, and frozen—across five North American biome types. Ground-state labels are derived from biome-

specific SFCC-based probabilistic labelling (developed in Chapter 1), isolating high-confidence binary end-members while explicitly filtering ambiguous transitional observations from training. Model generalisability is enforced through DBSCAN-based spatial block cross-validation to prevent leakage from spatial autocorrelation. Evaluated against a three-product unanimous consensus pseudo-truth (FT-SMAP, FT-ESDR, and FT-SMOS), the model achieves match rates of 78.8–98.2% and Cohen's Kappa values of 0.44–0.87 across biomes, reflecting a performance gradient from canopy-dense Mixed Forests to open Tundra. Thermodynamic validation against ERA5 near-surface air temperature and *in situ* soil records confirms that the satellite-derived transitional class physically anchors to the latent heat of fusion, providing a scalable and physically consistent framework for mapping zero-curtain dynamics at the continental scale.

Chapter 4 — Article 3 addresses Objective 3. Under the title *Zero-Curtain and Frozen Ground Spatiotemporal Variability Across North American Biomes: Environmental Controls and Implications for Cold-Season Ecosystem Respiration*, this article applies the FT-CUSTOM retrieval (developed in Chapter 2), corroborated by the independent FT-SMOS product, to characterise the spatial baseline and interannual variability of zero-curtain duration and frozen ground frequency across five North American biomes over 2015–2024. A key finding is that zero-curtain duration follows a non-latitudinal pattern: it peaks in mid-latitude mixed forests (57.4 days) and collapses to a minimum in Arctic tundra (13.7 days). Biome-level co-variation analysis identifies fall vegetation density (NDVI) as showing the clearest and most monotonic correspondence with zero-curtain duration across biomes, while within-biome pixel-level regressions yield uniformly low R^2 values, confirming that these variables capture ecosystem-type differences at the continental scale rather than continuous pixel-scale drivers. SHAP analysis shows spring and fall atmospheric temperatures dominate total frozen ground frequency (zero-curtain and strictly frozen periods combined) (mean impacts of 17.5 and 12.1 days, respectively). Piecewise regression of AmeriFlux ecosystem respiration (R_{eco}) against the continuous Frozenness Index (D) (developed in Chapter 2) demonstrates that the metabolic shutdown threshold aligns with the satellite-derived onset of the zero-curtain phase, and boundary line analysis reveals an exponential decay in maximum respiratory potential as liquid water is progressively depleted by freezing. These results position D as a physically grounded, landscape-scale proxy for detecting the critical tipping point at which cold-season ecosystem respiration decouples from temperature and becomes governed by soil cryospheric state.

Chapter 5 — General Conclusion synthesises the findings of the three articles, situates their collective contributions within the broader context of cryosphere science, land surface modelling, and global carbon cycle research, and identifies priority directions for future work. It reflects on the multi-scale coherence of the framework developed across the three studies and discusses the implications of the documented zero-curtain dynamics for Earth system projections under

ongoing climate change.

1.5 References

P. Ala-Aho, A. Autio, J. Bhattacharjee, E. Isokangas, K. Kujala, H. Marttila, M. Menberu, L.-J. Meriö, H. Postila, A. Rauhala, A.-K. Ronkanen, P. M. Rossi, M. Saari, A. T. Haghighi, and B. Kløve. What conditions favor the influence of seasonally frozen ground on hydrological partitioning? a systematic review. *Environmental Research Letters*, 16(4):043008, 2021. doi: 10.1088/1748-9326/abe82c.

S. K. Amankwah, A. M. Ireson, and R. Brannen. An improved model and field calibration technique for measuring liquid water content in unfrozen and frozen soils with dielectric probes. *Vadose Zone Journal*, 21(5):e20225, Sept. 2022. ISSN 1539-1663, 1539-1663. doi: 10.1002/vzj2.20225. URL https://acsess.onlinelibrary.wiley.com/doi/10.1002/vzj2.20225.

K. A. Arndt, J. Hashemi, S. M. Natali, L. D. Schiferl, and A.-M. Virkkala. Recent Advances and Challenges in Monitoring and Modeling Non-Growing Season Carbon Dioxide Fluxes from the Arctic Boreal Zone. *Current Climate Change Reports*, 9(2):27–40, Oct. 2023. ISSN 2198-6061. doi: 10.1007/s40641-023-00190-4. URL https://link.springer.com/10.1007/s40641-023-00190-4.

R. Bai, Y. Lai, M. Zhang, and F. Yu. Theory and application of a novel soil freezing characteristic curve. *Applied Thermal Engineering*, 129:1106–1114, Jan. 2018. ISSN 1359-4311. doi: 10.1016/j.applthermaleng.2017.10.121. URL https://www.sciencedirect.com/science/article/pii/S1359431117352316.

T. Beach and J. M. Flood. *Soil Water*, pages 1–7. John Wiley & Sons, Ltd, Oxford, UK, Mar. 2017.

L. Y. Chang, C. L. Dai, and H. C. Liao. Research overview on hydrological effects of frozen soil. *Advanced Materials Research*, 550-553:2459–2465, 2012. doi: 10.4028/www.scientific.net/AMR.550-553.2459.

Y. Chen, Z. Zhou, J. Wang, Y. Zhao, and Z. Dou. Quantification and division of unfrozen water content during the freezing process and the influence of soil properties by low-field nuclear magnetic resonance. *J. Hydrol.*, 602:126719, Nov. 2021.

G. Davesne, F. Domine, and D. Fortier. Effects of meteorology and soil moisture on the spatio-temporal evolution of the depth hoar layer in the polar desert snowpack. *Journal of Glaciology*, 68(269):457–472, 2022. doi: 10.1017/jog.2021.105.

K. L. M. Decker, D. Wang, C. Waite, and T. Scherbatskoy. Snow Removal and Ambient Air Temperature Effects on Forest Soil Temperatures in Northern Vermont. *Soil Science Society of America Journal*, 67(4):1234–1242, July 2003. ISSN 03615995. doi: 10.2136/sssaj2003.1234. URL http://doi.wiley.com/10.2136/sssaj2003.1234.

C. Derksen, X. Xu, R. Scott Dunbar, A. Colliander, Y. Kim, J. S. Kimball, T. A. Black, E. Euskirchen, A. Langlois, M. M. Loranty, P. Marsh, K. Rautiainen, A. Roy, A. Royer, and J. Stephens. Retrieving landscape freeze/thaw state from Soil Moisture Active Passive (SMAP) radar and radiometer measurements. *Remote Sensing of Environment*, 194:48–62, June 2017. ISSN 00344257. doi: 10.1016/j.rse.2017.03.007. URL https://linkinghub.elsevier.com/retrieve/pii/S0034425717300998.

K. Donahue, J. S. Kimball, J. Du, F. Bunt, A. Colliander, M. Moghaddam, J. Johnson, Y. Kim, and M. A. Rawlins. Deep learning estimation of northern hemisphere soil freeze-thaw dynamics using satellite multi-frequency microwave brightness temperature observations. *Frontiers in Big Data*, 6:1243559, Nov. 2023. ISSN 2624-909X. doi: 10.3389/fdata.2023.1243559. URL https://www.frontiersin.org/articles/10.3389/fdata.2023.1243559/full.

E. Du, Z. Zhou, P. Li, L. Jiang, X. Hu, and J. Fang. Winter soil respiration during soil-freezing process in a boreal forest in northeast china. *Journal of Plant Ecology*, 6(5):349–357, 2013. doi: 10.1093/jpe/rtt012.

Q. Fu, R. Hou, T. Li, R. Jiang, P. Yan, Z. Ma, and Z. Zhou. Effects of soil water and heat relationship under various snow cover during freezing-thawing periods in Songnen Plain, China. *Scientific Reports*, 8(1):1325, Jan. 2018. ISSN 2045-2322. doi: 10.1038/s41598-018-19467-y. URL https://www.nature.com/articles/s41598-018-19467-y.

S. Harrysson Drotz, T. Sparrman, J. Schleucher, M. Nilsson, and M. G. Öquist. Effects of soil organic matter composition on unfrozen water content and heterotrophic co2 production of frozen soils. *Geochimica et Cosmochimica Acta*, 74(8):2281–2290, 2010. ISSN 0016-7037. doi: 10.1016/j.gca.2010.01.026. URL https://www.sciencedirect.com/science/article/pii/S0016703710000438.

M. Hayashi. The cold vadose zone: Hydrological and ecological significance of frozen-soil processes. *Vadose Zone Journal*, 12(4):1–8, 2013. doi: 10.2136/vzj2013.03.0064.

G. Hu, L. Zhao, X. Zhu, X. Wu, T. Wu, R. Li, C. Xie, and J. Hao. Review of algorithms and parameterizations to determine unfrozen water content in frozen soil. *Geoderma*, 368:114277, June 2020.

M. S. Kersten. Thermal Properties of Soils, June 1949. URL https://hdl.handle.net/11299/124271. Accessed: October 2025.

Y. Kim, J. S. Kimball, K. C. McDonald, and J. Glassy. Developing a global data record of daily landscape freeze/thaw status using satellite passive microwave remote sensing. *IEEE Transactions on Geoscience and Remote Sensing*, 49(3):949–960, 2011. doi: 10.1109/TGRS.2010.2070515.

Y. Kim, J. Kimball, K. Zhang, and K. McDonald. Satellite detection of increasing northern hemisphere non-frozen seasons from 1979 to 2008: Implications for regional vegetation growth. *Remote Sensing of Environment*, 121:472–487, 2012. doi: 10.1016/j.rse.2012.02.014.

R. W. R. Koopmans and R. D. Miller. Soil Freezing and Soil Water Characteristic Curves. *Soil Science Society of America Journal*, 30(6):680–685, Nov. 1966. ISSN 0361-5995, 1435-0661. doi: 10.2136/sssaj1966.03615995003000060011x. URL https://acsess.onlinelibrary.wiley.com/doi/10.2136/sssaj1966.03615995003000060011x.

D. Lei, Y. Yang, C. Cai, Y. Chen, and S. Wang. The Modelling of Freezing Process in Saturated Soil Based on the Thermal-Hydro-Mechanical Multi-Physics Field Coupling Theory. *Water*, 12(10):2684, Sept. 2020. ISSN 2073-4441. doi: 10.3390/w12102684. URL https://www.mdpi.com/2073-4441/12/10/2684.

T. Li, Y.-Z. Chen, L.-J. Han, L.-H. Cheng, Y.-H. Lv, B.-J. Fu, X.-M. Feng, and X. Wu. Shortened duration and reduced area of frozen soil in the northern hemisphere. *The Innovation*, 2(3):100146, 2021. doi: 10.1016/j.xinn.2021.100146.

A. L. MacKinney. Effects of Forest Litter on Soil Temperature and Soil Freezing in Autumn and Winter. *Ecology*, 10(3):312–321, July 1929. ISSN 0012-9658, 1939-9170. doi: 10.2307/1929507. URL https://esajournals.onlinelibrary.wiley.com/doi/10.2307/1929507.

A. Mavrovic, O. Sonnentag, J. Lemmetyinen, C. Voigt, N. Rutter, P. Mann, J.-D. Sylvain, and A. Roy. Environmental controls of winter soil carbon dioxide fluxes in boreal and tundra environments. *Biogeosciences*, 20(24):5087–5108, Dec. 2023. ISSN 1726-4170. doi: 10.5194/bg-20-5087-2023. URL https://bg.copernicus.org/articles/20/5087/2023/. Publisher: Copernicus GmbH.

M. Meredith, M. Sommerkorn, S. Cassotta, C. Derksen, A. Ekaykin, A. Hollowed, G. Kofinas, A. Mackintosh, J. Melbourne-Thomas, M. M. C. Muelbert, G. Ottersen, H. Pritchard, and E. A. G. Schuur. Polar regions. In H.-O. Pörtner, D. C. Roberts, V. Masson-Delmotte, P. Zhai, M. Tignor, E. Poloczanska, K. Mintenbeck, A. Alegría, M. Nicolai, A. Okem, J. Petzold, B. Rama, and N. M. Weyer, editors, *IPCC Special Report on the Ocean and Cryosphere in a Changing Climate*, pages 203–320. Cambridge University Press, Cambridge, UK and New York, NY, USA, 2019. doi: 10.1017/9781009157964.005. URL https://doi.org/10.1017/9781009157964.005.

C. J. Mikan, J. P. Schimel, and A. P. Doyle. Temperature controls of microbial respiration in arctic tundra soils above and below freezing. *Soil Biology and Biochemistry*, 34(11): 1785–1795, Nov. 2002. ISSN 00380717. doi: 10.1016/S0038-0717(02)00168-2. URL https://linkinghub.elsevier.com/retrieve/pii/S0038071702001682.

K. Muzalevskiy and Z. Ruzicka. Detection of soil freeze/thaw states in the arctic region based on combined smap and amsr-2 radio brightness observations. *International Journal of Remote Sensing*, 41(14):5046–5061, 2020. doi: 10.1080/01431161.2020.1724348.

S. M. Natali, J. D. Watts, B. M. Rogers, S. Potter, S. M. Ludwig, A.-K. Selbmann, P. F. Sullivan, B. W. Abbott, K. A. Arndt, L. Birch, M. P. Björkman, A. A. Bloom, G. Celis, T. R. Christensen, C. T. Christiansen, R. Commane, E. J. Cooper, P. Crill, C. Czimczik, S. Davydov, J. Du, J. E. Egan, B. Elberling, E. S. Euskirchen, T. Friborg, H. Genet, M. Göckede, J. P. Goodrich, P. Grogan, M. Helbig, E. E. Jafarov, J. D. Jastrow, A. A. M. Kalhori, Y. Kim, J. S. Kimball, L. Kutzbach, M. J. Lara, K. S. Larsen, B.-Y. Lee, Z. Liu, M. M. Loranty, M. Lund, M. Lupascu, N. Madani, A. Malhotra, R. Matamala, J. McFarland, A. D. McGuire, A. Michelsen, C. Minions, W. C. Oechel, D. Olefeldt, F.-J. W. Parmentier, N. Pirk, B. Poulter, W. Quinton, F. Rezanezhad, D. Risk, T. Sachs, K. Schaefer, N. M. Schmidt, E. A. G. Schuur, P. R. Semenchuk, G. Shaver, O. Sonnentag, G. Starr, C. C. Treat, M. P. Waldrop, Y. Wang, J. Welker, C. Wille, X. Xu, Z. Zhang, Q. Zhuang, and D. Zona. Large loss of co2 in winter observed across the northern permafrost region. *Nature Climate Change*, 9(11):852–857, 2019. doi: 10.1038/s41558-019-0592-8.

K. T. Osman. *Soils: Principles, Properties and Management*. Springer Science & Business Media, Dec. 2012.

S. I. Outcalt, F. E. Nelson, and K. M. Hinkel. The zero-curtain effect: Heat and mass transfer across an isothermal region in freezing soil. *Water Resources Research*, 26(7):1509–1516, 1990. doi: 10.1029/WR026i007p01509.

R. Pardo Lara, A. A. Berg, J. Warland, and G. Parkin. Implications of measurement metrics

on soil freezing curves: A simulation of freeze–thaw hysteresis. *Hydrological Processes*, 35(7):e14269, July 2021. ISSN 0885-6087, 1099-1085. doi: 10.1002/hyp.14269. URL https://onlinelibrary.wiley.com/doi/10.1002/hyp.14269.

M. Prince, A. Roy, A. Royer, and A. Langlois. Timing and spatial variability of fall soil freezing in boreal forest and its effect on SMAP L-band radiometer measurements. *Remote Sensing of Environment*, 231:111230, Sept. 2019. ISSN 00344257. doi: 10.1016/j.rse.2019.111230. URL https://linkinghub.elsevier.com/retrieve/pii/S0034425719302494.

M. Rantanen, A. Y. Karpechko, A. Lipponen, et al. The arctic has warmed nearly four times faster than the globe since 1979. *Communications Earth & Environment*, 3:168, Aug 2022. doi: 10.1038/s43247-022-00498-3. URL https://doi.org/10.1038/s43247-022-00498-3.

K. Rautiainen, J. Lemmetyinen, M. Schwank, A. Kontu, C. B. Ménard, C. Mätzler, M. Drusch, A. Wiesmann, J. Ikonen, and J. Pulliainen. Detection of soil freezing from l-band passive microwave observations. *Remote Sensing of Environment*, 147:206–218, 2014. doi: 10.1016/j.rse.2014.03.007.

K. Rautiainen, M. Holmberg, J. Cohen, A. Mialon, M. Schwank, J. Lemmetyinen, A. de la Fuente, and Y. Kerr. An operational smos soil freeze–thaw product. *Earth System Science Data*, 17 (10):5337–5353, 2025. doi: 10.5194/essd-17-5337-2025.

A. Roy, A. Royer, C. Derksen, L. Brucker, A. Langlois, A. Mialon, and Y. H. Kerr. Evaluation of spaceborne l-band radiometer measurements for terrestrial freeze/thaw retrievals in canada. *IEEE Journal of Selected Topics in Applied Earth Observations and Remote Sensing*, 8(9): 4442–4459, 2015. doi: 10.1109/JSTARS.2015.2476358.

E. A. G. Schuur, A. D. McGuire, C. Schädel, G. Grosse, J. W. Harden, D. J. Hayes, G. Hugelius, C. D. Koven, P. Kuhry, D. M. Lawrence, S. M. Natali, D. Olefeldt, V. E. Romanovsky, K. Schaefer, M. R. Turetsky, C. C. Treat, and J. E. Vonk. Climate change and the permafrost carbon feedback. *Nature*, 520(7546):171–179, 2015. doi: 10.1038/nature14338.

E. J. A. Spaans and J. M. Baker. The Soil Freezing Characteristic: Its Measurement and Similarity to the Soil Moisture Characteristic. *Soil Science Society of America Journal*, 60(1):13–19, Jan. 1996. ISSN 0361-5995, 1435-0661. doi: 10.2136/sssaj1996.03615995006000010005x. URL https://acsess.onlinelibrary.wiley.com/doi/10.2136/sssaj1996.03615995006000010005x.

J. Tao, Q. Zhu, W. J. Riley, and R. B. Neumann. Improved ELMv1-ECA simulations of zero-curtain periods and cold-season ch_4 and co_2 emissions at Alaskan Arctic tundra sites. *The Cryosphere*, 15(12):5281–5307, 2021. doi: 10.5194/tc-15-5281-2021.

H. Tian, C. Wei, H. Wei, and J. Zhou. Freezing and thawing characteristics of frozen soils: Bound water content and hysteresis phenomenon. *Cold Reg. Sci. Technol.*, 103:74–81, July 2014.

Y. Wang, H. Liu, H. Chung, L. Yu, Z. Mi, Y. Geng, X. Jing, S. Wang, H. Zeng, G. Cao, X. Zhao, and J.-S. He. Non-growing-season soil respiration is controlled by freezing and thawing processes in the summer monsoon-dominated tibetan alpine grassland. *Global Biogeochem. Cycles*, 28(10):1081–1095, Oct. 2014.

K. Watanabe and Y. Osada. Simultaneous measurement of unfrozen water content and hydraulic conductivity of partially frozen soil near 0°c. *Cold Reg. Sci. Technol.*, 142:79–84, Oct. 2017.

J. D. Watts, S. M. Natali, C. Minions, D. Risk, K. Arndt, D. Zona, E. S. Euskirchen, A. V. Rocha, O. Sonnentag, M. Helbig, A. Kalhori, W. Oechel, H. Ikawa, M. Ueyama, R. Suzuki, H. Kobayashi, G. Celis, E. A. G. Schuur, E. Humphreys, Y. Kim, B.-Y. Lee, S. Goetz, N. Madani, L. D. Schiferl, R. Commane, J. S. Kimball, Z. Liu, M. S. Torn, S. Potter, J. A. Wang, M. T. Jorgenson, J. Xiao, X. Li, and C. Edgar. Soil respiration strongly offsets carbon uptake in alaska and northwest canada. *Environ. Res. Lett.*, 16(8):084051, Aug. 2021.

P. J. Williams and M. W. Smith. *The Frozen Earth: Fundamentals of Geocryology*. Cambridge University Press, 1 edition, Oct. 1989. ISBN 978-0-521-36534-5 978-0-521-42423-3 978-0-511-56443-7. doi: 10.1017/CBO9780511564437. URL https://www.cambridge.org/core/product/identifier/9780511564437/type/book.

X. Xu, R. Dunbar, C. Derksen, A. Colliander, Y. Kim, and J. Kimball. Smap enhanced l3 radiometer global and northern hemisphere daily 9 km ease-grid freeze/thaw state, version 4, 2023.

Y. Yang, X. Wang, Z. Li, T. Wang, and T. Che. Shortened thawing and freezing intervals in the northern hemisphere since 1990 from sites observations and remote sensing. *Remote Sensing of Environment*, 328:114881, 2025a. doi: 10.1016/j.rse.2025.114881.

Z. Yang, T. Zhao, Q. Wang, L. Peng, Y. Ran, Y. Bai, J. Zheng, P. Yao, Z. Peng, J. Zhu, X. Kou, Y.-A. Liou, and J. Shi. Comparative analysis of microwave indices for freeze/thaw state monitoring and adaptive thresholding implications. *Science of Remote Sensing*, 11:100239, 2025b. doi: 10.1016/j.srs.2025.100239.

K. Yoshikawa and P. P. Overduin. Comparing unfrozen water content measurements of frozen soil using recently developed commercial sensors. *Cold Regions Science and Technology*, 42 (3):250–256, Nov. 2005. ISSN 0165232X. doi: 10.1016/j.coldregions.2005.03.001. URL https://linkinghub.elsevier.com/retrieve/pii/S0165232X05000315.

M. Zhang, X. Zhang, J. Lu, W. Pei, and C. Wang. Analysis of volumetric unfrozen water contents in freezing soils. *Experimental Heat Transfer*, 32(5):426–438, Sept. 2019.

S. Zhang and H. Pei. Determining the bound water content of montmorillonite from molecular simulations. *Eng. Geol.*, 294:106353, Dec. 2021.

T. Zhang. Distributing of seasonally and perennially frozen ground in the northern hemisphere. In *Proceedings of the 8th International Conference on Permafrost, 21–25 July 2003, Zurich, Switzerland*, pages 1289–1294. AA Balkema, 2003.

T. Zhang. Influence of the seasonal snow cover on the ground thermal regime: An overview. *Reviews of Geophysics*, 43(4):2004RG000157, Dec. 2005. ISSN 8755-1209, 1944-9208. doi: 10.1029/2004RG000157. URL https://agupubs.onlinelibrary.wiley.com/doi/10.1029/2004RG000157.

Y. Zhao, C. Zheng, A. Gelfan, K. Watanabe, H. Liu, S. Wright, X. Wu, W. Quinton, Y. Wang, S. Yi, Y. Zhang, Y. Shi, and W. Jiao. Frozen soil hydrological processes and their effects: A review and synthesis. *Reviews of Geophysics*, 64(1), 2026. doi: 10.1029/2024RG000839.

X. Zhou, J. Zhou, W. Kinzelbach, and F. Stauffer. Simultaneous measurement of unfrozen water content and ice content in frozen soil using gamma ray attenuation and TDR. *Water Resources Research*, 50(12):9630–9655, Dec. 2014. ISSN 0043-1397, 1944-7973. doi: 10.1002/2014WR015640. URL https://agupubs.onlinelibrary.wiley.com/doi/10.1002/2014WR015640.

B. Zuerndorfer, A. England, M. Dobson, and F. Ulaby. Mapping freeze/thaw boundaries with smmr data. *Agricultural and Forest Meteorology*, 52(1):199–225, 1990. ISSN 0168-1923. doi: 10.1016/0168-1923(90)90106-G. URL https://www.sciencedirect.com/science/article/pii/016819239090106G.

Chapter 2

In situ Monitoring of Seasonally Frozen Ground Using Soil Freezing Characteristic Curve in Permittivity–Temperature Space

Article Information

French Title:	Mesure des sols saisonnièrement gelés à l'aide de la courbe caractéristique de gel du sol dans l'espace permittivité-température
Authors:	Hesam Salmabadi, Renato Pardo Lara, Aaron Berg, Alex Mavrovic, Chelene Hanes, Benoit Montpetit, and Alexandre Roy
Journal:	The Cryosphere
Publisher:	Copernicus Publications
DOI:	https://doi.org/10.5194/tc-20-1635-2026
Publication Status:	Published

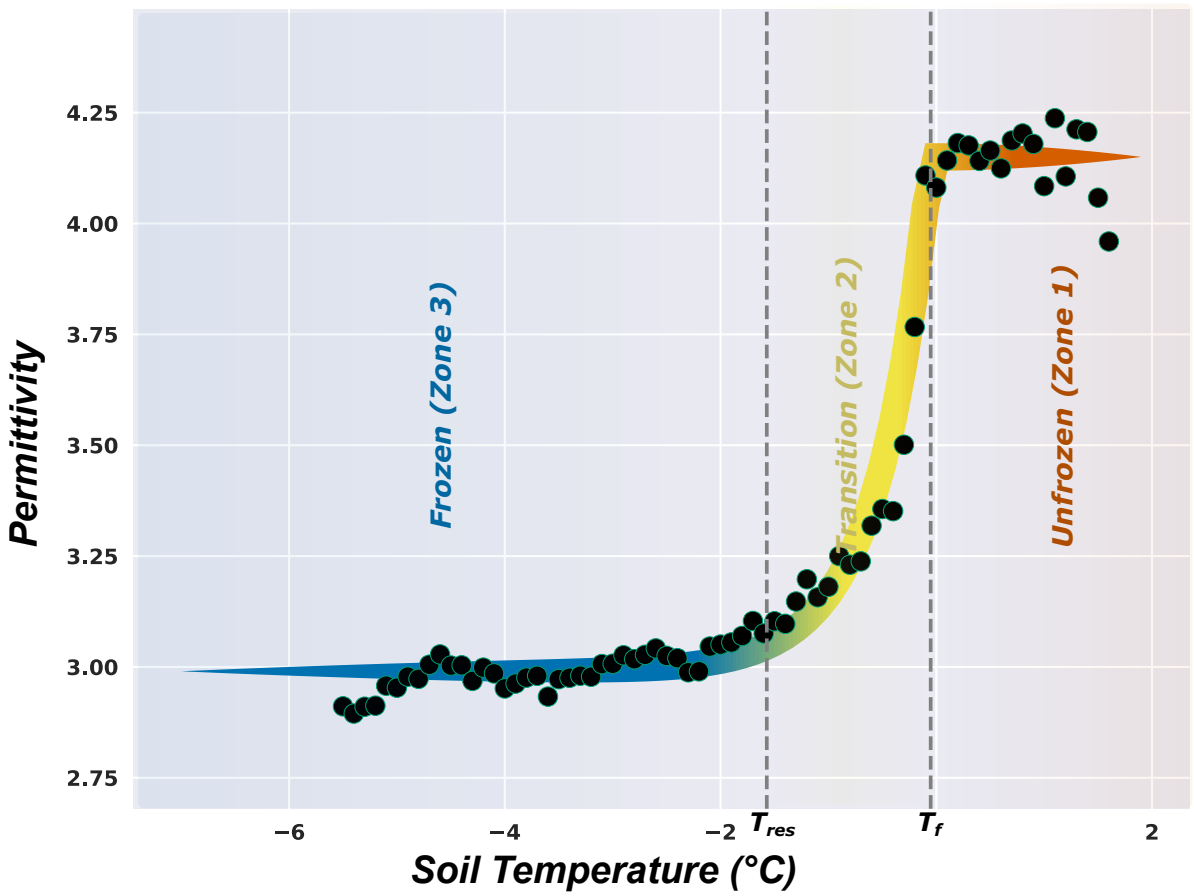
Résumé

Le sol saisonnièrement gelé (SSG) est une composante essentielle de la cryosphère, mais la dynamique de son gel est souvent trop simplifiée dans les cadres de surveillance à grande échelle — en particulier en télédétection et dans les modéles écosystémiques — par l'utilisation de seuils binaires de 0°C. Cette approche néglige l'état de « transition », physiquement significatif, où l'eau liquide et la glace coexistent, ce qui entraîne des erreurs systématiques dans la quantification de la période et de la durée de la saison de gel. Pour y remédier, nous avons reformulé le cadre de la courbe caractéristique de gel du sol (SFCC, pour *Soil Freezing Characteristic Curve*) directement dans l'espace permittivité–température. En opérant dans l'espace diélectrique, nous contournons la forte incertitude associée aux étalonnages de la teneur en eau liquide spécifiques aux sols et permettons une catégorisation robuste du sol en états non gelé, de transition et gelé. Nous avons ajusté ce modèle à des mesures *in situ* provenant de huit réseaux de surveillance (87 sites) à travers les écozones de la forêt boréale, des prairies et de la toundra canadiennes. À l'aide d'une approche bayésienne hiérarchique avec regroupement partiel (*partial pooling*), nous avons obtenu des estimations du début du gel (T_f) et de la netteté de la transition (b). À l'échelle du réseau, T_f variait de 0.15 à 0.44°C, tandis que b variait de 0.92 à 3.47°C^{-1}, reflétant des régimes de gel distincts. Nous avons constaté que l'état de transition est une caractéristique saisonnière dominante sur ces sites, remettant en question les approches binaires basées sur 0°C utilisées dans l'évaluation des données de télédétection. Dans les sites très humides caractérisés par une épaisse couche isolante organique (par exemple, dans les réseaux observés de la forêt boréale de l'Est), cet état a persisté pendant plus de 100 jours — soit pratiquement tout l'hiver — malgré des températures de l'air constamment inférieures à zéro. En revanche, les sites des réseaux de la forêt boréale de l'Ouest et des prairies, qui sont généralement dépourvus d'épaisses couches organiques en surface et présentent une humidité du sol plus faible, ont affiché des périodes de transition plus courtes mais néanmoins significatives (30 et 60 jours, respectivement). Même dans le froid extrême des sites du réseau de la toundra, la phase de transition a persisté pendant plus de 40 jours. Ces résultats confirment que l'isolation de surface et l'humidité du sol, plutôt que la seule température de l'air, régissent le régime des SSG aux emplacements observés, fournissant ainsi un cadre de référence reproductible et fondé sur des principes physiques pour la prochaine génération de produits de gel–dégel.

Abstract

Seasonally frozen ground (SFG) is a critical component of the cryosphere, yet its freezing dynamics are often oversimplified in large-scale monitoring frameworks—particularly in remote sensing (RS) and land surface modeling—through the use of binary 0°C thresholds. This approach overlooks the physically significant "transitional" state where liquid water and ice coexist, leading to systematic errors in quantifying the timing and duration of the frozen season. To address this, we recast the Soil Freezing Characteristic Curve (SFCC) framework directly into permittivity–temperature space. By operating in dielectric space, we bypass the high uncertainty associated with soil-specific liquid water content calibrations and enable a robust categorization of soil into unfrozen, transitional, and frozen states. We fitted this model to *in situ* measurements from eight monitoring networks (87 sites) across Canadian boreal forest, prairie, and tundra ecozones. Using Bayesian hierarchical partial pooling, we derived stabilized estimates of the freezing onset (T_f) and transition sharpness (b). Network-level T_f ranged from 0.15 to 0.44°C, while b varied from 0.92 to 3.47°C^{-1}, reflecting distinct freezing regimes. We found that the transitional state is a dominant seasonal feature at these sites, challenging binary 0°C assumptions used in RS evaluation. In high-moisture sites characterized by thick organic insulation (e.g., within the observed eastern boreal forest networks), this state persisted for over 100 days—effectively the entire winter—despite persistent subzero air temperatures. In contrast, sites in the western boreal and prairie networks, which generally lack thick surface organic layers and have lower soil moisture, exhibited shorter but still significant transitional periods (30 and 60 days, respectively). Even in the extreme cold of the tundra network sites, the transitional phase persisted for over 40 days. These results confirm that surface insulation and soil moisture, rather than air temperature alone, govern the SFG regime at the observed locations, providing a reproducible, physically-based reference framework for the next generation of freeze–thaw products.

Graphical Abstract



2.1 Introduction

Seasonally frozen ground (SFG), affecting most land areas above 45°N latitude [Zhang, 2003], is defined as a condition in which pore water turns into ice [Williams and Smith, 1989]. It plays a major role in the land surface energy and water balance, impacting ecological, hydrological, and biological processes in cold regions [Ala-Aho et al., 2021, Hayashi, 2013, Ping et al., 2015, Loranty et al., 2018]. By affecting hydrological partitioning, SFG regulates key processes such as infiltration, groundwater recharge, water chemistry, and runoff characteristics [Ala-Aho et al., 2021]. Furthermore, SFG impacts soil respiration—the primary pathway of carbon emissions to the atmosphere—as microbial activity is largely regulated by soil temperature and liquid water availability [Davidson and Janssens, 2006, Lei et al., 2022, Nikrad et al., 2016, Arndt et al., 2023, Azizi-Rad et al., 2022, Mikan et al., 2002, Mavrovic et al., 2023]. Therefore, accurately quantifying the timing, extent, and duration of SFG is critical for tracking environmental shifts and predicting changes in these vital ecosystem processes.

A common approach to monitoring SFG is the use of a simplistic temperature threshold—typically 0°C—to distinguish between frozen and unfrozen states. However, this binary classification fails to capture the physically significant "transitional" phase where liquid water and ice coexist. This limitation is particularly prevalent in the remote sensing (RS) community; many freeze–thaw (FT) studies, ranging from foundational work [Kim et al., 2011, Zhang and Armstrong, 2001] to recent applications [Donahue et al., 2023, Taghipourjavi et al., 2024, Gao et al., 2020, Kou et al., 2017, Roy et al., 2020, Derksen et al., 2017], rely on 0°C soil or air temperature thresholds for model training and evaluation. By neglecting the partially frozen state, these models may misrepresent the timing and duration of the frozen season. Only recently have researchers begun integrating soil moisture and temperature dynamics via the Soil Freezing Characteristic Curve (SFCC) into FT model evaluation [Rautiainen et al., 2025]. The SFCC defines the relationship between liquid water content (θ_{lw}) and subzero temperatures [Spaans and Baker, 1996, Koopmans and Miller, 1966], offering a framework for capturing the complexities of the soil freezing process across three distinct zones: the unfrozen zone, the transitional zone, and the residual zone (Fig. 2.1, see Supplementary Material Sect. S1 for further details).

Dielectric-based methods are widely used to estimate θ_{lw} by exploiting the high permittivity contrast between liquid water ($\varepsilon_{\mathrm{lw}} \approx 80$), soil minerals ($\varepsilon_{\mathrm{soil}} \approx 5$), and ice ($\varepsilon_{\mathrm{ice}} \approx 3.2$) [Seyfried and Murdock, 1996, Michael W Smith and Tice, 1988]. However, relating bulk permittivity ($\varepsilon_{\mathrm{eff}}$) to θ_{lw} in frozen soils remains challenging. Dielectric mixing models require accurate ice content estimates, which are difficult to obtain *in situ*, while empirical models often rely on calibrations developed for unfrozen soils that do not account for the dielectric contribution of ice [Amankwah et al., 2022, Zhou et al., 2014, Yoshikawa and Overduin, 2005]. These

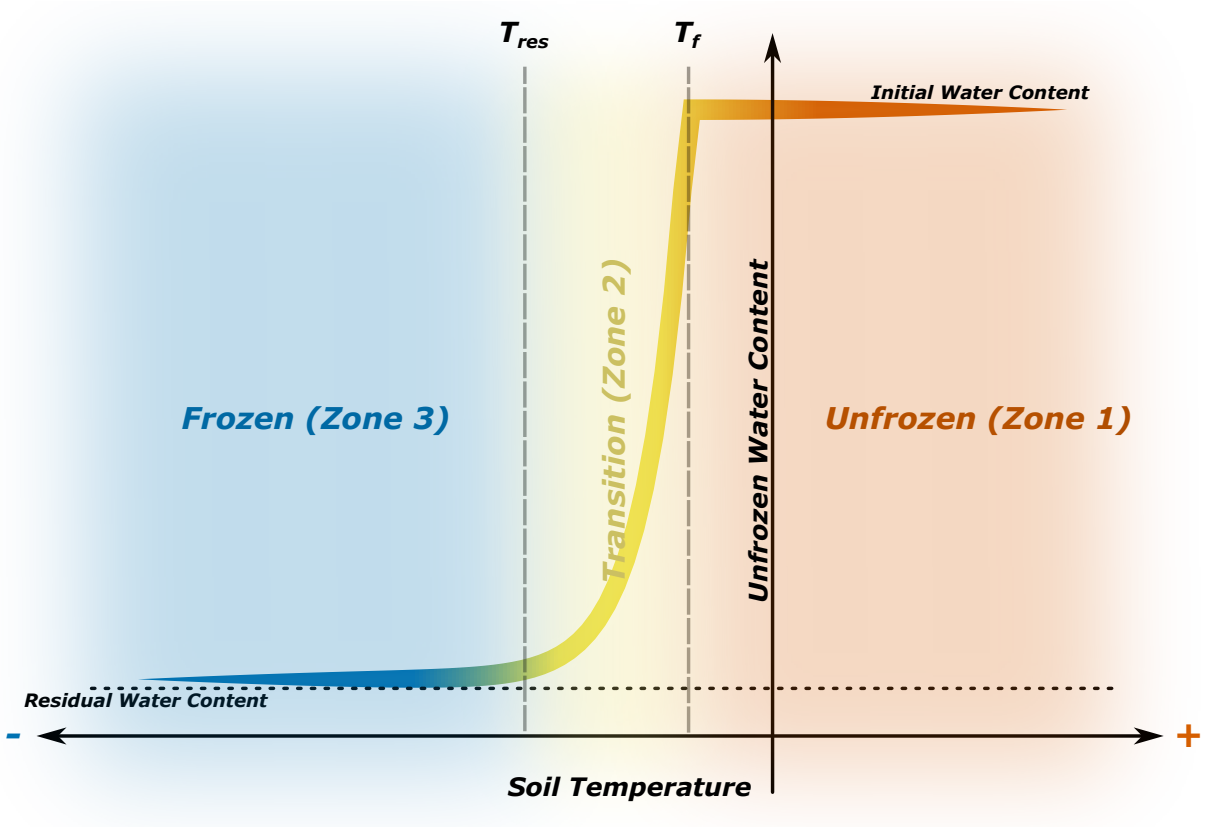


Figure 2.1: A typical Soil Freezing/Thawing Characteristic Curve (SFCC/STCC), adapted from Zhang et al. [2019]. T_f marks the temperature at which soil begins to freeze, while T_{res} indicates the temperature at which the liquid water content stabilizes near the residual water content.

limitations make constructing a traditional moisture-based SFCC problematic in dynamic field environments (see Supplementary Material Sect. S2 for further details). To address this, we recast the SFCC directly into permittivity–temperature space. This demonstrates that for qualitative state classification (frozen, transitional, or unfrozen), the problematic conversion of permittivities into water content is effectively unnecessary.

Beyond air temperature, soil freezing is primarily regulated by surface cover—including snowpack, vegetation, and organic (humus) layers—as well as soil moisture [MacKinney, 1929]. Collectively, surface cover acts as a thermal buffer, moderating soil–atmosphere heat exchange and reducing frost penetration [Fu et al., 2018, Zhang, 2005, Decker et al., 2003]. Meanwhile, soil moisture exerts a dual control: latent heat delays freezing onset, while ice formation increases thermal conductivity, accelerating subsequent cooling [Kersten, 1949, Lei et al., 2020].

In this study, we apply the SFCC framework in permittivity–temperature space to monitor SFG across 87 sites in eight Canadian monitoring networks spanning boreal forest, prairie, and tundra ecozones. Using measurements from three sensor types (HydraProbe, TEROS12, and CS616), we derive soil freezing probabilities and investigate how freezing dynamics vary across

distinct landscapes. This framework establishes a reproducible methodology to bridge the gap between *in situ* monitoring and the validation requirements of the RS community. Furthermore, the dataset generated through this analysis is directly applicable for the training, evaluation, and refinement of satellite-based freeze–thaw algorithms and land surface models.

2.2 Materials and Methods

2.2.1 Data Collection

2.2.1.1 In Situ Soil Measurements

This study leverages *in situ* measurements of ε_{eff} and soil temperature to monitor the soil freezing processes. Our research spans eight networks located in diverse ecozones (Table 2.1 and Fig. 2.2), including Montmorency Forest (FM), La Romaine (LR), James Bay (BJ), Chapleau (CP) in eastern boreal forests, Candle Lake (BT) in western boreal forest, Kenaston (KN) in prairies, and Trail Valley Creek (TV) and George River (GR) in tundra. Three types of soil moisture sensors—HydraProbe (Stevens Water), TEROS12 (METER Group), and CS616 (Campbell Scientific)—were deployed based on availability across the monitoring networks. HydraProbe and TEROS12 simultaneously measure soil temperature and moisture, whereas the CS616 requires a separate soil temperature sensor (CS109SS-L) for temperature measurements. We provided an overview of these sensors, including their measurement principles and operational specifics, in Appendix 2.A. At most sites, soil moisture probes were horizontally inserted to a depth of 5 cm, primarily within the organic layer unless it was notably thin, in which case measurements extended into the mineral layer. For the TEROS12 and HydraProbe, insertion was horizontal at this depth. In the Chapleau network, the CS616, with its 30 cm needle, was inserted at a 20° angle to integrate measurements over the top 10 cm of soil, with the midpoint depth set at 5 cm, thereby ensuring comparability with other sites (Fig. A1). Each site typically features a single sensor, except for Chapleau and Trail Valley Creek. Chapleau includes 24 CS616 sensors distributed across four 200×200 m plots, each representing a different forest type [Hanes et al., 2023]. Since only one soil temperature sensor was available in the middle of each plot, data from multiple CS616 sensors were averaged to represent the soil conditions of that plot. At Trail Valley Creek, 12 HydraProbes were distributed across six sites [Montpetit et al., 2024a,b], and data from each sensor were analyzed separately. Site- and sensor-specific calibration was not performed prior to installation; however, the use of manufacturer specifications and previously published validation studies provides confidence in the measurement accuracy of the deployed sensors within their expected uncertainty ranges [Seyfried and Murdock, 2004, Pardo Lara et al., 2021, Kelleners et al., 2005, Logsdon, 2009, Cominelli et al., 2024, Fragkos et al., 2024]. A

general quality control procedure was applied by removing physically implausible values, defined as soil temperatures outside the range of −60 to 60 °C and permittivity values outside the range of 1 to 90. All *in situ* measurements were then subjected to a standardized preprocessing workflow. Data were resampled to a uniform hourly resolution, and a continuous time index was constructed to ensure temporal consistency. Missing values were filled using linear interpolation; however, interpolated values were used solely for categorical soil state labeling and were excluded from all curve-fitting analyses to preserve the integrity of model-derived parameters. The distribution of sites within each network is strategically designed to capture the ecological diversity and maximize spatial variability, influenced by the challenging terrain and limited accessibility of the network areas. Detailed characteristics for each site—including geographic coordinates, soil textural composition (clay, sand, and silt percentages), organic content, specific soil types, elevation and stratification of soil layers—are available through an interactive map hosted in a GitHub repository (Soil-Temperature-Permittivity-Monitoring-Sites) [Salmabadi et al., 2025].

Table 2.1: Summary of soil moisture sensor deployment across our networks

Ecozone	Network Name	Sensor Type†	Sensor Depth (cm)	Number of Sites (Probes)	Temporal Coverage
Eastern boreal forest	James Bay	TEROS 12	5	9 (9)	2020-08 to 2022-06
	Montmorency Forest	TEROS 12	5	10 (10)	2020-10 to 2024-06
	La Romaine	TEROS 12	5	3 (3)	2022-08 to 2023-07
	Chapleau	CS616	0–10†	4 (24)	2017-08 to 2022-06
Western boreal forest	Candle Lake	HydraProbe	5	17 (17)	2022-08 to 2023-05
Prairies	Kenaston	HydraProbe	5	37 (37)	2014-08 to 2018-06
Tundra	Trail Valley Creek	HydraProbe	5	6 (12)	2018-09 to 2019-03
	George River	TEROS 12	5	1 (1)	2022-09 to 2023-07

† All sensors include built-in soil temperature measurement, except the CS616, which requires a separate soil temperature sensor (CS109SS-L).
† The CS616 is angled at 20°, measuring the top 10 cm of soil with a midpoint at 5 cm.

2.2.1.2 Ancillary Data

Air temperature data were obtained from the ERA5-Land reanalysis developed by the European Centre for Medium-Range Weather Forecasts (ECMWF; [Copernicus Climate Change Service (C3S), 2023]). ERA5-Land provides hourly 2 m air temperature at 0.25° spatial resolution and assimilates global observations within a physics-based numerical model to produce a consistent reanalysis extending from 1940 to the present. Snow cover data were derived from the Interactive Multisensor Snow and Ice Mapping System (IMS) produced by the U.S. National Ice Center [U.S. National Ice Center, 2004], which provides daily binary snow-cover maps for the Northern Hemisphere at 4 km resolution since 2004. The IMS product integrates multisensor satellite imagery and *in situ* observations. For each study site, snow-cover and air-temperature values were extracted from the corresponding IMS and ERA5-Land grid cells. Soil texture and organic



Figure 2.2: Geographic distribution of monitoring networks across Canadian landscapes. The land cover map is adapted from Latifovic [2019].

carbon were obtained from the 100 m soil landscape grids of Canada (CanSIS; [Geng et al., 2025]). This dataset provides soil attributes at 100 m resolution using machine-learning-based predictive mapping. For this study, we extracted values specifically for the 0–5 cm depth interval at each site.

2.2.2 Data Preprocessing

The data preprocessing stage began by converting the raw outputs of the sensors into ε_{eff} for the bulk soil. This process varied depending on the sensor type, as each sensor produced different raw outputs. Detailed explanations of these sensor-specific preprocessing steps are provided in Appendix 2.A. Next, we identified freezing and thawing cycles based on trends in soil temperature and ε_{eff}. A freezing cycle was defined as the period when soil temperature started decreasing and reached its minimum, while a thawing cycle extended from this minimum until temperatures rose

above zero. This approach aimed to capture the main freezing and thawing events while excluding minor fluctuations, where temperatures briefly rose above or fell below zero within a narrow range, resulting in incomplete or transient freezing or thawing. Specifically, any fluctuations within $\pm 2\sigma_T$ of 0°C, where σ_T represents the instrument-specific temperature uncertainty, were ignored (see Appendix 2.A for details on sensor uncertainty). If, during a freezing cycle, the soil temperature never dropped below the $-\sigma_T$ threshold and ε_{eff} remained relatively unchanged, we classified these sites as never frozen. Although curve fitting was not feasible for these cycles due to insufficient data in Zones 2 and 3, they were retained for subsequent analysis of freeze monitoring across our networks. We assumed that the total water content in the system remained equal to the initial water content and did not change during the freezing or thawing processes [He and Dyck, 2013]. We monitored ε_{eff} throughout both freezing and thawing cycles to validate this assumption. We interpreted significant, sudden surges in ε_{eff} as indicators of additional water entering the system, violating this assumption. Consequently, we excluded such cycles from further analysis. While this assumption generally held during freezing cycles, it was often invalid during thawing cycles, primarily due to snowmelt introducing substantial amounts of water into the soil. As a result, the SFCC could be reliably constructed for freezing cycles, but constructing the STCC from *in situ* measurements during thawing cycles was not feasible. Therefore, in this study we focused exclusively on freezing cycles, excluding thawing cycles from further analysis.

The final step in the preprocessing of *in situ* data involved ensuring a balanced dataset to prevent overfitting during the curve-fitting process. In practice, the distribution of data across temperature ranges was often uneven, which could bias the fitting process. We averaged ε_{eff} values within a 0.1°C temperature range to address this imbalance, corresponding to the sensors' temperature resolution. This approach not only compensated for the uneven distribution but also reduced noise caused by diurnal temperature fluctuations. Such fluctuations, while absent in controlled laboratory settings, were common in *in situ* environments.

2.2.3 Data Processing

2.2.3.1 SFCC Model

In this study, we applied the theoretical model introduced by Bai et al. to construct the SFCC, which estimates liquid water content as a function of soil temperature:

$$\theta_{lw} = \begin{cases} (\theta_{\text{int}} - \theta_{\text{res}}) e^{b(T_{\text{soil}} - T_f)} + \theta_{\text{res}} & \text{if } T_{\text{soil}} < T_f \\ \theta_{\text{int}} & \text{if } T_{\text{soil}} \geq T_f \end{cases} \tag{2.1}$$

where θ_{lw}, θ_{int}, and θ_{res} represent the liquid, total (initial water content prior to freezing), and residual water content, respectively. T_{soil} is the soil temperature, T_f is the freezing onset

temperature, and b controls the transition sharpness, representing the shape factor of the distribution function ($^{\circ}C^{-1}$).

The relationship between the ε_{eff} and θ_{lw} can be physically derived using mixing models [Amankwah et al., 2022, Kelleners and Norton, 2012, Roth et al., 1990], which express effective (bulk) permittivity as a volume-weighted average of soil components:

$$\varepsilon_{\text{eff}}^{\alpha} = \theta_{lw}\varepsilon_{lw}^{\alpha} + \theta_{\text{ice}}\varepsilon_{\text{ice}}^{\alpha} + (n - \theta_{lw} - \theta_{\text{ice}})\varepsilon_{\text{air}}^{\alpha} + (1 - n)\varepsilon_{\text{soil}}^{\alpha} \tag{2.2}$$

where n represents the soil porosity, and ε_{eff}, $\varepsilon_{\text{soil}}$, ε_{lw}, ε_{ice}, and ε_{air} are the relative dielectric permittivities (dimensionless) of bulk soil, soil solids, liquid water, ice, and air, respectively. The parameter α depends on soil structure and composition, ranging from -1 (parallel arrangement) to 1 (series arrangement), with $\alpha \neq 0$ [Amankwah et al., 2022]. Solving for θ_{lw} gives:

$$\theta_{lw} = \frac{\varepsilon_{\text{eff}}^{\alpha} - (1 - n)\varepsilon_{\text{soil}}^{\alpha} - n\varepsilon_{\text{air}}^{\alpha} - \theta_{\text{ice}}\left(\varepsilon_{\text{ice}}^{\alpha} - \varepsilon_{\text{air}}^{\alpha}\right)}{\varepsilon_{lw}^{\alpha} - \varepsilon_{\text{air}}^{\alpha}} \tag{2.3}$$

This equation defines the relationship between θ_{lw} and ε_{eff}, where ε_{air}, ε_{lw}, and ε_{ice} are known constants with minimal temperature dependence, while n, α, and $\varepsilon_{\text{soil}}$ vary with soil composition and structure and are treated as unknowns. We modified the model by Bai et al. [2018] (Eq. 2.1) by incorporating Eq. (2.3) to implement the SFCC in permittivity-temperature space. The detailed solution process is presented in Appendix 2.A.4. The modified equation is:

$$\varepsilon_{\text{eff}}(T) = \begin{cases} \left(\left(\varepsilon_{\text{int}}^{\alpha} - \varepsilon_{\text{res}}^{\alpha}\right) e^{b(T_{\text{soil}} - T_f)} + \varepsilon_{\text{res}}^{\alpha}\right)^{\frac{1}{\alpha}} & \text{if } T < T_f \\ \varepsilon_{\text{int}} & \text{if } T \geq T_f \end{cases} \tag{2.4}$$

Here, ε_{int} represents the pre-freezing ε_{eff}, corresponding to the system's total water content, which is assumed to approximate the initial water content [He and Dyck, 2013]. ε_{res} is the ε_{eff} associated with the residual water content. The parameter α, as mentioned earlier, is an exponent that depends on the soil structure and composition. In short, by incorporating a dielectric mixing model into the Bai et al.'s model, we formulated the SFCC in the permittivity–temperature space, where ε_{eff} is expressed as a function of soil temperature through parameters b ($1/^{\circ}C$), T_f, ε_{int}, and ε_{res}, derived via curve fitting.

2.2.3.2 SFCC Model Fitting and Parameter Estimation

To derive the model parameters—ε_{int}, ε_{res}, b, and T_{f}—and construct the SFCC, we applied a systematic data processing and curve-fitting approach tailored to our SFCC model (Eq. 2.4). We used non-linear least squares optimization with initial guesses and parameter bounds. The curve

fitting was conducted using the *curve_fit* function from the SciPy library (version 1.13.1) in Python [Virtanen et al., 2020], employing the Trust Region Reflective (TRF) algorithm, which optimizes parameter values while keeping them within predefined bounds. Since the fitting is performed independently for each site and cycle, variations in absolute ε_{eff} values, caused by differences in probe operating frequencies—due to the frequency-dependent dielectric properties of water and bulk soil—do not affect soil state monitoring.

To ensure that the data used for model fitting primarily reflect the freezing process, we included only measurements where $T_{\text{soil}} \leq 2°\text{C}$, capturing temperatures where freezing processes are actively occurring. During initial analyses, α, the exponent representing soil structure in the dielectric mixing model (Eq. 2.3), consistently converged to boundary values without improving model fit, indicating low sensitivity. This issue likely stems from eliminating parameter B when deriving the SFCC model from Bai et al. [2018]'s framework (Eq. A.20). This reduction decreases the model's dependence on soil parameters such as porosity and soil solid permittivity, both of which influence α. To enhance model stability and interpretability, we fixed α at 0.5, a commonly used value [Pardo Lara et al., 2020, Seyfried et al., 2005]. We set the lower bound of ε_{res} at 1, the lowest measurable probe range, and constrained the upper bound to remain below ε_{int} to prevent unrealistic values. The initial effective permittivity, ε_{int}, representing pre-freezing soil permittivity, was initialized as the mean ε_{eff} within $\sigma_T °\text{C} \leq T_{\text{soil}} \leq 2°\text{C}$, where σ_T represents the instrument-specific temperature uncertainty (see Appendix 2.A for details on sensor uncertainty). This range ensures that mainly unfrozen-state data (Zone 1) contribute to the estimate, accounting for sensor uncertainty. The bounds for ε_{int} were set as the observed minimum and maximum ε_{eff} within this range. The exponential constant b, which controls the transition from ε_{int} to ε_{res}, was initialized at 1.0, with a lower bound of 0.1 to prevent overly gradual transitions and no upper bound. For the T_f, we allowed values up to +1°C to accommodate known measurement biases and sensor discrepancies. For instance, Pardo Lara et al. [2020, 2021] suggested that dielectric sensors may detect permittivity changes indicative of freezing before thermistors register subzero temperatures, likely due to differences in placement, thermal inertia, or measurement volume. These discrepancies can cause T_f to register as slightly positive.

To assess the robustness and uncertainty of fitted parameters ($\varepsilon_{\text{int}}, \varepsilon_{\text{res}}, b, T_f$), we applied bootstrapping, resampling *in situ* soil temperature and ε_{eff} data 1,000 times. To ensure representative selection across temperature ranges, we divided the data into blocks and resampled within each block with replacement. This approach preserved the natural distribution of ε_{eff} across the soil temperature range while introducing variability across iterations. The resulting bootstrapped parameter distributions were used to compute mean values and standard deviations. Subsequently, a Monte Carlo framework with N = 15,000 simulations was employed for each measurement point (i.e., each hourly soil temperature observation). Soil temperature was modeled as a normal

distribution, $T_{\text{sim}} \sim \mathcal{N}(T_{\text{obs}}, \sigma_T^2)$, with sensor-specific standard deviations. Each parameter (M)—where $M \in \{T_f, \varepsilon_{\text{int}}, \varepsilon_{\text{res}}, b\}$—was independently sampled from a normal distribution, $\mathcal{N}(\mu_M, \sigma_M^2)$, where μ_M and σ_M were derived from the bootstrap analysis. Simulations violating physical constraints (i.e., $\varepsilon_{\text{int}} < \varepsilon_{\text{res}}$) were discarded to maintain physical validity. For each valid simulation, the modeled effective permittivity $\varepsilon_{\text{fitted},i}$ was computed for each realization, and the ensemble mean was used as the expected effective permittivity, $\overline{\varepsilon_{\text{fitted}}} = \frac{1}{N}\sum_{i=1}^{N} \varepsilon_{\text{fitted},i}$.

Following parameter estimation, a multi-step filtering process was applied to ensure the physical validity and reliability of the fitted SFCCs. Only cycles occurring during fall and winter (1 September–1 March), hereafter referred to as the freezing season, were retained, while short transient events observed in spring were excluded. The filtering process removed cycles with $R^2 < 0.6$, visually detected anomalies (e.g., irregular water content changes during freezing), and unreliable parameter estimates (boundary values for T_f or b, or excessively wide confidence intervals). Extreme outliers in T_f and b were also excluded by retaining only the central 95% of the distribution (2.5th–97.5th percentiles).

We applied Bayesian hierarchical partial pooling in *PyMC* to obtain stabilized estimates of b and T_f across sites and networks within ecozones. This hierarchical structure allowed information sharing among data-sparse sites and networks, reducing uncertainty while preserving genuine spatial differences. For b, we modeled $\log b$ with network- and site-level random intercepts in a non-centered parameterization, using a Student-t likelihood with heteroskedastic scales equal to the bootstrap standard error (SE) of $\log b$ combined with a residual term. For T_f, we used an analogous hierarchy on the original °C scale, with observation-level SEs and an additional residual variance. Weakly informative Normal priors were assigned to means, and Half-Student-t priors to variance components. Models were fit using the No-U-Turn Sampler (NUTS), and convergence ($\hat{R} \leq 1.01$, high effective sample sizes) and numerical stability (no or rare divergences) were confirmed. Sampler energy diagnostics were adequate (E-BFMI ≥ 0.50), and out-of-sample performance was reliable (PSIS-LOO with 100% of points $\hat{k} \leq 0.7$). Analogous hierarchical pooling was performed at the biome levels, with the resulting stabilized estimates presented in Tables S3 and S4.

2.2.4 Data Postprocessing

2.2.4.1 Probability of Seasonally Frozen Ground

The probability of SFG (P_{frozen}; hereafter referred to as the freezing probability), which can also be interpreted as the degree of soil freezing at the network level, was computed by propagating uncertainty from the hierarchical posterior distributions of T_f and b. For each network, paired posterior samples $\{(T_f^{(s)}, b^{(s)})\}_{s=1}^{S}$ were drawn from the *PyMC* hierarchical models, where

$b^{(s)} = \exp(b_j^{(s)})$ restores the parameter to its original scale. Soil temperature observations were perturbed according to sensor uncertainty, $T_{\text{sim}}^{(s)} \sim \mathcal{N}(T_{\text{obs}}, \sigma_T^2)$, where σ_T was assigned based on the sensor type. For each posterior draw, the freezing probability was evaluated using the normalized SFCC, and the results were averaged across all Monte Carlo samples to obtain the mean freezing probability at each timestamp.

2.3 Results

2.3.1 Evaluation of SFCC Fits and Parameter Analysis

A total of 96 freezing cycles across all networks passed the filtering criteria and were retained for analysis. The performance of the SFCC curve-fitting process were evaluated by comparing fitted permittivity values $\varepsilon_{\text{eff}_{\text{fitted}}}$ with *in situ* measurements of $\varepsilon_{\text{eff}_{\text{observed}}}$ (Fig. 2.3). Goodness of fit was quantified using the coefficient of determination (R^2), root mean square error (RMSE), and mean absolute error (MAE). Relative RMSE and MAE were normalized by the per-network dynamic range ($\varepsilon_{\text{eff}_{\text{int}}} - \varepsilon_{\text{eff}_{\text{res}}}$; Table 2.2). Overall, the SFCC model reproduced the observed permittivity well, achieving a mean R^2 of 0.95 and relative RMSE and MAE of 5% and 3%, respectively. The best performance was observed in the BT and KN networks ($R^2 > 0.9$; relative RMSE < 5%), whereas slightly lower fits ($R^2 \approx 0.67$) were observed in FM and GR networks, likely reflecting sparse sampling of the transitional zone as freezing progressed rapidly.

Table 2.2: Performance of SFCC curve fitting by network. Relative RMSE and MAE (shown in parentheses) were normalized by the per-network dynamic range. "Overall (balanced)" represents random subsampling with an equal number of samples per network to mitigate overrepresentation effects.

Network	R^2	**RMSE**	**MAE**
BJ	0.93	1.20 (7.2%)	0.94 (5.7%)
BT	0.95	0.29 (3.7%)	0.18 (2.3%)
CP	0.82	0.80 (8.6%)	0.61 (6.6%)
FM	0.66	2.34 (11.7%)	1.70 (8.5%)
GR	0.67	2.13 (8.4%)	1.17 (4.6%)
KN	0.95	1.14 (3.8%)	0.71 (2.4%)
LR	0.87	0.43 (7.4%)	0.25 (4.2%)
TV	0.86	2.07 (6.5%)	1.19 (3.8%)
Overall	0.95	1.26 (4.0%)	0.72 (2.3%)
Overall (balanced)	0.89	1.54 (4.9%)	0.86 (2.7%)

Figure 2.4 presents the cumulative distribution functions (CDFs) of residuals, highlighting key patterns in SFCC curve-fitting performance across networks and illustrating the residual

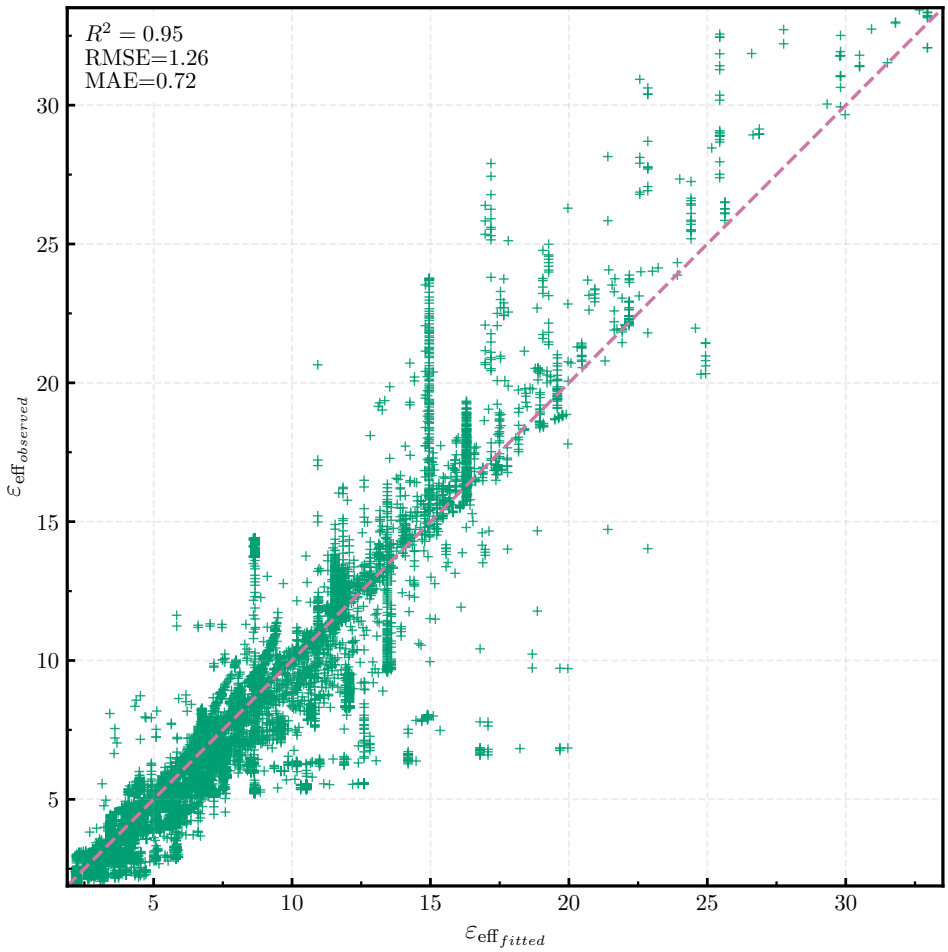


Figure 2.3: Comparison of observed and fitted effective permittivity values for freezing cycles.

distributions as a function of soil temperature. Across all networks, residuals are smallest at temperatures below T_f, demonstrating the strong ability of the SFCC fitting to reproduce $\varepsilon_{\mathrm{eff}}$ under stable frozen conditions. Residuals increase near T_f, where sparse data in the transitional zone limits the robustness of the curve fitting. Above T_f, residuals remain higher than subfreezing conditions, likely reflecting fluctuations in water content caused by rainfall, transpiration, or drainage. The CDFs exhibit steep slopes near zero across all networks, indicating minimal systematic bias and confirming that most residuals are small, supporting the overall robustness of fitting process. However, underprediction and overprediction are evident in the tails of distributions, corresponding to rapid freezing cycles that the SFCC cannot fully capture.

Figure 2.5 shows the forest plots of T_f (panel a) and b (panel b) across monitoring networks(Detailed network-level soil properties and mean initial water contents are provided in Tables S1 and S2 of the Supplementary Material). Black circles denote cycle-level estimates with 95% confidence intervals, while red squares represent network-level means. Networks are

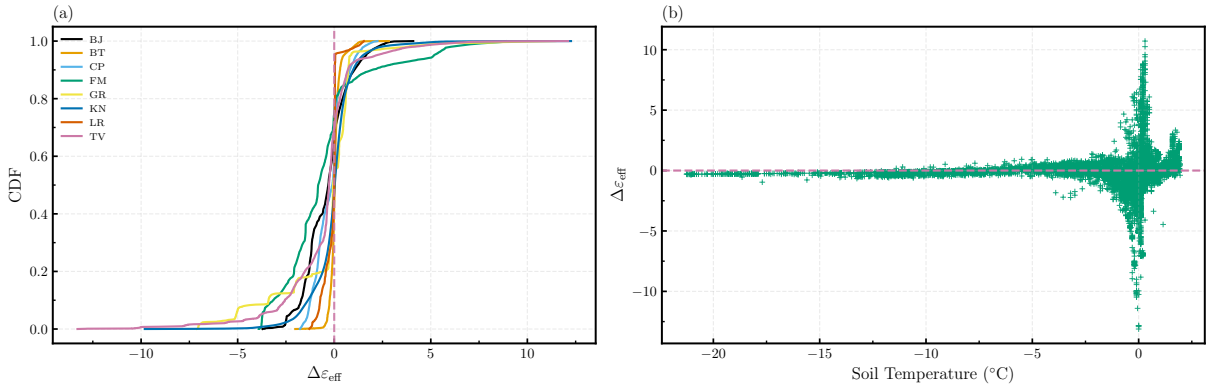


Figure 2.4: CDFs of residuals across networks (**a**), showing most residuals are small with steep slopes near zero, indicating minimal bias. Residuals as a function of soil temperature (**b**), with random subsampling of an equal number of samples per network for balanced representation.

ordered by mean T_f, with sample sizes (N) indicated. To integrate information across sites, networks, and ecozones and stabilize estimates in data-sparse regions, we applied Bayesian hierarchical (partial-pooling) models for both parameters. Table 2.3 reports posterior means and 95% credible intervals for b and T_f under hierarchical partial pooling. Across all $N = 96$ freezing cycles, b values ranged from 0.14 to 5.25, with most cycle-level estimates falling between 0.6 and 2.1 $°C^{-1}$. Network-level posterior means from the hierarchical model ranged from 0.92 to 3.47 $°C^{-1}$, revealing distinct differences in transition sharpness across networks. KN (prairie) and BT (western boreal) exhibited the lowest $\hat{b}$ (< 1.5), indicating gradual soil freezing transitions, while all other networks (BJ, CP, FM, LR, GR, TV) showed higher $\hat{b}$ (> 3), consistent with sharper phase-change behavior. Posterior credible intervals widened with increasing $\hat{b}$, reflecting higher uncertainty in steep, rapidly changing transitions (Fig. 2.5). Cycle-level T_f ranged from –0.54 °C to 0.85 °C, with most estimates between −0.01 °C and 0.40 °C. Network-level posterior means were slightly positive (0.15 – 0.44 °C). BJ, FM, LR, and CP exhibited the highest freezing points ($\hat{T}_f \approx 0.40$ °C), whereas KN, GR, and TV showed the lowest ($\hat{T}_f \approx 0.15$ °C).

2.3.2 Model Application to Field Data

To illustrate the application of our SFCC model (Eq. 2.4) and its integration with *in situ* data, we present four example sites from different networks and ecozones, each representing a distinct freezing regime: EC17 from KN (prairie; Fig. 2.6), BT17 from BT (western boreal forest; Fig. 2.7), BJ01 from BJ (eastern boreal forest; Fig. 2.8), and GR01 from GR (tundra; Fig. 2.9). Each example includes two panels: panel (a) shows the fitted SFCC overlaid on *in situ* soil temperature and ε_{eff} measurements with T_f marked; panel (b) presents the corresponding time series of soil temperature, freezing probability, ERA5 air temperature, and IMS snow cover. To

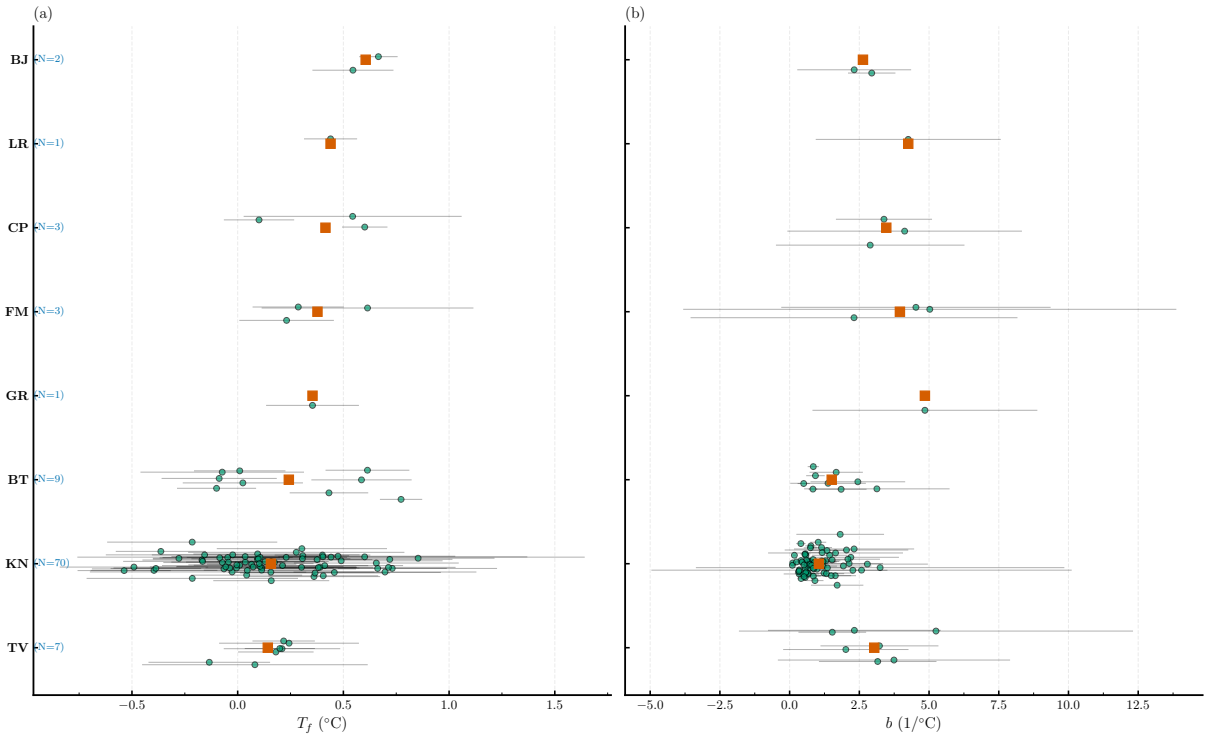


Figure 2.5: Forest plots showing the distribution of model parameters across networks: freezing point T_f **(a)** and shape factor b **(b)**. Squares indicate network means, and circles represent individual freezing cycles with vertical bars showing 95% confidence intervals.

summarize all networks, Fig. 2.10 displays the monthly mean freezing probability, with monthly mean air and soil temperatures overlaid on each tile. To compare networks quantitatively, soil states were classified at hourly resolution as frozen if $P_{\text{frozen}} > 0.75$, unfrozen if $P_{\text{frozen}} < 10^{-6}$, and transitional (partially frozen) otherwise. Daily states were assigned by majority rule.

BJ, CP, FM, and LR—located in the eastern boreal forest—remained predominantly unfrozen or partially frozen throughout the freezing season, with no periods of complete freezing despite persistent snow cover (> 90% from December to February) and subzero air temperatures. Their soils stayed near 0°C, yielding moderate freezing probabilities ($P_{\text{frozen}} \leq 0.65$). For instance, FM and CP remained partially frozen for approximately 125 days, while BJ and LR showed shorter transitional periods ($\approx$ 100 days) with $\approx$ 75 unfrozen days. In contrast, BT (western boreal) exhibited extensive freezing from December onward (90 frozen and 30 transitional days), coinciding with subzero air temperatures and complete snow cover. Tundra networks (TV, GR) recorded the coldest soil and air temperatures from December to February (soil and air consistently below $-2\,^{\circ}$C and $-10\,^{\circ}$C, respectively) and persistent snow cover ($\approx$ 100%), resulting in almost continuous frozen conditions ($P_{\text{frozen}} > 0.95$) lasting 135 and 95 days for TV and GR respectively. The KN (prairie) network showed an intermediate response: although mean air temperatures

Table 2.3: Posterior means and 95% credible intervals of b and T_f from hierarchical partial pooling across networks.

Network	$\hat{b}$ (°C^{-1})	$\hat{b}_{2.5\%}$ (°C^{-1})	$\hat{b}_{97.5\%}$ (°C^{-1})	$\hat{T_f}$ (°C)	$\hat{T_f}_{2.5\%}$ (°C)	$\hat{T_f}_{97.5\%}$ (°C)
TV	2.99	1.77	4.32	0.15	-0.08	0.40
GR	3.14	1.40	5.18	0.17	-0.16	0.54
BT	1.42	0.90	1.99	0.22	-0.02	0.46
BJ	2.43	0.88	4.25	0.44	-0.01	0.88
FM	3.47	1.75	5.43	0.40	0.12	0.69
LR	2.02	0.74	3.90	0.28	-0.11	0.61
CP	3.43	1.86	5.27	0.41	0.12	0.67
KN	0.92	0.74	1.09	0.15	0.07	0.24

(≈ -3°C) were comparable to eastern forest networks, soil cooling began earlier (November, $T_{\text{soil}} \approx 0.9$ °C) and remained frozen through February ($P_{\text{frozen}} > 0.9$) under shallow or intermittent snow (50 – 95%). On average, about 70 days were classified as frozen and 60 days as transitional at KN. Overall, while all networks experienced similar subzero air temperatures and persistent snow cover from December to February, only tundra (TV, GR), western boreal (BT), and prairie (KN) networks exhibited sustained frozen states, whereas eastern forest networks (BJ, CP, LR, FM) remained largely in transitional or unfrozen conditions.

2.4 Discussion

Our results were generally consistent with the physical factors known to govern the SFCC, particularly soil texture and initial water content [Chai et al., 2018, Bi et al., 2023a]. For instance, the KN network, which features the highest clay content ($\approx$ 27%), exhibited the most gradual freezing transition ($b \approx 0.92$), a result consistent with soil physics principles where small pores and clay surfaces create a broad distribution of matric suctions that allow liquid water to persist at temperatures well below 0°C [Tian et al., 2014, Zhang et al., 2019, Bi et al., 2023b]. Conversely, the GR network, characterized by high initial water content (VWC ≈ 0.40) and sandy texture (> 60% sand, < 8% clay), exhibited a much sharper transition ($b \approx 3.24$) [Tian et al., 2014, Zhang et al., 2019, Bi et al., 2023b]. It is worth noting that while higher moisture content increases latent heat and delays the onset of freezing—a thermal timing effect clearly visible in our heatmaps where GR begins freezing a month later than the drier TV network—the SFCC b value itself is not a measure of thermal velocity; instead, it reflects the fact that once freezing begins in such coarse, wet soils, the water in large pores transitions to ice abruptly. Similarly, the BT network ($b \approx 1.53$) demonstrates that even in sandy soils (> 80% sand), extremely low initial water content (< 8%) can lead to a more gradual transition as the remaining water is held as thin

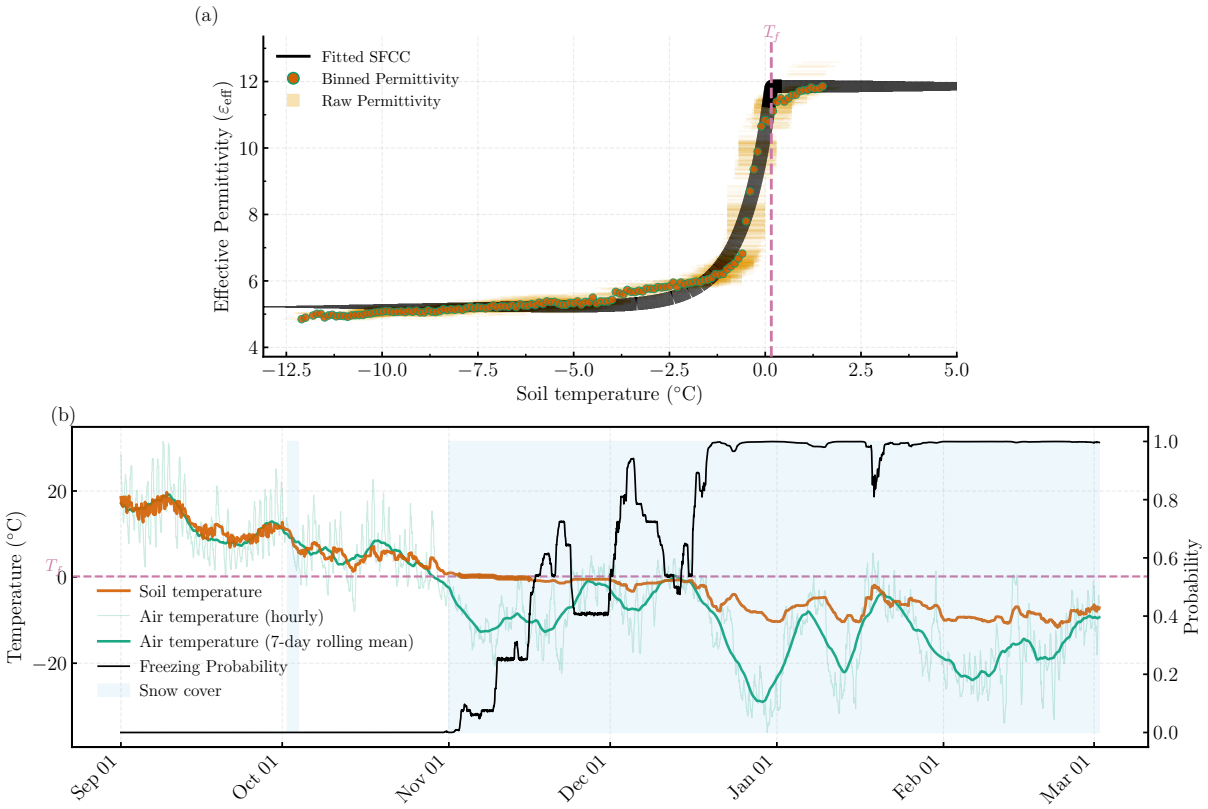


Figure 2.6: Fitted SFCC **(a)** and corresponding time series of soil temperature, air temperature, snow cover, and freezing probability **(b)** for the EC17 site in the Kenaston network (prairie). The site location is available via the interactive map on GitHub: Soil-Temperature-Permittivity-Monitoring-Sites.

films under higher suction. Despite recognizing these controlling factors, fully disentangling their individual contributions within a natural, open-system environment is inherently challenging. Multiple drivers operate simultaneously and interact nonlinearly, making it difficult to isolate each parameter's effect.

Differences in soil freezing across the networks primarily reflect the combined effects of insulation and soil texture and moisture rather than air temperature alone. Eastern boreal networks (BJ, FM, LR, and CP) remained largely unfrozen throughout winter due to thicker moss and organic layers, denser canopy cover, and higher soil moisture. These features collectively buffer ground heat loss, dampen temperature fluctuations, prolong the zero-curtain phase, and keep the soil in a transitional state for extended periods. This interpretation aligns with modeling results from boreal forests in eastern Canada, where soils were shown to remain near 0°C throughout winter despite mean air temperatures around −16°C [Oogathoo et al., 2022, Lawrence et al., 2008]. Such multilayer insulation reduces conductive and radiative heat exchange between the atmosphere and the soil, thereby limiting frost penetration even under severe cold conditions. In

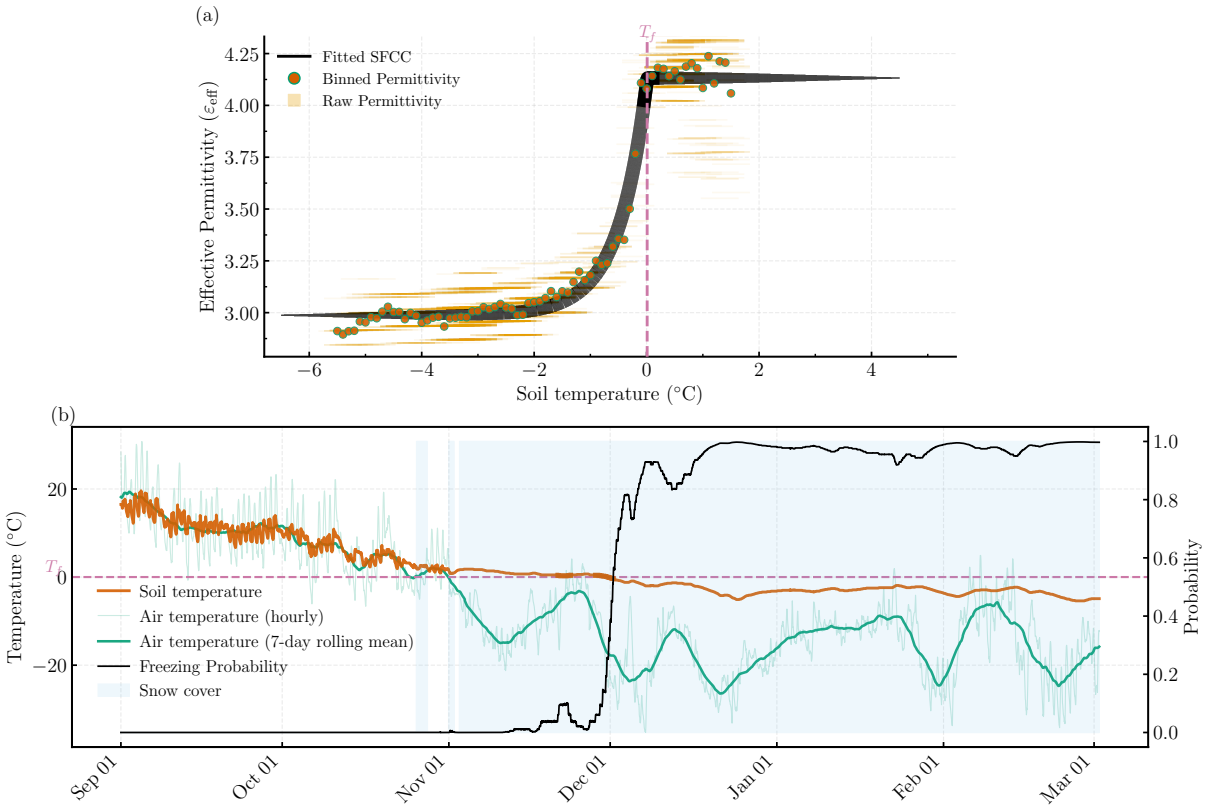


Figure 2.7: Similar to Fig. 2.6, but for the BT17 site in the Candle Lake network (western boreal forest).

contrast, BT—a dry boreal network with sparse vegetation and thin organic horizons—and KN, which lacks vegetation and organic cover, exhibited earlier and deeper freezing. Tundra networks (GR and TV) experienced prolonged freezing driven by extreme cold and minimal insulation; soil freezing began almost immediately after air temperatures fell below 0°C, although GR's higher soil moisture delayed freeze onset relative to TV.

A major source of systematic error in permittivity-based sensors is the volume mismatch between the permittivity-sensing domain and the temperature-sensing thermistor [Pardo Lara et al., 2020, 2021]. As shown by Pardo Lara et al. [2021], this mismatch can lead to apparent hysteresis and positive freezing-point depression artifacts, where permittivity sensors detect freezing before the thermistor. This occurs because permittivity sensors integrate over a larger, water-biased volume—one that shrinks in wetter soils—while thermistors measure temperature within a much smaller, localized, and water-independent zone [Hansson and Lundin, 2006, Logsdon, 2009, Pardo Lara et al., 2021]. Sensor geometry also plays a role. The thermistor in the TEROS12 is embedded in the central needle, minimizing spatial offset, while in the HydraProbe it is located in the base plate. The CS616 lacks a built-in thermistor, requiring external placement, which can exacerbate mismatch effects. However, the primary constraint in estimating T_f remains sensor

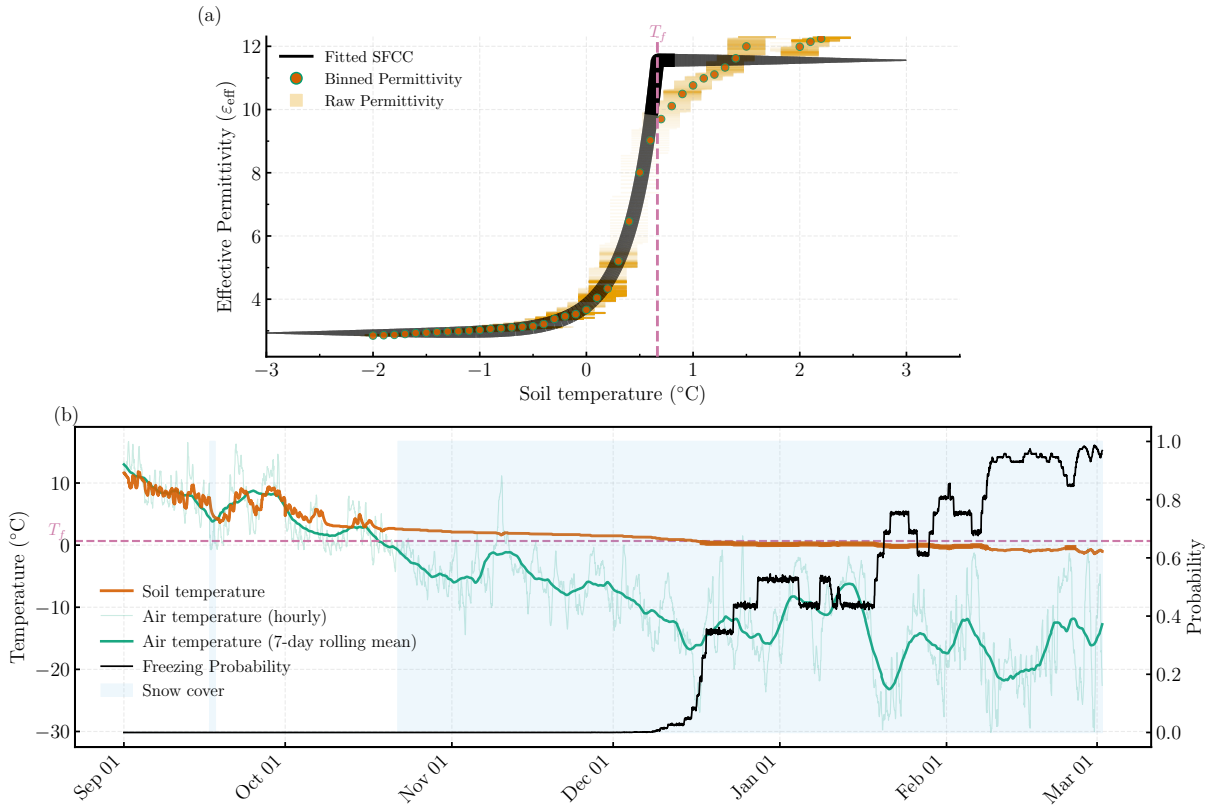


Figure 2.8: Similar to Fig. 2.6, but for the BJ01 site in the Baie-James network (eastern boreal forest).

accuracy. The stated accuracies of ±0.3°C for the HydraProbe and ±0.5°C for the TEROS12 are significant within the narrow freezing transitional zone. In our analysis, approximately 90% of T_f values from the HydraProbe and all values from the TEROS12 and CS616 fell within their respective sensor uncertainty ranges ($\pm 2\sigma$°C). This suggests that while volume mismatch may contribute to T_f variability, the observed positive offsets are primarily a function of sensor accuracy bounds rather than a significant systematic bias in the freezing process itself.

One key limitation of this study, as well as any attempt to construct SFCCs from *in situ* measurements, lies in the assumption that the total water content remains equal to the pre-freezing water content throughout the freezing period [He and Dyck, 2013]. In an open system, soil moisture can fluctuate due to rainfall events, intermittent snowmelt, other hydrological inputs, or water redistribution during freezing. This makes identifying a stable "initial" water content (or corresponding ε_{eff}) particularly challenging. However, we found that averaging the permittivity within a small temperature range (e.g., σ_T°C to 2°C, where σ_T represents the instrument-specific temperature uncertainty) before the onset of sustained cooling provides a reasonable proxy for the initial moisture conditions. Nevertheless, our results indicate that under freezing conditions—before major thawing or significant water inputs—this assumption holds reasonably well, lending

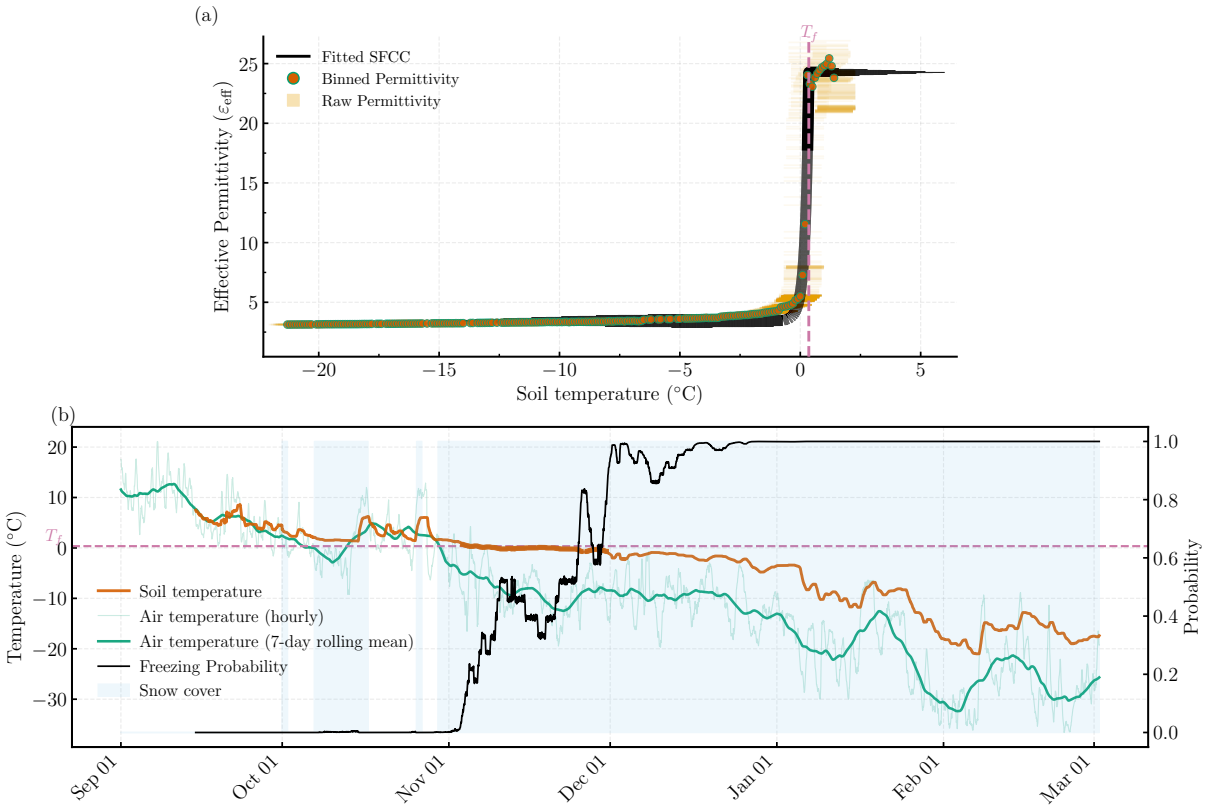


Figure 2.9: Similar to Fig. 2.6, but for the GR01 site in the George River network (tundra).

credibility to the use of the derived SFCC parameters to define soil states. Thawing cycles were excluded from this analysis because constructing a reliable STCC from *in situ* measurements is not feasible. Once air temperatures rise above 0°C, the continuous influx of water—primarily from snowmelt—violates the assumption of constant total moisture content required for curve fitting. Because the model cannot identify a stable moisture baseline, the resulting uncertainty in the fitted parameters becomes unacceptably high. Ultimately, this external influx prevents the isolation of temperature-driven phase changes from changes in the total soil water volume. Another practical challenge in applying the SFCC *in situ* is identifying distinct freezing and thawing periods. In controlled laboratory settings, these phases are straightforward to define due to precisely managed temperature profiles. In natural environments, however, air temperatures fluctuate continuously—often with pronounced diurnal cycles—leading to brief or incomplete freeze–thaw events that are difficult to isolate. These fluctuations are particularly common during the fall and spring shoulder seasons, precisely when soils transition between unfrozen and frozen states. Notably, these transitional periods also provide the critical data needed for deriving T_f and b, making SFCC construction even more challenging. For practical purposes and to improve the reliability of SFCC fitting, we recommend focusing on the main, more sustained freezing

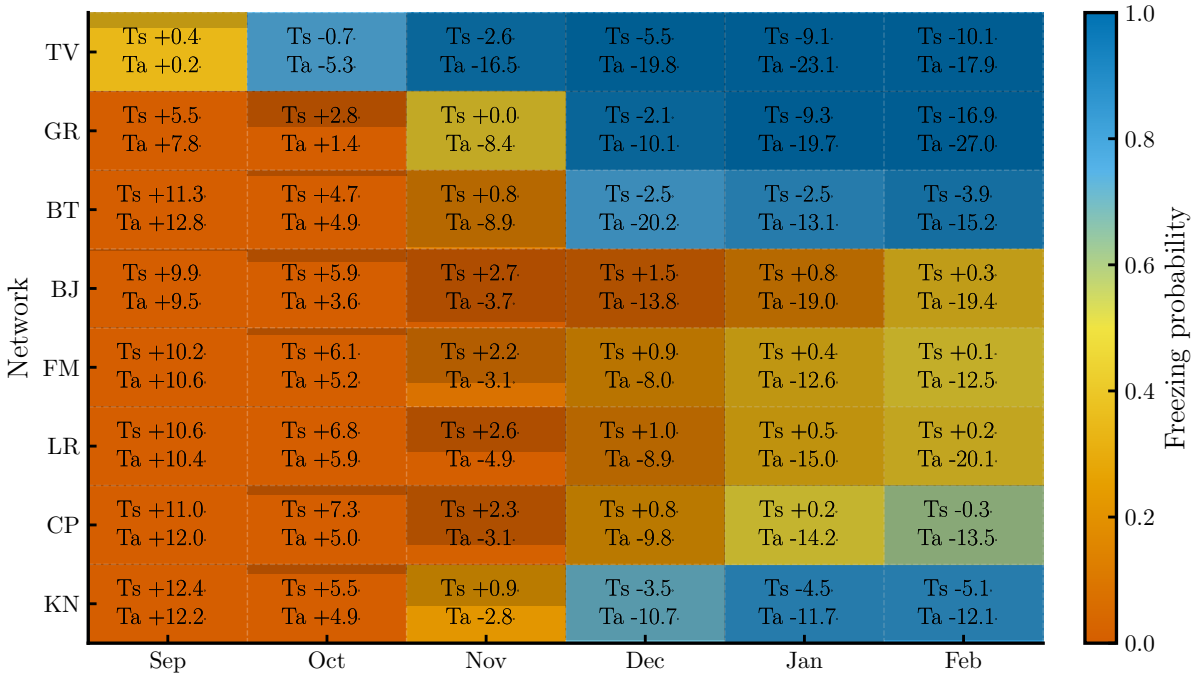


Figure 2.10: Monthly mean freezing probability for each network. Numbers within cells indicate monthly mean soil and air temperatures (T_s, T_a; °C), while the semi-transparent black fill of each cell represents the monthly mean snow cover (%).

periods while disregarding minor, short-lived fluctuations near 0°C. Although this approach may exclude some small-scale freezing cycles, prioritizing the most clearly defined freeze–thaw phases balances the complexities of natural systems with the need for practical, reliable SFCC parameter estimation. Another challenge encountered during SFCC curve fitting arose when freezing progressed rapidly. The limited temporal resolution of the sensors restricted the number of observations within the transitional zone, reducing the model's ability to resolve steep transitions and increasing the uncertainty in the estimated b values. Consequently, the bootstrap confidence intervals of b widened systematically with increasing b (Fig. 2.5).

For SFG monitoring, sensors that measure both soil temperature and permittivity are essential. The HydraProbe is advantageous as it directly measures permittivity components, while the TEROS12, despite requiring empirical conversion, offers exceptional energy efficiency. The CS616 is less suitable due to its lack of integrated temperature measurement, undefined permittivity conversion, and poor reliability in cold conditions observed at our CP network. Electrical conductivity (EC) is the most influential factor affecting dielectric sensor accuracy [Seyfried and Murdock, 2004]. Increased EC elevates the imaginary permittivity component, leading to signal attenuation and overestimated permittivity values [Seyfried et al., 2005]. However, EC values at our sites were generally low—below 0.03 S m^{-1} in boreal and tundra regions (Fig. S1) and

below 0.2 S m^{-1} in KN's top 20 cm [Tetlock et al., 2019]—well within acceptable thresholds (0.05 – 0.14 S m^{-1} depending on the sensor). Permittivity for TEROS12 and CS616 was derived from raw sensor output using manufacturer-recommended or physically based models. For CS616, we applied the formulation by Kelleners et al. [2005], using generalized calibration coefficients from prior studies [Kelleners et al., 2005, Logsdon, 2009, Hansson and Lundin, 2006]. While this may introduce minor biases, the impact on freezing cycle detection is negligible. For TEROS12, we used a third-order polynomial to convert frequency to permittivity (see Equation A.2), though underestimation has been reported in saturated conditions [Cominelli et al., 2024, Fragkos et al., 2024]. This is unlikely to affect our analysis, as saturated soils are rare during freezing periods—except at FM, where soil rarely freezes. Importantly, SFCCs can also be constructed directly from raw sensor output, with negligible differences compared to permittivity-based curves (Fig. S2). Both approaches reveal the clear signal drop needed to identify freezing transitions. Soil texture and organic matter may also affect permittivity measurements [Seyfried and Murdock, 2004, Seyfried et al., 2005], but most sites exhibit low clay and organic content, with only a few exceptions in KN and FM. Overall, the permittivity uncertainty is approximately 1 – 2 units for CS616 and TEROS12, and about 0.1 – 0.2 units for the HydraProbe—values that are well below the typical permittivity shifts observed during soil freezing and thawing. As long as a discernible permittivity change occurs, the SFCC fitting method can reliably identify the freezing transition. In rare instances where the change is too subtle—e.g., below the measurement uncertainty threshold—the curve-fitting algorithm fails to converge, and such data are automatically excluded from further analysis. Importantly, the SFCC approach is based on the relative change in permittivity with temperature rather than the absolute permittivity values, meaning that minor calibration errors or site-specific variability do not compromise our ability to detect meaningful freezing events. Furthermore, sensor measurement uncertainty (σ_T and σ_ε) was explicitly propagated through Monte Carlo simulations in all probabilistic analyses, ensuring that parameter estimation and freezing probabilities reflect the true uncertainty associated with the sensors.

2.5 Conclusions

This study applied an SFCC in permittivity–temperature space to enable robust monitoring of seasonally frozen ground (SFG) states using standard dielectric sensors, without the calibration challenges inherent in estimating liquid water content. The key insight from our multi-network analysis is that variations in freezing behavior are dominated by local ground surface properties rather than regional air temperature patterns. Importantly, the transitional (partially frozen) state accounts for the majority of the freezing season in eastern boreal networks and persists for at least

one month even in western boreal and tundra networks—dynamics that binary frozen/unfrozen classifications fail to capture. These findings reinforce that air temperature alone cannot predict SFG extent, demonstrating that remote sensing products and land surface models must account for spatial variations in ground surface properties to accurately represent freeze-thaw dynamics at regional scales. The practical value of this approach lies in its compatibility with widely deployed sensor networks and its systematic, straightforward methodology for constructing SFCCs from *in situ* measurements. Numerous soil monitoring networks across cold regions (e.g., RISMA, SNOTEL, AmeriFlux) already measure both soil temperature and dielectric permittivity. These existing infrastructures could readily adopt the methodology presented in this study to monitor seasonally SFG. This is particularly important given the rapid warming of high-latitude regions and the need for ground-truth evaluation of satellite-based freeze-thaw products, which currently rely primarily on air or soil temperature observations for training and evaluation [Rautiainen et al., 2025, Donahue et al., 2023, Roy et al., 2020, Kou et al., 2017, Gao et al., 2020, Taghipourjavi et al., 2024, Kim et al., 2011, Zhang and Armstrong, 2001].

Code and Data Availability

Scripts used for analysis and plotting, primarily written in Python 3.9, are available upon request from the authors. The dataset used to create the interactive site map is publicly accessible on GitHub (GitHub Repository). The raw sensor outputs, including effective permittivity of bulk soil (computed from the direct raw measurements of the probes), uncalibrated soil moisture data, and soil temperature measurements, along with the final study output (degree of soil freezing), are available upon request for future research applications.

Author Contributions

H.S.: Conceptualization, Methodology, Software, Data Curation, Formal Analysis, Validation, Visualization, Funding Acquisition, Writing — Original Draft, Writing — Review & Editing. R.P.L.: Methodology, Writing — Review & Editing. A.B.: Supervision, Funding Acquisition, Investigation, Writing — Review & Editing. A.R.: Supervision, Methodology, Funding Acquisition, Investigation, Writing — Review & Editing. A.M.: Investigation, Data Curation, Writing — Review & Editing. C.H.: Investigation, Data Curation, Writing — Review & Editing. B.M.: Investigation, Data Curation, Writing — Review & Editing.

Competing Interests

The contact author has declared that none of the authors has any competing interests.

Acknowledgements

We extend our gratitude to Joshua King, who passed away in February 2023, for his invaluable contributions to this field, particularly his work on instrumentation within the Trail Valley Creek dataset. We also thank the Centre d'Études Nordiques (CEN) for their logistical support. This work was further supported by the Natural Sciences and Engineering Research Council of Canada (NSERC), Hydro-Québec, and Environment and Climate Change Canada. Finally, we acknowledge the invaluable assistance of our colleagues Camille Roy, Alex Gélinas, Azza Gorrab, Esteban Hamel-Jomphe, and Kayla Wicks, whose assistance was essential during fieldwork.

Financial Support

This research was supported by the Fonds de recherche du Québec – Nature et technologies [grant no. 330450; Salmabadi, 2025] and the Canadian Space Agency (grant no. 19FAQCT B19).

2.A Appendix

2.A.1 CS616 (Campbell Scientific)

The CS616 water content reflectometer measures soil dielectric permittivity by recording the period (in microseconds) of a square-wave oscillation. This oscillation is generated by an electromagnetic pulse that travels along the sensor's 30 cm stainless steel rods, reflects off their ends, and returns to the circuit board to trigger the next pulse. Since the wave velocity depends on the dielectric properties of the surrounding medium, the measured period is directly related to the effective relative permittivity (ε_{eff}). A physically based equation derived by Kelleners et al. [2005] can be used to convert the raw output to ε_{eff}:

$$\varepsilon_{\text{eff}} = \left(\frac{(t - 2t_d)c}{4L} \right)^2 \tag{A.1}$$

where $t = \tau / S_t$ is the scaled time period (with $S_t = 1024$ and τ the temperature-corrected raw output in seconds), t_d is the delay time correction (commonly 5.4×10^{-9} s), L is the effective rod length (typically 0.261 m for the CS616), and c is the speed of light in a vacuum (3×10^8 m/s) [Hansson and Lundin, 2006, Kelleners et al., 2005, Logsdon, 2009]. Although L and t_d can vary slightly between CS616 probes, studies have shown minimal variability [Kelleners et al., 2005, Hansson and Lundin, 2006, Logsdon, 2009]. These generalized constants yield acceptable permittivity estimates when sensor-specific calibration is not feasible. Validation against standard reference fluids showed excellent agreement ($R^2 > 0.99$), and comparisons with TDR, HydraProbe, and Topp's model confirm reliable performance across soils. The accuracy of the CS616 may decline in soils with high EC ($> 0.05\,\text{S m}^{-1}$), clay content (>30 %), or organic matter (> 5 %) due to signal attenuation and delayed pulse detection. However, the CS616's relatively high operating frequency (~175 MHz) reduces sensitivity to dispersive effects. The CS616's sensing volume averages permittivity over a non-uniform electric field, which is biased toward wetter zones. While this may slightly inflate permittivity in heterogeneous soils, it helps reduce the influence of small-scale spatial variability. While the CS616 does not measure soil temperature directly, it can be paired with the CS109SS-L sensor for temperature measurements. The CS109SS-L operates over a temperature range of −40°C to +70°C, with an accuracy of ±0.60°C from −40°C to −20°C and ±0.49°C from −20°C to +70°C.

2.A.1.1 TEROS12 (METER Group)

The TEROS12 (METER Group, Inc.) uses capacitance-based technology to estimate soil dielectric permittivity. Operating at 70 MHz, it sends an oscillating signal through three 5.5 cm prongs, which act as a capacitor with the surrounding soil as the dielectric medium. The sensor measures

the charge time, which reflects the soil's dielectric properties, and outputs a scaled frequency (`RAW`) value. This value is converted to ε_{eff} using a third-order polynomial calibration equation provided in the manual:

$$\varepsilon_{\text{eff}} = \left(2.887 \times 10^{-9} \times \text{RAW}^3 - 2.080 \times 10^{5} \times \text{RAW}^2 + 5.276 \times 10^{2} \times \text{RAW} - 43.39\right)^2 \quad \text{(A.2)}$$

The sensor's reported accuracy is ±1 unit for $\varepsilon_{\text{eff}} \in [1, 40]$ and ±15% for values above 40. However, studies have shown that the TEROS 12 can systematically underestimate dielectric permittivity in highly saturated soils and exhibits increased sensitivity under saline conditions [Cominelli et al., 2024, Fragkos et al., 2024]. While the manufacturer lists a nominal sensing volume of approximately 1010 cm^3, experimental evaluations report a smaller effective volume in moist sand (approximately 423 cm^3) and a further reduction in pure water (down to 84 cm^3). The sensor also demonstrates strong thermal stability, with temperature-induced changes in permittivity typically remaining below 1 unit across the $10 - 40\,^{\circ}\text{C}$ range [Cominelli et al., 2024]. The TEROS 12 also incorporates an internal thermistor embedded in the central needle to measure temperature. These temperature readings range from −40 to 60°C, with an accuracy of ±0.5°C from −40 to 0°C and ±0.3°C from 0 to 60°C.

2.A.2 HydraProbe (Stevens Water)

The HydraProbe (Stevens Water Monitoring Systems) uses coaxial impedance dielectric reflectometry to measure the real and imaginary components of complex dielectric permittivity. It features a coaxial waveguide with four stainless steel tines (0.3 cm diameter, 5.7 cm length) arranged in a circle around a central tine, protruding from a 4.2 cm metal base plate. A 50 MHz signal is transmitted through the tines, and the sensor analyzes the amplitude ratio of incident to reflected waves to solve Maxwell's equations. This allows separate estimation of the real (ε_{r}') and imaginary (ε_{r}'') components of ε_{eff}, computed as follows [Von Hippel and Morgan, 1955, Topp et al., 1980]:

$$\varepsilon_{\text{eff}} = \frac{\varepsilon_{\text{r}}'}{2}\left(1 + \sqrt{1 + \left(\frac{\varepsilon_{\text{r}}''}{\varepsilon_{\text{r}}'}\right)^2}\right) \quad \text{(A.3)}$$

Laboratory tests confirm that the HydraProbe provides precise and consistent permittivity measurements, with inter-sensor variability typically below ±0.5 units and < 1% coefficient of variation in fluids [Seyfried and Murdock, 2004]. It performs reliably up to soil EC values of $\sim 0.14\text{Sm}^{-1}$, beyond which accuracy declines. Loss tangent values above ~ 1.45 lead to unstable

readings. Despite lacking internal temperature correction, temperature effects are minor—e.g., ~ 0.0077 units° C^{-1} in air and up to $\pm 0.06 m^3 m^{-3}$ in saturated clay soils over a 40°C range. The nominal sensing volume of the HydraProbe is approximately 4.0×10^4 mm^3, but it can expand up to $\sim 3.5 \times 10^5$ mm^3 depending on soil conditions. The effective sensing volume increases in soils with lower permittivity—such as dry or frozen soils—and contracts in wetter soils with higher permittivity. Temperature is measured via a thermistor in contact with the base plate, with a range of −40°C to +75°C, an accuracy of ±0.3°C, and a resolution of 0.1°C.

2.A.3 Instrumentation Setup

Figure A1 illustrates the insertion depths and orientations of each probe (CS616, HydraProbe, and TEROS12), along with their standard needle lengths. Accompanying the schematic are actual images of the probes to enhance visual recognition and familiarity with their designs.

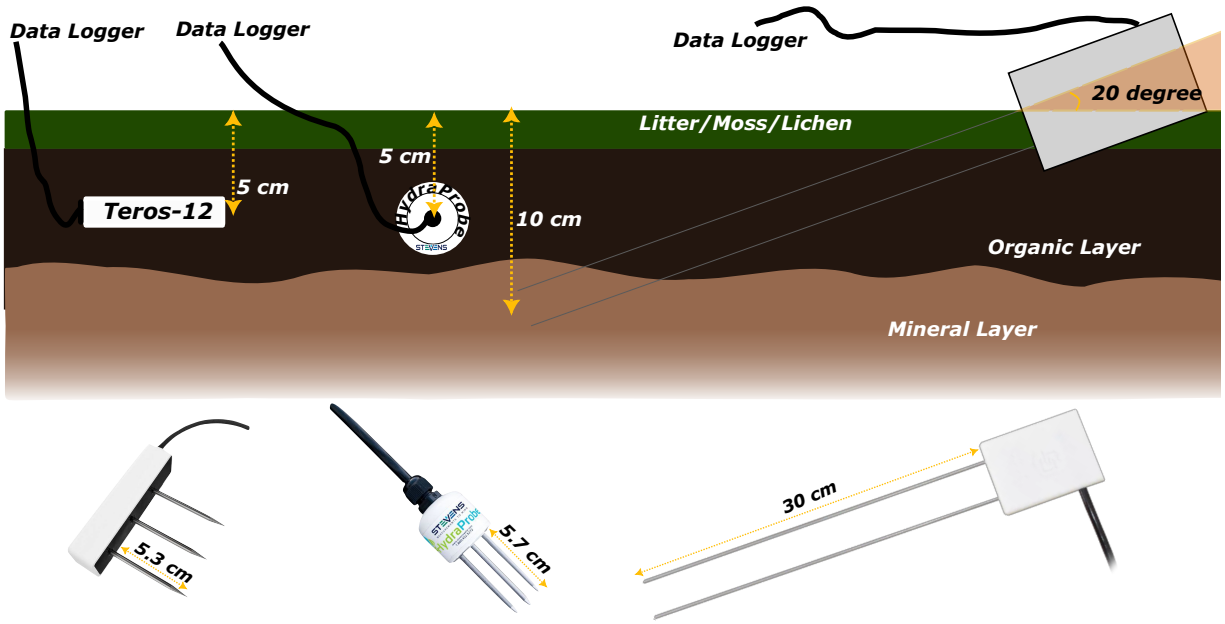


Figure A1: Instrumentation setup for soil moisture probes (CS616, HydraProbe, and TEROS12), with a schematic and corresponding probe images.

2.A.4 Derivation of Bai et al.'s Model in Permittivity-Temperature Space

In this section, we present the detailed steps that transform the Eq. (2.1) from liquid water content-soil temperature space into permittivity-soil temperature space. The resulting equation expresses the soil's effective permittivity as a function of soil temperature, as shown in Eq.(2.4).

2.A.4.1 For $T > T_{\text{soil}}$

The simplified form of Eq.(2.3) is:

$$\theta_{lw} = A\varepsilon_{\text{eff}}^{\alpha} + B - \theta_{\text{ice}}C \tag{A.4}$$

where A, B, and C are defined as:

$$A = \frac{1}{\varepsilon_{lw}^{\alpha} - \varepsilon_{\text{air}}^{\alpha}}, \tag{A.5}$$

$$B = \frac{(n-1)\varepsilon_{\text{soil}}^{\alpha} - n\varepsilon_{\text{air}}^{\alpha}}{\varepsilon_{lw}^{\alpha} - \varepsilon_{\text{air}}^{\alpha}}, \tag{A.6}$$

$$C = \frac{\varepsilon_{\text{ice}}^{\alpha} - \varepsilon_{\text{air}}^{\alpha}}{\varepsilon_{lw}^{\alpha} - \varepsilon_{\text{air}}^{\alpha}}. \tag{A.7}$$

For $T > T_{\text{soil}}$, we know that $\theta_{\text{ice}} = 0$. Therefore, we have:

$$\theta_{\text{lw}} = A\varepsilon_{\text{eff}}^{\alpha} + B \tag{A.8}$$

Additionally, the liquid water content θ_{int} is given by:

$$\theta_{\text{int}} = A\varepsilon_{\text{int}}^{\alpha} + B \tag{A.9}$$

Thus, for $T > T_{\text{soil}}$:

$$\varepsilon_{\text{eff}} = \varepsilon_{\text{int}} \tag{A.10}$$

2.A.4.2 For $T \leq T_{\text{soil}}$

For $T \leq T_{\text{soil}}$, we can express θ_{ice} in terms of θ_{int} and θ_{res}:

$$\theta_{\text{ice}} = \theta_{\text{int}} - \theta_{\text{lw}} \tag{A.11}$$

Step 1: Substitute θ_{ice} into θ_{res}:

$$\theta_{\text{res}} = A\varepsilon_{\text{res}}^{\alpha} + B - (\theta_{\text{int}} - \theta_{\text{res}})C \tag{A.12}$$

Step 2: Simplify the equation:

$$\theta_{\text{res}} = A\varepsilon_{\text{res}}^{\alpha} + B - \theta_{\text{int}}C + \theta_{\text{res}}C \tag{A.13}$$

Step 3: Bring like terms together:

$$\theta_{\text{res}}(1 - C) = A\varepsilon_{\text{res}}^{\alpha} + B - \theta_{\text{int}}C \tag{A.14}$$

Step 4: Solve for θ_{res}:

$$\theta_{\text{res}} = \frac{A\varepsilon_{\text{res}}^{\alpha} + B - \theta_{\text{int}}C}{1 - C} \tag{A.15}$$

Step 5: Similarly, for θ_{lw}:

$$\theta_{\text{lw}} = \frac{A\varepsilon_{\text{eff}}^{\alpha} + B - \theta_{\text{int}}C}{1 - C} \tag{A.16}$$

Step 6: Substitute these expressions into the Bai et al.'s model for $T \leq T_{\text{soil}}$:

$$\theta_{\text{lw}} = (\theta_{\text{int}} - \theta_{\text{res}})e^{b(T_{\text{soil}} - T_f)} + \theta_{\text{res}} \tag{A.17}$$

Step 7: Express $\theta_{\text{int}} - \theta_{\text{res}}$:

$$\theta_{\text{int}} - \theta_{\text{res}} = \frac{A\left(\varepsilon_{\text{int}}^{\alpha} - \varepsilon_{\text{res}}^{\alpha}\right)}{1 - C} \tag{A.18}$$

Step 8: Substitute back and simplify:

$$\frac{A\varepsilon_{\text{eff}}^{\alpha} + B - \theta_{\text{int}}C}{1 - C} = \frac{A\left(\varepsilon_{\text{int}}^{\alpha} - \varepsilon_{\text{res}}^{\alpha}\right)}{1 - C}e^{b(T_{\text{soil}} - T_f)} + \frac{A\varepsilon_{\text{res}}^{\alpha} + B - \theta_{\text{int}}C}{1 - C} \tag{A.19}$$

Step 9: Multiply both sides by $1 - C$ to eliminate denominator:

$$A\varepsilon_{\text{eff}}^{\alpha} + B - \theta_{\text{int}}C = A\left(\varepsilon_{\text{int}}^{\alpha} - \varepsilon_{\text{res}}^{\alpha}\right)e^{b(T_{\text{soil}} - T_f)} + A\varepsilon_{\text{res}}^{\alpha} + B - \theta_{\text{int}}C \tag{A.20}$$

Step 10: Subtract common terms from both sides:

$$A\varepsilon_{\text{eff}}^{\alpha} = A\left(\varepsilon_{\text{int}}^{\alpha} - \varepsilon_{\text{res}}^{\alpha}\right)e^{b(T_{\text{soil}} - T_f)} + A\varepsilon_{\text{res}}^{\alpha} \tag{A.21}$$

Step 11: Divide both sides by A:

$$\varepsilon_{\text{eff}}^{\alpha} = \left(\varepsilon_{\text{int}}^{\alpha} - \varepsilon_{\text{res}}^{\alpha}\right)e^{b(T_{\text{soil}} - T_f)} + \varepsilon_{\text{res}}^{\alpha} \tag{A.22}$$

Thus, we finally arrive at:

$$\varepsilon_{\text{eff}} = \left(\left(\varepsilon_{\text{int}}^{\alpha} - \varepsilon_{\text{res}}^{\alpha}\right)e^{b(T_{\text{soil}} - T_f)} + \varepsilon_{\text{res}}^{\alpha}\right)^{\frac{1}{\alpha}} \tag{A.23}$$

Supplementary Material

S1 Extended Context on Soil Freezing Theory and Measurement

The Soil Freezing Characteristic Curve (SFCC), which defines the relationship between liquid water content (θ_{lw}) and subzero temperatures [Spaans and Baker, 1996, Koopmans and Miller, 1966], provides a physically-based framework for capturing the complexities of soil freezing processes [Pardo Lara et al., 2020]. As illustrated in Fig. 2.1, a typical SFCC is characterized by three distinct physical regimes [Zhang et al., 2019]. The first, termed the "unfrozen zone," occurs when the soil temperature is above the freezing point. In this regime, the liquid water content is independent of the soil temperature; while θ_{lw} may fluctuate due to external meteorological forcing, such as precipitation or evapotranspiration, it is not governed by thermal phase change. This regime is followed by the "transitional zone," which begins immediately after the freezing point (T_f). In this zone, a sharp decrease in liquid water content occurs as the soil–water system reaches a thermodynamic balance between θ_{lw} and ice. Finally, the SFCC enters the "residual zone" at the temperature (T_{res}) where θ_{lw} stabilizes [Kozlowski, 2007, Chen et al., 2021]. At this stage, bulk and capillary water have largely frozen, and the remaining liquid exists as a thin film of unfreezable or bound water held against soil particles.

The presence and behavior of θ_{lw}, and consequently the shape of the SFCC, are influenced by numerous interrelated factors, including soil mineral composition, particle size, plasticity, initial water content, dry density, solute concentration, freezing rate, confining stress, and freeze-thaw history [Chai et al., 2018, Bi et al., 2023a,b, and references therein]. The T_f decreases as initial water content decreases. For example, Zhang et al. [2019] found that decreasing soil water content from 37.60% to 14.52% lowered T_f from -0.06°C to -0.75°C. Soil texture also influences the SFCC. Fine-grained soils show greater freezing point depression and gradual changes in θ_{lw}, while coarse-grained soils exhibit rapid water loss during freezing [Tian et al., 2014, Zhang et al., 2019, Bi et al., 2023b]. Additionally, the freezing rate, by altering pore ice formation dynamics, solute distribution, and ice grain size, can affect both the slope and curvature of the SFCC [Watanabe and Osada, 2017]. To construct the SFCC, measurements of θ_{lw} and soil temperature are required. While measuring soil temperature is relatively straightforward, accurately quantifying the θ_{lw} in frozen soil poses significant challenges, especially under field conditions.

The hysteresis between SFCC and STCC has been widely documented, particularly under laboratory conditions [Wu et al., 2017, Mavrovic et al., 2020, Pardo Lara et al., 2020]. *In situ* studies, such as Tomaškovičová and Ingeman-Nielsen [2024], reported approximately 10% higher unfrozen water content during freezing than during thawing at equivalent temperatures within

the active layer of saturated, fine-grained permafrost-affected soils, reflecting latent heat effects, cryosuction, and slow pore-water redistribution. Similarly, Overduin et al. [2006] documented asymmetric freezing–thawing transitions in saturated silty clays caused by latent heat and moisture migration. By contrast, near-surface, non-permafrost measurements found hysteresis to be theoretically expected but generally weak or indistinguishable [Pardo Lara et al., 2020].

S2 Extended Context on Technical Challenges in Estimating Unfrozen Water Content from Dielectric Measurements

Typically, both physically based models, such as dielectric mixing models, and empirical models are employed to relate ε_{eff} to θ_{uw} when using dielectric probes. To apply dielectric mixing models, the ice component must be incorporated into the model [Amankwah et al., 2022]. However, solving these models is not feasible without accurate knowledge of the ice content, a challenging parameter to measure, particularly *in situ*, where the total water content is often unknown and uncontrollable [He and Dyck, 2013]. As demonstrated by Amankwah et al. [2022], without prior knowledge of the total water content before freezing, dielectric measurements can only provide a range for the unfrozen water content rather than the exact value. Neglecting the ice component in dielectric mixing models introduces significant uncertainty and leads to overestimation of θ_{uw} [Zhou et al., 2014]. This overestimation occurs because frozen soils, at identical liquid water contents, exhibit a higher ε_{eff} than drying soils, due to the higher ε_r of ice (≈ 3.2) compared to air (≈ 1). Consequently, calibrations from unfrozen soils results in systematic overprediction of θ_{uw} in frozen soils, as the increased ε_{eff} is incorrectly attributed to additional liquid water rather than the presence of ice [Spaans and Baker, 1995]. Empirical models also face limitations. Most calibration equations are developed for unfrozen soils under thawed conditions [Yoshikawa and Overduin, 2005], rendering them inapplicable to frozen soils [He and Dyck, 2013]. Calibration equations specifically developed for frozen soils are often limited to saturated soils [Michael W Smith and Tice, 1988] or specific soil types that require knowledge of the soil's total water content prior to freezing [Spaans and Baker, 1995]. As Spaans and Baker [1995] demonstrated, a single, universal calibration equation for measuring unfrozen water content in frozen soils using dielectric probes is unattainable. Given these challenges, constructing the SFCC based on measurements of θ_{uw} is problematic, especially in dynamic field environments.

S3 Modeled Soil Data

Soil physical property data were obtained from Geng et al. [2025]. A summary of these properties at the network level is presented in Table S1, while site-specific data for each monitoring station are available at https://hesam-salmabadi.github.io/Soil-Temperature-Permittivity-Monitoring-

Table S1: Modeled soil physical properties and organic carbon across networks.

Network Name	Count	Sand (%)	Clay (%)	Silt (%)	SOC	BD (g/cm^3)
James Bay (BJ)	14	87.7%	1.4%	10.9%	0.74	1.32
Candle Lake (BT)	17	83.3%	4.2%	12.5%	2.91	1.06
La Romaine (LR)	3	70.0%	3.9%	26.2%	1.57	1.19
Montmorency Forest (FM)	29	60.0%	11.2%	28.8%	4.66	1.13
George River (GR)	1	60.2%	7.8%	32.0%	5.40	1.15
Chapleau (CP)	4	46.7%	8.4%	45.0%	2.25	1.26
Kenaston (KN)	37	36.4%	27.6%	36.0%	3.17	1.16
Trail Valley Creek (TV)	12	31.2%	22.2%	46.5%	3.02	1.17

S4 Extended SFCC Parameter Data

Table S2 summarizes the average initial volumetric water content (VWC) at the network level (values converted from initial permittivity measurements using manufacturer-specific calibrations). The table also provides the arithmetic means for the b and T_f parameters across each network, along with the total number of recorded freezing cycles analyzed for each network.

Table S2: Soil Freezing Characteristic Curve (SFCC) parameters by network.

Network	Cycle Count	Avg. b-parameter	Avg. T_f (°C)	Avg. initial VWC (m^3/m^3)
Kenaston (KN)	70	1.05	0.16	0.278
George River (GR)	1	4.85	0.35	0.393
Montmorency (FM)	3	3.96	0.38	0.258
Trail Valley (TV)	7	3.03	0.14	0.239
James Bay (BJ)	2	2.63	0.61	0.220
Chapleau (CP)	3	3.47	0.42	0.199
La Romaine (LR)	1	4.25	0.44	0.122
Candle Lake (BT)	9	1.51	0.24	0.076

S5 Biome-Level Parameter Estimation

Site-level land cover information was obtained from the MODIS/Terra+Aqua Land Cover Type Yearly L3 Global 500m SIN Grid (V061), utilizing the University of Maryland (UMD) classification scheme for this analysis [Friedl and Sulla-Menashe, 2022]. In addition to the network-level analysis, we performed hierarchical partial pooling at the biome level to further account for regional variability. The resulting b and T_f values from this analysis are presented in Tables S3 and S4 for additional reference.

Table S3: Biome-level b parameters with 95% Highest Density Intervals (HDI).

Biome	**Mean**	**HDI 2.5%**	**HDI 97.5%**
Croplands	1.000	0.480	1.574
Evergreen Needleleaf Forests	1.572	0.254	3.554
Mixed Forests	3.149	1.324	5.193
Open Shrublands	2.863	1.288	4.531
Savannas	2.230	0.703	4.020
Woody Savannas	1.675	0.832	2.671

Table S4: Biome-level T_f (°C) parameters with 95% Highest Density Intervals (HDI).

Biome	**Mean**	**HDI 2.5%**	**HDI 97.5%**
Croplands	0.139	−0.159	0.419
Evergreen Needleleaf Forests	0.004	−0.788	0.794
Mixed Forests	0.327	0.002	0.648
Open Shrublands	0.151	−0.177	0.445
Savannas	0.395	−0.079	0.883
Woody Savannas	0.230	−0.084	0.537

S6 Supplementary Figures

2.7 References

P. Ala-Aho, A. Autio, J. Bhattacharjee, E. Isokangas, K. Kujala, H. Marttila, M. Menberu, L.-J. Meriö, H. Postila, A. Rauhala, A.-K. Ronkanen, P. M. Rossi, M. Saari, A. T. Haghighi, and B. Kløve. What conditions favor the influence of seasonally frozen ground on hydrological partitioning? A systematic review. *Environmental Research Letters*, 16(4):043008, Apr. 2021. ISSN 1748-9326. doi: 10.1088/1748-9326/abe82c. URL https://iopscience.iop.org/article/10.1088/1748-9326/abe82c.

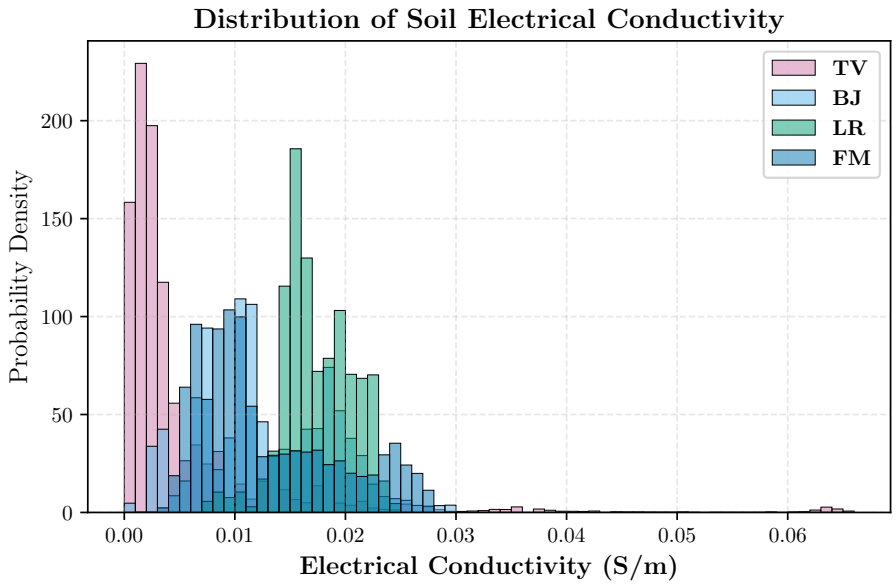


Figure S1: Histogram of electrical conductivity (EC) values measured at Trail Valley Creek (TV), James Bay (BJ), La Romaine (LR), and Montmorency Forest (FM) sites.

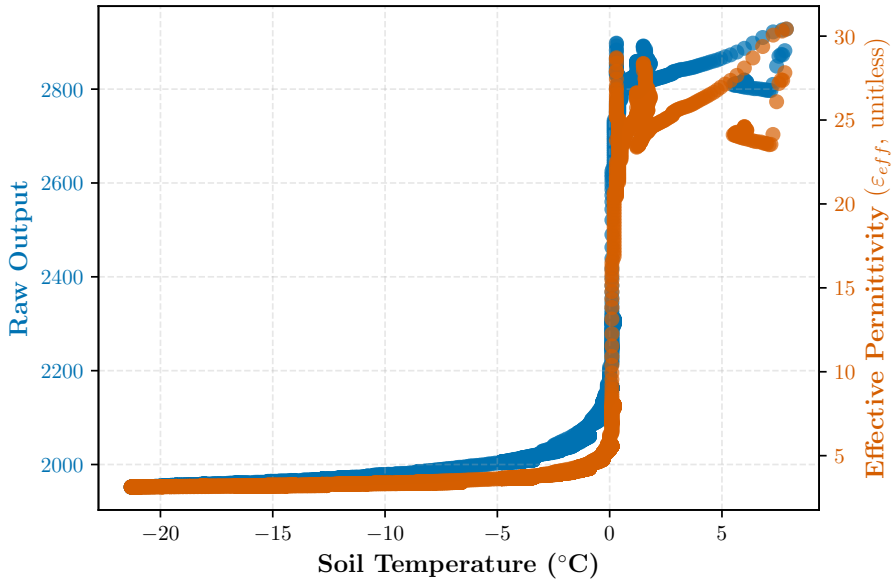


Figure S2: Soil Freezing Characteristic Curve (SFCC) visualized in both sensor raw output–temperature space and permittivity–temperature space. These representations highlight the freezing transition as captured directly by the sensor output and after conversion to effective permittivity.

S. K. Amankwah, A. M. Ireson, and R. Brannen. An improved model and field calibration technique for measuring liquid water content in unfrozen and frozen soils with dielectric probes. *Vadose Zone Journal*, 21(5):e20225, Sept. 2022. ISSN 1539-1663, 1539-1663. doi:

10.1002/vzj2.20225. URL https://acsess.onlinelibrary.wiley.com/doi/10.1002/vzj2.20225.

K. A. Arndt, J. Hashemi, S. M. Natali, L. D. Schiferl, and A.-M. Virkkala. Recent Advances and Challenges in Monitoring and Modeling Non-Growing Season Carbon Dioxide Fluxes from the Arctic Boreal Zone. *Current Climate Change Reports*, 9(2):27–40, Oct. 2023. ISSN 2198-6061. doi: 10.1007/s40641-023-00190-4. URL https://link.springer.com/10.1007/s40641-023-00190-4.

M. Azizi-Rad, G. Guggenberger, Y. Ma, and C. A. Sierra. Sensitivity of soil respiration rate with respect to temperature, moisture and oxygen under freezing and thawing. *Soil Biology and Biochemistry*, 165:108488, Feb. 2022. ISSN 00380717. doi: 10.1016/j.soilbio.2021.108488. URL https://linkinghub.elsevier.com/retrieve/pii/S003807172100362X.

R. Bai, Y. Lai, M. Zhang, and F. Yu. Theory and application of a novel soil freezing characteristic curve. *Applied Thermal Engineering*, 129:1106–1114, Jan. 2018. ISSN 1359-4311. doi: 10.1016/j.applthermaleng.2017.10.121. URL https://www.sciencedirect.com/science/article/pii/S1359431117352316.

J. Bi, G. Wang, Z. Wu, H. Wen, Y. Zhang, G. Lin, and T. Sun. Investigation on unfrozen water content models of freezing soils. *Frontiers in Earth Science*, 10:1039330, Jan. 2023a. ISSN 2296-6463. doi: 10.3389/feart.2022.1039330. URL https://www.frontiersin.org/articles/10.3389/feart.2022.1039330/full.

J. Bi, Z. Wu, Y. Lu, H. Wen, Y. Zhang, Y. Shen, T. Wei, and G. Wang. Study on soil freezing characteristic curve during a freezing-thawing process. *Frontiers in Earth Science*, 10:1007342, Jan. 2023b. ISSN 2296-6463. doi: 10.3389/feart.2022.1007342. URL https://www.frontiersin.org/articles/10.3389/feart.2022.1007342/full.

M. Chai, J. Zhang, H. Zhang, Y. Mu, G. Sun, and Z. Yin. A method for calculating unfrozen water content of silty clay with consideration of freezing point. *Applied Clay Science*, 161:474–481, Sept. 2018. ISSN 01691317. doi: 10.1016/j.clay.2018.05.015. URL https://linkinghub.elsevier.com/retrieve/pii/S016913171830228X.

Y. Chen, Z. Zhou, J. Wang, Y. Zhao, and Z. Dou. Quantification and division of unfrozen water content during the freezing process and the influence of soil properties by low-field nuclear magnetic resonance. *Journal of Hydrology*, 602:126719, Nov. 2021. ISSN 00221694. doi: 10.1016/j.jhydrol.2021.126719. URL https://linkinghub.elsevier.com/retrieve/pii/S0022169421007691.

S. Cominelli, L. D. Rivera, W. G. Brown, T. E. Ochsner, and A. Patrignani. Calibration of TEROS 10 and TEROS 12 electromagnetic soil moisture sensors. *Soil Science Society of America Journal*, 88(6):2104–2122, Nov. 2024. ISSN 0361-5995, 1435-0661. doi: 10.1002/saj2.20777. URL https://acsess.onlinelibrary.wiley.com/doi/10.1002/saj2.20777.

Copernicus Climate Change Service (C3S). Era5 hourly data on single levels from 1940 to present, 2023. URL https://cds.climate.copernicus.eu/doi/10.24381/cds.adbb2d47. Accessed: 17-Oct-2025.

E. A. Davidson and I. A. Janssens. Temperature sensitivity of soil carbon decomposition and feedbacks to climate change. *Nature*, 440(7081):165–173, Mar. 2006. ISSN 0028-0836, 1476-4687. doi: 10.1038/nature04514. URL https://www.nature.com/articles/nature04514.

K. L. M. Decker, D. Wang, C. Waite, and T. Scherbatskoy. Snow Removal and Ambient Air Temperature Effects on Forest Soil Temperatures in Northern Vermont. *Soil Science Society of America Journal*, 67(4):1234–1242, July 2003. ISSN 03615995. doi: 10.2136/sssaj2003.1234. URL http://doi.wiley.com/10.2136/sssaj2003.1234.

C. Derksen, X. Xu, R. Scott Dunbar, A. Colliander, Y. Kim, J. S. Kimball, T. A. Black, E. Euskirchen, A. Langlois, M. M. Loranty, P. Marsh, K. Rautiainen, A. Roy, A. Royer, and J. Stephens. Retrieving landscape freeze/thaw state from Soil Moisture Active Passive (SMAP) radar and radiometer measurements. *Remote Sensing of Environment*, 194:48–62, June 2017. ISSN 00344257. doi: 10.1016/j.rse.2017.03.007. URL https://linkinghub.elsevier.com/retrieve/pii/S0034425717300998.

K. Donahue, J. S. Kimball, J. Du, F. Bunt, A. Colliander, M. Moghaddam, J. Johnson, Y. Kim, and M. A. Rawlins. Deep learning estimation of northern hemisphere soil freeze-thaw dynamics using satellite multi-frequency microwave brightness temperature observations. *Frontiers in Big Data*, 6:1243559, Nov. 2023. ISSN 2624-909X. doi: 10.3389/fdata.2023.1243559. URL https://www.frontiersin.org/articles/10.3389/fdata.2023.1243559/full.

A. Fragkos, D. Loukatos, G. Kargas, and K. G. Arvanitis. Response of the TEROS 12 Soil Moisture Sensor under Different Soils and Variable Electrical Conductivity. *Sensors*, 24(7):2206, Jan. 2024. ISSN 1424-8220. doi: 10.3390/s24072206. URL https://www.mdpi.com/1424-8220/24/7/2206. Number: 7 Publisher: Multidisciplinary Digital Publishing Institute.

M. Friedl and D. Sulla-Menashe. MODIS/Terra+Aqua Land Cover Type Yearly L3 Global 500m SIN Grid V061, 2022. URL https://www.earthdata.nasa.gov/data/catalog/lpcloud-mcd12q1-061.

Q. Fu, R. Hou, T. Li, R. Jiang, P. Yan, Z. Ma, and Z. Zhou. Effects of soil water and heat relationship under various snow cover during freezing-thawing periods in Songnen Plain, China. *Scientific Reports*, 8(1):1325, Jan. 2018. ISSN 2045-2322. doi: 10.1038/s41598-018-19467-y. URL https://www.nature.com/articles/s41598-018-19467-y.

H. Gao, N. Nie, W. Zhang, and H. Chen. Monitoring the spatial distribution and changes in permafrost with passive microwave remote sensing. *ISPRS Journal of Photogrammetry and Remote Sensing*, 170:142–155, Dec. 2020. ISSN 09242716. doi: 10.1016/j.isprsjprs.2020.10.011. URL https://linkinghub.elsevier.com/retrieve/pii/S0924271620302823.

X. Geng, J. He, V. Grima, Y. Jiang, M. Tetreau, S. Crittenden, S. Kiley, A. J. VandenBygaart, and J. Vanrobaeys. 100 m soil landscape grids of Canada. *Scientific Data*, 12(1):1178, July 2025. ISSN 2052-4463. doi: 10.1038/s41597-025-05460-4. URL https://www.nature.com/articles/s41597-025-05460-4.

C. C. Hanes, M. Wotton, L. Bourgeau-Chavez, D. G. Woolford, S. Bélair, D. Martell, and M. D. Flannigan. Evaluation of new methods for drought estimation in the Canadian Forest Fire Danger Rating System. *International Journal of Wildland Fire*, 32(6):836–853, Apr. 2023. ISSN 1448-5516. doi: 10.1071/WF22112. URL https://www.publish.csiro.au/wf/WF22112. Publisher: CSIRO PUBLISHING.

K. Hansson and L.-C. Lundin. Water Content Reflectometer Application to Construction Materials and its Relation to Time Domain Reflectometry. *Vadose Zone Journal*, 5(1):459–468, 2006. ISSN 1539-1663. doi: 10.2136/vzj2005.0053. URL https://onlinelibrary.wiley.com/doi/abs/10.2136/vzj2005.0053. _eprint: https://onlinelibrary.wiley.com/doi/pdf/10.2136/vzj2005.0053.

M. Hayashi. The Cold Vadose Zone: Hydrological and Ecological Significance of Frozen-Soil Processes. *Vadose Zone Journal*, 12(4):1–8, Nov. 2013. ISSN 1539-1663, 1539-1663. doi: 10.2136/vzj2013.03.0064. URL https://acsess.onlinelibrary.wiley.com/doi/10.2136/vzj2013.03.0064.

H. He and M. Dyck. Application of Multiphase Dielectric Mixing Models for Understanding the Effective Dielectric Permittivity of Frozen Soils. *Vadose Zone Journal*, 12(1):vzj2012.0060, 2013. ISSN 1539-1663. doi: 10.2136/vzj2012.0060. URL https://onlinelibrary.wiley.com/doi/abs/10.2136/vzj2012.0060. _eprint: https://onlinelibrary.wiley.com/doi/pdf/10.2136/vzj2012.0060.

T. J. Kelleners and J. B. Norton. Determining Water Retention in Seasonally Frozen Soils Using Hydra Impedance Sensors. *Soil Science Society of America Journal*, 76(1):36–50,

Jan. 2012. ISSN 0361-5995, 1435-0661. doi: 10.2136/sssaj2011.0222. URL https://acsess.onlinelibrary.wiley.com/doi/10.2136/sssaj2011.0222.

T. J. Kelleners, M. S. Seyfried, J. M. Blonquist, J. Bilskie, and D. G. Chandler. Improved Interpretation of Water Content Reflectometer Measurements in Soils. *Soil Science Society of America Journal*, 69(6):1684–1690, Nov. 2005. ISSN 0361-5995, 1435-0661. doi: 10.2136/sssaj2005.0023. URL https://acsess.onlinelibrary.wiley.com/doi/10.2136/sssaj2005.0023.

M. S. Kersten. Thermal Properties of Soils, June 1949. URL https://hdl.handle.net/11299/124271. Accessed: October 2025.

Y. Kim, J. S. Kimball, K. C. McDonald, and J. Glassy. Developing a Global Data Record of Daily Landscape Freeze/Thaw Status Using Satellite Passive Microwave Remote Sensing. *IEEE Transactions on Geoscience and Remote Sensing*, 49(3):949–960, Mar. 2011. ISSN 0196-2892, 1558-0644. doi: 10.1109/TGRS.2010.2070515. URL http://ieeexplore.ieee.org/document/5599863/.

R. W. R. Koopmans and R. D. Miller. Soil Freezing and Soil Water Characteristic Curves. *Soil Science Society of America Journal*, 30(6):680–685, Nov. 1966. ISSN 0361-5995, 1435-0661. doi: 10.2136/sssaj1966.03615995003000060011x. URL https://acsess.onlinelibrary.wiley.com/doi/10.2136/sssaj1966.03615995003000060011x.

X. Kou, L. Jiang, S. Yan, T. Zhao, H. Lu, and H. Cui. Detection of land surface freeze-thaw status on the Tibetan Plateau using passive microwave and thermal infrared remote sensing data. *Remote Sensing of Environment*, 199:291–301, Sept. 2017. ISSN 00344257. doi: 10.1016/j.rse.2017.06.035. URL https://linkinghub.elsevier.com/retrieve/pii/S0034425717302948.

T. Kozlowski. A semi-empirical model for phase composition of water in clay–water systems. *Cold Regions Science and Technology*, 49(3):226–236, Sept. 2007. ISSN 0165232X. doi: 10.1016/j.coldregions.2007.03.013. URL https://linkinghub.elsevier.com/retrieve/pii/S0165232X07000729.

R. Latifovic. Canada's land cover (ver. 2015), 2019. URL https://ostrnrcan-dostrncan.canada.ca/handle/1845/137173. Accessed: October 2025.

D. M. Lawrence, A. G. Slater, V. E. Romanovsky, and D. J. Nicolsky. Sensitivity of a model projection of near-surface permafrost degradation to soil column depth and representation of soil organic matter. *Journal of Geophysical Research: Earth Surface*, 113(F2):2007JF000883,

June 2008. ISSN 0148-0227. doi: 10.1029/2007JF000883. URL https://agupubs.onlinelibrary.wiley.com/doi/10.1029/2007JF000883.

D. Lei, Y. Yang, C. Cai, Y. Chen, and S. Wang. The Modelling of Freezing Process in Saturated Soil Based on the Thermal-Hydro-Mechanical Multi-Physics Field Coupling Theory. *Water*, 12(10):2684, Sept. 2020. ISSN 2073-4441. doi: 10.3390/w12102684. URL https://www.mdpi.com/2073-4441/12/10/2684.

N. Lei, H. Wang, Y. Zhang, and T. Chen. Components of respiration and their temperature sensitivity in four reconstructed soils. *Scientific Reports*, 12(1):6107, Apr. 2022. ISSN 2045-2322. doi: 10.1038/s41598-022-09918-y. URL https://www.nature.com/articles/s41598-022-09918-y.

S. D. Logsdon. CS616 Calibration: Field versus Laboratory. *Soil Science Society of America Journal*, 73(1):1–6, Jan. 2009. ISSN 0361-5995, 1435-0661. doi: 10.2136/sssaj2008.0146. URL https://acsess.onlinelibrary.wiley.com/doi/10.2136/sssaj2008.0146. Publisher: Wiley.

M. M. Loranty, B. W. Abbott, D. Blok, T. A. Douglas, H. E. Epstein, B. C. Forbes, B. M. Jones, A. L. Kholodov, H. Kropp, A. Malhotra, S. D. Mamet, I. H. Myers-Smith, S. M. Natali, J. A. O'Donnell, G. K. Phoenix, A. V. Rocha, O. Sonnentag, K. D. Tape, and D. A. Walker. Reviews and syntheses: Changing ecosystem influences on soil thermal regimes in northern high-latitude permafrost regions. *Biogeosciences*, 15(17):5287–5313, Aug. 2018. ISSN 1726-4189. doi: 10.5194/bg-15-5287-2018. URL https://bg.copernicus.org/articles/15/5287/2018/.

A. L. MacKinney. Effects of Forest Litter on Soil Temperature and Soil Freezing in Autumn and Winter. *Ecology*, 10(3):312–321, July 1929. ISSN 0012-9658, 1939-9170. doi: 10.2307/1929507. URL https://esajournals.onlinelibrary.wiley.com/doi/10.2307/1929507.

A. Mavrovic, R. Pardo Lara, A. Berg, F. Demontoux, A. Royer, and A. Roy. Soil dielectric characterization at L-band microwave frequencies during freeze-thaw transitions, July 2020. URL https://hess.copernicus.org/preprints/hess-2020-291/hess-2020-291.pdf.

A. Mavrovic, O. Sonnentag, J. Lemmetyinen, C. Voigt, N. Rutter, P. Mann, J.-D. Sylvain, and A. Roy. Environmental controls of winter soil carbon dioxide fluxes in boreal and tundra environments. *Biogeosciences*, 20(24):5087–5108, Dec. 2023. ISSN 1726-4170. doi: 10.5194/bg-20-5087-2023. URL https://bg.copernicus.org/articles/20/5087/2023/. Publisher: Copernicus GmbH.

Michael W Smith and A. R. Tice. Measurement of the Unfrozen Water Content of Soils. Comparison of NMR (Nuclear Magnetic Resonance) and TDR (Time Domain Reflectometry) Methods. *CRREL Rep. 88-18. U.S. Army Corps of Engineers, Cold Regions Research and Engineering Lab, Hannover, NH.*, 1988. URL https://apps.dtic.mil/sti/tr/pdf/ADA203082.pdf. Accessed: 2024-09-20.

C. J. Mikan, J. P. Schimel, and A. P. Doyle. Temperature controls of microbial respiration in arctic tundra soils above and below freezing. *Soil Biology and Biochemistry*, 34(11): 1785–1795, Nov. 2002. ISSN 00380717. doi: 10.1016/S0038-0717(02)00168-2. URL https://linkinghub.elsevier.com/retrieve/pii/S0038071702001682.

B. Montpetit, J. King, J. Meloche, C. Derksen, P. Siqueira, J. M. Adam, P. Toose, M. Brady, A. Wendleder, V. Vionnet, and N. R. Leroux. Retrieval of airborne Ku-Band SAR Using Forward Radiative Transfer Modeling to Estimate Snow Water Equivalent: The Trail Valley Creek 2018/19 Snow Experiment, Mar. 2024a. URL https://egusphere.copernicus.org/preprints/2024/egusphere-2024-651/.

B. Montpetit, J. King, J. Meloche, C. Derksen, P. Siqueira, J. M. Adam, P. Toose, M. Brady, A. Wendleder, V. Vionnet, and N. R. Leroux. Retrieval of snow and soil properties for forward radiative transfer modeling of airborne Ku-band SAR to estimate snow water equivalent: the Trail Valley Creek 2018/19 snow experiment. *The Cryosphere*, 18(8):3857–3874, Aug. 2024b. ISSN 1994-0424. doi: 10.5194/tc-18-3857-2024. URL https://tc.copernicus.org/articles/18/3857/2024/.

M. P. Nikrad, L. J. Kerkhof, and M. M. Häggblom. The subzero microbiome: microbial activity in frozen and thawing soils. *FEMS Microbiology Ecology*, 92(6):fiw081, June 2016. ISSN 1574-6941. doi: 10.1093/femsec/fiw081. URL https://academic.oup.com/femsec/article-lookup/doi/10.1093/femsec/fiw081.

S. Oogathoo, D. Houle, L. Duchesne, and D. Kneeshaw. Evaluation of simulated soil moisture and temperature for a Canadian boreal forest. *Agricultural and Forest Meteorology*, 323: 109078, Aug. 2022. ISSN 01681923. doi: 10.1016/j.agrformet.2022.109078. URL https://linkinghub.elsevier.com/retrieve/pii/S0168192322002660.

P. Overduin, D. Kane, and W. Van Loon. Measuring thermal conductivity in freezing and thawing soil using the soil temperature response to heating. *Cold Regions Science and Technology*, 45(1):8–22, June 2006. ISSN 0165232X. doi: 10.1016/j.coldregions.2005.12.003. URL https://linkinghub.elsevier.com/retrieve/pii/S0165232X06000048.

R. Pardo Lara, A. A. Berg, J. Warland, and E. Tetlock. In Situ Estimates of Freezing/Melting Point Depression in Agricultural Soils Using Permittivity and Temperature Measurements. *Water Resources Research*, 56(5):e2019WR026020, 2020. ISSN 1944-7973. doi: 10.1029/2019WR026020. URL https://onlinelibrary.wiley.com/doi/abs/10.1029/2019WR026020. _eprint: https://onlinelibrary.wiley.com/doi/pdf/10.1029/2019WR026020.

R. Pardo Lara, A. A. Berg, J. Warland, and G. Parkin. Implications of measurement metrics on soil freezing curves: A simulation of freeze–thaw hysteresis. *Hydrological Processes*, 35(7):e14269, July 2021. ISSN 0885-6087, 1099-1085. doi: 10.1002/hyp.14269. URL https://onlinelibrary.wiley.com/doi/10.1002/hyp.14269.

C. L. Ping, J. D. Jastrow, M. T. Jorgenson, G. J. Michaelson, and Y. L. Shur. Permafrost soils and carbon cycling. *SOIL*, 1(1):147–171, Feb. 2015. ISSN 2199-398X. doi: 10.5194/soil-1-147-2015. URL https://soil.copernicus.org/articles/1/147/2015/.

K. Rautiainen, M. Holmberg, J. Cohen, A. Mialon, M. Schwank, J. Lemmetyinen, A. De La Fuente, and Y. Kerr. An operational SMOS soil freeze–thaw product. *Earth System Science Data*, 17(10):5337–5353, Oct. 2025. ISSN 1866-3516. doi: 10.5194/essd-17-5337-2025. URL https://essd.copernicus.org/articles/17/5337/2025/.

K. Roth, R. Schulin, H. Flühler, and W. Attinger. Calibration of time domain reflectometry for water content measurement using a composite dielectric approach. *Water Resources Research*, 26(10):2267–2273, Oct. 1990. ISSN 0043-1397, 1944-7973. doi: 10.1029/WR026i010p02267. URL https://agupubs.onlinelibrary.wiley.com/doi/10.1029/WR026i010p02267.

A. Roy, P. Toose, A. Mavrovic, C. Pappas, A. Royer, C. Derksen, A. Berg, T. Rowlandson, M. El-Amine, A. Barr, A. Black, A. Langlois, and O. Sonnentag. L-Band response to freeze/thaw in a boreal forest stand from ground- and tower-based radiometer observations. *Remote Sensing of Environment*, 237:111542, Feb. 2020. ISSN 00344257. doi: 10.1016/j.rse.2019.111542. URL https://linkinghub.elsevier.com/retrieve/pii/S0034425719305620.

H. Salmabadi. Development of New Microwave Multi-Sensor Freeze/Thaw Products for Improving Growing Season Monitoring in North America, 2025. URL https://doi.org/10.69777/330450. Application No.\ 330450.

H. Salmabadi, A. Berg, A. Mavrovic, A. Gorrab ep El Khedhri, H. C. MacRae, C. Hanes, and A. Roy. Improving Seasonally Frozen Ground Monitoring Using Soil Freezing Characteristic Curve in Permittivity-Temperature Space: Sites Metadata, Feb. 2025. URL https://zenodo.org/doi/10.5281/zenodo.14837416. Version Number: v1.1.

M. S. Seyfried and M. D. Murdock. CALIBRATION OF TIME DOMAIN REFLECTOMETRY FOR MEASUREMENT OF LIQUID WATER IN FROZEN SOILS:. *Soil Science*, 161(2): 87–98, Feb. 1996. ISSN 0038-075X. doi: 10.1097/00010694-199602000-00002. URL http://journals.lww.com/00010694-199602000-00002.

M. S. Seyfried and M. D. Murdock. Measurement of Soil Water Content with a 50-MHz Soil Dielectric Sensor. *Soil Science Society of America Journal*, 68(2):394–403, 2004. ISSN 1435-0661. doi: 10.2136/sssaj2004.3940. URL https://onlinelibrary.wiley.com/doi/abs/10.2136/sssaj2004.3940. _eprint: https://onlinelibrary.wiley.com/doi/pdf/10.2136/sssaj2004.3940.

M. S. Seyfried, L. E. Grant, E. Du, and K. Humes. Dielectric Loss and Calibration of the Hydra Probe Soil Water Sensor. *Vadose Zone Journal*, 4(4):1070–1079, 2005. ISSN 1539-1663. doi: 10.2136/vzj2004.0148. URL https://onlinelibrary.wiley.com/doi/abs/10.2136/vzj2004.0148. _eprint: https://onlinelibrary.wiley.com/doi/pdf/10.2136/vzj2004.0148.

E. J. A. Spaans and J. M. Baker. Examining the use of time domain reflectometry for measuring liquid water content in frozen soil. *Water Resources Research*, 31(12):2917–2925, Dec. 1995. ISSN 0043-1397, 1944-7973. doi: 10.1029/95WR02769. URL https://agupubs.onlinelibrary.wiley.com/doi/10.1029/95WR02769.

E. J. A. Spaans and J. M. Baker. The Soil Freezing Characteristic: Its Measurement and Similarity to the Soil Moisture Characteristic. *Soil Science Society of America Journal*, 60(1):13–19, Jan. 1996. ISSN 0361-5995, 1435-0661. doi: 10.2136/sssaj1996.03615995006000010005x. URL https://acsess.onlinelibrary.wiley.com/doi/10.2136/sssaj1996.03615995006000010005x.

S. Taghipourjavi, C. Kinnard, and A. Roy. Sentinel-1-Based Soil Freeze–Thaw Detection in Agro-Forested Areas: A Case Study in Southern Québec, Canada. *Remote Sensing*, 16(7): 1294, Apr. 2024. ISSN 2072-4292. doi: 10.3390/rs16071294. URL https://www.mdpi.com/2072-4292/16/7/1294.

E. Tetlock, B. Toth, A. Berg, T. Rowlandson, and J. T. Ambadan. An 11-year (2007–2017) soil moisture and precipitation dataset from the Kenaston Network in the Brightwater Creek basin, Saskatchewan, Canada. *Earth System Science Data*, 11(2):787–796, June 2019. ISSN 1866-3508. doi: 10.5194/essd-11-787-2019. URL https://essd.copernicus.org/articles/11/787/2019/. Publisher: Copernicus GmbH.

H. Tian, C. Wei, H. Wei, and J. Zhou. Freezing and thawing characteristics of frozen soils: Bound water content and hysteresis phenomenon. *Cold Regions Science and Technology*,

103:74–81, July 2014. ISSN 0165232X. doi: 10.1016/j.coldregions.2014.03.007. URL https://linkinghub.elsevier.com/retrieve/pii/S0165232X14000627.

S. Tomaškovičová and T. Ingeman-Nielsen. Quantification of freeze–thaw hysteresis of unfrozen water content and electrical resistivity from time lapse measurements in the active layer and permafrost. *Permafrost and Periglacial Processes*, 35(2):79–97, Apr. 2024. ISSN 1045-6740, 1099-1530. doi: 10.1002/ppp.2201. URL https://onlinelibrary.wiley.com/doi/10.1002/ppp.2201.

G. C. Topp, J. L. Davis, and A. P. Annan. Electromagnetic determination of soil water content: Measurements in coaxial transmission lines. *Water Resources Research*, 16(3):574–582, 1980. ISSN 1944-7973. doi: 10.1029/WR016i003p00574. URL https://onlinelibrary.wiley.com/doi/abs/10.1029/WR016i003p00574. _eprint: https://onlinelibrary.wiley.com/doi/pdf/10.1029/WR016i003p00574.

U.S. National Ice Center. IMS Daily Northern Hemisphere Snow and Ice Analysis at 1 km, 4 km, and 24 km Resolutions, Version 1, 2004. URL https://nsidc.org/data/G02156/versions/1.

P. Virtanen, R. Gommers, T. E. Oliphant, M. Haberland, T. Reddy, D. Cournapeau, E. Burovski, P. Peterson, W. Weckesser, J. Bright, S. J. Van Der Walt, M. Brett, J. Wilson, K. J. Millman, N. Mayorov, A. R. J. Nelson, E. Jones, R. Kern, E. Larson, C. J. Carey, I. Polat, Y. Feng, E. W. Moore, J. VanderPlas, D. Laxalde, J. Perktold, R. Cimrman, I. Henriksen, E. A. Quintero, C. R. Harris, A. M. Archibald, A. H. Ribeiro, F. Pedregosa, P. Van Mulbregt, A. Vijaykumar, A. P. Bardelli, A. Rothberg, A. Hilboll, A. Kloeckner, A. Scopatz, A. Lee, A. Rokem, C. N. Woods, C. Fulton, C. Masson, C. Häggström, C. Fitzgerald, D. A. Nicholson, D. R. Hagen, D. V. Pasechnik, E. Olivetti, E. Martin, E. Wieser, F. Silva, F. Lenders, F. Wilhelm, G. Young, G. A. Price, G.-L. Ingold, G. E. Allen, G. R. Lee, H. Audren, I. Probst, J. P. Dietrich, J. Silterra, J. T. Webber, J. Slavič, J. Nothman, J. Buchner, J. Kulick, J. L. Schönberger, J. V. De Miranda Cardoso, J. Reimer, J. Harrington, J. L. C. Rodríguez, J. Nunez-Iglesias, J. Kuczynski, K. Tritz, M. Thoma, M. Newville, M. Kümmerer, M. Bolingbroke, M. Tartre, M. Pak, N. J. Smith, N. Nowaczyk, N. Shebanov, O. Pavlyk, P. A. Brodtkorb, P. Lee, R. T. McGibbon, R. Feldbauer, S. Lewis, S. Tygier, S. Sievert, S. Vigna, S. Peterson, S. More, T. Pudlik, T. Oshima, T. J. Pingel, T. P. Robitaille, T. Spura, T. R. Jones, T. Cera, T. Leslie, T. Zito, T. Krauss, U. Upadhyay, Y. O. Halchenko, and Y. Vázquez-Baeza. SciPy 1.0: fundamental algorithms for scientific computing in Python. *Nature Methods*, 17(3):261–272, Mar. 2020. ISSN 1548-7091, 1548-7105. doi: 10.1038/s41592-019-0686-2. URL https://www.nature.com/articles/s41592-019-0686-2.

A. R. Von Hippel and S. O. Morgan. Dielectric Materials and Applications. *Journal of The Electrochemical Society*, 102(3):68C, 1955. ISSN 00134651. doi: 10.1149/1.2430014. URL https://iopscience.iop.org/article/10.1149/1.2430014.

K. Watanabe and Y. Osada. Simultaneous measurement of unfrozen water content and hydraulic conductivity of partially frozen soil near 0 °C. *Cold Regions Science and Technology*, 142:79–84, Oct. 2017. ISSN 0165232X. doi: 10.1016/j.coldregions.2017.08.002. URL https://linkinghub.elsevier.com/retrieve/pii/S0165232X17303671.

P. J. Williams and M. W. Smith. *The Frozen Earth: Fundamentals of Geocryology*. Cambridge University Press, 1 edition, Oct. 1989. ISBN 978-0-521-36534-5 978-0-521-42423-3 978-0-511-56443-7. doi: 10.1017/CBO9780511564437. URL https://www.cambridge.org/core/product/identifier/9780511564437/type/book.

Y. Wu, S. Nakagawa, T. J. Kneafsey, B. Dafflon, and S. Hubbard. Electrical and seismic response of saline permafrost soil during freeze - Thaw transition. *Journal of Applied Geophysics*, 146:16–26, Nov. 2017. ISSN 09269851. doi: 10.1016/j.jappgeo.2017.08.008. URL https://linkinghub.elsevier.com/retrieve/pii/S0926985117302914.

K. Yoshikawa and P. P. Overduin. Comparing unfrozen water content measurements of frozen soil using recently developed commercial sensors. *Cold Regions Science and Technology*, 42 (3):250–256, Nov. 2005. ISSN 0165232X. doi: 10.1016/j.coldregions.2005.03.001. URL https://linkinghub.elsevier.com/retrieve/pii/S0165232X05000315.

M. Zhang, X. Zhang, J. Lu, W. Pei, and C. Wang. Analysis of volumetric unfrozen water contents in freezing soils. *Experimental Heat Transfer*, 32(5):426–438, Sept. 2019. ISSN 0891-6152, 1521-0480. doi: 10.1080/08916152.2018.1535528. URL https://www.tandfonline.com/doi/full/10.1080/08916152.2018.1535528.

T. Zhang. Distributing of seasonally and perennially frozen ground in the northern hemisphere. In *Proceedings of the 8th International Conference on Permafrost, 21–25 July 2003, Zurich, Switzerland*, pages 1289–1294. AA Balkema, 2003.

T. Zhang. Influence of the seasonal snow cover on the ground thermal regime: An overview. *Reviews of Geophysics*, 43(4):2004RG000157, Dec. 2005. ISSN 8755-1209, 1944-9208. doi: 10.1029/2004RG000157. URL https://agupubs.onlinelibrary.wiley.com/doi/10.1029/2004RG000157.

T. Zhang and R. L. Armstrong. Soil freeze/thaw cycles over snow-free land detected by passive microwave remote sensing. *Geophysical Research Letters*, 28(5):763–766, Mar.

2001. ISSN 0094-8276, 1944-8007. doi: 10.1029/2000GL011952. URL https://agupubs.onlinelibrary.wiley.com/doi/10.1029/2000GL011952.

X. Zhou, J. Zhou, W. Kinzelbach, and F. Stauffer. Simultaneous measurement of unfrozen water content and ice content in frozen soil using gamma ray attenuation and TDR. *Water Resources Research*, 50(12):9630–9655, Dec. 2014. ISSN 0043-1397, 1944-7973. doi: 10.1002/2014WR015640. URL https://agupubs.onlinelibrary.wiley.com/doi/10.1002/2014WR015640.

Chapter 3

Non-Binary Retrievals of Soil Freeze–Thaw Dynamics Using Multi-Frequency Passive Microwave Data

Article Information

French Title:	Restitutions non binaires de la dynamique de gel–dégel du sol à l'aide de données micro-ondes passives multifréquences
Authors:	Hesam Salmabadi, Aaron Berg, and Alexandre Roy
Target Journal:	Remote Sensing of Environment
Publisher:	Elsevier (Preprint available via SSRN)
DOI:	http://dx.doi.org/10.2139/ssrn.6626104
Publication Status:	Under Review

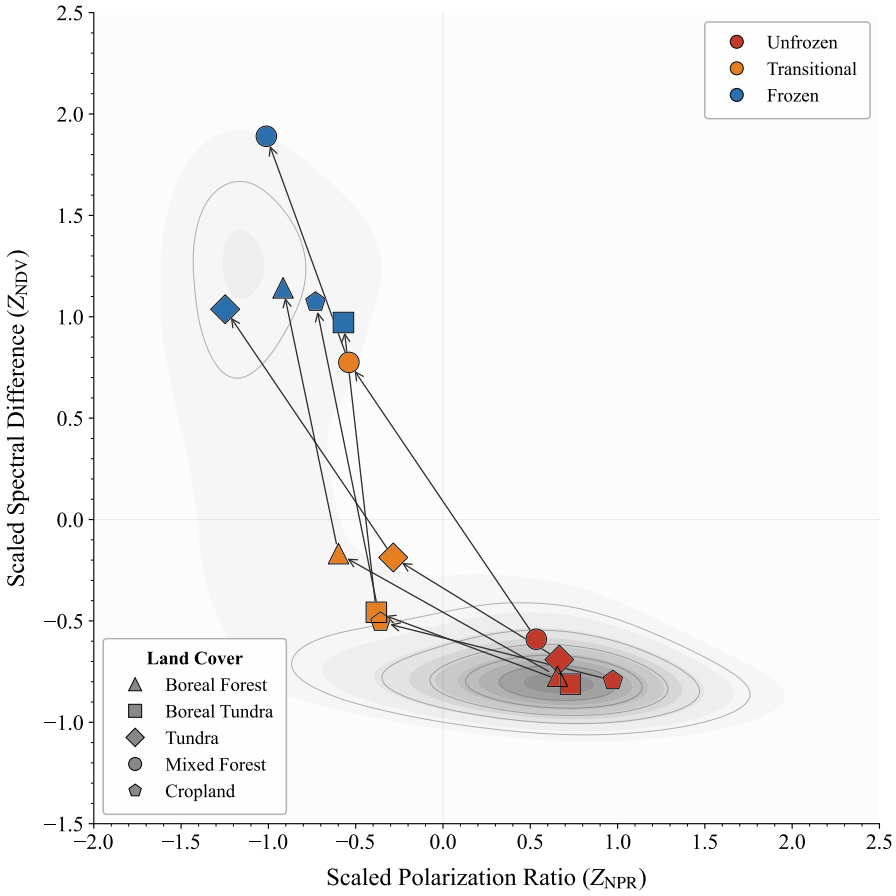
Résumé

Les transitions saisonnières de gel–dégel (FT, pour *freeze–thaw*) du sol régissent des processus hydrologiques et biogéochimiques critiques à travers les paysages nordiques. Bien que l'état physique du sol en cours de gel existe sur un continuum fortement influencé par l'effet de zéro rideau (*zero-curtain effect*) — une période thermodynamique prolongée où l'échange de chaleur latente stabilise les températures près de 0°C, permettant à l'eau liquide et à la glace de coexister — les algorithmes opérationnels basés sur les micro-ondes passives s'appuient principalement sur des classifications binaires. Cela masque la période de gel partiel, qui est prolongée et biogéochimiquement active. Dans cette étude, nous avons développé un modèle logistique probabiliste de détection non binaire du gel–dégel piloté par des observations micro-ondes passives multifréquences. Ce cadre intègre le rapport de polarisation normalisé en bande L (Z_{NPR}) de la mission SMAP (*Soil Moisture Active Passive*) avec l'indice de différence normalisée en polarisation verticale (Z_{NDV}) de l'instrument AMSR2 (*Advanced Microwave Scanning Radiometer 2*), dérivé des canaux verticaux de 18.7 et 36.5 GHz. Pour assurer une généralisabilité robuste, le modèle a été entraîné et validé de manière croisée en utilisant des températures de la couche superficielle du sol harmonisées et mesurées *in situ* à travers divers biomes en Amérique du Nord. Plutôt que de s'appuyer sur un seuil binaire rigide, nous avons employé une approche probabiliste d'étiquetage de l'état du sol utilisant des courbes caractéristiques de gel du sol (SFCC) spécifiques au biome afin d'atténuer l'ambiguïté de la cible et d'isoler des données d'entraînement de haute confiance. Les résultats démontrent que ce modèle parcimonieux à deux caractéristiques discrimine efficacement les états non gelé, de transition et complètement gelé. Lors de son évaluation par rapport à trois produits existants (FT-SMAP, FT-ESDR et FT-SMOS) sur un échantillon spatial aléatoire, le modèle a atteint des taux de concordance de 78.8 à 98.2 % et des valeurs de Kappa de Cohen de 0.44 à 0.87 à travers cinq biomes, reflétant un gradient de performance clair depuis les forêts mixtes à canopée dense jusqu'aux environnements de toundra ouverts, avec des scores F1 validés de manière croisée allant de 0.36 à 0.91. La validation thermodynamique par rapport à la température de l'air près de la surface d'ERA5 et aux enregistrements *in situ* du sol confirme que cette zone de transition définie mathématiquement s'ancre physiquement à la chaleur latente de fusion. En fin de compte, ce cadre interprétable offre une méthodologie évolutive et physiquement cohérente pour cartographier la dynamique de l'effet de zéro rideau, fournissant des données de référence non binaires critiques pour la modélisation globale du climat et du cycle du carbone.

Abstract

Seasonal soil freeze–thaw (FT) transitions govern critical hydrological and biogeochemical processes across northern landscapes. While the physical state of freezing soil exists on a continuum heavily influenced by the zero-curtain effect—a prolonged thermodynamic period where latent heat exchange stabilizes temperatures near 0°C, allowing liquid water and ice to coexist—operational passive microwave algorithms predominantly rely on binary classifications. This masks the extended and biogeochemically active partially frozen period. In this study, we developed a probabilistic, non-binary FT detection logistic model driven by multi-frequency passive microwave observations. This framework integrates the Soil Moisture Active Passive (SMAP) L-band Normalized Polarization Ratio (Z_{NPR}) with the Advanced Microwave Scanning Radiometer 2 (AMSR2) Normalized Difference V-Pol index (Z_{NDV}), derived from the 18.7 and 36.5 GHz vertical channels. To ensure robust generalizability, the model was trained and cross-validated using harmonized *in situ* topsoil temperatures across diverse biomes in North America. Rather than relying on a rigid binary threshold, we employed a probabilistic ground-state labeling approach utilizing biome-specific Soil Freezing Characteristic Curves (SFCC) to mitigate target ambiguity and isolate high-confidence training data. Results demonstrate that the parsimonious two-feature model effectively discriminates between unfrozen, transitional, and fully frozen states. When evaluated against a 3-way unanimous consensus pseudo-truth (FT-SMAP, FT-ESDR, and FT-SMOS) across a randomized spatial sample, the model achieved match rates of 78.8–98.2% and Cohen's Kappa values of 0.44–0.87 across five biomes, reflecting a clear performance gradient from canopy-dense Mixed Forests to open Tundra environments, with cross-validated F1 scores ranging from 0.36 to 0.91. Thermodynamic validation against ERA5 near-surface air temperature and *in situ* soil records confirms that this mathematically defined transitional zone physically anchors to the latent heat of fusion. Ultimately, this interpretable framework offers a scalable, physically consistent methodology for mapping zero-curtain dynamics, providing critical non-binary baseline data for global carbon and climate modeling.

Graphical Abstract



3.1 Introduction

Affecting over half of the Northern Hemisphere's terrestrial area [Zhang, 2003], seasonal soil freeze–thaw (FT) cycles serve as highly sensitive indicators of climate change [Frauenfeld and Zhang, 2011, Henry, 2007, Peng et al., 2016]. These dynamics influence a broad spectrum of physical, chemical, and biological processes within the vadose zone [Hayashi, 2013]. Hydrologically, FT transitions regulate infiltration, and drive surface runoff generation [Yang and Wang, 2019, Zhang and Sun, 2011, Wang et al., 2009]. Biogeochemically, the FT cycle acts as a primary physical regulator of microbial activity and biomass, controlling soil carbon and nitrogen turnover rates and governing the seasonal atmospheric release of greenhouse gases (CO_2, CH_4, and N_2O) [Nikrad et al., 2016, Kurganova et al., 2007, Song et al., 2017, Larsen et al., 2002, Wagner-Riddle et al., 2017]. Notably, in permafrost regions, soil thawing can trigger a positive climate feedback loop by mobilizing historically stored organic carbon into CO_2 and CH_4 [Mavrovic et al., 2023, 2025, Knoblauch et al., 2018, Johnston et al., 2014]. Physically, mechanisms like frost heave impact both infrastructure stability [Zhao et al., 2019] and the structural integrity of soil aggregates [Oztas and Fayetorbay, 2003]. Therefore, accurate monitoring and reliable prediction of soil FT dynamics are critical for advancing our understanding of coupled land-atmosphere processes and for informing risk mitigation and land management in seasonally frozen environments.

The physical state of soil is not strictly binary; rather, it exists on a continuum of fully frozen, transitional, and unfrozen [Koopmans and Miller, 1966]. This transitional phase is heavily influenced by the zero-curtain effect, a thermodynamic period during which soil temperatures stabilize near the freezing point as latent heat is continuously exchanged, allowing liquid water and ice to coexist within the soil pores [Outcalt et al., 1990]. *In situ* monitoring across diverse Canadian landscapes highlights that this transitional state is, in fact, an extended condition of the soil [Salmabadi et al., 2026, Prince et al., 2019, Devoie et al., 2022]. Observations during the freezing period between September and February reveal that soils across the tundra, prairies, and boreal forests remain in a transitional state for 30 to over 100 days, with the eastern boreal forest of Canada experiencing particularly prolonged durations [Salmabadi et al., 2026]. Accurately monitoring this transitional phase is essential, as soils in this state possess thermal, hydrological, and biogeochemical properties fundamentally distinct from fully frozen ground [Mikan et al., 2002, Nikrad et al., 2016, Mavrovic et al., 2023]. For instance, although high-latitude ecosystems typically function as net carbon sinks during the growing season, continuous microbial respiration throughout the transitional and fully frozen phases of the non-growing season can offset this uptake, effectively converting these landscapes into carbon sources [Arndt et al., 2023, Natali et al., 2019]. During the zero-curtain period, the persistence of liquid water sustains highly active microbial respiration, making liquid water content—rather than temperature—the dominant driver

of carbon emissions [Mavrovic et al., 2023]. Consequently, this transitional phase generates cumulative CO_2 emissions that can equal or exceed those of the entire winter season [Arndt et al., 2023]. Properly integrating zero-curtain dynamics into standard carbon models has been shown to improve non-growing season CO_2 respiration estimates by up to 70% [Tao et al., 2021]. With climate change progressively lengthening this transitional window [Arndt et al., 2023, Zona, 2021, Tao et al., 2021], moving beyond simple binary FT classifications to accurately detect this transitional state has become a fundamental requirement for reliable global carbon modeling. However, current operational passive microwave products generally utilize binary outputs, which presents challenges for capturing these zero-curtain phases regionally and globally.

Passive microwave remote sensing has proven effective for large-scale FT monitoring due to the stark contrast in dielectric permittivity at microwave frequencies between liquid water and ice [Rautiainen et al., 2016, Derksen et al., 2017, Rautiainen et al., 2025, Roy et al., 2015, Feng et al., 2025, Kim et al., 2017]. As soil freezes, the phase transition of water significantly reduces its dielectric properties, sharply increasing microwave emissivity and altering the observed brightness temperature (Tb). This dielectric contrast is maximized at L-band frequencies (~1.4 GHz) [Rautiainen et al., 2014]. These longer wavelengths penetrate deeper into vegetation canopies and near-surface soils, allowing for direct monitoring of underlying permittivity changes [Roy et al., 2020]. Conversely, higher frequencies (e.g., 18.7 and 36.5 GHz) feature shallower emitting depths and lower dielectric contrast; thus, they are highly sensitive to FT variations in the immediate surface, vegetation, and snowpack, while serving as strong proxies for land surface temperature [Zuerndorfer and England, 1992, Kim et al., 2011]. Key satellite instruments leveraging these dynamics include the multi-frequency Advanced Microwave Scanning Radiometer (AMSR-E and AMSR2) [Maeda et al., 2016], alongside dedicated L-band missions such as the Soil Moisture Active Passive (SMAP) [Entekhabi et al., 2010] and SMOS [Mecklenburg et al., 2016]. To discriminate soil FT states, current passive microwave algorithms utilize various indices and classification methods. Single-frequency products primarily rely on pixel-level thresholding; for instance, SMAP and SMOS utilize the Normalized Polarization Ratio (NPR) to generate binary or partially-frozen classifications, while the long-term FT-ESDR record applies empirical thresholds to the 36.5 GHz vertical channel ($TB_{36.5V}$) which serves as a proxy for land surface temperature, to identify the onset of the freezing transition. An alternative classification strategy, the Discriminant Function Algorithm (DFA), integrates $TB_{36.5V}$ as a temperature proxy with quasi-emissivity (Q_e) to capture dielectric phase transitions [Zhao et al., 2011, Feng et al., 2025]. Furthermore, algorithms based on Diurnal Amplitude Variation (DAV) detect FT transitions by monitoring the variance in brightness temperature between daily ascending and descending passes. This approach captures diurnal surface transitions without relying on static reference data [Hu et al., 2025, Lv et al., 2022]. Recent advancements demonstrate that integrating

multi-frequency observations improves classification accuracy over single-frequency baselines. For example, deep learning models achieve optimal performance only when simultaneously ingesting SMAP and AMSR data [Donahue et al., 2023]. Muzalevskiy and Ruzicka [2020] demonstrated that integrating L-band and C-band reflectivities into a Modified Polarization Ratio (MPR) successfully separates seasonal FT reference states. Furthermore, pairing a dual-frequency Q_e index (combining 1.4 GHz horizontal and 36.5 GHz vertical polarizations) with the DFA approach has proven robust across diverse geographic networks [Yang et al., 2025].

Many current FT detection methods rely on binary classifications that categorize soil as either strictly frozen or unfrozen. While some approaches have begun to address the gradual nature of soil phase transitions—such as the operational SMOS product [Rautiainen et al., 2025], which includes a partially frozen (transitional) class—there remains a need for models that capture intermediate FT dynamics in a physically transparent and spatially generalizable manner. To address this gap, this study introduces a probabilistic, multi-frequency logistic regression framework that fuses SMAP L-band and AMSR2 Ka/Ku-band observations to map the full FT continuum across five biomes in North America. Ground-state labels are derived from biome-specific Soil Freezing Characteristic Curves (SFCC), isolating high-confidence binary end-members while explicitly filtering ambiguous transitional observations from the training set. Model generalizability is assessed through spatially independent cross-validation using DBSCAN-derived spatial blocks to prevent leakage from spatial autocorrelation. Performance is evaluated against a 3-way unanimous consensus pseudo-truth (FT-SMAP, FT-ESDR, and FT-SMOS) and independently validated against ERA5 near-surface air temperature and *in situ* soil temperature records to confirm thermodynamic anchoring of the transitional class to the zero-curtain period.

3.2 Data and Methods

3.2.1 Ground Reference Data

3.2.1.1 In Situ Sites and Quality Control

A heterogeneous dataset of *in situ* topsoil temperatures was compiled from multiple monitoring networks across Canada and Alaska [Pacheco, 2019, Dorigo et al., 2021, Salmabadi et al., 2026]. Measurements at 5 cm depth were primarily utilized, with adjacent depths (4–7 cm) substituted where necessary to maintain spatial continuity. Data underwent quality control to address sensor noise and ensure physical plausibility. Observations outside the range of −37.5°C to +30°C were removed, and unphysical jumps were smoothed using a Hampel filter (24-hour window, 2σ threshold). Small gaps (< 3 hours) were linearly interpolated. To ensure spatial representativeness,

a land cover matching filter was applied using MODIS Terra/Aqua products. A station was only retained if its local 500 m land cover class (MCD12Q1) [Friedl and Sulla-Menashe, 2022b] matched the dominant land cover class of its corresponding 9 km EASE-Grid 2.0 (EPSG:6931) cell (MCD12C1, University of Maryland (UMD) scheme) [Friedl and Sulla-Menashe, 2022a, Rautiainen et al., 2025]. For any 9 km pixel containing multiple representative stations, the valid *in situ* readings were averaged to produce a single, mean soil temperature record for that pixel.

3.2.1.2 Probabilistic Ground State Labeling

To mitigate label noise caused by transitional months and sensor uncertainty, ground states were determined using a probabilistic approach based on Soil Freezing Characteristic Curves (SFCC). A normalized SFCC model, parameterized for local ecozones, was utilized alongside a Monte Carlo simulation ($N = 3000$ iterations) to propagate measurement ($\sigma = 0.3$–0.5°C) and parameter uncertainties [Salmabadi et al., 2026]. The probability of frozen conditions, $P(\text{frozen})$, was estimated using a normalized exponential decay function:

$$P(\text{frozen}) = \frac{1}{N}\sum_{i=1}^{N}\phi_i, \quad \text{where } \phi_i = \begin{cases} 1 - \exp\left[b_i(T_{\text{sim},i} - T_{f,i})\right] & \text{if } T_{\text{sim},i} < T_{f,i} \\ 0 & \text{if } T_{\text{sim},i} \geq T_{f,i} \end{cases} \tag{3.1}$$

The parameter b represents freezing transition steepness, ranging from gradual in Croplands ($b \approx 1.0$) to sharp in Tundra ($b \approx 3.0$), while T_f accounts for biome-specific offsets from 0°C driven by soil texture and dielectric effects [Salmabadi et al., 2026]. Unlike a rigid 0°C threshold, incorporating the SFCC provides critical information regarding the soil's transitional state and has recently gained traction for labeling partially frozen ground [Rautiainen et al., 2025, Cohen et al., 2021, Pardo Lara et al., 2020, Salmabadi et al., 2026]. This probabilistic approach identifies high-confidence frozen and unfrozen periods, filtering out phase transitions that contain mixed signals known to confound training.

3.2.1.3 Spatio-Temporal Harmonization

In situ measurements were harmonized with satellite observations by converting timestamps to Local Solar Time (LST) and applying a 5-hour centered rolling mean. This smoothing accounts for soil thermal inertia and bridges the temporal gap between AMSR2 (~01:30/13:30) and SMAP (~06:00/18:00) overpasses. Data were extracted at 03:00 LST and 15:00 LST as representative temporal midpoints for morning and afternoon satellite acquisitions. Classification thresholds were determined via K-means clustering ($k = 3$) on the *in situ* probabilities, yielding boundaries of ≈0.2 and ≈0.65. Observations falling between these thresholds were excluded to restrict the

training dataset to high-confidence observations. However, as these derived probabilities serve as statistical proxies rather than absolute physical measurements, intermediate values may not strictly correspond to true physical transitions, and high-confidence classifications retain inherent methodological uncertainty. Finally, to prevent radiometric contamination from standing water, samples were screened using static water fraction maps (SPL3SMP_E v006), discarding pixels with a water areal fraction exceeding 25%.

3.2.2 Passive Microwave Satellite Observations

3.2.2.1 Sensor Specifications and Preprocessing

This study integrates passive microwave observations from the Soil Moisture Active Passive (SMAP) and Advanced Microwave Scanning Radiometer 2 (AMSR2) sensors for the period of March 31, 2015, to January 1, 2024. The SMAP Enhanced L-band (1.41 GHz) Brightness Temperature product (NSIDC-0738 V2/V3) was utilized [Brodzik et al., 2021, Long et al., 2023], which employs Scatterometer Image Reconstruction (rSIR) to post observations at 9 km on the EASE-Grid 2.0 North Polar projection. L-band was selected for its superior penetration depth and minimal attenuation by moderate vegetation, enabling direct sensitivity to the soil water permittivity state through the FT transition [Rautiainen et al., 2014, Roy et al., 2015, 2020]. Ka-band (36.5 GHz) and Ku-band (18.7 GHz) data were obtained from the AMSR2 Level-3 Global Equirectangular product (resolution of 10 km) and reprojected to the 9 km SMAP grid using bilinear interpolation [Maeda et al., 2016]. These higher frequencies possess shallower optical depths and are sensitive to scattering from snow microstructure [Kim et al., 2011, 2021, Zhao et al., 2011]. Both datasets underwent identical quality control, where raw brightness temperatures were range-checked and masked for validity. To construct continuous time series, gaps were filled via linear interpolation using a maximum 5-day window, followed by a 5-day centered rolling median filter to suppress high-frequency noise while preserving sharp FT transitions.

3.2.2.2 Microwave Indices and Reference Baselines

Spectral and polarization indices were derived from harmonized brightness temperature (TB) time series to distinguish frozen from thawed ground. The Normalized Polarization Ratio (NPR) was calculated using SMAP L-band data to isolate the polarization signature of soil liquid water [Rautiainen et al., 2016, Derksen et al., 2017]:

$$NPR = \frac{TB_V^L - TB_H^L}{TB_V^L + TB_H^L} \tag{3.2}$$

Liquid water exhibits a high relative permittivity (≈80), creating a strong divergence between

vertical and horizontal emissivities via Fresnel reflection [Roy et al., 2020, Rautiainen et al., 2016]. Consequently, unfrozen, moist soil produces high polarization contrast and high NPR values. Upon freezing, liquid water transitions to ice (permittivity ≈3.2), collapsing the polarization difference and driving NPR toward near-zero.

For AMSR2, the Normalized Difference V-Pol (NDV) was derived from 18.7 and 36.5 GHz vertical channels to capture volume scattering [Cavalieri et al., 1984, Gloersen and Cavalieri, 1986]:

$$NDV = \frac{TB_V^{18.7} - TB_V^{36.5}}{TB_V^{18.7} + TB_V^{36.5}} \tag{3.3}$$

Frozen ground and snow scatter shorter wavelengths (36.5 GHz) more efficiently than longer wavelengths (18.7 GHz). This spectral gradient yields positive NDV values during winter, whereas thawed surfaces exhibit near-zero or negative values. Thus, NDV integrates signals from both the initial soil freeze and the overlying snowpack. To maximize the seasonal anomaly's dynamic range, the cross-polarized Normalized Difference H-Pol (NDH) was calculated [Cavalieri et al., 1984, Gloersen and Cavalieri, 1986]:

$$NDH = \frac{TB_H^{18.7} - TB_V^{36.5}}{TB_H^{18.7} + TB_V^{36.5}} \tag{3.4}$$

NDH physically couples the substantial drop in H-pol soil reflection during freeze-up with the subsequent onset of V-pol volume scattering.

To enable inter-pixel comparison, static summer reference statistics (July–August) were derived using an asymmetric ranking approach. Because wet soil maximizes polarization, the NPR reference (μ_{thaw}) was defined as the median of the 50 highest summer values [Rautiainen et al., 2025]. Conversely, since thawed surfaces minimize spectral gradients, the NDV and NDH references were defined as the medians of the 50 lowest values. The reference maps are presented in Fig. S1 of the Supplementary Material. Time series were normalized into Z-scores for each pixel p and time step t:

$$Z_{p,t} = \frac{X_{p,t} - \mu_{thaw,p}}{\sigma_{total,p}} \tag{3.5}$$

where $X_{p,t}$ is the instantaneous index value and $\sigma_{total,p}$ is the standard deviation across the period of record.

Finally, Diurnal Amplitude Variation (DAV) was calculated for the AMSR2 36.5 GHz and SMAP L-band vertical channels [Hu et al., 2025, Lv et al., 2022]. Defined as the absolute difference between afternoon (ascending) and morning (descending) brightness temperatures, DAV was included to assess whether diurnal thermal inertia signatures enhance classification. To

complement the normalized indices, the cross-polarized spectral ratio (Q_e) was calculated [Zhao et al., 2011, Feng et al., 2025]:

$$Q_e = \frac{TB_H^{18.7}}{TB_V^{36.5}} \tag{3.6}$$

While NDH and NDV act as bounded differences to minimize the influence of physical surface temperature variations, the Q_e ratio provides an unbounded proportional contrast between soil-sensitive 18.7H and snow-sensitive 36.5V effective emissivities. The raw 36.5 GHz vertical brightness temperature ($TB_V^{36.5}$) was also retained as a candidate feature.

3.2.3 Data Preparation and Exploratory Analysis

3.2.3.1 Biome Stratification and Thermal Filtering

The study domain was stratified into five primary biomes using the MODIS-derived UMD classification scheme (V061) [Friedl and Sulla-Menashe, 2022a]. This stratification, detailed in Table 3.1, accounts for the distinct radiative transfer regimes and uneven spatial distribution of *in situ* stations across the study area. To minimize class imbalance, the dataset was filtered to exclude warm months (May–September) for vegetated and agricultural biomes (mixed forest, boreal borest, and cropland), while tundra and boreal tundra regions were retained year-round to preserve sufficient representation of unfrozen conditions. Finally, to mitigate diurnal thermal variability, models were trained exclusively on morning (AM) overpasses. Early morning observations exhibit greater thermal stability and more uniform vertical temperature profiles, providing a more reliable microwave signal for soil FT detection.

Table 3.1: Biome stratification and UMD land cover aggregation.

Biome Class	UMD Classes	Description
Mixed Forest	1–5	Evergreen/deciduous needleleaf and broadleaf forests
Boreal Tundra	6–7	Closed and open shrublands
Boreal Forest	8–9	Woody savannas and similarly structured vegetation
Tundra	10	Low-lying vegetation and unique snow-scattering regimes
Cropland	12	Managed agricultural soils with distinct dielectric signatures

3.2.3.2 Spatial Partitioning and Cross-Validation

A critical challenge in training machine learning models on geospatial data is the risk of spatial autocorrelation, where proximity-based similarity inflates validation metrics [Meyer and Pebesma, 2022]. To enforce rigorous spatial independence and prevent data leakage, a Density-Based

Spatial Clustering of Applications with Noise (DBSCAN) algorithm was implemented [Rehman et al., 2014]. *In situ* station coordinates were clustered in EASE-Grid pixel space using a neighborhood tolerance of 20 pixels, grouping geographically proximate stations into a single "spatial block" (Fig. 3.1). To ensure the validation set is both statistically representative and spatially independent, a stratified group cross-validation strategy was employed using these spatial blocks as the grouping variable. This guarantees that all temporal observations from a given spatial block are assigned entirely to either the training or testing fold, maintaining a strict physical buffer between partitions. Simultaneously, stratification ensures that the ratio of frozen to unfrozen observations remains consistent across folds. To address the combined effect of temporal and spatial sampling imbalance, a joint spatial-block and class frequency weighting scheme was applied during training. For each training sample i, its weight was computed as:

$$w_i = \frac{N}{K \cdot n_{(g_i, c_i)}} \tag{3.7}$$

where N is the total number of training samples, K is the number of unique spatial-block–class combinations, and $n_{(g_i,c_i)}$ is the count of samples sharing both the same spatial block g_i and class label c_i as sample i. This scheme simultaneously prevents data-rich spatial blocks from dominating the learned boundary and ensures that rare class observations within each block are up-weighted proportionally.

3.2.3.3 Feature Separability and Selection

Prior to model training, a systematic feature utility analysis was performed to optimize the input vector and reduce dimensionality while maintaining physical discriminability. To prevent bias from dominant land cover classes, a diagnostic subset was constructed using stratified random undersampling to ensure balanced representation across all biomes and FT states. Within this balanced set, feature redundancy was evaluated via Pearson multicollinearity analysis, while non-linear dependencies were quantified using Mutual Information (MI) scores [Cover and Thomas, 2005]. MI quantifies the reduction in uncertainty about the target variable given an observed feature; a score of zero denotes complete statistical independence, while higher values indicate greater predictive utility for classifying the FT state [Cover and Thomas, 2005]. The final parsimonious feature vector was determined through a feature ablation study, using the Precision-Recall Area Under Curve ($PR\ AUC$) to prioritize the most informative radiometric channels across different biomes (see Sect. 3.2.4.1 for details regarding the $PR\ AUC$ metric)

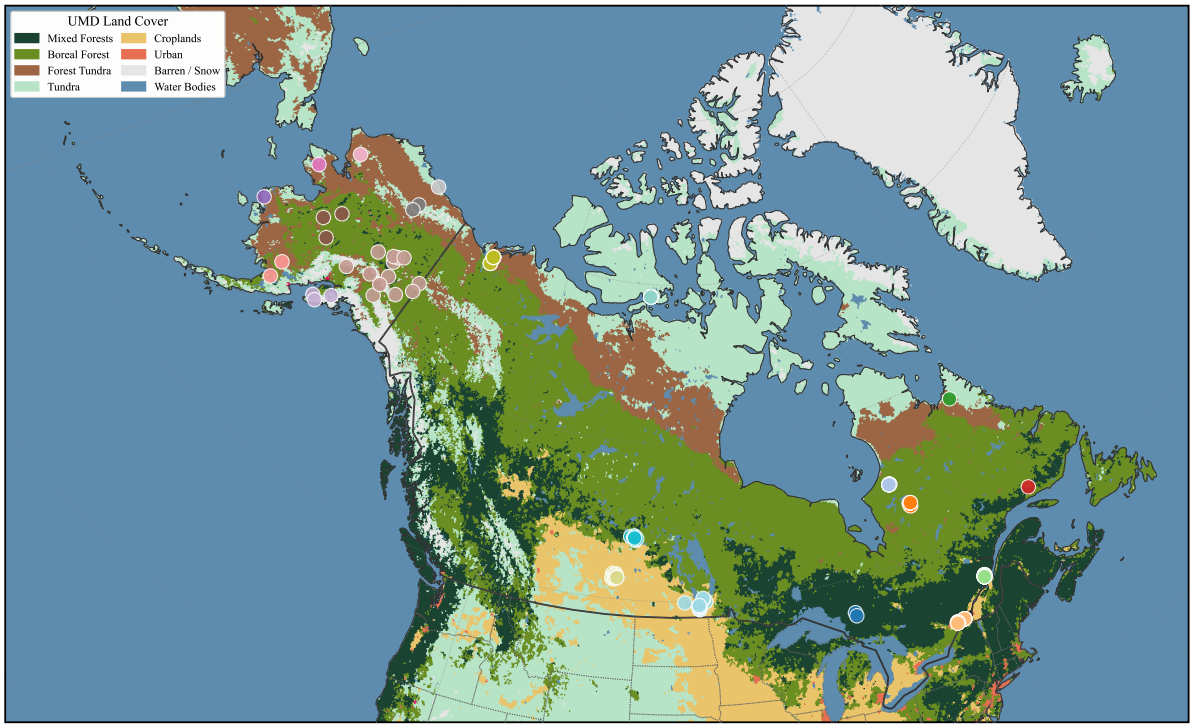


Figure 3.1: Spatial distribution of the *in situ* validation stations overlaid on the study domain's land cover classification map. Sites assigned to the same DBSCAN-derived spatial block are represented in the same color.

3.2.3.4 Validation of Pixel-wise Normalization

Raw passive microwave observations were converted into local standardized anomalies to isolate dynamic soil FT signatures from static landscape heterogeneity. Because stable environmental factors—such as canopy density, woody biomass, and surface roughness—establish unique radiometric baselines for individual pixels, the direct use of raw spatial data introduces structural bias that can obscure the state transition. To validate the efficacy of the local scaling approach, an ablation analysis compared the radiometric distributions of the *in situ* training subset against a broad environmental background sample of up to 300,000 observations (500 randomly selected pixels per biome $\times$ 600 randomly sampled time steps each), representing the wider study domain at the biome level. Alignment between the two groups was quantified using the two-sample Kolmogorov–Smirnov (K-S) D-statistic [Virtanen et al., 2020], which measures the maximum vertical distance between two cumulative distributions. This test was applied twice: first to the raw, unscaled observations, and then to the locally scaled anomalies. A reduction in D after scaling indicates that the normalization successfully collapsed diverse pixel-level radiometric behaviors into a unified signature, bringing the training distribution closer to the broader environmental population.

3.2.3.5 Domain Representativeness Assessment

To ensure the training subset adequately captured the radiometric diversity of the broader study domain, a representativeness assessment was conducted. Visually, feature space alignment was evaluated using 1D Kernel Density Estimation (KDE) histograms for individual variables and 2D KDE contour maps to ensure the joint multivariate relationship was preserved. Quantitatively, the congruence between the *in situ* training data and the environmental background was measured using three distinct metrics. The K-S test [Virtanen et al., 2020] quantified the maximum divergence between the marginal cumulative distributions of each feature. The Wasserstein distance, or "Earth Mover's Distance," [Rubner et al., 2000] quantified the minimum effort required to transform one distribution into another. Furthermore, the Maximum Mean Discrepancy (MMD) [Gretton et al., 2012] assessed the similarity of the joint 2D Z_{NPR}–Z_{NDV} distribution. The MMD utilized a Gaussian kernel, with the bandwidth parameter dynamically selected via the median heuristic based on pairwise Euclidean distances. To ensure the computational tractability of the $O(N^2)$ kernel matrix, the MMD evaluation was conducted on a random subsample of 3,000 observations per group.

3.2.4 Model Training and Evaluation

3.2.4.1 Logistic Regression and Regularization

Logistic regression was selected for this study due to the sparsity of the training data. Given a dataset of ≈180 pixels—clustered into ≈20 spatial blocks across vast, heterogeneous landscapes—data-heavy models such as deep learning or random forests risk severe spatial overfitting [James et al., 2021, Hastie et al., 2009, Pedregosa et al., 2011]. Under these conditions, complex models tend to memorize localized noise rather than learn generalized physical relationships. In contrast, the high-bias, low-variance framework of penalized logistic regression enforces a constrained, physically interpretable boundary. This prevents overfitting and ensures robust extrapolation across unobserved regions. Logistic regression provides a direct, probabilistic estimation of the ground state, where the learned coefficients (β) quantify the model's physical sensitivity to each microwave index. The probability of frozen ground, $P(y = 1|\mathbf{x})$, is modeled as:

$$P(y = 1|Z_{NPR}, Z_{NDV}) = \frac{1}{1 + \exp\left[-(\beta_0 + \beta_1 Z_{NPR} + \beta_2 Z_{NDV})\right]} \tag{3.8}$$

where β_0 is the intercept, and β_1 and β_2 are the learned coefficients for the Z_{NPR} and Z_{NDV}, respectively.

The model was trained strictly on distinct seasonal end-members representing high-confidence frozen and unfrozen ground states. The training process for each land cover class followed a

standardized protocol. First, all input features were standardized to zero mean and unit variance (Z-scores) using a single global scaler. Because the monitoring stations in this study span widely varying observational records—some covering a year while others provide over a decade of continuous measurements—fitting the scaler directly on fold-specific training data would allow data-rich blocks to disproportionately anchor the feature statistics, and would cause those statistics to shift across folds. To prevent this, the scaler was derived from a dedicated climatological reference pool: only spatial blocks with at least six months of observations were retained to ensure seasonal representativeness, and each block was resampled to a common size equal to the network-wide median, so that every block contributes equally to the estimated means and standard deviations. The same fixed scaler is then applied identically across all cross-validation folds and during operational upscaling, ensuring that coefficient magnitudes are physically interpretable and directly comparable across biomes. We then employed an L1-regularized logistic regression framework (regularization strength $C = 0.05$). The L1 penalty (Lasso) promotes model parsimony by shrinking irrelevant coefficients toward zero, mitigating overfitting risks. To counteract temporal or spatial imbalances, a joint spatial-block and class frequency weighting scheme was applied during training, ensuring that all spatial blocks contributed equitably to the learned decision boundary. The decision threshold for each land cover class was determined using the Equal Error Rate (EER) criterion , which identifies the operating point on the Receiver Operating Characteristic (ROC) curve [Fawcett, 2006] where sensitivity and specificity are equal. This balanced criterion is appropriate for geophysical FT classification, where false alarms and missed detections carry comparable operational costs. Model performance was evaluated using $PR\ AUC$ [Davis and Goadrich, 2006]. The PR curve plots precision—the fraction of pixels predicted frozen that are truly frozen—against recall—the fraction of true frozen pixels that are correctly detected—across all decision thresholds. Formally, at threshold k:

$$P_k = \frac{TP_k}{TP_k + FP_k}, \qquad R_k = \frac{TP_k}{TP_k + FN_k} \tag{3.9}$$

where TP, FP, and FN denote true positives, false positives, and false negatives with respect to the frozen class, respectively. The $PR\ AUC$ is the interpolated area under this curve:

$$\text{PR AUC} = \sum_k (R_k - R_{k-1})\, P_k \tag{3.10}$$

A score of 1.0 reflects perfect discrimination, while a score equal to the frozen class prevalence is the random-chance baseline. Unlike the $ROC\ AUC$, the $PR\ AUC$ is directly sensitive to the model's ability to correctly identify the minority (frozen) class and does not reward correct classification of the abundant unfrozen observations, making it the appropriate primary metric for the class-imbalanced training data used here.

3.2.4.2 Transition Zone Modeling

Because the logistic regression model is trained exclusively on discrete end-members (high-confidence frozen and unfrozen states), the physical FT transition period is not treated as an independent training class. Instead, it manifests as a probabilistic continuum between these extremes. To mathematically accommodate this physical uncertainty and isolate the active phase change, an analytical transitional zone was defined based on physical distances (D) from the optimized decision boundary. The boundaries of this active transition zone were derived by standardizing the log-odds shift against the Euclidean norm of the model coefficients to calculate the geometric distance for any given probability (P).

$$D(P) = \frac{\ln\left(\frac{P}{1-P}\right) - \ln\left(\frac{\tau_{\text{optimal}}}{1-\tau_{\text{optimal}}}\right)}{\sqrt{\beta_1^2 + \beta_2^2}} \tag{3.11}$$

To constrain this zone to the most physically ambiguous observations, the nominal logit distances corresponding to highly certain unfrozen ($P = 0.10$) and frozen ($P = 0.90$) states were scaled by a factor of 0.5. This tightening isolates the zone strictly around the decision boundary and establishes specific negative and positive distance limits (D_{lower} and D_{upper}) relative to the optimal threshold line ($D = 0$). These explicit bounds are then used to partition the continuous feature space into three discrete operational labels. Observations where $D < D_{\text{lower}}$ are classified as high-confidence unfrozen, and pixels where $D > D_{\text{upper}}$ are classified as high-confidence frozen. Any pixels falling within the boundaries ($D_{\text{lower}} \leq D \leq D_{\text{upper}}$) are flagged as transitional. By quantifying the progressive shift from the unfrozen to the frozen domain, this standardized distance D effectively functions as a continuous index of landscape frozenness. This framework dynamically maps the intermediate radiometric signals occurring during seasonal phase changes, providing a robust, multidimensional measure of physical uncertainty alongside the binary classification.

3.2.4.3 Auxiliary Data and Processing Mask

To mitigate erroneous FT classifications arising from signal ambiguities or residual radio frequency interference (RFI), a supplementary processing mask (PM) was implemented following the operational SMOS Level-3 Soil Freeze-Thaw algorithm protocol [Rautiainen et al., 2025]. This dynamic state machine tracks the seasonal trajectory of each pixel across time batches to prevent physically implausible phase transitions. The PM was constructed using near-surface meteorological data, specifically the daily 2 m air temperature and its 10-day rolling average derived from the ERA5-Land reanalysis dataset [Service, 2019], alongside daily binary snow cover information from the Interactive Multisensor Snow and Ice Mapping System (IMS) [Center,

2004]. Following the SMOS protocol, the mask characterizes the landscape into eight distinct seasonal states: summer (1), late summer (2), early freezing period (3), evolved freezing period (4), winter (5), late winter (6), melting period (7), and end phase of melting period (8). The temporal evolution of the pixel state is governed by a strict rule-based logic flow. For instance, summer states are dictated by temperatures remaining above 0°C, while the transition to an evolved freezing or deep winter state requires prolonged periods below −1°C or −3°C, respectively. During the spring thaw, the melting states are activated when air temperatures rise above 3°C and are subsequently modulated by the depletion of the IMS snow cover. By tracking these state transitions longitudinally, the PM establishes a robust seasonal context that restricts anomalous microwave retrievals, ensuring the final classifications remain thermodynamically consistent with the broader meteorological environment. Specifically, the processing mask prevents gross classification anomalies, such as a pixel being erroneously flagged as frozen during peak summer or thawed during deep winter. It does not directly influence the model training or the underlying decision boundary; rather, it serves strictly as a post-processing filter to enforce physical plausibility in the final outputs.

3.2.5 Evaluation and Benchmarking

3.2.5.1 Satellite Benchmarking and Consensus Evaluation

To evaluate the spatial generalizability of the proposed framework, a unanimous consensus ensemble approach was employed to benchmark the optimized logistic regression model against the operational FT-SMAP [Xu et al., 2023], FT-ESDR [Kim et al., 2021], and FT-SMOS [Rautiainen et al., 2025] products. A randomized spatial sample of 400 pixels per target biome was generated across the study domain, explicitly masking areas with a water areal fraction exceeding 25%. Analyses were strictly restricted to morning (AM) overpasses to maintain thermal consistency. Missing orbital observations across any dataset were dynamically masked to ensure an equitable comparison. Furthermore, the evaluation was strictly limited to the non-summer months; all summer observations (states 1 and 2) were excluded using the processing mask (Sect. 3.2.4.3) to prevent trivial warm-season classifications from artificially inflating performance metrics. Because legacy products predominantly output binary classifications, the continuous probabilities generated by the logistic model were hard-classified into binary states using the biome-specific optimized thresholds. Similarly, to enable direct comparison, the discrete "partially frozen" transitional class provided by the FT-SMOS product was aggregated into the frozen category. A rigorous pseudo-truth was then established by isolating only those space-time pixels where all three reference datasets (FT-SMAP, FT-ESDR, and FT-SMOS) unanimously agreed on the physical ground state. The logistic model was subsequently evaluated against this 3-way

consensus using standard classification metrics. Finally, two supplementary evaluations were conducted to provide broader context. First, the proposed model and the operational satellite products were independently benchmarked against the *in situ* soil temperature networks to assess localized algorithmic performance. Second, a comprehensive pairwise agreement analysis was performed across the spatial domain to quantify inter-mission consistency and highlight expected variances between the operational products themselves.

3.2.6 Physical Validation and Thermodynamic Consistency

An independent, domain-wide physical validation was conducted to evaluate the three-state classification capability of the model across the diverse biomes of Northern America. Model-derived classifications (unfrozen, transitional, and frozen) were cross-referenced against near-surface air temperature records from the ERA5 reanalysis dataset [Service, 2019] and *in situ* soil temperature measurements. Given the inherent thermal inertia of soil and its response to sustained energy fluxes, a 10-day rolling mean air temperature was utilized as the primary atmospheric metric to evaluate the model's alignment with seasonal thermal gradients rather than transient weather fluctuations.

Statistical validation of the three-state thermal ordering employed two complementary non-parametric tests applied to rank-ordered temperature observations grouped by model classification. First, the Kruskal-Wallis H-test [Kruskal and Wallis, 1952] assessed whether the unfrozen, transitional, and frozen classes occupy thermally distinct regimes. Because large sample sizes ($N > 400{,}000$) can render even trivial differences statistically significant, the rank-based epsilon-squared (ε^2) effect size [Cohen, 2013] was computed alongside the H-statistic to quantify the proportion of total temperature variance explained by the classification. Second, the Jonckheere-Terpstra test [Jonckheere, 1954, Terpstra, 1952] was applied to test the directional ordered hypothesis—that median temperature decreases monotonically from unfrozen to transitional to frozen—providing a more specific and statistical confirmation of the thermodynamic ordering than an omnibus test alone.

To measure how continuously the index of frozenness (D) tracks physical cooling, Spearman's rank correlation coefficient (ρ) was computed between D and the 10-day mean air temperature and *in situ* soil temperature, with a strong negative correlation hypothesized. The physical validity of the transitional state was further confirmed by evaluating the fraction of observations from each class falling within a thermally expected window near the freezing point: -7°C to 2°C for the 10-day mean air temperature, and -2°C to 2°C for *in situ* soil temperature. The air temperature window reflects the expected range over which a sustained atmospheric forcing drives the surface through an active phase change [Peng et al., 2016], while the narrower soil band targets the latent

heat plateau characteristic of the zero-curtain effect.

To complete the physical validation, phase change trajectories were mapped within the bivariate feature space. For each biome, bivariate centroids (mean Z_{NPR} and Z_{NDV}) were calculated for the three classifications. Plotting the trajectories connecting these centroids allows for a visual assessment of how dielectric and scattering properties evolve, verifying that the statistical classifications follow theoretically sound microwave radiative transfer pathways.

3.3 Results

3.3.1 Feature Selection and Physical Validation

Statistical screening through Pearson correlation (Fig. S2 in Supplementary Material), Global Mutual Information (MI) rankings (Fig. 3.2 and Table 3.2), and visual class separability analysis (Fig S3 and S4 in Supplementary Material) revealed that while high-frequency brightness temperatures ($TB_{36.5V}$), Q_e, and Z_{NDH} possess high discriminatory power, they exhibit strong inter-correlation (r = 0.66 to 0.79). Conversely, Z_{NPR} and Z_{NDV} emerged as a complementary pair: Z_{NPR} effectively captures the dielectric phase change in open biomes (Tundra/Cropland MI $\geq$ 0.34), while Z_{NDV} remains robust in canopy-dominated regions (Boreal/Mixed Forest MI $\geq$ 0.30) where woody biomass tends to mask the surface polarization signal. A more detailed analysis is provided in Supplementary Material S2. A feature ablation study (Table S1) confirmed that the combination of Z_{NPR} and Z_{NDV} provides the optimal balance between classification performance and cross-biome stability. Removing Z_{NDV} resulted in a drastic Precision-Recall AUC drop (up to -0.381 in mixed forests), while adding redundant features like raw $TB_{36.5V}$ often destabilized the model optimization, likely due to multicollinearity.

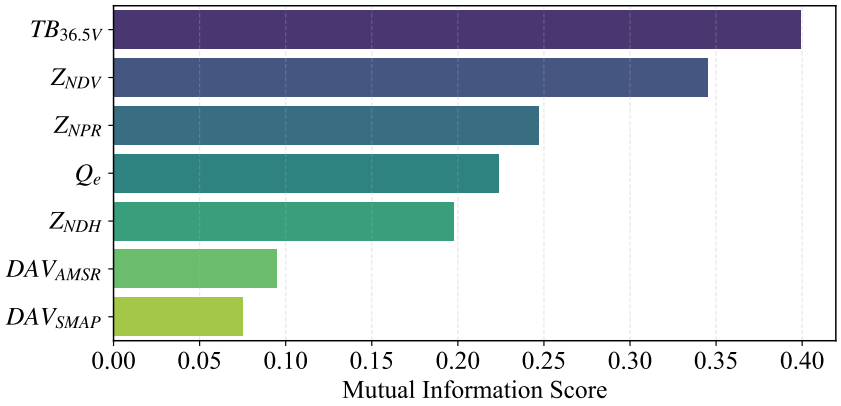


Figure 3.2: Global feature importance ranking based on Mutual Information (MI) scores. The bar chart quantifies the non-linear dependency between each feature and the binary targets.

Table 3.2: Mutual information (MI) scores stratified by biome.

	Z_{NPR}	Z_{NDV}	Z_{NDH}	Q_e	DAV_{AMSR}	DAV_{SMAP}	$TB_{36.5V}$
Tundra	0.37	0.35	0.37	0.34	0.15	0.12	0.44
Boreal Tundra	0.14	0.29	0.18	0.26	0.21	0.05	0.33
Boreal Forest	0.25	0.33	0.36	0.36	0.01	0.05	0.28
Mixed Forest	0.20	0.30	0.29	0.41	0.06	0.02	0.32
Cropland	0.34	0.52	0.11	0.13	0.21	0.15	0.51

The seasonal evolution of the standardized signals (Z_{NPR} and Z_{NDV}) alongside *in situ* soil temperatures captures the temporal dynamics of the phase change (Fig. 3.3). During unfrozen months, both signals oscillate near a stable zero baseline. As freeze-up begins, the signals rapidly diverge in response to the freezing. During deep winter, the Z_{NPR} signal plateaus as near-surface moisture fully converts to ice, demonstrating that further temperature drops do not significantly alter the bulk dielectric constant. Conversely, the Z_{NDV} signal exhibits continued variance as it responds to ongoing volume scattering from winter snowpack evolution. Based on these statistical and physical justifications, Z_{NPR} and Z_{NDV} were finalized as the input vector for the FT algorithm.

3.3.2 Preprocessing Validation and Training Representativeness

To isolate dynamic temporal signals from static environmental noise (e.g., canopy structure and surface roughness), a pixel-level local scaling step was applied to the input features. This standardization improved the spatial alignment of features, reducing the K-S D-statistic by 30% to 60% across heterogeneous biomes (see Supplementary Sect. S3 and Figs. S6–S7). This process ensures a stable, standardized feature space where radiometric anomalies can be directly attributed to dielectric phase changes rather than static landscape characteristics.

The radiometric representativeness of the resulting *in situ* training subset was validated against the broader environmental background. Quantitative metrics (Supplementary Table S2) demonstrate high marginal and joint-space alignment; notably, the MMD scores remained low (≤ 0.016) across all land cover classes. While complex landscapes like Mixed Forest exhibited minor marginal divergence in Z_{NPR} due to limited spatial sampling, the physical covariance between Z_{NPR} and Z_{NDV} remained intact. Visual inspection of 2D density contours (Fig. 3.4) confirms that the training subset accurately envelopes the primary density nodes of the global background. Collectively, these results confirm that the *in situ* training data provides a physically sound and representative foundation for the logistic model. A more detailed analysis of these results is provided in Supplementary Material S3.2.

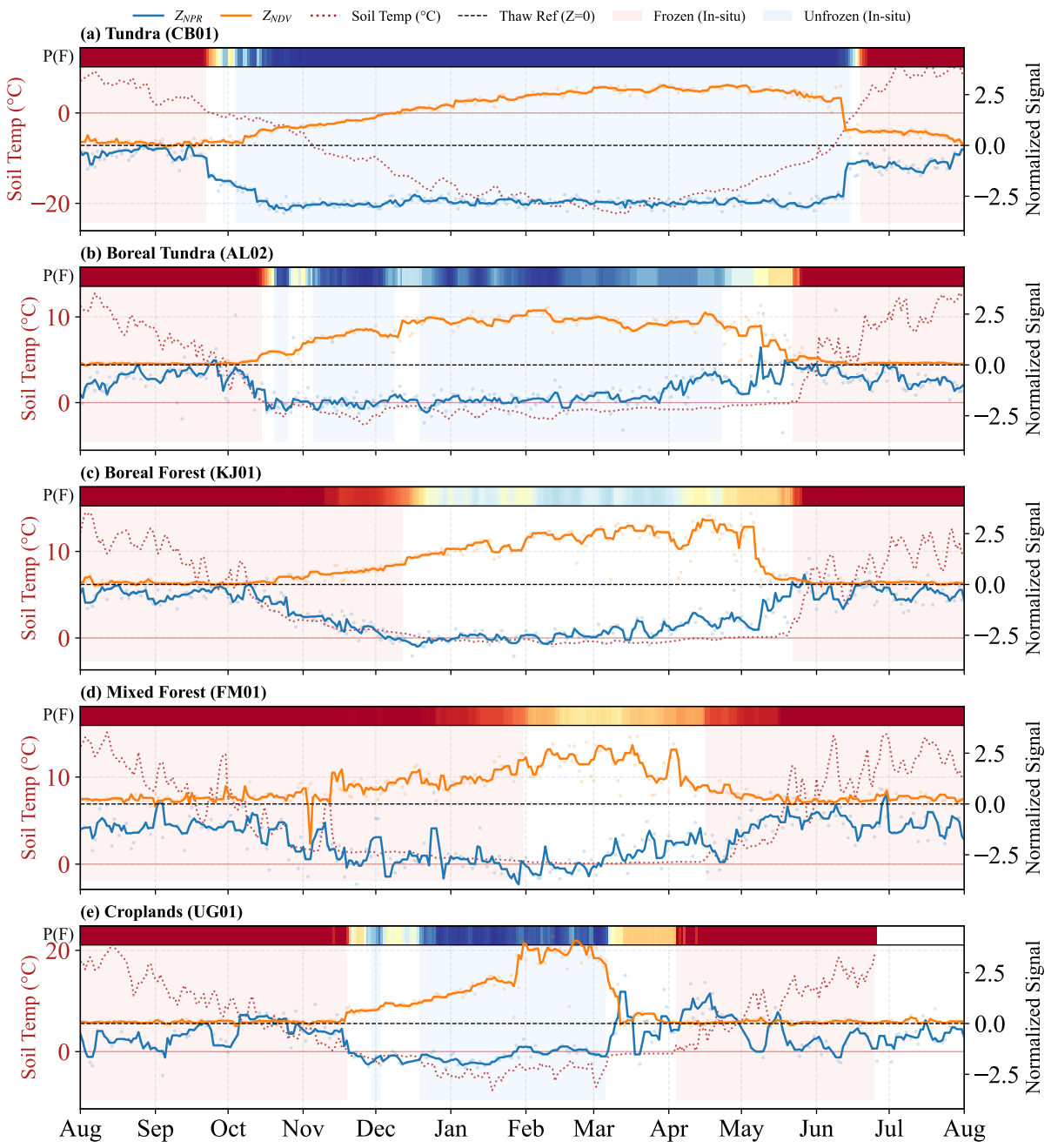


Figure 3.3: Time series of standardized radiometric anomalies for the Normalized Polarization Ratio (Z_{NPR}) and the Normalized Spectral Difference (Z_{NDV}) overlaid with *in situ* soil temperatures for five representative sites across distinct biomes. The top horizontal color bar, denoted as $P(F)$, represents the continuous probability of the frozen state calculated with the normalized SFCC. Within this probability bar, dark red indicates a high-confidence unfrozen classification, dark blue indicates a high-confidence frozen classification.

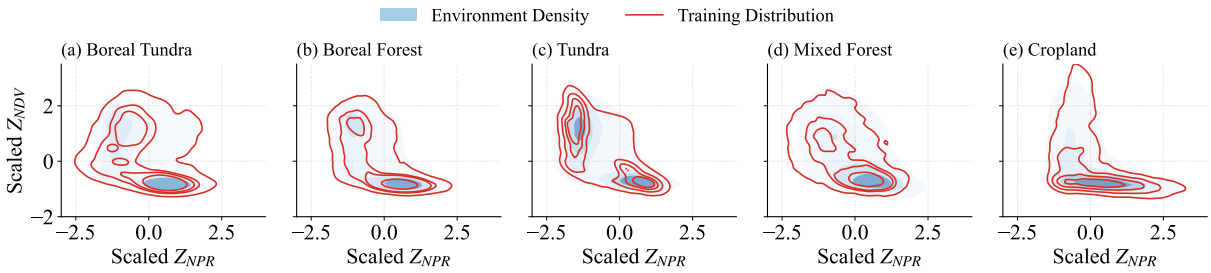


Figure 3.4: Two-dimensional KDE contour maps illustrating the joint multivariate feature space (Z_{NPR} versus Z_{NDV}) across five biomes. The plots display the spatial representativeness of the *in situ* training subset (red contours) overlaid on the primary density nodes of the broader environment background (blue shaded regions).

3.3.3 Physical Interpretation of Regional Model Dynamics

The 2D decision boundaries mapped across the target biomes (Fig. 3.5), alongside the finalized model parameters (Table 3.3), revealed distinct regional shifts in the physical drivers of FT detection. Model performance, quantified by the cross-validation PR AUC, exhibited a clear gradient based on vegetation density. Open biomes, including Cropland, Boreal Tundra, and Tundra, achieved high classification accuracy (PR AUC > 0.95), while Boreal Forest demonstrated strong performance (PR AUC = 0.894±0.139), and Mixed Forest exhibited the greatest uncertainty (PR AUC = 0.780 ± 0.237) due to signal attenuation by woody biomass. Because input features were standardized, the magnitudes of the learned coefficients (β_1 and β_2) directly reflected their physical importance in adapting to these environments. In the Cropland biome, the polarization ratio carried slightly greater weight ($\beta_1 = -1.844$, $\beta_2 = 1.457$), consistent with microwave scattering theory: the absence of dense canopy cover allows the sensor to directly detect the sharp decrease in soil dielectric permittivity upon freezing. Across all other biomes, the spectral difference index (β_2) carried greater or comparable weight, with its relative dominance increasing with vegetation density.

This sensitivity shift was most pronounced in the Boreal Tundra, where the spectral index coefficient reached its highest magnitude across all biomes ($\beta_2 = 3.549$, $\beta_1 = -0.823$), suggesting that high-frequency volume scattering from frozen shrub canopies and overlying snow became the primary detection mechanism. In contrast, in the Mixed Forest the polarization ratio exhibited its lowest sensitivity ($\beta_1 = -0.802$), confirming that dense woody biomass effectively masked the surface soil signal. The intermediate transition zone (highlighted in yellow in Fig. 3.5) effectively captured the physical ambiguity between high-confidence end-members. The width of this zone provided a quantitative measure of physical uncertainty during the seasonal shift. Boreal Tundra exhibited the sharpest transition (Width = 0.603), indicative of rapid and radiometrically definitive phase change, while Mixed Forest displayed the widest transition zone (Width = 1.439),

reflecting thermal buffering where the canopy and soil layers may exist in conflicting phase states simultaneously. The EER-optimized thresholds deviated moderately from the 0.50 neutral point across most biomes (range: 0.547–0.566), reflecting slight asymmetry in the probability distributions of the frozen and unfrozen end-members. The most notable deviation occurred in the Boreal Tundra ($\tau_{\text{optimal}} = 0.341$), where the model required a substantially lower decision threshold to equalize sensitivity and specificity, likely a consequence of the high cross-validation variability in the spectral index coefficient ($\beta_2 = 3.549 \pm 1.02$) and the resulting spread of predicted probabilities in this biome.

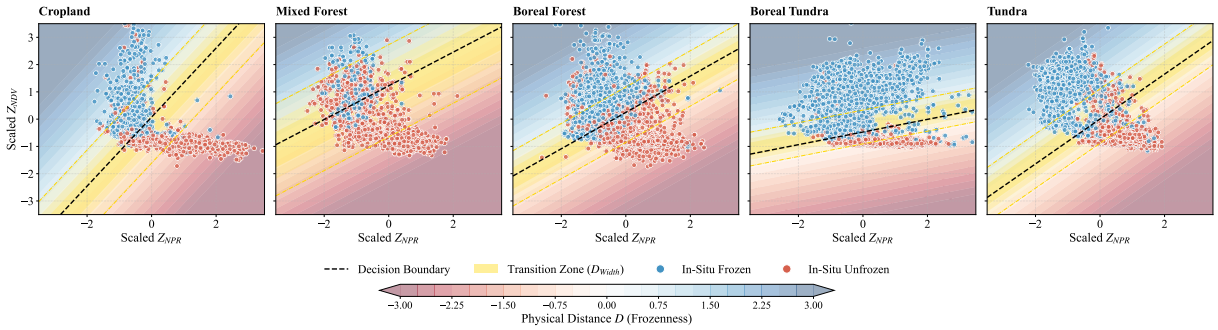


Figure 3.5: Two-dimensional physical feature space of the Normalized Polarization Ratio (Z_{NPR}) versus the Normalized Spectral Difference (Z_{NDV}) illustrating the logistic model decision boundaries across five distinct biomes. Blue and red points represent *in situ* high-confidence frozen and unfrozen observations respectively. The background gradient indicates the standardized physical distance (D, frozenness) from the decision boundary (dashed black line), with the yellow band representing the probabilistic transition zone.

Table 3.3: Production logistic regression parameters and cross-validation evaluation metrics, stratified by biome. Model coefficients (β_0, β_1, β_2) and the EER-optimized threshold (τ_{opt}) are from the final production model trained on all available data (script 06). The transition bounds ($[D_{\text{lower}}, D_{\text{upper}}]$) denote the standardized 10% and 90% probability distances from the decision boundary, scaled by 0.5. PR AUC (mean ± std) is reported from spatially independent cross-validation (script 05) and represents the honest out-of-sample performance estimate.

Land Cover	τ_{opt}	β_1	β_2	β_0	$[D_{\text{lower}}, D_{\text{upper}}]$	**PR AUC**
Cropland	0.566	−1.844	1.457	0.155	[−0.524, 0.411]	0.951 ± 0.012
Mixed Forest	0.559	−0.802	1.299	−1.349	[−0.797, 0.642]	0.780 ± 0.237
Boreal Forest	0.547	−1.444	2.166	−0.347	[−0.458, 0.386]	0.894 ± 0.139
Boreal Tundra	0.341	−0.823	3.549	1.018	[−0.211, 0.392]	0.965 ± 0.046
Tundra	0.442	−1.814	2.205	−0.242	[−0.344, 0.425]	0.955 ± 0.035

To provide a more granular view of classification errors, Table 3.4 reports confusion-matrix-derived metrics aggregated across all spatially independent cross-validation test folds per biome.

The results reinforce the vegetation-density gradient observed in the PR AUC. Boreal Tundra achieved the highest sensitivity (0.962) and F1 score (0.911), confirming reliable frozen-state detection in open shrubland environments. Cropland and Tundra also exhibited well-balanced error structures, with sensitivity and specificity within 0.05 of each other and balanced accuracies of 0.855 and 0.870, respectively. Boreal Forest showed a characteristic asymmetry: high sensitivity (0.873) combined with lower precision (0.686), indicating a tendency to over-predict frozen states, likely driven by snow-covered soil and canopy contributions that mimic frozen-ground microwave signatures. Mixed Forest produced the most degraded metrics across all categories, with precision collapsing to 0.232—meaning that the majority of predicted frozen observations were false positives—while sensitivity remained moderate (0.771). This asymmetry reflects the fundamental ambiguity imposed by dense woody biomass, which attenuates the soil dielectric signal and causes the model to trigger the frozen state on woody canopy scattering alone.

Table 3.4: Cross-validation classification metrics aggregated across all spatially independent test folds, stratified by biome. *N* denotes the total number of test observations pooled across unique (non-padding) folds. Sensitivity and specificity are computed with respect to the frozen class. Balanced accuracy is the arithmetic mean of sensitivity and specificity.

Biome	*N*	**Sensitivity**	**Specificity**	**Precision**	**F1**	**Bal. Acc.**
Cropland	14,276	0.845	0.865	0.865	0.855	0.855
Mixed Forest	3,796	0.771	0.661	0.232	0.357	0.716
Boreal Forest	32,346	0.873	0.837	0.686	0.768	0.855
Boreal Tundra	13,403	0.962	0.841	0.865	0.911	0.901
Tundra	22,607	0.941	0.799	0.832	0.883	0.870

3.3.4 Comparative Classification Accuracy

When evaluated against the 3-way unanimous consensus pseudo-truth across a randomized spatial sample during non-summer months, the logistic model demonstrated strong spatial generalizability, with performance exhibiting a clear gradient from open to forested environments (Table 3.5). The highest agreement was achieved in the Tundra and Boreal Tundra biomes, where match rates reached 98.24% and 96.98%, respectively, with F1 scores of 0.990 and 0.984 and Cohen's Kappa values of 0.870 and 0.783. These biomes also yielded the highest consensus ratios (84.0% and 73.0%), reflecting that inter-mission agreement among the three reference datasets is greatest in open, low-vegetation landscapes—a finding independently corroborated by the domain-wide pairwise agreement analysis (Sect. S4.1 in Supplementary Material). Boreal Forest maintained similarly high fidelity against the consensus (match rate: 94.60%; F1: 0.970; consensus ratio: 72.7%), while Cropland, despite a lower consensus ratio of 63.1%, still achieved a match

rate of 96.11%, suggesting that when the three reference datasets do converge in agricultural environments, the logistic model reliably reproduces that consensus. Mixed Forest represented the most challenging biome across both dimensions: the consensus ratio fell to 56.7%—the lowest among all biomes—indicating substantial inter-mission disagreement even before the logistic model is considered, while the match rate declined to 78.82% (Kappa: 0.443), reflecting that classification errors remained elevated even among unanimously agreed observations. A characteristic asymmetry was observed within this biome: precision (0.975) substantially outpaced recall (0.771), indicating that errors manifest predominantly as missed frozen detections rather than false alarms—consistent with the model's conservative behavior under complex, heavily vegetated canopies. Across all remaining biomes, both precision and recall exceeded 0.955, confirming balanced and reliable detection across the diverse northern ecotones comprising the study domain. The same biome-dependent performance gradient was further documented when all products were benchmarked against spatially harmonized *in situ* soil temperature networks, with consistent degradation in forested environments observed across the entire retrieval community (Sect. S4.2 in Supplementary Material); notably, however, this analysis is not an independent evaluation of the logistic model given its training labels were derived from the same network. Beyond accuracy metrics, binary products such as FT-SMAP and FT-ESDR are susceptible to classification flickering during shoulder seasons, where minor diurnal fluctuations repeatedly cross a hard decision boundary [Johnston et al., 2020]; the proposed transition zone effectively absorbs this sub-seasonal radiometric noise, maintaining stable classifications through the zero-curtain without forcing a binary state change (Fig. 3.6).

Table 3.5: Performance of the optimized logistic model evaluated against a 3-way unanimous consensus pseudo-truth (FT-SMAP, FT-ESDR, and FT-SMOS). The evaluation was conducted over a randomized spatial sample across North America during non-summer months. The Consensus Ratio indicates the percentage of non-summer days where all three reference datasets unanimously agreed on the physical ground state.

Biome	Consensus Ratio (%)	Match Rate (%)	F1 Score	Kappa	Precision	Recall
Cropland	63.1	96.11	0.979	0.755	0.971	0.987
Mixed Forest	56.7	78.82	0.861	0.443	0.975	0.771
Boreal Forest	72.7	94.60	0.970	0.703	0.984	0.956
Boreal Tundra	73.0	96.98	0.984	0.783	0.973	0.994
Tundra	84.0	98.24	0.990	0.870	0.986	0.995

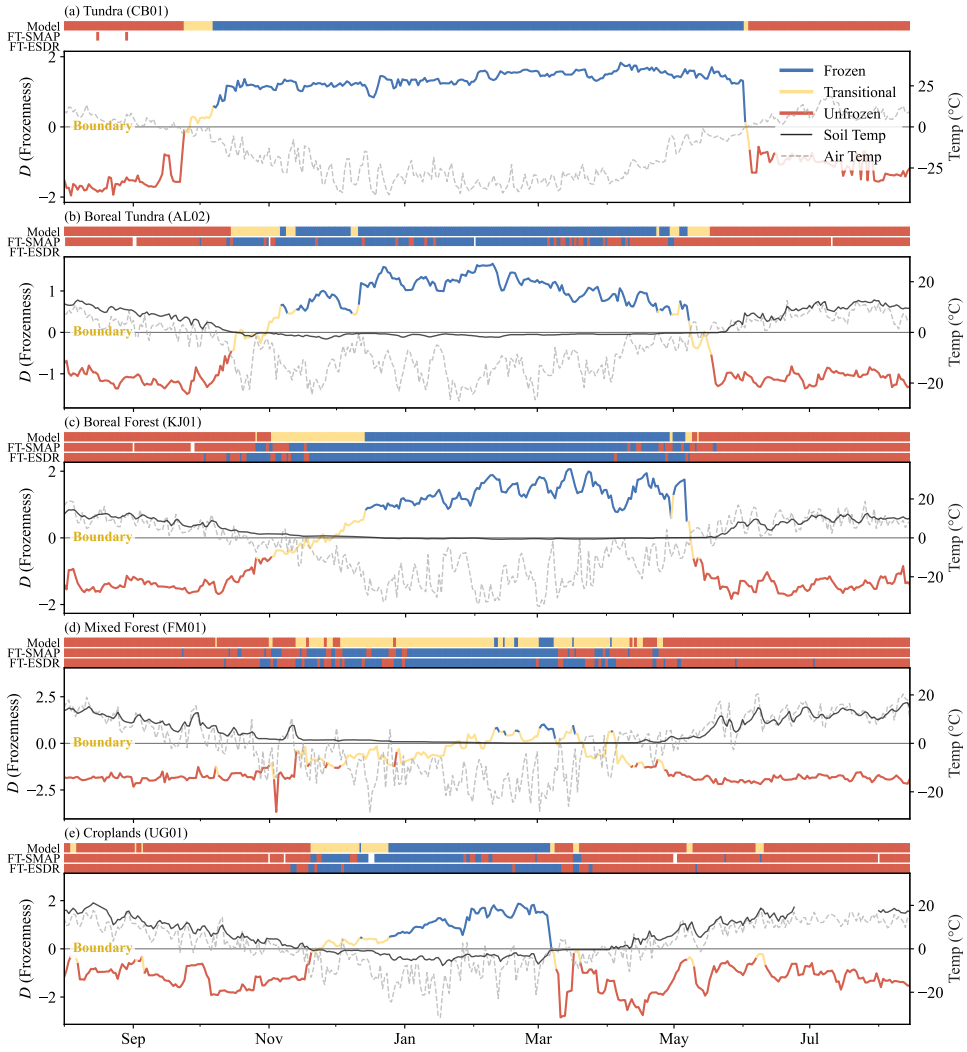


Figure 3.6: Temporal evolution of the continuous physical distance D (Frozenness index), plotted alongside *in situ* soil and ERA5 air temperatures at a representative station. The top categorical ribbons compare the proposed logistic model's classification against the binary FT-SMAP, FT-ESDR, and FT-SMOS products.

3.3.5 Thermodynamic Validation of the Transition Zone

Across all biomes, the transitional class was consistently concentrated within the thermally expected window near the freezing point (Table 3.6; Fig. 3.7). For the 10-day rolling mean air temperature, the fraction of transitional observations falling within the −7°C to 2°C band ranged from 44.1% in Mixed Forest to 69.3% in Tundra, exceeding the corresponding unfrozen fractions (14.5%–22.2%) and, in most biomes, the frozen fractions as well. This thermal anchoring was even more pronounced against *in situ* soil temperature, where the fraction of transitional observations within the ±2°C zero-curtain band reached 83.0% in Boreal Forest, 94.4% in

Tundra, and 97.6% in Mixed Forest (Fig. 3.8)—confirming that the model's transitional state is thermodynamically anchored to the latent heat plateau rather than representing an arbitrary radiometric partition. Notably, in forested biomes the frozen class also exhibits a high fraction of near-zero soil temperatures (83.9% in Boreal Forest; 98.1% in Mixed Forest), reflecting the thermodynamic decoupling between the radiometric emitting layer and the buffered 5 cm probe: as the canopy and soil skin freeze and drive a frozen classification, the subsurface probe remains locked near 0°C within the zero-curtain. This indicates that while the model's transitional detections are thermodynamically genuine, the full spatial and temporal extent of the zero-curtain at depth is underestimated in densely vegetated environments—a known consequence of the radiometric depth mismatch [Rowlandson et al., 2018] in forested terrain. Spearman's rank correlation between D and the 10-day mean air temperature was strongly negative across all biomes ($\rho = -0.694$ to -0.800; all $p < 0.001$; Fig. S9), while correlations against *in situ* soil temperature were comparably robust, with Tundra exhibiting the strongest coupling ($\rho = -0.845$; Fig. S10). The Jonckheere-Terpstra test confirmed monotonic thermal ordering across all biomes and temperature sources (all $p < 0.001$), verifying that the three classes are not merely thermally distinct but arranged in the thermodynamically expected direction. The rank-based ε^2 effect size from the Kruskal-Wallis test ranged from 0.345 to 0.749 across biomes and temperature sources, indicating that the model's classification consistently explains a large proportion of temperature variance, with Cropland exhibiting the strongest global thermal separation and Tundra the most modest.

Table 3.6: Physical validation statistics for model-derived freeze–thaw states across diverse biomes. Columns report the in-band temperature fraction (%) for each class, Spearman's rank correlation (ρ), rank-based epsilon-squared effect size (ε^2), and the Jonckheere-Terpstra standardized statistic (Z).

Land Cover	Source	Unfrozen In-Band (%)	Transitional In-Band (%)	Frozen In-Band (%)	ρ	ε^2 (3-class)	JT (Z)
Boreal Forest	Air 10d Mean	17.3	51.2	18.2	-0.800	0.691	618.8
	In-Situ Soil	24.1	83.0	83.9	-0.638	0.477	191.8
Boreal Tundra	Air 10d Mean	14.5	65.8	14.4	-0.702	0.510	535.5
	In-Situ Soil	38.2	78.4	56.8	-0.567	0.345	65.2
Cropland	Air 10d Mean	14.5	66.6	32.4	-0.794	0.749	618.5
	In-Situ Soil	20.1	50.0	41.0	-0.706	0.713	178.2
Mixed Forest	Air 10d Mean	18.6	44.1	29.5	-0.788	0.682	577.7
	In-Situ Soil	26.4	97.6	98.1	-0.625	0.421	114.7
Tundra	Air 10d Mean	22.2	69.3	17.3	-0.694	0.414	442.2
	In-Situ Soil	35.8	94.4	29.9	-0.845	0.458	76.6

All Jonckheere-Terpstra $p < 0.001$; all Spearman $p < 0.001$ (nominal).

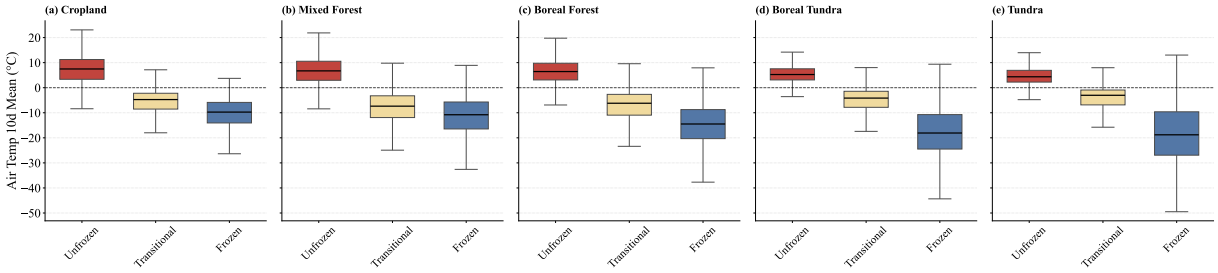


Figure 3.7: Distribution of the 10-day rolling mean air temperature (ERA5) across model-derived unfrozen, transitional, and frozen states. Central black lines represent the median temperatures, with outliers omitted for visual clarity. The distinct staircase progression of medians supports the large ε^2 effect sizes reported in Table 3.6 and confirms the monotonic thermal ordering validated by the Jonckheere-Terpstra test.

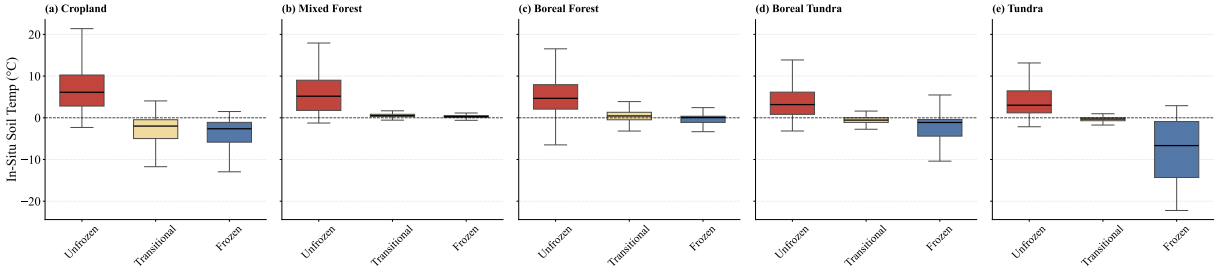


Figure 3.8: Distribution of *in situ* soil temperature measurements (5 cm) categorized by model state. The transitional class (gold) is effectively pinned to the 0°C isotherm across all biomes, with the Tundra showing exceptional alignment to the latent heat plateau. This provides robust empirical evidence that the model accurately isolates the zero-curtain effect.

3.4 Discussion and Conclusion

The seasonal transition of soil between frozen and unfrozen states is a protracted thermodynamic continuum governed by the zero-curtain effect. Because legacy operational algorithms enforce discrete binary classifications, they effectively erase this critical, biogeochemically active transitional phase. To address this, we developed a probabilistic framework for non-binary freeze/thaw (FT) detection. By integrating multi-frequency passive microwave data—specifically the SMAP L-band polarization ratio (Z_{NPR}) and the AMSR2 Ka/Ku-band spectral index (Z_{NDV})—into an L1-regularized logistic regression model, we captured these intermediate phase dynamics. This parsimonious, spatially balanced approach demonstrated superior generalization across diverse northern ecotones relative to single-feature models and alternative spectral combinations (Supplementary Table S1). It not only isolated the physical transitional zone—mitigating the high-frequency classification "flickering" typical of shoulder seasons—but also reduced the systemic false-positive bias endemic to operational products in heavily vegetated environments. For example, in the challenging Mixed Forest biome—where canopy emission dominates the

radiometric signal and inter-product disagreement is highest—the model achieved a precision of 0.975 against the three-product unanimous consensus, with classification errors manifesting predominantly as missed detections rather than false alarms.

Phase change trajectories mapped within the standardized bivariate feature space confirm that these statistical classifications follow theoretically sound microwave radiative transfer pathways. The directionality of these trajectories is physically interpretable: as soil transitions from unfrozen to frozen, Z_{NPR} decreases (reflecting the collapse of liquid water permittivity) and Z_{NDV} increases (reflecting enhanced high-frequency volume scattering from the freezing soil surface, canopy, and accumulating snow). The biome-specific regression coefficients (Table 3.3) further illuminate the physical roles of each feature: Cropland is the only biome where Z_{NPR} carries greater weight than Z_{NDV} ($|\beta_1| = 1.844 > |\beta_2| = 1.457$), consistent with its sparse canopy allowing direct soil permittivity sensing. In all other biomes Z_{NDV} dominates, most extremely in Boreal Tundra ($|\beta_2| = 3.549$ vs. $|\beta_1| = 0.823$), where the model relies almost entirely on high-frequency volume scattering to detect soil freeze onset beneath transitional shrub canopy.

Although thermodynamic validation demonstrates consistent anchoring of the transitional class to the zero-curtain across all biomes, residual uncertainty in model performance persists — particularly in heavily vegetated environments where the radiometric emitting layer and the subsurface probe are thermodynamically decoupled [Rowlandson et al., 2018]. In forested biomes, the canopy freezes before the subsurface soil, driving the satellite signal into the frozen class while the 5 cm probe remains locked at 0°C; this depth mismatch makes it difficult to cleanly verify whether the model's transitional detections correspond to a genuine physical state or a sensor artifact. The Tundra biome removes this ambiguity: its organic, saturated surface releases latent heat uniformly through both the radiometric skin and the subsurface layer [Yi et al., 2019], so when the model assigns a transitional classification, the 5 cm probe is genuinely at 0°C — with 94.4% of transitional observations falling within the ±2°C zero-curtain band. Because Tundra is the only biome where the physics can be cleanly verified, its near-perfect alignment serves as the critical validation anchor: the model correctly isolates the zero-curtain where a clean test is possible, which lends credibility to its transitional detections in the more complex environments where such a direct test is not.

The algorithm-independent nature of the Mixed Forest limitation — affecting the logistic model, AMSR-based retrieval, SMAP, and SMOS equally — is documented in the supplementary *in situ* benchmark (Table S4): F1 scores collapsed below 0.15 despite near-complete recall (0.91–1.00), with false alarm rates exceeding 62% for every algorithm. This uniform collapse confirms that the challenge is not an artefact of the logistic formulation but a fundamental physical constraint: when a dense, multi-layered canopy freezes before the underlying soil, the radiometric signal is dominated by canopy emission rather than soil permittivity, rendering any

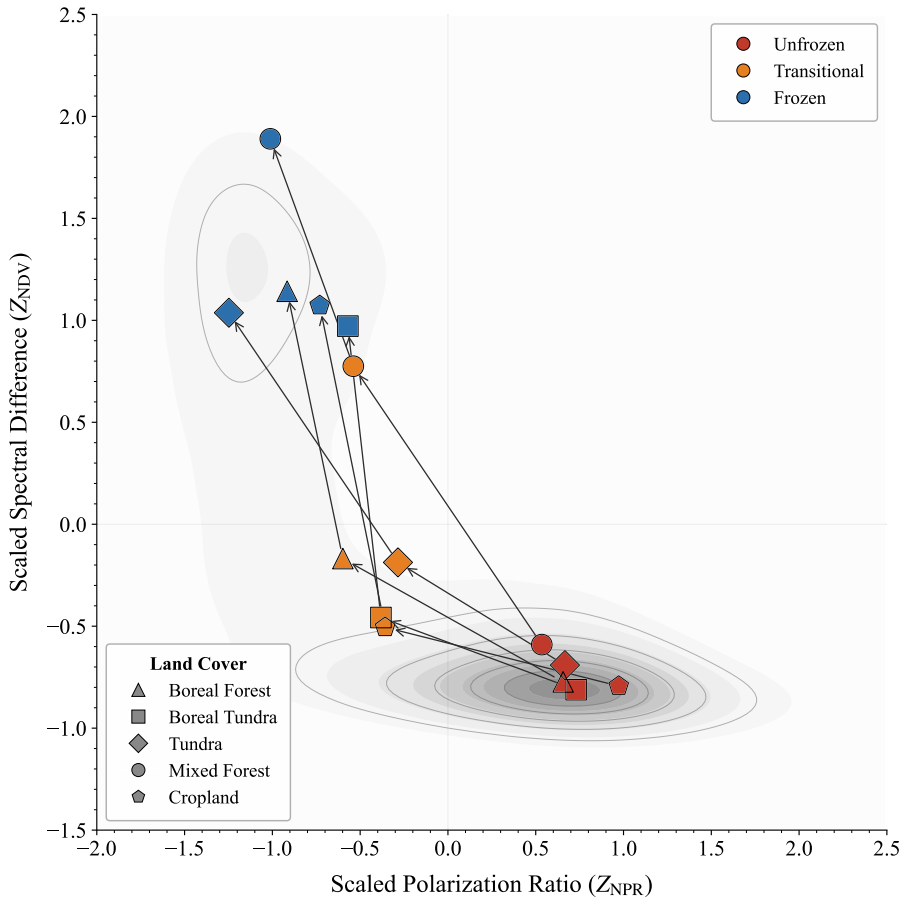


Figure 3.9: Phase change trajectories illustrating the shift in physical state across the two-dimensional microwave feature space (Normalized Polarization Ratio, Z_{NPR}, vs. Normalized Difference V-Pol, Z_{NDV}). Markers represent the bivariate centroids (mean feature values) for unfrozen, transitional, and frozen classifications within each biome. The connecting dashed lines trace the passive microwave phase-state trajectory through the bivariate feature space from the unfrozen to the frozen end-member.

surface-sensitive passive microwave classifier unreliable when validated against a 5 cm subsurface probe. Compounding this, mixed forest also exhibits the lowest consensus ratio among all five biomes (56.7%; Table 3.5), meaning the three operational reference products themselves disagree most frequently in this environment. The result is a double uncertainty — labels derived from any single reference in Mixed Forest are noisiest, and the pseudo-truth used for evaluation is also least confident — which explains the low cross-validated F1 (0.36) and Kappa (0.44) without these values being a purely algorithmic failure.

While recently developed machine learning based models [Kumawat et al., 2025, Donahue et al., 2023, Walker et al., 2022] inherently produce probabilistic outputs, they are predominantly trained on binary labels or peak-season end-members. Consequently, their probabilistic outputs often represent statistical algorithmic uncertainty rather than a physically meaningful thermodynamic state. For instance, although Walker et al. [2022] trained a Hidden Markov Model restricted to transitional seasons and noted that intermediary probabilities might be due to a partially frozen surface, and both Kumawat et al. [2025] and Donahue et al. [2023] utilized deep learning architectures (an autoencoder and a convolutional neural network, respectively) that yield continuous probability measures, none of these studies explicitly validated whether these intermediate probabilities physically correlate with the zero-degree curtain. Furthermore, contemporary machine learning models typically ingest raw brightness temperatures—as seen in the deep learning networks by Donahue et al. [2023] and the autoencoder by Kumawat et al. [2025] —or they minimally process inputs by relying on raw Normalized Polarization Ratios (NPR), as done by Walker et al. [2022]. However, even sophisticated neural networks would benefit from physical preprocessing steps to remove static noise, enabling the model to focus strictly on the dynamic physical signal.

To mitigate label noise while relying exclusively on temperature data, our ground-state labeling utilized a moisture-independent normalized Soil Freezing Characteristic Curve (SFCC). While we parameterized this curve using b (phase-change rates) and T_f (point depression) values specifically calibrated for different biomes [Salmabadi et al., 2026] to act as a rigorous filter, it does not explicitly quantify the absolute unfrozen liquid water content, which is heavily dependent on antecedent moisture and soil texture. Consequently, residual physical ambiguity remained within the filtered observational data. This inherent mismatch prevented the reliable training of a direct 3-category classifier from the outset, necessitating our approach of training on high-confidence binary end-members and mathematically deriving the transitional state from the probabilistic boundary. Although this physically based framework relies on generalized parameters (T_f and b) for each biome [Salmabadi et al., 2026], it offers an alternative to universal binary thresholds or rigid temperature exclusion windows [Kumawat et al., 2025], which risk eliminating critical thermodynamic variance and generating unrepresentative training data. By incorporating regional

variations in freezing point depression and phase-change rates, this approach effectively filters uncertain transitional data while accounting for landscape-specific thermal dynamics.

Spatial uncertainty in our approach is introduced through both geographic constraints and the inherent scale mismatch between point-based *in situ* measurements (e.g., at 5 cm depth) and the coarse 9 km satellite footprint. Sub-pixel heterogeneity—driven by varied topography, dynamic snowdrift, mixed vegetation canopies, and sub-grid water bodies—significantly complicates the aggregate radiometric signal observed by the satellite. To overcome this scale gap, recent studies have successfully leveraged high-spatial-resolution active microwave data, such as C-band synthetic aperture radar (SAR), to create regional benchmarking datasets that evaluate coarse footprints [Bartsch et al., 2025]. These high-resolution SAR assessments reveal that treating sparse *in situ* observations as absolute "ground truth" introduces inherent uncertainty into the validation process, particularly because the "none-soil" fraction—such as water bodies and bare bedrock—within a single coarse cell can be highly variable and substantial. This issue is further compounded by the uneven spatial distribution of measurement sites; while some 9 km training pixels contain dense clusters of nearly ten observation stations, others rely on a single isolated data point. Furthermore, our model was calibrated exclusively using *in situ* networks across North America. This geographic constraint may limit the immediate generalizability of the learned parameters to other circumpolar regions, such as Eurasia, which possess different soil profiles and vegetation structures.

Domain-wide application demonstrates that the biome-stratified framework scales coherently to the continental extent, with the transitional zone migrating southward during autumn freeze-up and retreating northward through spring thaw (Figs. 3.10 and 3.11), without introducing regional artifacts or discontinuities at biome boundaries. Moving forward, the non-binary FT baseline established by this framework provides critical input for regional and global carbon models, enabling more accurate simulations of shoulder-season respiration. Future work should focus on integrating dynamic soil moisture parameters into the SFCC labeling process, exploring downscaling techniques to bridge the gap between satellite footprints and localized eco-hydrological dynamics, and testing the framework's robustness across broader Pan-Arctic domains.

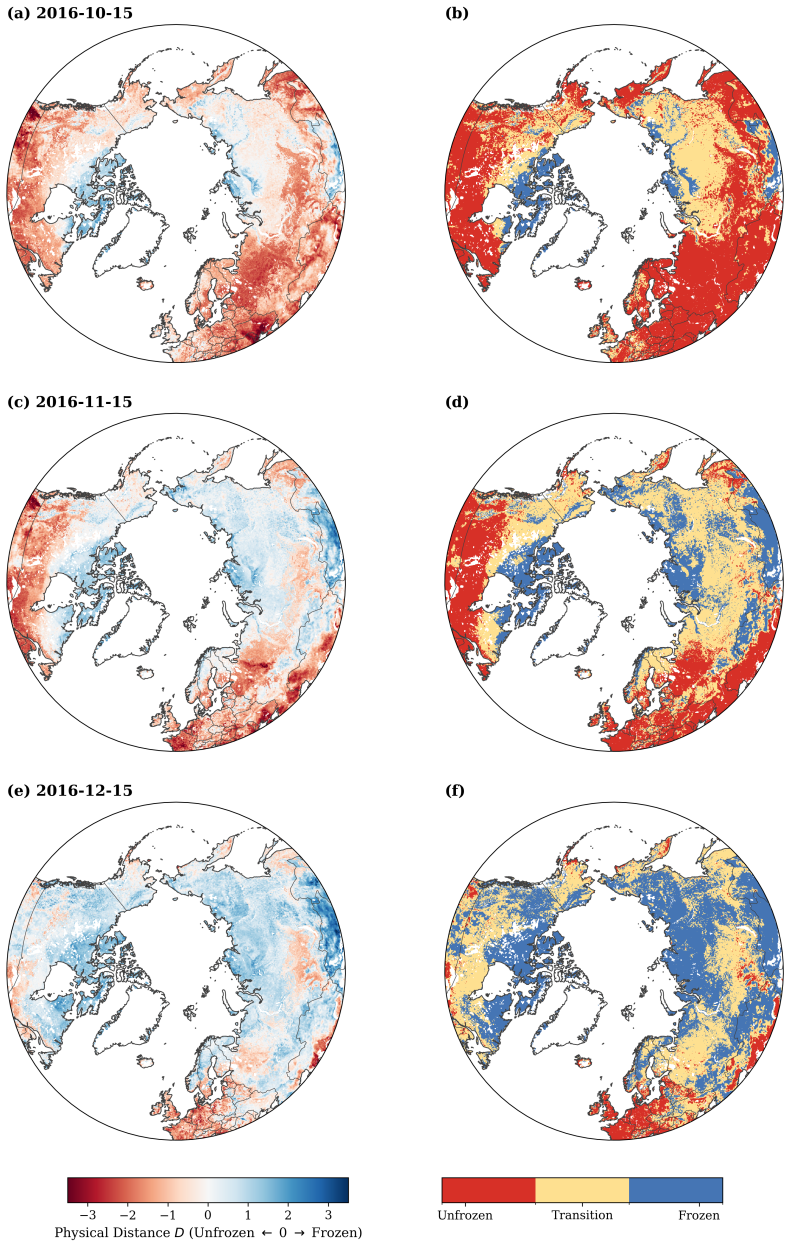


Figure 3.10: Domain-wide application of the logistic model across the Northern Hemisphere during the autumn freeze-up (October to December 2016). The left column illustrates the continuous physical distance (D, Frozenness), capturing the thermodynamic intensity of the phase state. The right column displays the corresponding categorical classifications, highlighting the southward migration of the transitional phase boundary as the freezing front advances.

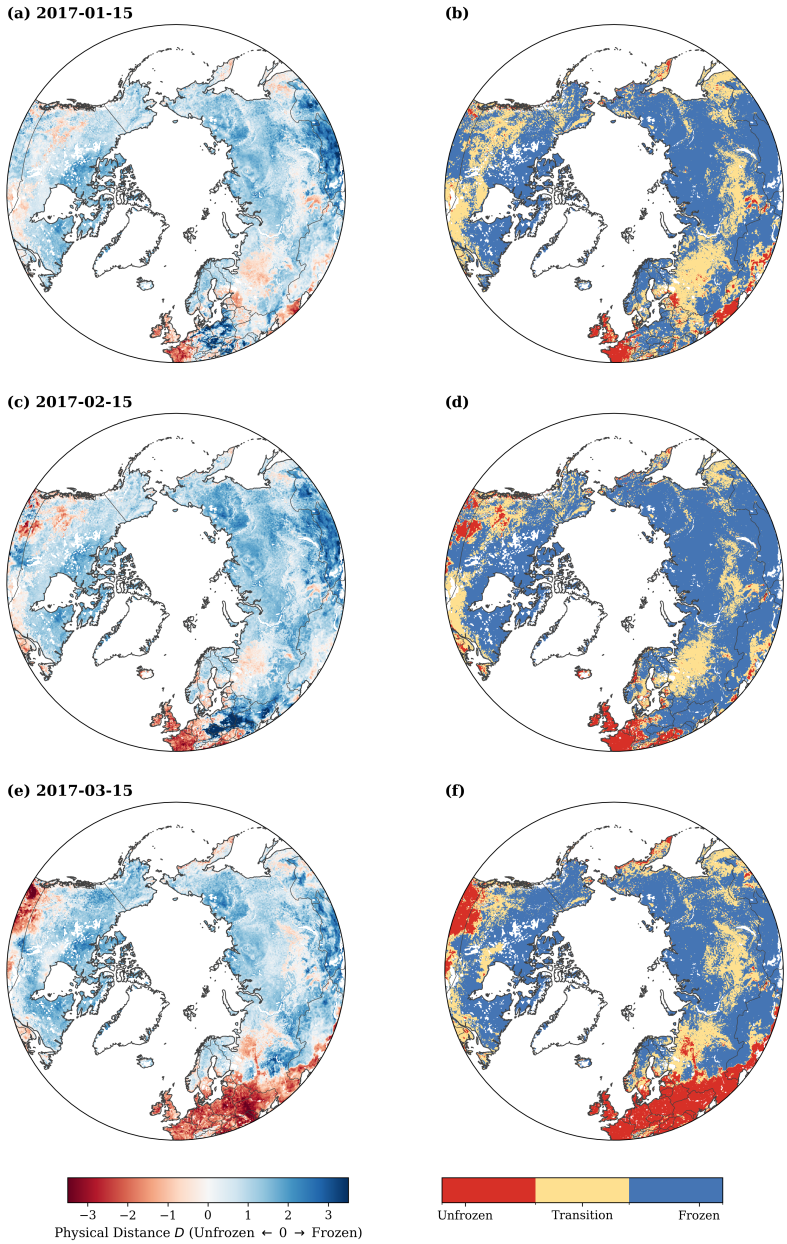


Figure 3.11: Same as Fig. 3.10, but for the spring thaw period (January to March 2017). The continuous distance maps capture the gradual retreat of the frozen state, while the categorical maps illustrate the northward migration of the transitional boundary as the thaw progresses.

Acknowledgements

We would like to thank the Centre d'Études Nordiques (CEN) for their logistical support. This work was further supported by contributions from Hydro-Quebec and Environment and Climate Change Canada.

Funding

This work was supported by the Fonds de recherche du Quebec – Nature et technologies [grant number 330450, [Salmabadi, 2023]]; the Canadian Space Agency [grant number 19FAQCT B19]; the Natural Sciences and Engineering Research Council of Canada (NSERC).

Declaration of Competing Interest

The authors declare that they have no known competing financial interests or personal relationships that could have appeared to influence the work reported in this paper.

Supplementary Material

S1 Microwave Indices and Reference Baselines

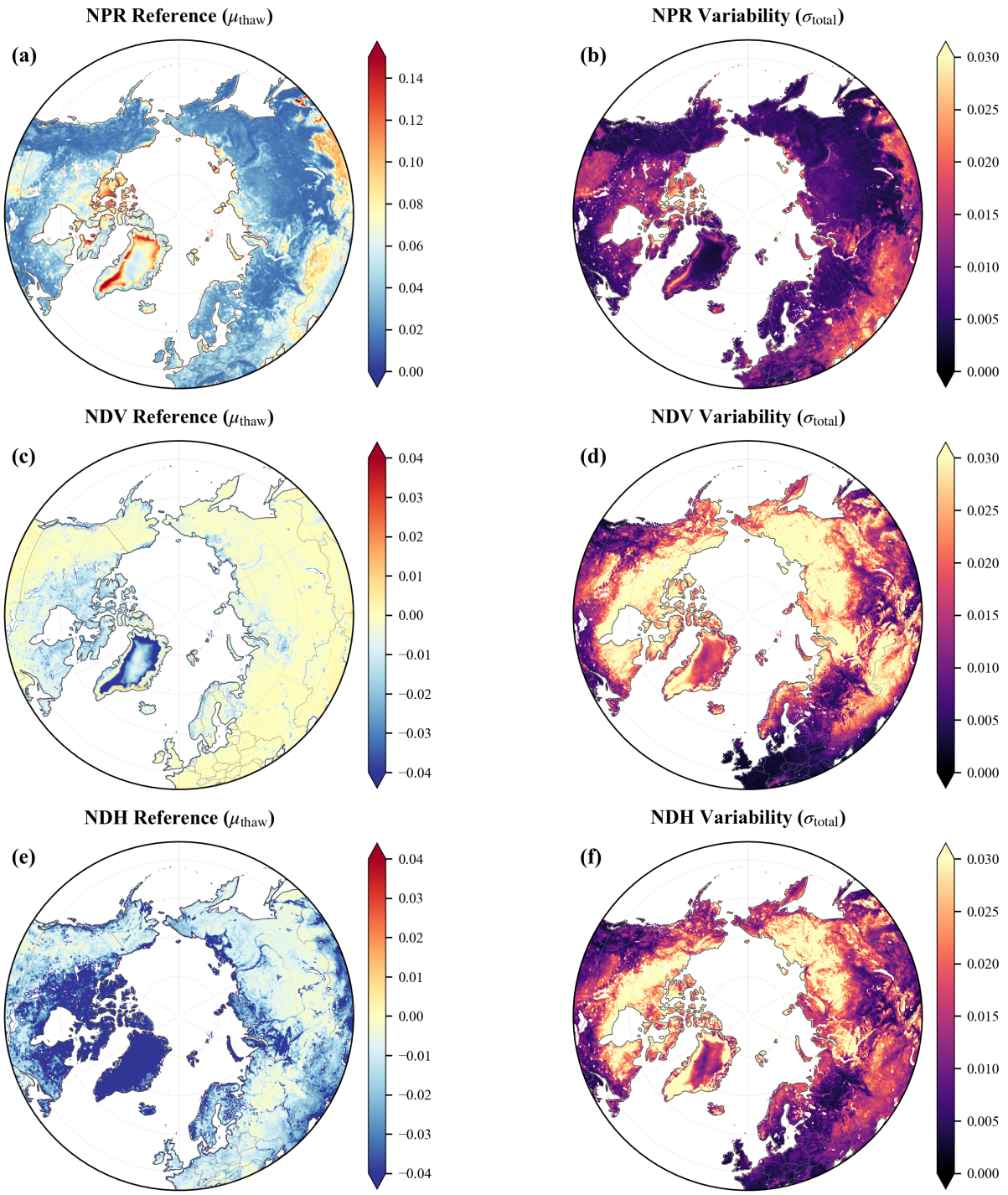


Figure S1: Spatial distribution of reference statistics used for index normalization.

S2 Feature Discriminability and Physical Validation

Pearson correlation analysis (Fig. S2) showed the expected interrelationships among the refined feature candidates. The spectral and quasi-emissivity indices (Z_{NDV}, Z_{NDH}, and Q_e) displayed strong positive correlations with each other (r = 0.66 to 0.79) and strong negative correlations with the 36.5 GHz brightness temperature (r = −0.61 to −0.85), which is a direct consequence of their mathematical derivation from the high-frequency channels. Furthermore, the normalized polarization ratio (Z_{NPR}) exhibited only moderate correlation with these spectral and emissivity metrics ($|r|$ ranging from 0.38 to 0.55), confirming that it captures distinct physical mechanisms. Finally, the diurnal amplitude variations (DAV_{AMSR} and DAV_{SMAP}) showed weak linear correlations with all other radiometric variables ($|r| \leq 0.24$), indicating high statistical independence; however, Mutual Information analysis (Fig. 3.2) demonstrated that their overall discriminatory power remained low.

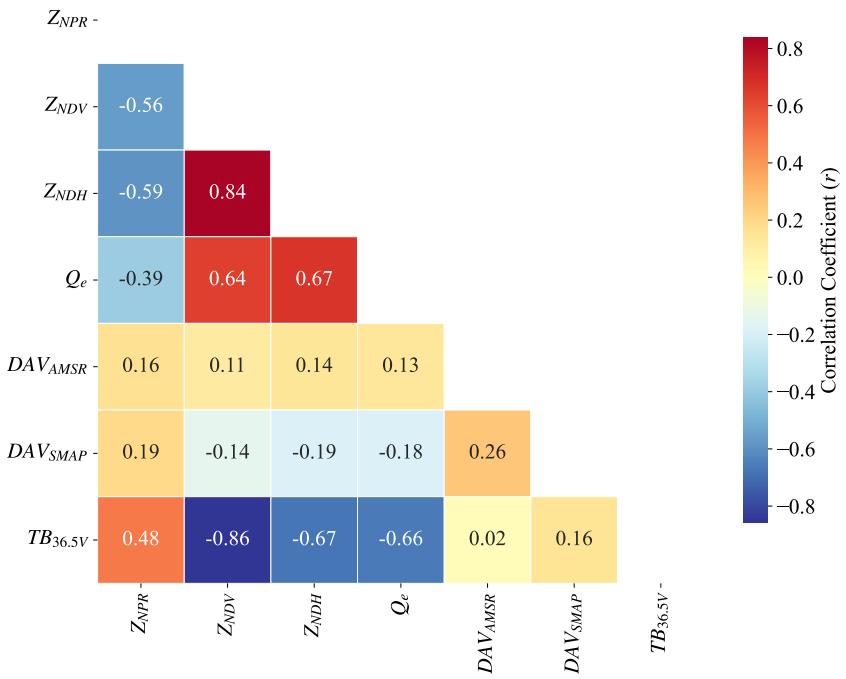


Figure S2: Pearson correlation matrix of all candidate input features computed across the double-balanced training set.

Global Mutual Information (MI) rankings (Fig. 3.2) identified a dominant set of five features: Ka-band brightness temperature ($TB_{36.5V}$), Z_{NDV}, Q_e, Z_{NPR}, and Z_{NDH}. Conversely, diurnal amplitude variations (DAV_{AMSR} and DAV_{SMAP}) exhibited consistently low MI scores globally and across all biomes (Table 3.2), indicating minimal contribution of unique information to the model. Stratified analysis revealed the critical complementarity of these top five features across

ecozones. In open biomes such as tundra and croplands, Z_{NPR} achieved its highest discriminatory power, with MI scores of 0.37 and 0.34, respectively, effectively capturing the dielectric phase change in the absence of significant canopy attenuation. However, in forested biomes, including boreal and mixed forests, the utility of Z_{NPR} decreased to 0.25 and 0.20, and fell to 0.14 in the boreal tundra transition zone, confirming that woody biomass masks the surface polarization signal. In these canopy-dominated regimes, Z_{NDV} and $TB_{36.5V}$ remained robust (MI $\geq$ 0.28), providing essential sensitivity to the frozen state via volume scattering. Furthermore, Z_{NDH} and Q_e demonstrated strong performance in forested environments—peaking at MI scores of 0.36 in boreal forests and 0.41 in mixed forests—though their utility declined sharply in croplands (MI scores of 0.11 and 0.13).

Complementing these metrics, the distributional separation of frozen and unfrozen classes was examined using box plots (Fig. S3 and S4). Diurnal amplitude variations (DAV_{AMSR} and DAV_{SMAP}) provided negligible separation, exhibiting nearly identical median values and substantial distributional overlap for both classes. Conversely, the high-frequency raw channel ($TB_{36.5V}$) and the derived standardized indices (Z_{NPR}, Z_{NDV}, Z_{NDH}, and Q_e) demonstrated strong overall separability. Among the spectral and quasi-emissivity metrics, Z_{NDV} consistently exhibited the most robust and distinct separation globally across all biome types. The distributional analysis also highlighted biome-specific limitations; the discriminatory power of the polarization ratio (Z_{NPR}) was degraded in transitional and vegetated regions, specifically mixed forests and the boreal tundra, where canopy masking reduces surface dielectric contrast.

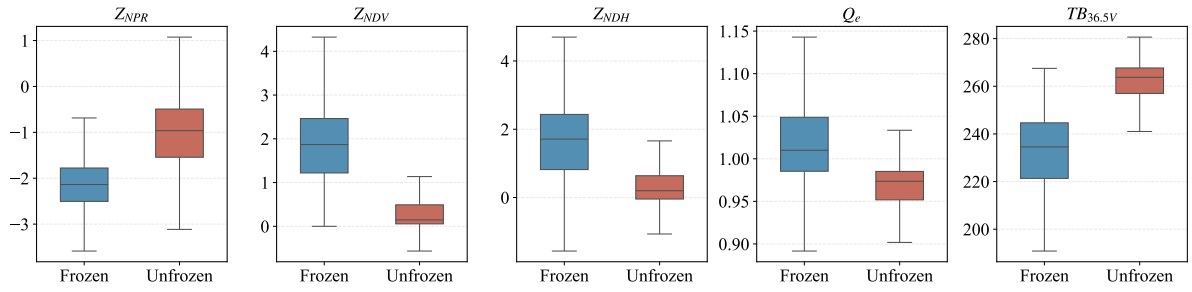


Figure S3: Global distributional separability of frozen and unfrozen samples for candidate features. Box plots display the median and interquartile range.

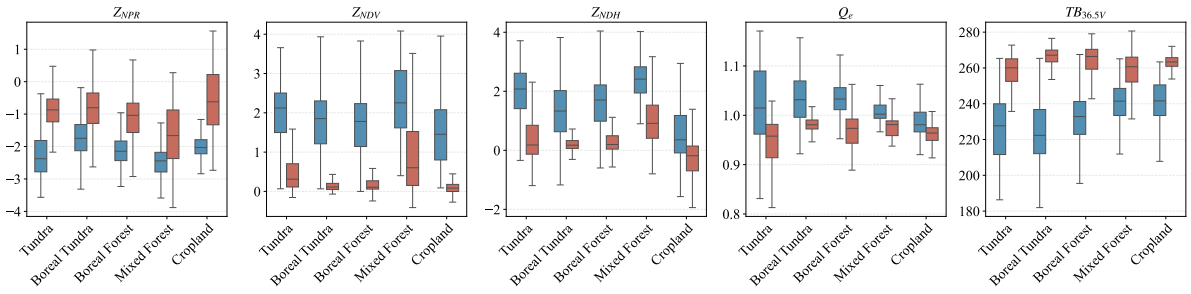


Figure S4: Distributional separability of frozen and unfrozen samples for candidate features, stratified by biome. Box plots display the median and interquartile range within each specific biome.

Z_{NPR} and Z_{NDV} emerged as the optimal feature combination. While raw $TB_{36.5V}$, Z_{NDH}, and Q_e exhibited high Mutual Information scores and strong distributional separation, their high inter-correlation with Z_{NDV} raised concerns regarding model stability and multicollinearity-induced overfitting. To verify the selection, a feature ablation and comparative study was conducted across all biomes (Table S1). Results showed that single-feature models degraded performance; removing Z_{NDV} caused PR AUC to drop across all land covers, most significantly in mixed forests (−0.381). Furthermore, substituting Z_{NDV} with alternative highly-correlated metrics, such as Q_e or Z_{NDH}, yielded only marginal gains in boreal forests (+0.047 for Q_e) and resulted in performance penalties in croplands and boreal tundra. Adding redundant features to the baseline consistently stagnated or reduced model performance. Specifically, including raw $TB_{36.5V}$ caused PR AUC in mixed forests to drop from 0.708 to 0.460, confirming that multicollinearity destabilizes coefficient optimization. Because the parsimonious baseline balances high discriminatory power with cross-biome stability, we finalized a two-feature input vector consisting of the standardized Normalized Polarization Ratio (Z_{NPR}) and the standardized vertical spectral index (Z_{NDV}). The bivariate relationship for a subset of observations is plotted in Fig. S5.

Table S1: Comparative feature ablation study across five major biomes. Values represent the change in Precision–Recall Area Under Curve (ΔPR AUC) when altering the baseline parsimonious model (Z_{NPR} + Z_{NDV}). Negative values indicate performance degradation relative to the baseline configuration.

Biome	**Baseline** (PR AUC)	**Only** Z_{NPR} (Δ)	**Only** $TB_{36.5V}$ (Δ)	$Z_{NPR} + Z_{NDH}$ (Δ)	$Z_{NPR} + Q_e$ (Δ)	$+TB_{36.5V}$ (Δ)
Mixed Forest	0.708	−0.381	−0.250	−0.021	+0.018	−0.249
Boreal Tundra	0.975	−0.101	+0.009	−0.064	−0.061	+0.007
Boreal Forest	0.888	−0.083	−0.020	+0.006	+0.047	−0.040
Tundra	0.970	−0.014	−0.011	−0.004	−0.007	+0.002
Cropland	0.941	−0.128	+0.006	−0.110	−0.104	+0.018

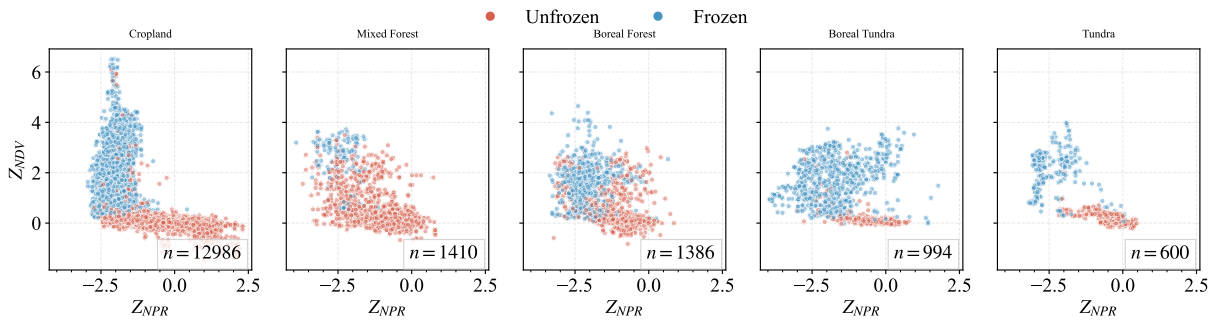


Figure S5: Scatter plots of Z_{NPR} against Z_{NDV} for a randomly selected subset of observations, stratified by land cover class: (a) Tundra, (b) Boreal Tundra, (c) Boreal Forest, (d) Mixed Forest, and (e) Cropland.

S3 Preprocessing Validation and Training Representativeness

S3.1 Validation of Local Radiometric Scaling

A pixel-level local scaling step was applied to isolate dynamic temporal signals from static environmental noise. For the Z_{NPR}, this standardization proved critical. By neutralizing the effects of static canopy structure and surface roughness, local scaling reduced spatial bias—measured via the K-S D-statistic—by 30% to 60% across all heterogeneous biomes (Fig S6). In contrast, Croplands, being the only inherently homogeneous environment in our study domain, saw only a marginal 5% improvement, as its baseline bias was already minimal. The impact of scaling on the Z_{NDV} varied across biomes (Fig S7). In heterogeneous landscapes like Mixed Forests and Tundra, local scaling drove substantial D-statistic improvements ranging from 31% to over 60%. Conversely, in environments that happened to exhibit negligible baseline bias in their raw spectral states, such as Croplands and the Boreal Tundra, the scaling introduced minor statistical divergence. Similarly, the D-statistic for the Boreal Forest remained virtually unchanged. However, despite these minor shifts, the absolute D-statistics remained universally acceptable across all domains. This confirms that the universal application of the local scaler successfully maintains spatial representativeness without degrading uniform regions, ensuring a stable, standardized feature space for model training.

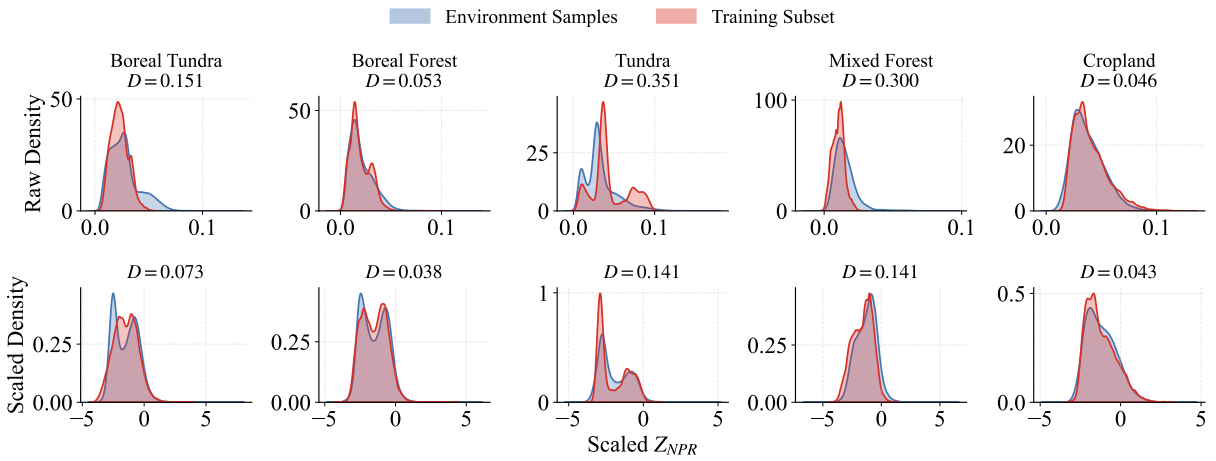


Figure S6: A/B preprocessing ablation study for Z_{NPR}. Kernel Density Estimation (KDE) distributions compare the *in situ* training pixels (red) against the broader environmental background samples (blue) across five biomes. The top row displays the raw, unscaled distributions, while the bottom row displays the locally scaled anomalies. The Two-Sample Kolmogorov-Smirnov D-statistic is provided to quantify the distributional alignment between the two samples.

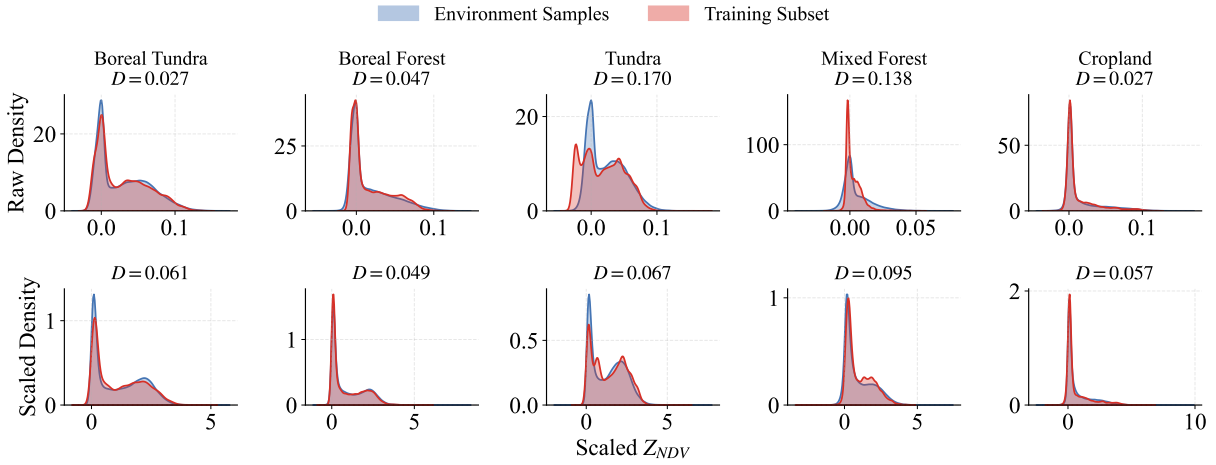


Figure S7: Same as Fig. S6, but for the vertical Normalized Difference Spectral Index (Z_{NDV}).

S3.2 Domain Representativeness of the Training Subset

A suite of 1D and 2D representativeness checks confirmed that the *in situ* training subset adequately captured the radiometric and physical diversity of the broader environmental background. The 1D marginal alignments were initially evaluated using Kernel Density Estimation (KDE) histograms (Fig. S8) and the K-S test. Across all biomes, the D-statistics remained low ($D \leq 0.141$ for Z_{NPR} and $D \leq 0.095$ for Z_{NDV}), indicating that the training data encompassed the full radiometric range of the global environmental background. This was corroborated by the Wasserstein Distance,

which remained minimal (< 0.12 standard deviations) for most landscapes. As anticipated, the structurally complex Mixed Forest exhibited moderate 1D divergence in Z_{NPR} (0.33 standard deviations). This divergence reflects a combined effect—the inherent radiometric complexity of mixed canopies, compounded by the limitations of our *in situ* sampling network, which was constrained to only three spatial blocks for this specific biome, restricting our ability to fully capture its absolute global variance. Despite this statistical divergence, visual inspection of the KDE histograms demonstrates that the actual difference between the distributions remains low. Visual inspection of the 2D KDE contour maps reveals that the training subset (contours) tightly envelopes the primary density nodes of the environmental background, accurately capturing the bivariate bimodal clusters. This visual congruence is quantitatively supported by the MMD test in the high-dimensional kernel space. The MMD results are outstanding across all land cover classes. Boreal Forest, Boreal Tundra, Cropland, and Tundra achieved near-perfect 2D alignment (MMD ≤ 0.0022). Crucially, the Mixed Forest class—despite its moderate 1D isolation—achieved an MMD score of 0.016. This demonstrates that although the absolute extremes of 1D Z_{NPR} may be underrepresented due to limited spatial sampling, the physical covariance and joint relationship between Z_{NPR} and Z_{NDV} remain intact. Collectively, these metrics confirm that the limited *in situ* training subset provides a representative multivariate foundation for training the logistic regression model across the broader domain.

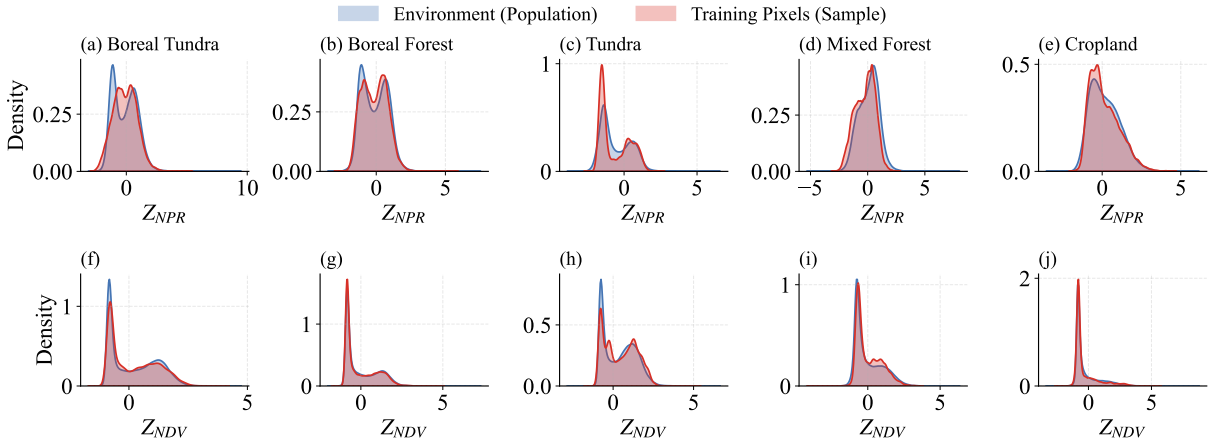


Figure S8: One-dimensional Kernel Density Estimation (KDE) histograms evaluating the spatial representativeness of the *in situ* training subset. The distributions compare the selected training pixels (red) against the broader environment samples (blue) across five biomes. The top row displays the marginal distributions for the scaled polarization ratio (Z_{NPR}), and the bottom row displays the marginal distributions for the scaled spectral index (Z_{NDV}).

Table S2: Quantitative assessment of spatial representativeness comparing the *in situ* training subset to the broader environmental background. The 1D marginal distributions are evaluated using the Two-Sample Kolmogorov-Smirnov D-statistic and Wasserstein Distance (in standard deviations). The 2D joint feature space (Z_{NPR} and Z_{NDV}) is evaluated using the Maximum Mean Discrepancy (MMD).

	K-S Test (D-statistic)		Wasserstein Distance		Joint MMD
Land Cover	Z_{NPR}	Z_{NDV}	Z_{NPR}	Z_{NDV}	2D Feature Space
Cropland	0.043	0.057	0.062	0.070	0.0017
Mixed Forest	0.141	0.095	0.331	0.101	0.0160
Boreal Forest	0.038	0.049	0.054	0.046	0.0008
Boreal Tundra	0.073	0.061	0.105	0.038	0.0008
Tundra	0.141	0.067	0.115	0.088	0.0022

S4 Extended Algorithmic Evaluation and Inter-Mission Benchmarking

S4.1 Inter-Mission Pairwise Agreement and Baseline Variance

A pairwise agreement analysis was conducted across study domain to quantify inter-mission consistency and contextualize the logistic model's position within the operational product ensemble (Table S3). Agreement followed the same biome gradient established in prior evaluations (Sect. 3.3.4), with all pairings achieving their highest consistency in Tundra and their lowest in Mixed Forest. Among the logistic model comparisons, alignment was strongest with FT-SMOS across all biomes (Agreement: 89.6%–95.1%; κ: 0.536–0.705), comparable to or exceeding the agreement observed between independent operational products such as AMSR vs. SMOS (84.5%–91.8%; κ: 0.379–0.587), indicating that the logistic model integrates naturally within the operational product ensemble. Conversely, FT-SMAP exhibited systematic divergence from all other datasets, consistently yielding the lowest pairwise agreements regardless of the comparison partner; the Logistic Model vs. FT-SMAP pairing produced the weakest values across the entire table, reaching a minimum of 58.7% (κ = 0.152) in Mixed Forest. This SMAP divergence was corroborated by the inter-product comparisons themselves, where AMSR vs. FT-SMAP and SMAP vs. SMOS consistently produced the lowest Kappa values among all operational pairings. In Mixed Forest, while SMAP-inclusive pairings collapsed to near-marginal agreement, the non-SMAP pairing (AMSR vs. SMOS: 83.8%, κ = 0.442) remained comparatively robust, suggesting that the inter-mission inconsistency in this biome is driven primarily by FT-SMAP's

algorithmic behavior under dense canopy rather than by a universal failure of passive microwave retrievals. Collectively, these baseline inter-product agreements establish the expected variance ceiling against which any individual product, including the proposed logistic model, should be interpreted.

Table S3: Pairwise agreement analysis quantifying inter-mission consistency across the study domain. Metrics represent the raw Agreement Percentage (%) and Cohen's Kappa (κ) between the proposed logistic model and the operational satellite products during non-summer months. This evaluation highlights the baseline variance expected between independent operational retrievals.

Pairwise Comparison	**Cropland** *Agr. % (κ)*	**Mixed Forest** *Agr. % (κ)*	**Boreal Forest** *Agr. % (κ)*	**Boreal Tundra** *Agr. % (κ)*	**Tundra** *Agr. % (κ)*
Logistic Model vs. FT-ESDR	87.2 (0.440)	72.3 (0.317)	88.0 (0.524)	91.8 (0.535)	92.3 (0.586)
Logistic Model vs. FT-SMAP	70.1 (0.241)	58.7 (0.152)	75.5 (0.280)	75.8 (0.215)	87.9 (0.475)
Logistic Model vs. FT-SMOS	89.6 (0.536)	75.6 (0.401)	90.0 (0.577)	94.1 (0.605)	95.1 (0.705)
FT-ESDR vs. FT-SMAP	67.4 (0.191)	63.4 (0.221)	77.1 (0.321)	76.1 (0.289)	87.3 (0.507)
FT-ESDR vs. FT-SMOS	84.5 (0.379)	83.8 (0.442)	88.1 (0.484)	91.1 (0.556)	91.8 (0.587)
FT-SMAP vs. FT-SMOS	74.3 (0.359)	66.2 (0.281)	80.2 (0.395)	78.7 (0.338)	88.9 (0.543)

S4.2 Localized Benchmarking Against *in situ* Soil Temperature Networks

Direct benchmarking against spatially harmonized *in situ* soil temperature records during non-summer months reveals a consistent pattern across all evaluated products: performance degrades systematically from open to forested environments, and the entire retrieval community fails uniformly in the Mixed Forest biome (Table S4). It should be noted that the proposed logistic model was trained on labels derived from the same *in situ* soil temperature network used here as the reference; its results in this table therefore do not constitute an independent evaluation and should not be interpreted as a fair head-to-head comparison against the operational products. This analysis is instead intended to contextualize the localized algorithmic behavior of the operational products and to document the inherent challenges of point-scale passive microwave validation. In Mixed Forest, F1 scores for all products collapsed below 0.150 despite near-complete recall (0.906–1.000), with false alarm rates exceeding 62% for every algorithm; this universal breakdown reflects the known thermodynamic decoupling between the radiometrically active emitting layer—frozen canopy and snow surface—and the 5 cm subsurface probe, which remains locked near 0°C during the zero-curtain phase. A similar but less severe high-recall, high-false-alarm pattern persists in Boreal Forest, where all products exhibited substantially elevated false alarm rates (AMSR: 81.6%, SMOS: 84.6%, SMAP: 76.1%). In Cropland and the Tundra biomes, operational products achieved competitive performance, with AMSR and SMOS reaching F1 scores above

0.920 and 0.930, respectively, while SMAP consistently exhibited lower recall and the lowest false alarm rates in open environments, confirming a systematic under-detection tendency across the sensor landscape. The generally suppressed Kappa values across all products—even where F1 scores are high—reflect the compounded uncertainty of validating coarse-footprint satellite retrievals against sparse point measurements at a mismatched depth, and should be interpreted as a lower bound on true algorithmic performance rather than an absolute accuracy estimate.

Table S4: Comparative accuracy assessment strictly isolating the non-summer period. Metrics evaluate the proposed logistic model against operational AMSR, SMAP, and SMOS products using spatially harmonized *in situ* soil temperature data. Summer months were masked using processing mask to prevent trivial classifications from inflating performance metrics.

Biome	Source	F1 Score	Kappa	MCC	Precision	Recall	False Alarm (%)
Cropland (LC 12)	Logistic Model	0.929	0.509	0.523	0.900	0.961	51.8
	AMSR	0.925	0.445	0.470	0.887	0.967	59.9
	SMAP	0.822	0.306	0.335	0.917	0.744	32.7
	SMOS	0.918	0.458	0.463	0.897	0.939	52.1
Mixed Forest (LC 5)	Logistic Model	0.113	0.011	0.049	0.060	0.906	82.5
	AMSR	0.127	0.026	0.106	0.068	0.972	78.5
	SMAP	0.146	0.049	0.142	0.079	0.927	62.9
	SMOS	0.126	0.025	0.112	0.067	1.000	81.4
Boreal Forest (LC 8)	Logistic Model	0.697	0.265	0.362	0.544	0.970	68.9
	AMSR	0.669	0.159	0.277	0.506	0.987	81.6
	SMAP	0.583	0.018	0.022	0.465	0.780	76.1
	SMOS	0.662	0.133	0.250	0.498	0.988	84.6
Boreal Tundra (LC 7)	Logistic Model	0.937	0.321	0.356	0.901	0.977	73.4
	AMSR	0.947	0.536	0.542	0.932	0.964	48.2
	SMAP	0.711	0.072	0.098	0.901	0.588	44.2
	SMOS	0.932	0.409	0.413	0.918	0.947	57.5
Tundra (LC 10)	Logistic Model	0.975	0.548	0.571	0.990	0.961	22.4
	AMSR	0.969	0.546	0.604	0.998	0.941	4.1
	SMAP	0.895	0.180	0.258	0.985	0.820	29.6
	SMOS	0.970	0.519	0.558	0.993	0.948	16.3

S5 Thermodynamic Validation of the Transition Zone

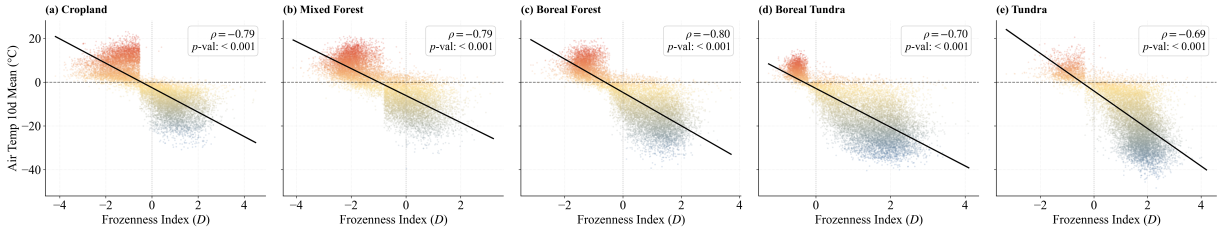


Figure S9: Spearman's rank correlation (ρ) between the continuous index of frozenness (D) and the 10-day rolling mean air temperature. Points are color-coded by temperature and anchored at -2.5°C (gold) to highlight the transition zone.

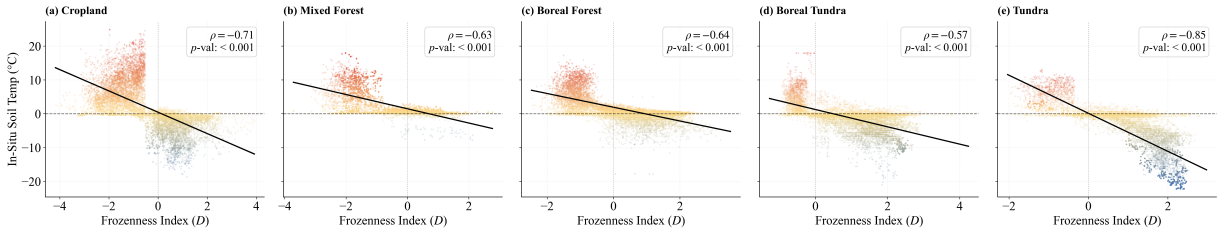


Figure S10: Scatter plot of index D versus *in situ* soil temperature. The concentration of observations at 0°C across the $D = 0$ decision boundary demonstrates the model's ability to capture the thermodynamic transition between zero-curtain and fully frozen states.

3.6 References

K. A. Arndt, J. Hashemi, S. M. Natali, L. D. Schiferl, and A.-M. Virkkala. Recent advances and challenges in monitoring and modeling non-growing season carbon dioxide fluxes from the arctic boreal zone. *Current Climate Change Reports*, 9(2):27–40, 2023. doi: 10.1007/s40641-023-00190-4.

A. Bartsch, X. Muri, M. Hetzenecker, K. Rautiainen, H. Bergstedt, J. Wuite, T. Nagler, and D. Nicolsky. Benchmarking passive-microwave-satellite-derived freeze-thaw datasets. *The Cryosphere*, 19(1):459–483, 2025. doi: 10.5194/tc-19-459-2025.

M. J. Brodzik, D. Long, and M. Hardman. Smap radiometer twice-daily rsir-enhanced ease-grid 2.0 brightness temperatures, version 2, 2021.

D. J. Cavalieri, P. Gloersen, and W. J. Campbell. Determination of sea ice parameters with the nimbus 7 smmr. *Journal of Geophysical Research: Atmospheres*, 89(D4):5355–5369, 1984. doi: 10.1029/JD089iD04p05355.

U. N. I. Center. Ims daily northern hemisphere snow and ice analysis at 1 km, 4 km, and 24 km resolutions, version 1, 2004.

J. Cohen. *Statistical Power Analysis for the Behavioral Sciences*. Routledge, 2013. doi: 10.4324/9780203771587.

J. Cohen, K. Rautiainen, J. Lemmetyinen, T. Smolander, J. Vehviläinen, and J. Pulliainen. Sentinel-1 based soil freeze/thaw estimation in boreal forest environments. *Remote Sensing of Environment*, 254:112267, 2021. doi: 10.1016/j.rse.2020.112267.

T. M. Cover and J. A. Thomas. *Elements of Information Theory*. Wiley, 2005. doi: 10.1002/047174882X.

J. Davis and M. Goadrich. The relationship between precision-recall and roc curves. *Proceedings of the 23rd international conference on Machine learning - ICML '06*, pages 233–240, 2006. doi: 10.1145/1143844.1143874.

C. Derksen, X. Xu, R. Scott Dunbar, A. Colliander, Y. Kim, J. S. Kimball, T. A. Black, E. Euskirchen, A. Langlois, M. M. Loranty, P. Marsh, K. Rautiainen, A. Roy, A. Royer, and J. Stephens. Retrieving landscape freeze/thaw state from soil moisture active passive (smap) radar and radiometer measurements. *Remote Sensing of Environment*, 194:48–62, 2017. doi: 10.1016/j.rse.2017.03.007.

E. G. Devoie, S. Gruber, and J. M. McKenzie. A repository of measured soil freezing characteristic curves: 1921 to 2021. *Earth System Science Data*, 14(7):3365–3377, 2022. doi: 10.5194/essd-14-3365-2022.

K. Donahue, J. S. Kimball, J. Du, F. Bunt, A. Colliander, M. Moghaddam, J. Johnson, Y. Kim, and M. A. Rawlins. Deep learning estimation of northern hemisphere soil freeze-thaw dynamics using satellite multi-frequency microwave brightness temperature observations. *Frontiers in Big Data*, 6, 2023. doi: 10.3389/fdata.2023.1243559.

W. Dorigo, I. Himmelbauer, D. Aberer, L. Schremmer, I. Petrakovic, L. Zappa, W. Preimesberger, A. Xaver, F. Annor, J. Ardö, D. Baldocchi, M. Bitelli, G. Blöschl, H. Bogena, L. Brocca, J.-C. Calvet, J. J. Camarero, G. Capello, M. Choi, M. C. Cosh, N. van de Giesen, I. Hajdu, J. Ikonen, K. H. Jensen, K. D. Kanniah, I. de Kat, G. Kirchengast, P. Kumar Rai, J. Kyrouac, K. Larson, S. Liu, A. Loew, M. Moghaddam, J. Martínez Fernández, C. Mattar Bader, R. Morbidelli, J. P. Musial, E. Osenga, M. A. Palecki, T. Pellarin, G. P. Petropoulos, I. Pfeil, J. Powers, A. Robock, C. Rüdiger, U. Rummel, M. Strobel, Z. Su, R. Sullivan, T. Tagesson, A. Varlagin, M. Vreugdenhil, J. Walker, J. Wen, F. Wenger, J. P. Wigneron, M. Woods, K. Yang, Y. Zeng, X. Zhang, M. Zreda, S. Dietrich, A. Gruber, P. van Oevelen, W. Wagner, K. Scipal, M. Drusch, and R. Sabia. The international soil moisture network: serving earth system science for over a decade. *Hydrology and Earth System Sciences*, 25(11):5749–5804, 2021. doi: 10.5194/hess-25-5749-2021.

D. Entekhabi, E. G. Njoku, P. E. O'Neill, K. H. Kellogg, W. T. Crow, W. N. Edelstein, J. K. Entin, S. D. Goodman, T. J. Jackson, J. Johnson, J. Kimball, J. R. Piepmeier, R. D. Koster, N. Martin, K. C. McDonald, M. Moghaddam, S. Moran, R. Reichle, J. C. Shi, M. W. Spencer, S. W. Thurman, L. Tsang, and J. Van Zyl. The soil moisture active passive (smap) mission. *Proceedings of the IEEE*, 98(5):704–716, 2010. doi: 10.1109/JPROC.2010.2043918.

T. Fawcett. An introduction to roc analysis. *Pattern Recognition Letters*, 27(8):861–874, 2006. doi: 10.1016/j.patrec.2005.10.010.

D. Feng, T. Zhao, J. Zheng, Y. Bai, Y. Ran, X. Kou, L. Jiang, Z. Zhang, P. Yu, J. Zhu, J. Pan, J. Shi, and Y.-A. Liou. A high-resolution (0.05°) global seamless continuity record (2002–2023) of near-surface soil freeze-thaw states via passive microwave and optical satellite data. *Earth System Science Data*, 17(11):6273–6293, 2025. doi: 10.5194/essd-17-6273-2025.

O. W. Frauenfeld and T. Zhang. An observational 71-year history of seasonally frozen ground changes in the eurasian high latitudes. *Environmental Research Letters*, 6(4):044024, 2011. doi: 10.1088/1748-9326/6/4/044024.

M. Friedl and D. Sulla-Menashe. Modis/terra+aqua land cover type yearly l3 global 0.05deg cmg v061, 2022a.

M. Friedl and D. Sulla-Menashe. Modis/terra+aqua land cover type yearly l3 global 500m sin grid v061, 2022b.

P. Gloersen and D. J. Cavalieri. Reduction of weather effects in the calculation of sea ice concentration from microwave radiances. *Journal of Geophysical Research: Oceans*, 91(C3): 3913–3919, 1986. doi: 10.1029/JC091iC03p03913.

A. Gretton, K. M. Borgwardt, M. J. Rasch, B. Schölkopf, and A. Smola. A kernel two-sample test. *Journal of Machine Learning Research*, 13(25):723–773, 2012. URL http://jmlr.org/papers/v13/gretton12a.html.

T. Hastie, R. Tibshirani, and J. Friedman. The elements of statistical learning. *Springer Series in Statistics*, 2009. doi: 10.1007/978-0-387-84858-7.

M. Hayashi. The cold vadose zone: Hydrological and ecological significance of frozen-soil processes. *Vadose Zone Journal*, 12(4):1–8, 2013. doi: 10.2136/vzj2013.03.0064.

H. A. L. Henry. Climate change and soil freezing dynamics: historical trends and projected changes. *Climatic Change*, 87(3-4):421–434, 2007. doi: 10.1007/s10584-007-9322-8.

Y. Hu, S. Lv, Z. Li, Y. Zeng, S. Li, J. Wen, and Z. Su. Improving soil freeze–thaw retrieval from spaceborne l-band measurements based on diurnal amplitude variation. *Journal of Remote Sensing*, 5, 2025. doi: 10.34133/remotesensing.0806.

G. James, D. Witten, T. Hastie, and R. Tibshirani. An introduction to statistical learning. *Springer Texts in Statistics*, 2021. doi: 10.1007/978-1-0716-1418-1.

C. E. Johnston, S. A. Ewing, J. W. Harden, R. K. Varner, K. P. Wickland, J. C. Koch, C. C. Fuller, K. Manies, and M. T. Jorgenson. Effect of permafrost thaw on co_2 and ch_4 exchange in a western alaska peatland chronosequence. *Environmental Research Letters*, 9(8):085004, 2014. doi: 10.1088/1748-9326/9/8/085004.

J. Johnston, V. Maggioni, and P. Houser. Comparing global passive microwave freeze/thaw records: Investigating differences between ka- and l-band products. *Remote Sensing of Environment*, 247:111936, 2020. doi: 10.1016/j.rse.2020.111936.

A. R. Jonckheere. A distribution-free k-sample test against ordered alternatives. *Biometrika*, 41 (1–2):133–145, 1954. doi: 10.1093/biomet/41.1-2.133. URL https://doi.org/10.1093/biomet/41.1-2.133.

Y. Kim, J. S. Kimball, K. C. McDonald, and J. Glassy. Developing a global data record of daily landscape freeze/thaw status using satellite passive microwave remote sensing. *IEEE Transactions on Geoscience and Remote Sensing*, 49(3):949–960, 2011. doi: 10.1109/TGRS.2010.2070515.

Y. Kim, J. S. Kimball, J. Glassy, and J. Du. An extended global earth system data record on daily landscape freeze-thaw status determined from satellite passive microwave remote sensing. *Earth System Science Data*, 9(1):133–147, 2017. doi: 10.5194/essd-9-133-2017.

Y. Kim, J. Kimball, J. Du, and J. Glassy. Measures global record of daily landscape freeze/thaw status, version 5, 2021.

C. Knoblauch, C. Beer, S. Liebner, M. N. Grigoriev, and E.-M. Pfeiffer. Methane production as key to the greenhouse gas budget of thawing permafrost. *Nature Climate Change*, 8(4):309–312, 2018. doi: 10.1038/s41558-018-0095-z.

R. W. R. Koopmans and R. D. Miller. Soil freezing and soil water characteristic curves. *Soil Science Society of America Journal*, 30(6):680–685, 1966. doi: 10.2136/sssaj1966.03615995003000060011x.

W. H. Kruskal and W. A. Wallis. Use of ranks in one-criterion variance analysis. *Journal of the American Statistical Association*, 47(260):583–621, 1952. doi: 10.1080/01621459.1952.10483441.

D. Kumawat, A. Ebtehaj, X. Xu, A. Colliander, and V. Kumar. An autoencoder architecture for l-band passive microwave retrieval of landscape freeze-thaw cycle. *IEEE Transactions on Geoscience and Remote Sensing*, 63:1–15, 2025. doi: 10.1109/TGRS.2025.3530356.

I. Kurganova, R. Teepe, and N. Loftfield. Influence of freeze-thaw events on carbon dioxide emission from soils at different moisture and land use. *Carbon Balance and Management*, 2(1), 2007. doi: 10.1186/1750-0680-2-2.

K. S. Larsen, S. Jonasson, and A. Michelsen. Repeated freeze-thaw cycles and their effects on biological processes in two arctic ecosystem types. *Applied Soil Ecology*, 21(3):187–195, 2002. doi: 10.1016/S0929-1393(02)00093-8.

D. G. Long, M. J. Brodzik, and M. Hardman. Evaluating the effective resolution of enhanced resolution smap brightness temperature image products. *Frontiers in Remote Sensing*, 4, 2023. doi: 10.3389/frsen.2023.1073765.

S. Lv, J. Wen, C. Simmer, Y. Zeng, Y. Guo, and Z. Su. A novel freeze-thaw state detection algorithm based on l-band passive microwave remote sensing. *Remote Sensing*, 14(19):4747, 2022. doi: 10.3390/rs14194747.

T. Maeda, Y. Taniguchi, and K. Imaoka. Gcom-w1 amsr2 level 1r product: Dataset of brightness temperature modified using the antenna pattern matching technique. *IEEE Transactions on Geoscience and Remote Sensing*, 54(2):770–782, 2016. doi: 10.1109/TGRS.2015.2465170.

A. Mavrovic, O. Sonnentag, J. Lemmetyinen, C. Voigt, N. Rutter, P. Mann, J.-D. Sylvain, and A. Roy. Environmental controls of winter soil carbon dioxide fluxes in boreal and tundra environments. *Biogeosciences*, 20(24):5087–5108, 2023. doi: 10.5194/bg-20-5087-2023.

A. Mavrovic, O. Sonnentag, C. Voigt, J. Lemmetyinen, M. Aurela, and A. Roy. Winter methane fluxes over boreal and arctic environments. *Geophysical Research Letters*, 52(21), 2025. doi: 10.1029/2025GL118367.

S. Mecklenburg, M. Drusch, L. Kaleschke, N. Rodriguez-Fernandez, N. Reul, Y. Kerr, J. Font, M. Martin-Neira, R. Oliva, E. Daganzo-Eusebio, J. Grant, R. Sabia, G. Macelloni, K. Rautiainen, J. Fauste, P. de Rosnay, J. Munoz-Sabater, N. Verhoest, H. Lievens, S. Delwart, R. Crapolicchio, A. de la Fuente, and M. Kornberg. Esa's soil moisture and ocean salinity mission: From science to operational applications. *Remote Sensing of Environment*, 180:3–18, 2016. doi: 10.1016/j.rse.2015.12.025.

H. Meyer and E. Pebesma. Machine learning-based global maps of ecological variables and the challenge of assessing them. *Nature Communications*, 13(1), 2022. doi: 10.1038/s41467-022-29838-9.

C. J. Mikan, J. P. Schimel, and A. P. Doyle. Temperature controls of microbial respiration in arctic tundra soils above and below freezing. *Soil Biology and Biochemistry*, 34(11):1785–1795, 2002. doi: 10.1016/S0038-0717(02)00168-2.

K. Muzalevskiy and Z. Ruzicka. Detection of soil freeze/thaw states in the arctic region based on combined smap and amsr-2 radio brightness observations. *International Journal of Remote Sensing*, 41(14):5046–5061, 2020. doi: 10.1080/01431161.2020.1724348.

S. M. Natali, J. D. Watts, B. M. Rogers, S. Potter, S. M. Ludwig, A.-K. Selbmann, P. F. Sullivan, B. W. Abbott, K. A. Arndt, L. Birch, M. P. Björkman, A. A. Bloom, G. Celis, T. R. Christensen, C. T. Christiansen, R. Commane, E. J. Cooper, P. Crill, C. Czimczik, S. Davydov, J. Du, J. E. Egan, B. Elberling, E. S. Euskirchen, T. Friborg, H. Genet, M. Göckede, J. P. Goodrich, P. Grogan, M. Helbig, E. E. Jafarov, J. D. Jastrow, A. A. M. Kalhori, Y. Kim,

J. S. Kimball, L. Kutzbach, M. J. Lara, K. S. Larsen, B.-Y. Lee, Z. Liu, M. M. Loranty, M. Lund, M. Lupascu, N. Madani, A. Malhotra, R. Matamala, J. McFarland, A. D. McGuire, A. Michelsen, C. Minions, W. C. Oechel, D. Olefeldt, F.-J. W. Parmentier, N. Pirk, B. Poulter, W. Quinton, F. Rezanezhad, D. Risk, T. Sachs, K. Schaefer, N. M. Schmidt, E. A. G. Schuur, P. R. Semenchuk, G. Shaver, O. Sonnentag, G. Starr, C. C. Treat, M. P. Waldrop, Y. Wang, J. Welker, C. Wille, X. Xu, Z. Zhang, Q. Zhuang, and D. Zona. Large loss of co2 in winter observed across the northern permafrost region. *Nature Climate Change*, 9(11):852–857, 2019. doi: 10.1038/s41558-019-0592-8.

M. P. Nikrad, L. J. Kerkhof, and M. M. Häggblom. The subzero microbiome: microbial activity in frozen and thawing soils. *FEMS Microbiology Ecology*, 92(6):fiw081, 2016. doi: 10.1093/femsec/fiw081.

S. I. Outcalt, F. E. Nelson, and K. M. Hinkel. The zero-curtain effect: Heat and mass transfer across an isothermal region in freezing soil. *Water Resources Research*, 26(7):1509–1516, 1990. doi: 10.1029/WR026i007p01509.

T. Oztas and F. Fayetorbay. Effect of freezing and thawing processes on soil aggregate stability. *CATENA*, 52(1):1–8, 2003. doi: 10.1016/S0341-8162(02)00177-7.

A. Pacheco. Real-time in-situ soil monitoring for agriculture (RISMA) network metadata [historical data], 2019. URL https://agriculture.canada.ca/SoilMonitoringStations/historical-data-en.html. Accessed: Mar. 16, 2021.

R. Pardo Lara, A. A. Berg, J. Warland, and E. Tetlock. In situ estimates of freezing/melting point depression in agricultural soils using permittivity and temperature measurements. *Water Resources Research*, 56(5), 2020. doi: 10.1029/2019WR026020.

F. Pedregosa, G. Varoquaux, A. Gramfort, V. Michel, B. Thirion, O. Grisel, M. Blondel, P. Prettenhofer, R. Weiss, V. Dubourg, J. Vanderplas, A. Passos, D. Cournapeau, M. Brucher, M. Perrot, and Édouard Duchesnay. Scikit-learn: Machine learning in python. *Journal of Machine Learning Research*, 12(85):2825–2830, 2011. URL http://jmlr.org/papers/v12/pedregosa11a.html.

X. Peng, O. W. Frauenfeld, B. Cao, K. Wang, H. Wang, H. Su, Z. Huang, D. Yue, and T. Zhang. Response of changes in seasonal soil freeze/thaw state to climate change from 1950 to 2010 across china. *Journal of Geophysical Research: Earth Surface*, 121(11):1984–2000, 2016. doi: 10.1002/2016JF003876.

M. Prince, A. Roy, A. Royer, and A. Langlois. Timing and spatial variability of fall soil freezing in boreal forest and its effect on smap l-band radiometer measurements. *Remote Sensing of Environment*, 231:111230, 2019. doi: 10.1016/j.rse.2019.111230.

K. Rautiainen, J. Lemmetyinen, M. Schwank, A. Kontu, C. B. Ménard, C. Mätzler, M. Drusch, A. Wiesmann, J. Ikonen, and J. Pulliainen. Detection of soil freezing from l-band passive microwave observations. *Remote Sensing of Environment*, 147:206–218, 2014. doi: 10.1016/j.rse.2014.03.007.

K. Rautiainen, T. Parkkinen, J. Lemmetyinen, M. Schwank, A. Wiesmann, J. Ikonen, C. Derksen, S. Davydov, A. Davydova, J. Boike, M. Langer, M. Drusch, and J. Pulliainen. Smos prototype algorithm for detecting autumn soil freezing. *Remote Sensing of Environment*, 180:346–360, 2016. doi: 10.1016/j.rse.2016.01.012.

K. Rautiainen, M. Holmberg, J. Cohen, A. Mialon, M. Schwank, J. Lemmetyinen, A. de la Fuente, and Y. Kerr. An operational smos soil freeze-thaw product. *Earth System Science Data*, 17 (10):5337–5353, 2025. doi: 10.5194/essd-17-5337-2025.

S. U. Rehman, S. Asghar, S. Fong, and S. Sarasvady. Dbscan: Past, present and future. *The Fifth International Conference on the Applications of Digital Information and Web Technologies (ICADIWT 2014)*, pages 232–238, 2014. doi: 10.1109/ICADIWT.2014.6814687.

T. L. Rowlandson, A. A. Berg, A. Roy, E. Kim, R. Pardo Lara, J. Powers, K. Lewis, P. Houser, K. McDonald, P. Toose, A. Wu, E. De Marco, C. Derksen, J. Entin, A. Colliander, X. Xu, and A. Mavrovic. Capturing agricultural soil freeze/thaw state through remote sensing and ground observations: A soil freeze/thaw validation campaign. *Remote Sensing of Environment*, 211: 59–70, 2018. doi: 10.1016/j.rse.2018.04.003.

A. Roy, A. Royer, C. Derksen, L. Brucker, A. Langlois, A. Mialon, and Y. H. Kerr. Evaluation of spaceborne l-band radiometer measurements for terrestrial freeze/thaw retrievals in canada. *IEEE Journal of Selected Topics in Applied Earth Observations and Remote Sensing*, 8(9): 4442–4459, 2015. doi: 10.1109/JSTARS.2015.2476358.

A. Roy, P. Toose, A. Mavrovic, C. Pappas, A. Royer, C. Derksen, A. Berg, T. Rowlandson, M. El-Amine, A. Barr, A. Black, A. Langlois, and O. Sonnentag. L-band response to freeze/thaw in a boreal forest stand from ground- and tower-based radiometer observations. *Remote Sensing of Environment*, 237:111542, 2020. doi: 10.1016/j.rse.2019.111542.

Y. Rubner, C. Tomasi, and L. J. Guibas. The earth mover's distance as a metric for image retrieval. *International Journal of Computer Vision*, 40(2):99–121, 2000. doi: 10.1023/A:1026543900054.

H. Salmabadi. Development of new microwave multi-sensor freeze/thaw products for improving growing season monitoring in north america, 2023. URL https://doi.org/10.69777/330450. Doctoral Research Scholarship.

H. Salmabadi, R. Pardo Lara, A. Berg, A. Mavrovic, C. Hanes, B. Montpetit, and A. Roy. In situ monitoring of seasonally frozen ground using soil freezing characteristic curve in permittivity–temperature space. *The Cryosphere*, 20(3):1635–1654, 2026. doi: 10.5194/tc-20-1635-2026.

C. C. C. Service. Era5-land hourly data from 1950 to present, 2019.

Y. Song, Y. Zou, G. Wang, and X. Yu. Altered soil carbon and nitrogen cycles due to the freeze-thaw effect: A meta-analysis. *Soil Biology and Biochemistry*, 109:35–49, 2017. doi: 10.1016/J.SOILBIO.2017.01.020.

J. Tao, Q. Zhu, W. J. Riley, and R. B. Neumann. Improved elmv1-eca simulations of zero-curtain periods and cold-season ch_4 and co_2 emissions at alaskan arctic tundra sites. *The Cryosphere*, 15(12):5281–5307, 2021. doi: 10.5194/tc-15-5281-2021.

T. J. Terpstra. The asymptotic normality and consistency of kendall's test against trend, when ties are present in one ranking. *Indagationes Mathematicae*, 14(3):327–333, 1952.

P. Virtanen, R. Gommers, T. E. Oliphant, M. Haberland, T. Reddy, D. Cournapeau, E. Burovski, P. Peterson, W. Weckesser, J. Bright, S. J. van der Walt, M. Brett, J. Wilson, K. J. Millman, N. Mayorov, A. R. J. Nelson, E. Jones, R. Kern, E. Larson, C. J. Carey, İ. Polat, Y. Feng, E. W. Moore, J. VanderPlas, D. Laxalde, J. Perktold, R. Cimrman, I. Henriksen, E. A. Quintero, C. R. Harris, A. M. Archibald, A. H. Ribeiro, F. Pedregosa, P. van Mulbregt, S. . Contributors, A. Vijaykumar, A. P. Bardelli, A. Rothberg, A. Hilboll, A. Kloeckner, A. Scopatz, A. Lee, A. Rokem, C. N. Woods, C. Fulton, C. Masson, C. Haggstrom, C. Fitzgerald, D. A. Nicholson, D. R. Hagen, D. V. Pasechnik, E. Olivetti, E. Martin, E. Wieser, F. Silva, F. Lenders, F. Wilhelm, G. Young, G. A. Price, G.-L. Ingold, G. E. Allen, G. R. Lee, H. Audren, I. Probst, J. P. Dietrich, J. Silterra, J. T. Webber, J. Slavic, J. Nothman, J. Buchner, J. Kulick, J. L. Schonberger, J. V. de Miranda Cardoso, J. Reimer, J. Harrington, J. L. C. Rodríguez, J. Nunez-Iglesias, J. Kuczynski, K. Tritz, M. Thoma, M. Newville, M. Kümmerer, M. Bolingbroke, M. Tartre, M. Pak, N. J. Smith, N. Nowaczyk, N. Shebanov, O. Pavlyk, P. A. Brodtkorb, P. Lee, R. T. McGibbon, R. Feldbauer, S. Lewis, S. Tygier, S. Sievert, S. Vigna, S. Peterson, S. More, T. Pudlik, T. Oshima, T. J. Pingel, T. P. Robitaille, T. Spura, T. R. Jones, T. Cera, T. Leslie, T. Zito, T. Krauss, U. Upadhyay, Y. O. Halchenko, and Y. Vázquez-Baeza. Scipy 1.0: fundamental algorithms for scientific computing in python. *Nature Methods*, 17(3):261–272, 2020. doi: 10.1038/s41592-019-0686-2.

C. Wagner-Riddle, K. A. Congreves, D. Abalos, A. A. Berg, S. E. Brown, J. T. Ambadan, X. Gao, and M. Tenuta. Globally important nitrous oxide emissions from croplands induced by freeze-thaw cycles. *Nature Geoscience*, 10(4):279–283, 2017. doi: 10.1038/NGEO2907.

V. A. Walker, A. Colliander, and J. S. Kimball. Satellite retrievals of probabilistic freeze-thaw conditions from smap and amsr brightness temperatures. *IEEE Transactions on Geoscience and Remote Sensing*, 60:1–11, 2022. doi: 10.1109/TGRS.2022.3174807.

G. Wang, H. Hu, and T. Li. The influence of freeze-thaw cycles of active soil layer on surface runoff in a permafrost watershed. *Journal of Hydrology*, 375(3-4):438–449, 2009. doi: 10.1016/j.jhydrol.2009.06.046.

X. Xu, R. Dunbar, C. Derksen, A. Colliander, Y. Kim, and J. Kimball. Smap enhanced l3 radiometer global and northern hemisphere daily 9 km ease-grid freeze/thaw state, version 4, 2023.

K. Yang and C. Wang. Water storage effect of soil freeze-thaw process and its impacts on soil hydro-thermal regime variations. *Agricultural and Forest Meteorology*, 265:280–294, 2019. doi: 10.1016/j.agrformet.2018.11.011.

Z. Yang, T. Zhao, Q. Wang, L. Peng, Y. Ran, Y. Bai, J. Zheng, P. Yao, Z. Peng, J. Zhu, X. Kou, Y.-A. Liou, and J. Shi. Comparative analysis of microwave indices for freeze/thaw state monitoring and adaptive thresholding implications. *Science of Remote Sensing*, 11:100239, 2025. doi: 10.1016/j.srs.2025.100239.

Y. Yi, J. S. Kimball, R. H. Chen, M. Moghaddam, and C. E. Miller. Sensitivity of active-layer freezing process to snow cover in arctic alaska. *The Cryosphere*, 13(1):197–218, 2019. doi: 10.5194/tc-13-197-2019.

T. Zhang. Distribution of seasonally and perennially frozen ground in the northern hemisphere. In *Proceedings of the 8th International Conference on Permafrost*, pages 1289–1294, Zurich, Switzerland, 2003. A.A. Balkema. 21–25 July 2003.

X. Zhang and S. Sun. The impact of soil freezing/thawing processes on water and energy balances. *Advances in Atmospheric Sciences*, 28(1):169–177, 2011. doi: 10.1007/s00376-010-9206-0. URL https://doi.org/10.1007/s00376-010-9206-0.

R. Zhao, S. Zhang, W. Gao, J. He, J. Wang, D. Jin, and B. Nan. Factors effecting the freeze thaw process in soils and reduction in damage due to frosting with reinforcement: a review. *Bulletin of Engineering Geology and the Environment*, 78(7):5001–5010, 2019. doi: 10.1007/s10064-018-1430-3.

T. Zhao, L. Zhang, L. Jiang, S. Zhao, L. Chai, and R. Jin. A new soil freeze/thaw discriminant algorithm using amsr-e passive microwave imagery. *Hydrological Processes*, 25(11):1704–1716, 2011. doi: 10.1002/hyp.7930.

D. Zona. Greenhouse gas flux measurements at the zero curtain, north slope, alaska, 2012-2021, 2021.

B. Zuerndorfer and A. England. Radiobrightness decision criteria for freeze/thaw boundaries. *IEEE Transactions on Geoscience and Remote Sensing*, 30(1):89–102, 1992. doi: 10.1109/36.124219.

Chapter 4

Zero-Curtain and Frozen Ground Spatiotemporal Variability Across North American Biomes: Environmental Controls and Implications for Cold-Season Ecosystem Respiration

Article Information

French Title:	Variabilité spatio-temporelle du zéro rideau et du sol gelé à travers les biomes nord-américains : contrôles environnementaux et implications pour la respiration des écosystèmes en saison froide
Authors:	Hesam Salmabadi, Aaron Berg, and Alexandre Roy
Target Journal:	To be determined
Publication Status:	In Preparation

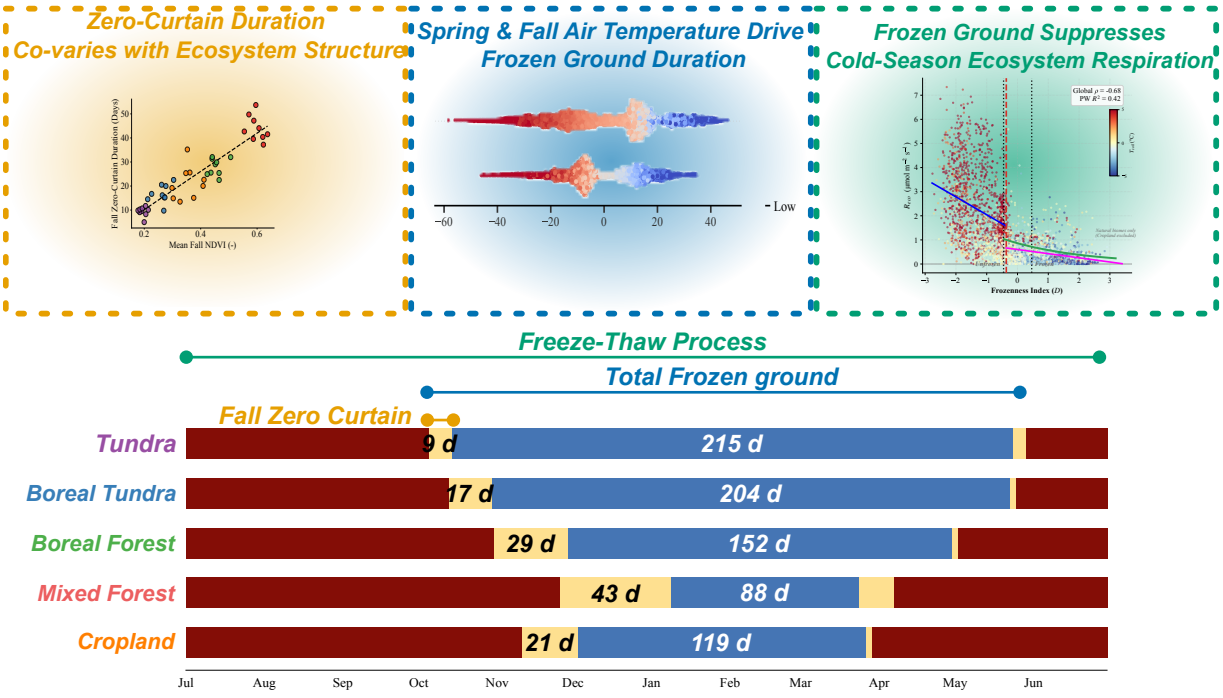
Résumé

Le sol saisonnièrement gelé et sa phase de zéro rideau associée subissent des changements documentés à l'échelle de l'hémisphère Nord. Cependant, les contrôles environnementaux à l'échelle du paysage régissant la durée du zéro rideau et leur couplage mécaniste avec les flux de carbone en saison froide demeurent mal quantifiés. Cette étude poursuivait deux objectifs : 1) quantifier spatio-temporellement les jours de gel et de zéro rideau à travers les biomes nord-américains et identifier les contrôles environnementaux dominants régissant la fréquence totale des sols gelés, et 2) établir un lien mécaniste entre un indice de gel (*Frozenness Index*, D) issu des micro-ondes passives et la respiration écosystémique (R_{eco}). À l'aide d'une restitution multifréquence du gel–dégel (FT-CUSTOM, dérivée d'AMSR et de SMAP), corroborée par le produit indépendant FT-SMOS, sur un registre allant de 2015 à 2024 sur une grille EASE-Grid 2.0 de 9 km, nous avons démontré que la durée du zéro rideau atteint un pic dans les forêts mixtes des latitudes moyennes (57,4 jours) et diminue dans la toundra du Haut-Arctique (13,7 jours) — un modèle non latitudinal qui co-varie le plus fortement avec la densité de la végétation automnale (NDVI) à l'échelle du biome, augmentant de façon monotone de la toundra clairsemée à la forêt mixte structurellement complexe, la température de l'air et le manteau neigeux automnaux suivant un gradient similaire parmi les biomes naturels. L'attribution XGBoost avec analyse SHAP a révélé que les températures atmosphériques printanières et automnales régissent la fréquence totale des sols gelés (l'agrégat des jours de zéro rideau et des jours strictement gelés) de manière globale (impacts moyens de 17,5 et 12,1 jours, respectivement), mais que la structure de la canopée déclenche un changement de régime dans les biomes forestiers où le manteau neigeux sous la canopée supplante le forçage thermique direct. La régression par morceaux de R_{eco} d'AmeriFlux par rapport à l'indice de gel (D) a démontré que le seuil d'arrêt métabolique s'aligne avec le début de la phase de zéro rideau dérivée par satellite, et l'analyse des lignes de démarcation (*boundary line analysis*) a révélé une décroissance exponentielle du potentiel respiratoire maximal à mesure que la teneur en eau liquide du sol s'épuise progressivement sous l'effet du gel. Ces résultats positionnent l'indice continu D comme un indicateur (*proxy*) physiquement fondé, à l'échelle du paysage, capable de détecter le point de basculement critique où la respiration de l'écosystème en saison froide se découple de la température et devient régie par l'état cryosphérique du sol.

Abstract

Seasonally frozen ground and its associated zero-curtain phase are undergoing documented shifts across the Northern Hemisphere. Yet the landscape-scale environmental controls governing zero-curtain duration and their mechanistic coupling to cold-season carbon fluxes remain poorly quantified. This study pursued two objectives: 1) to spatiotemporally quantify frozen and zero-curtain days across North American biomes and identify the dominant environmental controls governing total frozen ground frequency, and 2) to establish a mechanistic linkage between a passive microwave Frozenness Index (D) and ecosystem respiration (R_{eco}). Using a custom multi-frequency freeze–thaw retrieval (FT-CUSTOM, derived from AMSR and SMAP), corroborated by the independent FT-SMOS product, across a 2015–2024 record on a 9 km EASE-Grid 2.0 domain, we documented that zero-curtain duration peaks in mid-latitude mixed forests (57.4 days) and collapses in high-Arctic tundra (13.7 days)—a non-latitudinal pattern that co-varies most strongly with fall vegetation density (NDVI) at the biome scale, increasing monotonically from sparse tundra to structurally complex mixed forest, with fall air temperature and snowpack tracking a similar gradient among natural biomes. XGBoost attribution with SHAP analysis revealed that spring and fall atmospheric temperatures govern total frozen ground frequency (the aggregate of zero-curtain and strictly frozen days) globally (mean impacts of 17.5 and 12.1 days, respectively), but canopy structure triggers a regime shift in forested biomes where sub-canopy snowpack supersedes direct thermal forcing. Piecewise regression of AmeriFlux R_{eco} against D demonstrated that the metabolic shutdown threshold aligns with the satellite-derived onset of the zero-curtain phase, and boundary line analysis revealed an exponential decay in maximum respiratory potential as soil liquid water content is progressively depleted by freezing. These results position the continuous D index as a physically grounded, landscape-scale proxy capable of detecting the critical tipping point at which cold-season ecosystem respiration decouples from temperature and becomes governed by the soil cryospheric state.

Graphical Abstract



4.1 Nomenclature

Abbreviations

FT	Freeze–thaw
FT-CUSTOM	Custom multi-frequency freeze–thaw retrieval derived from AMSR and SMAP observations
FT-SMOS	SMOS L3 freeze–thaw product (morning overpasses)
EOS	End of growing season — the calendar date marking the onset of sustained freezing (≥10 consecutive frozen or zero-curtain days)
SOS	Start of growing season — the calendar date marking the onset of sustained thawing (≥10 consecutive unfrozen days)
NDVI	Normalized Difference Vegetation Index
SWE	Snow water equivalent
SHAP	SHapley Additive exPlanations
M-K	Mann-Kendall (non-parametric trend test)
OLS	Ordinary least squares
MI	Mutual Information
LWC	Liquid water content
AMSR	Advanced Microwave Scanning Radiometer
SMAP	Soil Moisture Active Passive
SMOS	Soil Moisture and Ocean Salinity

Symbols

D	Frozenness Index — a continuous microwave-derived metric of the soil cryospheric state
D_{lower}	Lower D threshold below which the soil is classified as unfrozen; marks the onset of the zero-curtain phase
D_{upper}	Upper D threshold above which the soil is classified as strictly frozen; marks the end of the zero-curtain phase
R_{eco}	Ecosystem respiration (μmol CO_2 m^{-2} s^{-1})
Q_{10}	Temperature sensitivity coefficient of soil respiration
R^2	Coefficient of determination

Terminological note on frequency and duration

Throughout this study, *frequency* refers to the aggregate count of daily soil-state labels assigned to a given phase (e.g., strictly frozen, zero-curtain) per season year, expressed in days. Because the FT products provide daily classifications, this count is functionally equivalent to the total

time spent in that phase; accordingly, *frequency* and *duration* are used interchangeably when referring to per-season-year day counts. The sole exception is *cold-season duration*, defined as the continuous phenological interval between EOS and SOS, which is reported separately in Fig. S9. Total frozen ground frequency/duration is aggregate of zero-curtain and strictly frozen day counts per season year.

4.2 Introduction

Over recent decades, observations have revealed a contraction of frozen ground across the Northern Hemisphere, characterized by shrinking areas and decreasing frozen durations and frequencies [Li et al., 2021b, Yang et al., 2024, 2025]. Passive microwave satellite data indicated that the duration and annual mean area of strictly frozen ground in the Northern Hemisphere decreased at rates of 1.3 days per decade and $0.49 \times 10^6 \text{km}^2$ per decade, respectively [Li et al., 2021b]. This area reduction aligns with land-surface reanalyses, which showed an annual frozen ground area decrease of $0.32 \times 10^6 \text{km}^2$ per decade [Yang et al., 2024]. Additionally, *in situ* soil temperature analyses across 85 Northern Hemisphere sites showed that frozen durations shortened at 57% of these monitored locations [Yang et al., 2025]. These shifts vary geographically; earlier spring thaws and delayed fall freezes lengthened the growing season by roughly 5 days per decade in North American evergreen conifer and tundra biomes, whereas simultaneous advancements of both thaw and freeze dates in Eurasian larch biomes resulted in no net change [Smith et al., 2004]. Zero-curtain (transitional) dynamics are also altering. Satellite records demonstrated that the spatial footprint of this zero-curtain state shrank by $0.34 \times 10^6 \text{km}^2$ per decade, even though its hemispheric duration showed no statistically significant trend [Li et al., 2021b]. Furthermore, *in situ* measurements indicated that total zero-curtain days shortened across most natural biomes, except in croplands [Yang et al., 2025]. The frequency of near-surface transitional (zero-curtain) days increased in the continental Arctic but decreased in warmer subpolar coastal zones [Migala et al., 2025]. While varying observational methodologies and state definitions can lead to discrepancies between individual studies, the overarching consensus indicates that the frequency and duration of completely unfrozen phases are lengthening across the hemisphere [Li et al., 2021b, Yang et al., 2024, 2025, Smith et al., 2004, Migala et al., 2025].

The spatiotemporal dynamics of seasonally frozen ground are governed by a complex, non-linear interplay between atmospheric thermal forcing—primarily near-surface air temperatures [Li et al., 2021b]—and localized surface conditions, specifically vegetation density, antecedent soil moisture, and snow cover [Cheng et al., 2007, Zhang et al., 2021b]. To disentangle these overlapping environmental controls across large spatial scales, recent macro-scale studies have

increasingly relied on advanced statistical frameworks and machine learning architectures. For instance, hemispheric-scale partial correlation analyses isolated air temperature and snowpack as the dominant drivers dictating the duration and spatial variance of soil freeze–thaw (FT) cycles by mathematically separating their overlapping effects [Li et al., 2021b]. Similarly, the application of spatial machine learning techniques, such as gradient boosting regression, proved effective in quantifying the relative importance of these physical drivers [Zheng et al., 2020]. These predictive models demonstrated that while surface temperatures fundamentally dictate the spatial distribution and depth of freezing, structural surface variables act as critical secondary modifiers that alter localized thermal conductivities and phase-change heat capacities.

The dynamics of soil FT cycles govern a vast spectrum of Earth processes—ranging from global energy balances and groundwater hydrology [Hayashi, 2013, Sokratov and Barry, 2002] to local infrastructure [Kreyling et al., 2007], with particularly critical consequences for soil respiration and terrestrial carbon fluxes [Johnston et al., 2014, Knoblauch et al., 2018]. Ecosystem respiration (R_{eco}), which encompasses both autotrophic plant and heterotrophic microbial respiration, is dominated by below-ground processes governed by soil temperature and moisture, particularly during the cold season. During the unfrozen phase, soil temperature is the primary thermodynamic driver of R_{eco} [Tefera et al., 2026, Azizi-Rad et al., 2022], with microbes and roots exhibiting a standard temperature sensitivity (Q_{10}) of 4.6 to 9.4 [Mikan et al., 2002]. However, as temperatures reach freezing, the soil enters the zero-curtain phase. Latent heat stalls thermal decline, and the conversion of liquid water to ice fundamentally alters ecosystem controls. Liquid water content (LWC) abruptly overtakes temperature as the master variable, governing up to 87% of flux variability [Mavrovic et al., 2023]. Advancing ice fronts physically squeeze and trap existing CO_2 [Elberling and Brandt, 2003, Wang et al., 2020] while inducing a "freezing drought" that subjects microbes to severe desiccation and osmotic stress [Stenberg et al., 1998]. Because traditional models rely solely on temperature, the apparent Q_{10} artificially spikes to between 16.0 and 237 [Mikan et al., 2002, Du et al., 2013]. This anomaly is not a biological reaction to cold, but a mechanical shutdown caused by LWC depletion [Panikov et al., 2006]. Once liquid water is depleted, the soil crosses into the strictly frozen phase. Control reverts to soil temperature, which governs the slow decay of remaining cold-adapted microbial activity [Panikov et al., 2006], and the Q_{10} stabilizes at a baseline of 3.5 [Du et al., 2013]. Collectively, this cold season is now recognized as a major contributor to the global carbon cycle, accounting for roughly % to 50% of total annual CO_2 fluxes [Elberling and Brandt, 2003, Zona et al., 2015, Wang et al., 2020]. Synthesizing these mechanics, it becomes clear that R_{eco} mirrors the physical state of the soil, transitioning through three distinct phases: the unfrozen phase, the zero-curtain phase, and the strictly frozen phase.

While categorical three-phase FT products (e.g., frozen, zero-curtain, unfrozen) have advanced

our ability to map seasonal boundaries, their landscape-scale application across North America remains limited. Specifically, the spatiotemporal variability of the zero-curtain period and the environmental variables driving its duration are not fully understood. To address this gap, this study evaluates non-binary FT dynamics across North America using a newly developed multi-frequency model (FT-CUSTOM). We first establish a spatial baseline of frozen, zero-curtain, and unfrozen days across core biomes. Subsequently, we deploy a machine-learning attribution framework (XGBoost with SHAP analysis) at both global and biome-specific scales to quantify the primary environmental controls dictating frozen ground duration, and to identify how these dominant physical drivers shift across distinct biomes. Finally, to elucidate the mechanistic relationship between frozen ground dynamics and carbon fluxes, we leverage the continuous Frozenness Index (D) derived from the FT-CUSTOM retrievals. By applying piecewise regression and boundary line analysis to AmeriFlux R_{eco} data, we demonstrate how this continuous dielectric signal tracks the exponential decay of respiratory potential, ultimately revealing the tipping points of cold-season R_{eco}.

4.3 Data and Methods

4.3.1 Study Domain and Spatial Stratification

The spatial domain of this study focused on North America (north of $\sim 48^{\circ}$N). To ensure the integrity of the terrestrial passive microwave signal, grid cells with a permanent open water fraction exceeding 25% were removed. All datasets utilized in this study were harmonized, reprojected, and resampled to the 9 km EASE-Grid 2.0 Northern Hemisphere projection (EPSG: 6931) to maintain pixel-to-pixel spatial correspondence. Because the mechanisms driving soil freezing (e.g., surface roughness, canopy closure, soil organic matter) vary across ecosystems, the analysis was stratified by terrestrial biome [Yang et al., 2025]. Land surface classifications were extracted from the MCD12Q1 MODIS Land Cover Type product using the University of Maryland (UMD) classification [Friedl and Sulla-Menashe, 2022]. The continuous landscape was aggregated into five core representative biomes: Croplands (Class 12), Mixed/Coniferous Forests (Classes 1–5), Boreal Forests (Classes 8–9), Boreal Tundra (Classes 6–7), and Tundra (Class 10).

4.3.2 Passive Microwave Freeze–Thaw Data Records

To identify the frequency and phenology of seasonally frozen ground, two passive microwave FT data records spanning from August 2015 to August 2024 were employed. The primary dataset utilized a custom multi-frequency FT retrieval algorithm derived from Advanced Microwave Scanning Radiometer (AMSR) and Soil Moisture Active Passive (SMAP) observations (hereafter

FT-CUSTOM). FT-CUSTOM ingests two normalized microwave indices computed from these sensors: the Normalized Polarization Ratio (Z_{NPR}), derived from multi-frequency AMSR brightness temperature polarization differences, and the Normalized Spectral Difference (Z_{NDV}), a cross-sensor index integrating AMSR higher-frequency channels with SMAP L-band observations. For each of the five biomes, a logistic regression classifier was trained on these two indices to discriminate three surface states: unfrozen, zero-curtain (transitional), and strictly frozen. Training was conducted on spatially blocked samples identified via DBSCAN clustering to mitigate spatial autocorrelation during cross-validation, and the resulting biome-specific decision boundaries were validated against an independent consensus of established FT products. The continuous Frozenness Index (D) is defined as each observation's standardized distance from its biome's logistic decision boundary, with D_{lower} and D_{upper} representing the 10th and 90th probability thresholds scaled by a factor of 0.5, delineating the onset and end of the zero-curtain phase, respectively. To corroborate findings and ensure algorithm independence, the SMOS L3 FT product (morning/AM overpasses) was used as an auxiliary dataset [hereafter FT-SMOS; Rautiainen et al., 2025]. All analyses conducted on the FT-CUSTOM product — including spatial frequency mapping, phenology extraction, trend analysis, and XGBoost attribution — were independently replicated on the FT-SMOS product; corroborating results are provided in the Appendix for reference. To capture continuous fall freeze-up and spring thaw cycles without bisecting the winter period, a "season year" was defined as spanning from August 1 to July 31 of the following calendar year.

4.3.3 Phenology Extraction and Frequency Metrics

Using the FT products (FT-CUSTOM and FT-SMOS), annual frequency and phenology metrics were calculated for each grid cell. The total frozen ground frequency per season year was calculated as the aggregate sum of zero-curtain and strictly frozen days. To allow for nuanced sub-seasonal analyses, the frequency of the strictly frozen and zero-curtain phases was also quantified independently. Because the FT products used in this study exhibit minimal day-to-day noise, the aggregate count of days assigned to each phase per season year closely approximates the true time spent in that state. Accordingly, *frequency* and *duration* are used interchangeably when referring to per-season-year day counts, except for cold-season duration, which is defined as the continuous interval between end of the growing season (EOS) and start of the growing season (SOS) (Fig. S9). To mitigate sensor gaps, these aggregations were restricted to grid cells with valid daily observations for at least 80% of the season year. Freeze and thaw phenology dates were established using a temporal persistence method to filter out transient weather events. The end of the growing season (EOS) was defined as the onset date of the first period in the season

year where the soil phase remained continuously frozen or zero-curtain for ≥ 10 consecutive days [Li et al., 2021b]. Conversely, the start of the growing season (SOS), constrained to the spring and summer months (January–June), was defined as the onset date of the first period where the soil phase remained continuously unfrozen for ≥ 10 consecutive days.

4.3.4 Spatiotemporal Trend Analysis

To quantify recent climatological shifts in the FT regime, robust grid-wise temporal trend analyses were conducted on the frequency of strictly frozen, fall and spring zero-curtain ground, SOS, and EOS. A non-parametric Mann-Kendall (M-K) trend test was employed to evaluate the statistical significance of monotonic trends. The magnitude of these temporal shifts was subsequently quantified using Sen's slope estimator. Trends were calculated globally across the North American domain and across the five core biomes to assess regionally distinct shifts in frozen and zero-curtain frequencies.

4.3.5 Environmental Predictors of Frozen Ground

To attribute spatial variance and temporal trends in total frozen ground frequency to specific physical controls, a suite of atmospheric, cryospheric, biological, and edaphic predictors was assembled. To strictly isolate true physical drivers and avoid algorithmic circularity, the initial feature space was rigorously pruned. Highly collinear variables were excluded based on Pearson correlation matrices, variance thresholds, and Mutual Information (MI) scores (feature selection metrics and the final correlation matrix are provided in Appendix S1.1). Finalized predictors were categorized into two functional groups: dynamic thermodynamic forcing and static structural modifiers. Dynamic variables included seasonal mean air temperatures from ERA5 [C3S, 2018] and seasonal snow water equivalent (SWE) [C3S, 2018], which were retained to capture pure thermal forcing and the thermal buffering capacity of the snowpack [Zhang et al., 2021b, Zhang, 2005]. Antecedent fall median soil moisture (SMAP Enhanced L3) [ONeill et al., 2020] was included to capture the pre-freeze hydrological state and latent heat dynamics [Li et al., 2021a]. Conversely, biological, topographic, and edaphic variables served as static structural constraints. Normalized Difference Vegetation Index (NDVI) amplitude—calculated as the difference between maximum summer and minimum fall NDVI (MODIS MOD13C2) [Didan, 2021]—was deployed to capture the magnitude of seasonal phenological variation. This allowed the model to differentiate structurally stable pixels (e.g., evergreen canopies, barren terrain) from those undergoing drastic seasonal transitions (e.g., deciduous stands, croplands), accounting for their distinct thermal buffering capacities [Cheng et al., 2007]. Finally, geographic variables (elevation, Terrain Ruggedness Index, latitude/northing) and soil properties accounted for baseline

spatial constraints and sub-grid microclimatic effects. Sand and clay fractions, together with soil organic carbon (SOC) concentration (reported in $\mathrm{dg\,kg^{-1}}$), were all extracted from the ISRIC SoilGrids v2.0 product at the 0–5 cm depth interval [Poggio et al., 2021]. SOC concentration was included as a proxy for the thermal and hydrological buffering capacity of the near-surface organic horizon, which is known to strongly modulate soil freeze–thaw dynamics in boreal and tundra ecosystems [Cheng et al., 2007, Li et al., 2021a]. We note that organic layer thickness — the physically more relevant variable for soil thermal buffering in boreal and tundra systems — is not available at 9 km resolution; SOC mass fraction is therefore used as an imperfect proxy.

4.3.6 Machine Learning Attribution and SHAP Analysis

An ensemble decision-tree machine learning architecture (XGBoost) was deployed to untangle the nonlinear interactions driving freeze duration [Chen and Guestrin, 2016]. A rigorous temporal cross-validation protocol (leave-P-years-out) was implemented, iteratively training models on a randomized subset of years and validating on strictly unseen, hold-out years. The training data was randomly undersampled to an equal number of pixels per landcover class to prevent class imbalance from skewing the model toward dominant biomes. Feature attribution was quantified using SHapley Additive exPlanations (SHAP), with mean absolute SHAP values extracted to rank the predictive power of each environmental variable [Lundberg and Lee, 2017]. This SHAP attribution framework was applied both globally (incorporating landcover as an encoded feature) and locally via independent, biome-specific XGBoost models to investigate regime shifts in physical controls across latitudes.

4.3.7 AmeriFlux Data and Frozenness Index Definition

To evaluate the ecological relationship between continuous soil freezing dynamics and actual carbon fluxes, this study utilized the microwave-derived frozenness index (D). Here, D serves as a continuous metric of the soil physical state, bounded by two empirical reference baselines: D_{lower} and D_{upper}, which represent the unfrozen and strictly frozen reference conditions, respectively. By quantifying the thermodynamic gradient between these two extremes, D effectively captures the gradual depletion of liquid water during the zero-curtain phase. To link this continuous physical index with biological activity, daily *in situ* ecosystem respiration (R_{eco}) observations (specifically the gap-filled `RECO_NT_VUT_REF` product) were obtained from the AmeriFlux FLUXNET dataset [Pastorello et al., 2020]. Tower coordinates were mapped to the 9 km EASE-Grid 2.0 projection, retaining only stations located within the defined North American study domain. Time series were rigorously filtered using quality control flags (`RECO_QC` $\in \{0, 1\}$) to remove artifacts. Furthermore, to prevent observation bias caused by missing data during severe winters, a temporal balance

filter was applied; stations were retained only if they possessed valid R_{eco} observations across all four meteorological seasons.

4.3.8 Piecewise Regression and Boundary Line Analysis

To identify the critical physical thresholds at which the soil frozenness index (D) induces a non-linear regime shift in ecosystem respiration [Du et al., 2013, Azizi-Rad et al., 2022, Tefera et al., 2026], a piecewise regression analysis was implemented. For each biome, daily R_{eco} was regressed against the corresponding satellite-derived D index. An exhaustive breakpoint search was conducted by iteratively splitting the dataset into two segments and fitting separate ordinary least squares (OLS) linear models to each. The optimal breakpoint (threshold) was mathematically defined as the specific D value that minimized the total sum of squared errors across the two fitted regressions. Ecologically, this threshold represented the critical cryospheric phase-change point at which soil microbial and plant root metabolic activities were either effectively suppressed by freezing or reactivated during the spring thaw [Arndt et al., 2019]. Finally, to establish a maximum cold-season flux limit, a boundary line analysis was applied to observations strictly within the cold season. By grouping D values into 0.5-interval bins and fitting an exponential decay function to the 75th percentile of R_{eco}, the theoretical upper envelope of biological activity was quantified as the soil progressively froze.

4.4 Results and Discussion

4.4.1 Baseline Spatial Patterns of the Freeze–Thaw Regime

To establish the baseline spatial dynamics of the seasonal FT cycle, the mean annual frequency of frozen, zero-curtain, and *total frozen ground*, along with phenological timing, was aggregated across five biomes (Table 4.1) and mapped continuously across the North American domain (Fig. 4.1). A complementary baseline map derived from the independent FT-SMOS product was provided for comparison in Fig. S3. As expected, the frequency of the strictly frozen ground generally followed a latitudinal and thermal gradient (Fig. 4.1a). The phenological timing maps further illustrated this dynamic, showing how the EOS propagates southwards (Fig. 4.1c) while the SOS propagates northwards (Fig. 4.1d). The frequency of strictly frozen predictably scaled from its lowest values in southern croplands to its maximum in the high-Arctic tundra. An exception occurred for mixed forests, where fewer strictly frozen days were detected (88.5 days) compared to the more southern croplands (118.7 days); instead, a massive portion of the cold season was allocated to the zero-curtain phase. Indeed, the spatial distribution of the zero-curtain phase exhibited a distinctly non-linear, slightly non-latitudinal pattern (Fig. 4.1b). The zero-curtain

duration peaked dramatically in mid-latitude mixed forests (57.4 days) before collapsing to a minimum in the Arctic tundra (13.7 days).

Croplands represented a known anomaly when compared to natural biomes [Yang et al., 2025]. Because croplands are largely barren in the winter and lack canopy insulation, their soil thermal dynamics are tightly coupled to air temperatures; furthermore, anthropogenic management, such as late-season irrigation, can alter soil moisture and thermal conductivity, causing croplands to freeze more abruptly than adjacent forested areas Yang et al. [2025]. However, it should be noted that the massive accumulation of zero-curtain days in mixed forests was likely exacerbated by known limitations of passive microwave remote sensing Rautiainen et al. [2025]. In a recent study by Yang et al. [2025], sites located in densely forested areas showed the lowest agreement with ground-truth observations. The dense canopy and multilayered vegetation cause surface heterogeneity and increased microwave scattering, which challenges accurate daily state detection and often blurs the distinction between frozen and unfrozen phases.

Furthermore, interannual trends and variability of the frozen, zero-curtain, and total frozen ground frequency and timing are detailed in Appendix S1.3; both FT-CUSTOM and FT-SMOS products showed strong directional agreement despite absolute offsets. Linear trends over this observational window were predominantly non-significant ($p > 0.05$), with the exception of the frequency of frozen days during the fall season in the tundra, which experienced a statistically significant decreasing trend. Although a significant overall decreasing trend in total frozen days was not observed, this specific decrease in fall frozen ground frequency aligns with well-established patterns reported for the Arctic [Smith et al., 2004]. Early remote sensing records reported that the North American tundra growing season was already lengthening by approximately 5.4 days per decade primarily due to delayed fall freezing, while more recent analyses based on air temperatures confirm a universal decline in the frequency of strictly frozen ice days at high latitudes [Migala et al., 2025].

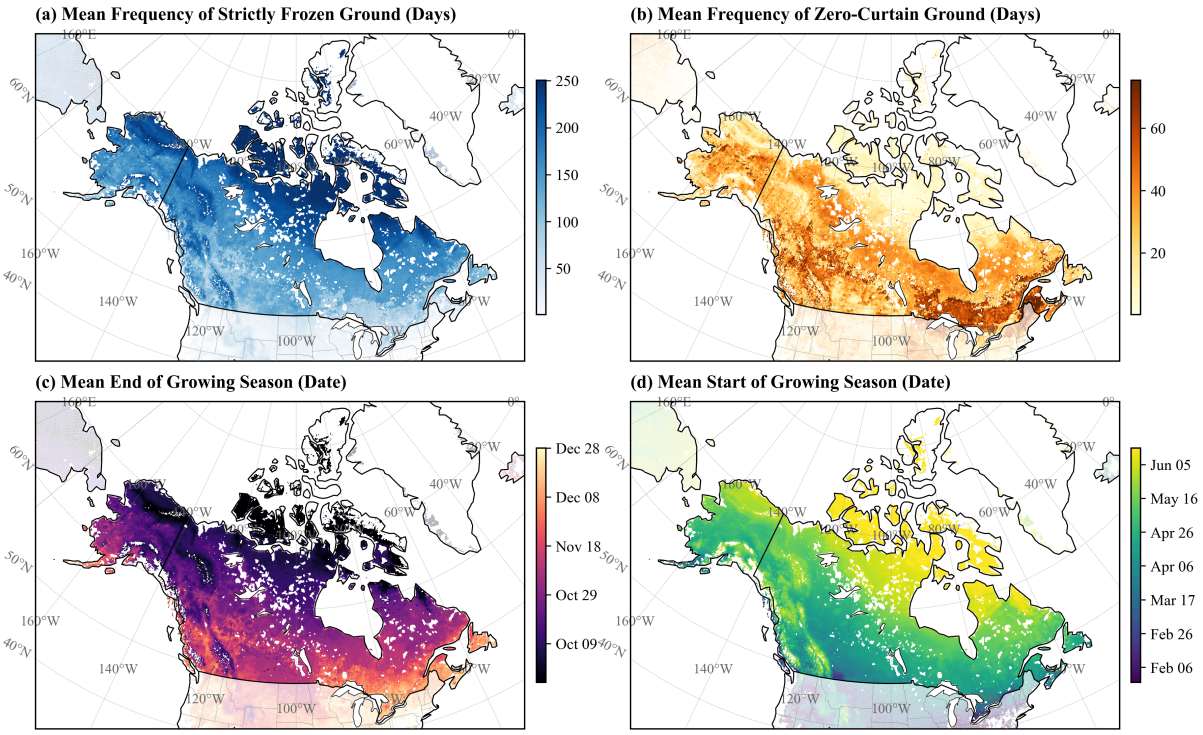


Figure 4.1: These maps display the mean spatial distribution of the freeze–thaw regime across North America (2015–2024) derived from the FT-CUSTOM product. They illustrate the multi-year mean accumulation of (a) strictly frozen days and (b) zero-curtain days. The lower panels display the corresponding mean phenological timing for the (c) end of growing season (EOS) and (d) start of growing season (SOS).

Table 4.1: Mean annual strictly frozen, zero-curtain, and total frozen ground days, alongside climatological freeze and thaw timing by biome, derived from the primary FT-CUSTOM product (2015–2024). Values in parentheses denote the number of zero-curtain days specifically occurring during the fall freeze-up phase. The corresponding FT-SMOS corroboration dataset is provided in Table S1.

Region / Landcover	Strictly Frozen	Zero-curtain (Fall)	Total Frozen	EOS	SOS
Overall	154.5	31.0 (25.1)	185.6	Oct 28	May 04
Cropland	118.7	23.9 (21.1)	142.6	Nov 11	Mar 29
Mixed Forest	88.5	57.4 (43.2)	145.9	Nov 26	Apr 07
Boreal Forest	151.8	31.6 (28.9)	183.4	Oct 31	May 02
Boreal Tundra	203.8	19.1 (17.0)	223.0	Oct 13	May 25
Tundra	215.1	13.7 (8.6)	228.7	Oct 05	May 29

4.4.1.1 Macro-Scale Drivers of the Fall Zero-Curtain Duration

To characterise the macro-scale environmental co-variation of fall zero-curtain duration, we compared biome-aggregated mean values across the five North American ecosystems, with pixel-level distributions shown as ±1 SD error bars (Fig. 4.2). NDVI provided the clearest and most monotonic between-biome separation, increasing from low-vegetation tundra (mean NDVI ≈ 0.20, fall zero-curtain frequency ≈ 10 days) to structurally complex mixed forest (mean NDVI ≈ 0.60, fall zero-curtain frequency ≈ 44 days), consistent with the role of dense canopies in intercepting outgoing longwave radiation and retaining soil moisture, thereby sustaining the latent heat release that prolongs the near-0°C phase-change period [Cheng et al., 2007, Li et al., 2021a]. It is further plausible that NDVI acts as an integrated proxy for surface organic layer thickness, since structurally complex, productive ecosystems accumulate thicker near-surface organic horizons that directly buffer soil thermal dynamics. This interpretation is not contradicted by the negligible biome-scale co-variation of SOC fraction with zero-curtain duration: SOC is measured in the mineral soil fine earth fraction and does not capture the surface organic horizon that governs thermal insulation. NDVI may therefore represent a more ecologically integrated surface indicator of organic layer presence than mineral soil SOC fraction, which explains why it provides the clearest biome-scale separation despite the absence of direct organic layer thickness data.

Fall air temperature and SWE tracked a similar gradient among natural biomes: colder, high-latitude ecosystems accumulated more early-season snowpack yet experienced shorter zero-curtain phases, consistent with the observation that early heavy snowfall in high-latitude environments is associated with rapid freeze-up dynamics rather than thermal buffering [Zhang, 2005, Zhang et al., 2021b]. Clay fraction showed insufficient between-biome variance to be informative, with four of five biomes clustering tightly around 190–200 $\mathrm{g\,kg^{-1}}$. Soil organic carbon did not produce a consistent monotonic pattern across biomes and could not be interpreted as an independent predictor at this spatial scale.

To test whether these between-biome patterns reflect continuous pixel-level physical mechanisms, we conducted within-biome pixel-level regressions for all predictors across all five biomes (Appendix Fig. S10). Within-biome R^2 values were uniformly low across all predictors (maximum $R^2 = 0.13$ for fall temperature within tundra), and this result was consistent when monthly rather than seasonal means were used as predictors, indicating that none of the satellite-derived or reanalysis variables employed here explains a meaningful fraction of spatial variance within any individual biome. These seasonal atmospheric, vegetation, and surface variables effectively discriminate between ecosystem types at the continental scale but lack the spatial granularity to resolve the local controls that likely govern pixel-to-pixel variation in zero-curtain duration, such as snow onset timing, soil organic layer depth, or micro-topographic drainage patterns.

It should further be noted that because FT-CUSTOM was calibrated independently per biome, the between-biome differences in zero-curtain duration reflect both genuine physical landscape differences and algorithm-level biome stratification; the biome-aggregated comparison is therefore best interpreted as descriptive of ecosystem-type co-variation rather than as evidence of any predictor operating as a continuous pixel-scale driver of zero-curtain duration.

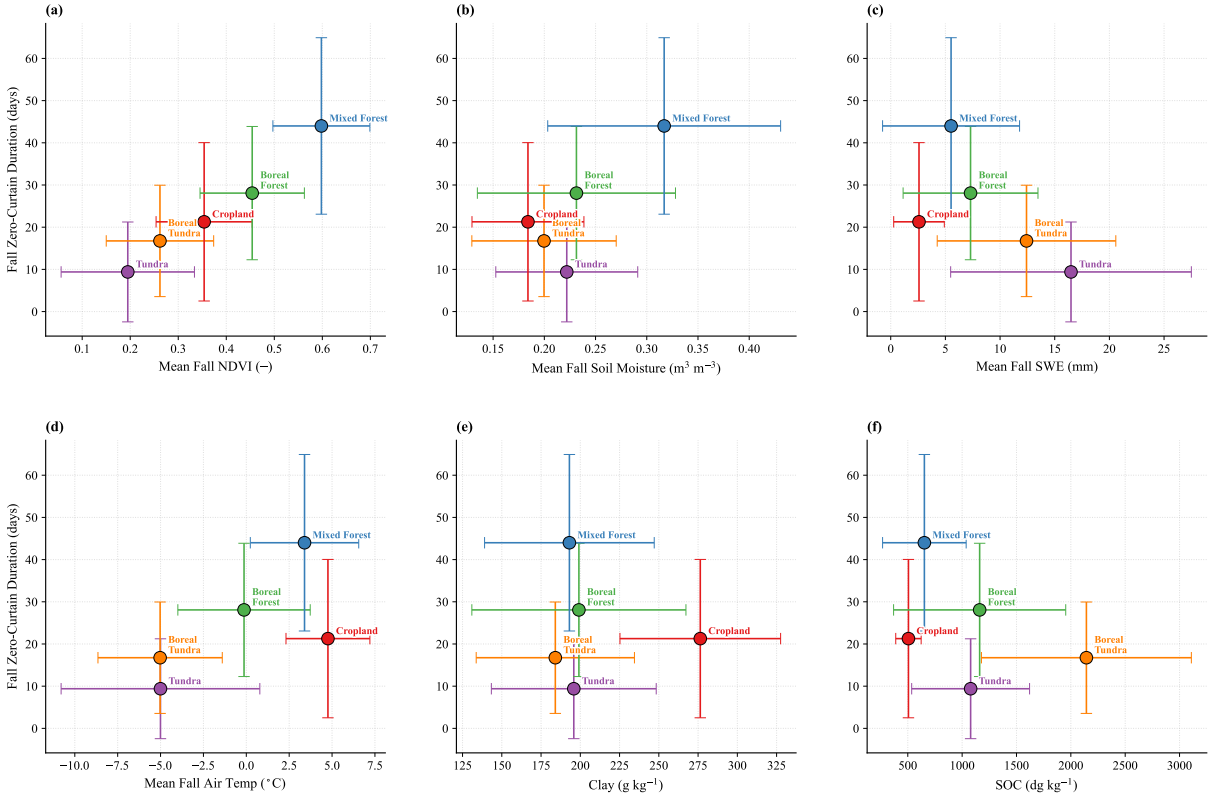


Figure 4.2: Biome-level co-variation between fall zero-curtain duration and six environmental predictors across five North American ecosystems. Each point represents a biome mean; error bars indicate ±1 standard deviation of pixel-level values within each biome. Panels show fall zero-curtain duration against: (a) mean fall NDVI, (b) mean fall soil moisture, (c) mean fall SWE, (d) mean fall air temperature, (e) clay fraction, and (f) soil organic carbon. The figure documents biome-level descriptive patterns rather than pixel-scale mechanistic relationships.

4.4.2 Machine Learning Attribution of Frozen Ground Frequency

4.4.2.1 Global Model Performance and Validation

The predictive capability of the XGBoost architecture was evaluated using a 5-fold temporal cross-validation protocol (leave-3-years-out). As summarized in Table 4.2, the primary global model trained on the FT-CUSTOM record demonstrated robust predictive skill across the entire North American domain. To assess the model's ability to generalize across diverse biome

conditions, we further validated this single global architecture against independent biome-specific subsets. Model accuracy exhibited physically meaningful variations when tested against these subsets, mirroring the structural complexity of the landscape. The global model achieved its highest predictive performance over open-canopy, structurally simple environments like the tundra ($R^2 = 0.897$). Performance gradually degraded when the global model was applied to forested zones (boreal and mixed forests) as canopy attenuation increased, ultimately exhibiting the lowest scores in highly modified, anthropogenic biomes such as croplands ($R^2 = 0.557 \pm 0.087$). To confirm these performance metrics are not an artefact of the FT-CUSTOM retrieval, the full XGBoost analysis was independently replicated using the FT-SMOS product; results are consistent and provided in Appendix S2.

Table 4.2: Cross-validated predictive performance of the XGBoost model trained on the primary FT-CUSTOM target, reported across global and biome-specific domains. R^2 and MAE values represent means ± standard deviation across leave-P-years-out cross-validation folds. The corresponding FT-SMOS product performance is provided in Table S2.

Domain / Biome	R^2	MAE (days)
Global (Overall)	0.894 (±0.013)	11.54 (±0.46)
Tundra	0.897 (±0.023)	11.90 (±1.21)
Boreal Forest	0.772 (±0.020)	10.02 (±0.41)
Boreal Tundra	0.698 (±0.153)	9.60 (±1.87)
Mixed Forest	0.703 (±0.034)	14.06 (±1.27)
Croplands	0.557 (±0.087)	14.50 (±0.73)

4.4.2.2 Global Environmental Drivers (SHAP Analysis)

Global SHAP values were extracted to quantify the relative impact and physical directionality of dynamic predictors on total frozen ground frequency. The global regime is overwhelmingly dictated by direct energy and mass fluxes. Mean spring and mean fall temperatures act as the undisputed primary controls, exerting average impacts of 17.5 and 12.1 days, respectively. This hierarchy aligns with hemispheric partial correlation analyses demonstrating that near-surface air temperature is the primary driver of soil freeze–thaw spatiotemporal variations [Li et al., 2021b]. Both temperature variables exhibited a strict negative correlation, where cooler temperatures linearly prolonged the frozen season. Mean summer temperature followed with a smaller negative impact, indicating a "thermal memory" effect. Higher atmospheric temperatures during the off-season pump thermal energy deep into the soil profile; when fall cooling begins, the ground must first dissipate this stored residual heat before phase change can occur, thereby delaying the onset of freezing and shortening the total duration. This thermodynamic memory corroborates

spatial machine learning regressions, which demonstrated that off-season surface temperatures act as critical controllers limiting winter frost severity [Zheng et al., 2020]. Mean winter temperature also ranked in the top five, demonstrating a moderate influence on frozen duration.

Crucially, SWE emerged as the dominant physical surface control. Both fall SWE (2.7 days) and spring SWE (1.9 days) exhibited positive correlations, confirming that a larger snowpack actively buffers the soil against thermal transitions and acts as a massive heat sink during the spring melt; the latent heat required to melt this accumulated snow consumes incoming solar radiation, effectively delaying the soil thaw and extending the total perceived frozen duration [Zhang, 2005, Zhang et al., 2021b].

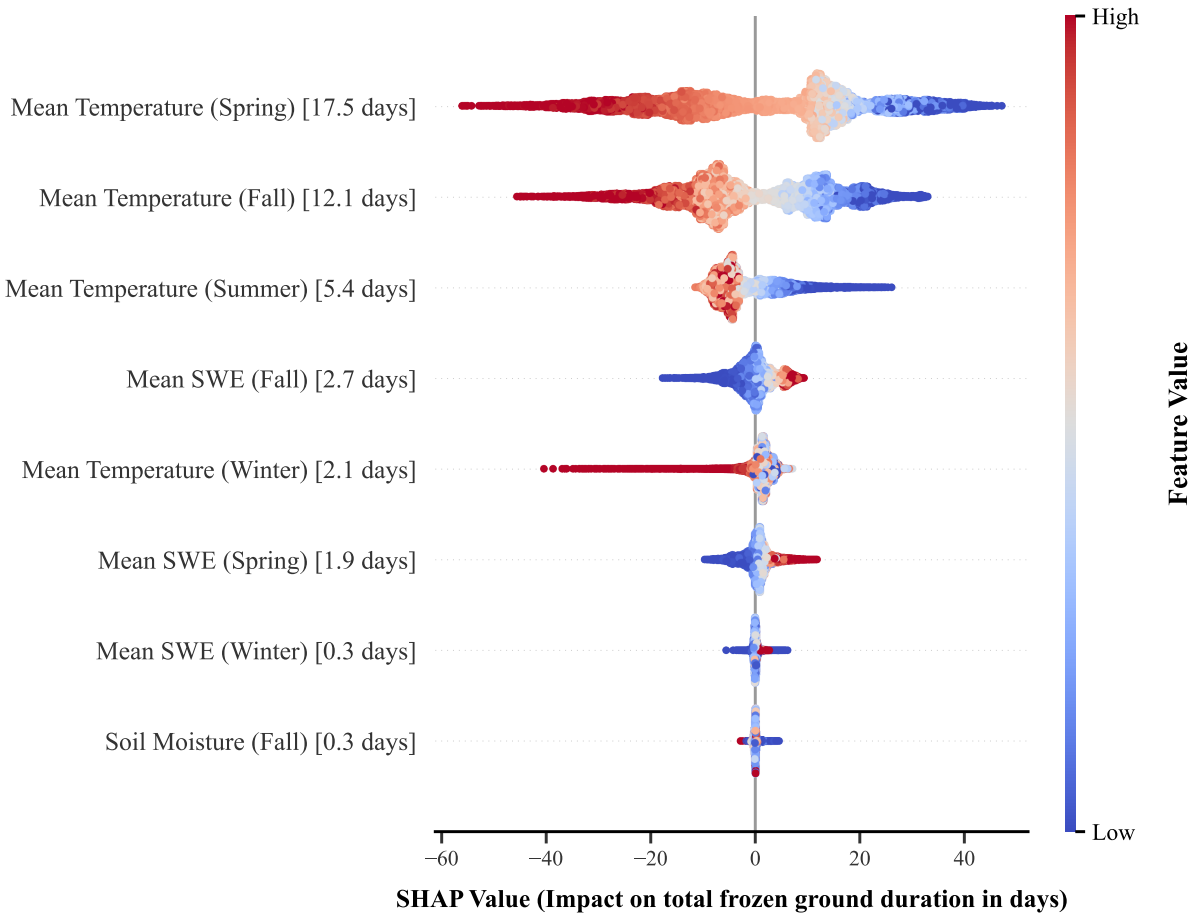


Figure 4.3: A SHAP summary beeswarm plot visualizes the primary global machine learning model (trained on the FT-CUSTOM target). Predictors are ranked on the y-axis by their mean absolute SHAP value, representing their average impact on the predicted total frozen duration (annotated in brackets). The x-axis illustrates the specific impact of individual pixel observations on the model output, measured in days. Dot color represents the raw feature value from low (blue) to high (red).

4.4.2.3 Biome-Dependent Shifts in Driver Importance

The biome-specific performance reported Table 4.2 reflects the generalization ability of the single global model when tested against independent biome subsets. To isolate the unique physical controls governing each ecosystem and enable unconfounded SHAP attribution, we additionally trained independent biome-specific XGBoost models (excluding landcover as a feature). These dedicated models, optimized within each biome's feature distribution, provided a more targeted decomposition of driver importance (as visualized in Fig. 4.4). In open-canopy, high-latitude environments, FT dynamics were almost exclusively dictated by atmospheric thermal forcing [Li et al., 2021b]. Within the tundra, the model ranked spring temperature (15.9 days) and fall temperature (12.4 days) as the dominant drivers. Furthermore, summer temperature emerged as the third most important feature; because the cold season is longer and begins earlier at these latitudes, pre-conditioning the soil via summer heating plays a highly pronounced role [Zheng et al., 2020].

A distinct regime shift occurred in structurally complex, forested biomes. In the mixed forest, atmospheric forcing was significantly dampened, with spring and fall temperatures reduced to 7.0 and 7.2 days, respectively. Canopy interception of outgoing radiation mutes the direct thermal forcing on the soil [Cheng et al., 2007]. Consequently, thermodynamic control shifted to the sub-canopy surface layer, causing fall and spring SWE to emerge as critical drivers (exerting positive impacts of 5.3 and 4.2 days, respectively).

In the boreal forest, the model identified NDVI amplitude as a highly specific structural indicator of canopy type, assigning a positive delay to the frozen frequency. Rather than indicating sparse vegetation, a high phenological amplitude in this region differentiates deciduous broadleaf stands from evergreen coniferous stands. The model physically recognized that leafless deciduous canopies permit greater sub-canopy snow accumulation (higher ground-level SWE) and lack the early-spring, low-albedo thermal warming provided by dark evergreen needles [Cheng et al., 2007]. Consequently, the algorithm correctly attributed a slightly longer frozen frequency to high-amplitude deciduous pixels due to the enhanced thermal buffering of deeper, shaded snowpacks.

Finally, the independent cropland model exhibited the lowest predictive performance (R^2 = 0.474). Because croplands generally occupy lower latitudes with a delayed cold season, winter and spring temperatures were the primary drivers, closely followed by fall. The severe degradation in model accuracy highlighted a fundamental reality: anthropogenic practices disrupt natural thermodynamic relationships [Yang et al., 2025]. High absolute errors indicated that total frozen frequency in these regions is influenced by agricultural practices—such as fall plowing, crop residue management, and tile drainage—which alter soil thermal conductivity and moisture retention, ultimately making predictions significantly less reliable.

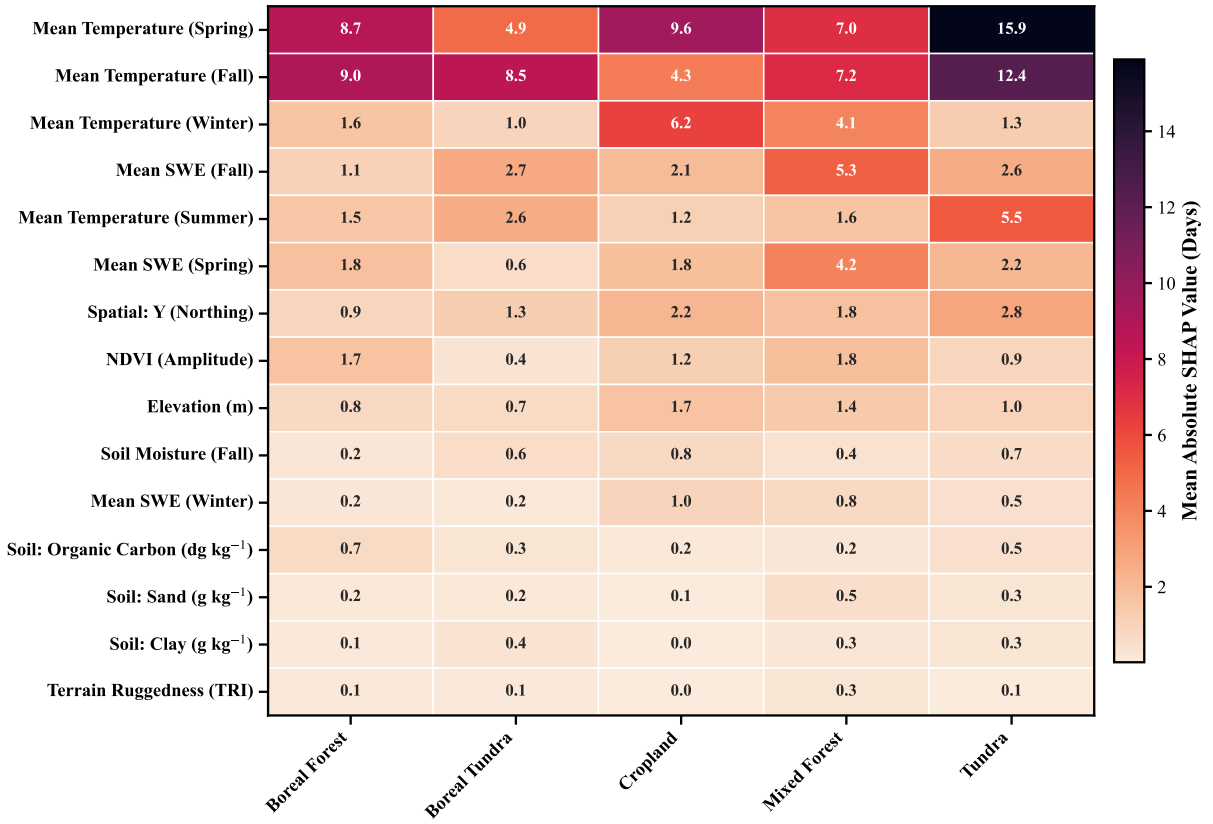


Figure 4.4: A heatmap depicts the shifting mean absolute SHAP values (impact in days), stratified by distinct structural landcover classes. Color intensity indicates the magnitude of each environmental predictor's influence on the total frozen ground duration. The visualization highlights a critical regime shift: while atmospheric temperatures strictly dominate the freeze–thaw dynamics in open biomes like the tundra, the relative influence of structural modifiers such as snow water equivalent (SWE) and vegetation density increases significantly in complex forested environments.

4.4.3 Mechanistic Linkage Between the Frozenness Index and Ecosystem Respiration

The Frozenness Index (D) is derived by calculating the distance of each observation to the decision boundary in our logistic regression FT machine learning model. We established lower (D_{lower}) and upper (D_{upper}) thresholds such that values below D_{lower} indicate an unfrozen phase, values above D_{upper} indicate a strictly frozen phase, and intermediate values represent the zero-curtain phase. While previous analysis has demonstrated that the zero-curtain phase identified by the satellite-derived D index effectively anchors to soil temperatures near 0°C, we demonstrate its direct mechanistic coupling to ecosystem biological activity. Across the evaluated biomes, the optimal metabolic breakpoint identified via piecewise regression on ecosystem respiration (R_{eco}) aligns exceptionally well with the satellite-derived lower boundary (D_{lower}), which marks the

onset of the zero-curtain phase in our model. Biologically, this statistical breakpoint represents a fundamental regime shift: it signifies the end of the thermally governed, unfrozen active phase and the abrupt initiation of a "freezing drought." During the unfrozen phase, soil temperature acts as the primary thermodynamic driver of microbial activity and CO_2 production, though fluxes remain co-limited by secondary environmental factors such as substrate availability and root dynamics [Azizi-Rad et al., 2022, Tefera et al., 2026]. This spatial co-occurrence illustrates that the physical onset of the freezing process directly gates biological activity.

This linkage is visually confirmed by the integration of independent, ground-measured soil temperature (T_{soil}) data; the continuous thermal overlay on the scatter plots, alongside the T_{soil} distributions in Fig, 4.6, reveals that the intermediate zero-curtain zone anchors strictly to near-0°C conditions. It is worth noting that in cropland ecosystems, the freeze–thaw transition behaves more as a binary process. The soil rapidly transitions from unfrozen to frozen, effectively bypassing a prolonged zero-curtain phase. This behavior aligns with our prior observation that cropland soil temperatures for both the zero-curtain and strictly frozen ground share nearly identical distributions. This rapid transition is physically consistent with typical agricultural environments, which lack the insulating layers of organic matter or snow found in forests and are often well-drained, depriving the soil of sufficient moisture to sustain the latent heat release necessary for a gradual temperature decline. Ultimately, by matching the structural breakpoint in R_{eco} with D_{lower}, we demonstrate that passive microwave indices can successfully detect the critical landscape-scale tipping point where ecosystem respiration decouples from temperature and becomes constrained by the physical freezing of soil water.

As the soil enters this zero-curtain phase, the ecosystem hits a physical bottleneck where ice formation severely restricts substrate diffusion [Mavrovic et al., 2023]. To isolate how this specific cryospheric limitation constrains fluxes, we applied a boundary line analysis (75th percentile envelope) to the cold season following the piecewise threshold. In unfrozen conditions, R_{eco} displays high variance because it is co-limited by multiple factors (e.g., substrate availability, solar radiation, gross primary production), meaning the ecosystem rarely operates at its theoretical thermal maximum [Azizi-Rad et al., 2022]. However, as freezing initiates, the progressive depletion of liquid water imposes an absolute thermodynamic ceiling. The resulting rapid, exponential decay of the maximum R_{eco} limit across all biomes confirms this phase change as a hard boundary on microbial metabolism. Because ice formation induces severe osmotic stress and structurally blocks extracellular diffusion [Panikov et al., 2006, Stenberg et al., 1998], maximum biological potential cannot exceed these cryospheric moisture limits, regardless of organic matter availability.

Because D is derived from microwave brightness temperatures, it is fundamentally sensitive to shifts in the soil's dielectric constant. By tracking the relative magnitude of this dielectric

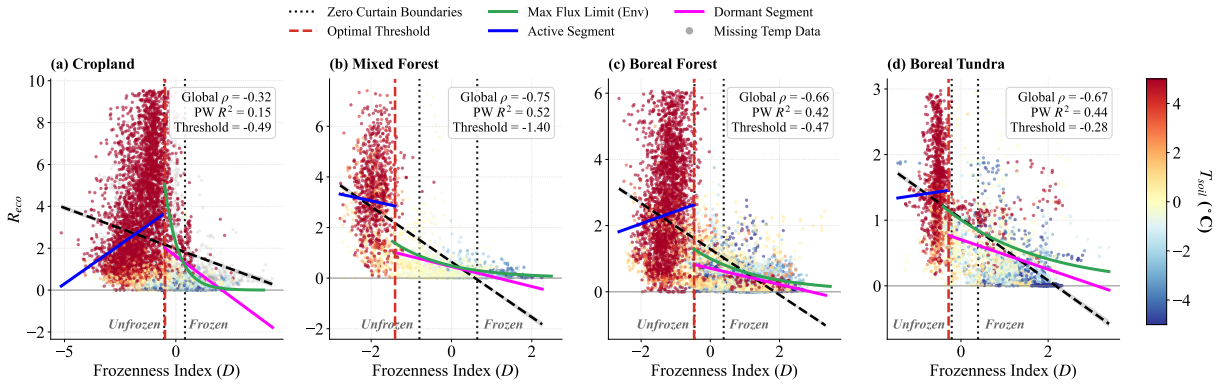


Figure 4.5: Scatter plots demonstrate the relationship between ecosystem respiration (R_{eco}) and the passive microwave Frozenness Index (D) across four biomes: (a) cropland, (b) mixed forest, (c) boreal forest, and (d) boreal tundra. The optimal threshold identified by piecewise regression (red dashed line) aligns closely with the lower boundary (D_{lower}, left dotted line), marking the onset of the zero-curtain phase. Data points are color-coded by ground-measured soil temperature (T_{soil}), illustrating that the zero-curtain zone anchors strictly to near-0°C conditions. The green line represents the maximum flux limit (75th percentile envelope) mapping the exponential decay of respiratory potential.

shift, D acts as an effective, landscape-scale proxy for the severity of soil freezing. Consequently, it successfully maps the exponential extinction of theoretical biological capacity driven by the progressive depletion of residual LWC. This physical–biological linkage is further corroborated by the distributional box plots, which demonstrate a clear, step-wise down-regulation of R_{eco} as the landscape progresses from the unfrozen, into the zero-curtain, and finally to the strictly frozen phase. Accurately capturing the progression into this deeply frozen phase is critical; as demonstrated by Wang et al. [2020], explicitly incorporating the zero-curtain duration and its associated latent heat dynamics significantly enhances terrestrial biosphere model performance when predicting cold-season CO_2 emissions. Furthermore, the magnitude of winter freezing ultimately dictates the dynamics of the subsequent spring thaw. As Zhang et al. [2021a] demonstrated, severe freezing (below -5°C) acts as a mechanical reset, physically bursting microbial cells and trapping gases to fuel a massive spring CO_2 burst that increases respiration by an average of 18.8% upon thawing. Because the continuous D index serves as a proxy for the severity of the freezing drought, future studies should investigate the relationship between the magnitude of deep-winter D values and spring thaw burst magnitude. Establishing this link would further validate the ecological relevance of the D index, positioning it not merely as a monitor of cold-season dormancy, but as a predictive tool for quantifying massive, transitional carbon release.

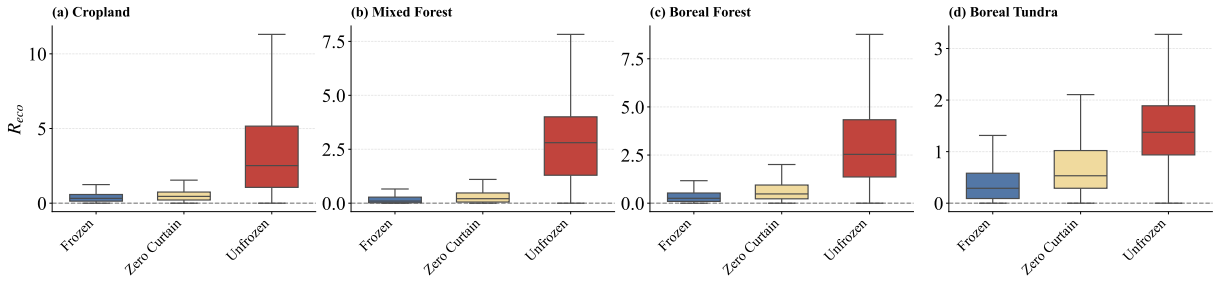


Figure 4.6: Distributional box plots illustrate ecosystem respiration (R_{eco}) categorized by soil phases (strictly frozen, zero-curtain, and unfrozen) across the four evaluated biomes. The distributions display a clear, step-wise down-regulation of biological activity as the landscape progresses through the freezing phase change, culminating in a deeply dormant phase with minimal flux variance during the strictly frozen period.

4.5 Conclusion

This study provides a biome-resolved characterization of North American freeze–thaw dynamics and their physical drivers, while establishing a direct mechanistic linkage between the passive microwave cryospheric state and ecosystem carbon flux. Spatial analysis of the zero-curtain phase reveals that its duration is not primarily a function of latitude or atmospheric temperature, but instead co-varies most strongly with the structural and hydrological properties of the land surface at the biome scale. Fall vegetation density (NDVI) showed the clearest and most monotonic between-biome co-variation with zero-curtain duration, increasing from sparse tundra to structurally complex mixed forest, while fall air temperature and snowpack tracked a similar gradient among natural biomes. This co-variation likely reflects a compound signal: direct canopy insulation of the soil surface and an indirect integration of organic layer thickness, since productive ecosystems accumulate thicker organic horizons that are not captured by standard mineral soil SOC products. Dense forest canopies intercept outgoing longwave radiation and retain soil moisture, thereby sustaining the latent heat release required to prolong the near-0°C phase transition; barren tundra surfaces, lacking this insulative architecture, decouple rapidly from atmospheric forcing and freeze almost instantaneously despite experiencing the most extreme temperatures on the continent. Within-biome pixel-level regressions confirmed, however, that none of the coarse-resolution seasonal variables employed here explains a meaningful fraction of spatial variance within any individual biome, indicating that ecosystem type acts as a discrete state variable governing zero-curtain duration at the landscape scale rather than any single predictor operating as a continuous pixel-scale driver. This pattern is consistent with the seemingly paradoxical finding that zero-curtain duration peaks in mid-latitude mixed forests (57.4 days) and reaches its minimum in the high-Arctic tundra (13.7 days). The XGBoost attribution framework confirmed that while spring and fall atmospheric temperatures constitute the dominant global

controllers of total frozen ground frequency, their relative influence progressively diminishes in structurally complex biomes. In forested environments, the sub-canopy snowpack emerges as the primary driver of frozen ground duration, physically decoupling the soil from atmospheric thermal forcing and shifting thermodynamic control to the ground surface layer. These biome-dependent regime shifts underscore that continental-scale models relying solely on air temperature as a predictor of frozen ground phenology will systematically underperform in forested landscapes.

Building on these physical characterizations, we demonstrate that the continuous Frozenness Index (D), derived from passive microwave dielectric signatures, successfully detects the critical ecological tipping point at which cold-season ecosystem respiration transitions from temperature-governed to cryospheric state-governed. Across evaluated biomes, the metabolic breakpoint identified by piecewise regression of AmeriFlux R_{eco} against D aligns with the satellite-derived lower zero-curtain boundary (D_{lower}), confirming that the physical onset of ice formation directly gates biological activity. Once freezing initiates, liquid water content supersedes temperature as the master variable controlling respiration, and the exponential decay of the maximum R_{eco} envelope—quantified via boundary line analysis—provides compelling evidence that progressive ice formation imposes a hard thermodynamic ceiling on microbial metabolism. Cropland ecosystems deviated from this pattern, exhibiting a near-binary freeze transition consistent with their low organic insulation and sparse vegetation, high drainage, and moisture-limited latent heat dynamics. These findings carry direct implications for terrestrial biosphere modeling: explicitly representing the zero-curtain phase and its associated latent heat dynamics, rather than treating frozen ground as a discrete on/off state, is necessary to accurately reproduce cold-season CO_2 emissions, which contribute approximately 39–50% of total annual fluxes.

Several limitations warrant acknowledgment. The coarse spatial resolution of the passive microwave retrievals (9 km) constrains the ability to resolve micro-scale interactions between the zero-curtain phase and surface heterogeneity, particularly within structurally complex mixed forests where canopy attenuation reduces retrieval accuracy. The observational record (2015–2024) is insufficient to robustly detect long-term climatological trends beyond specific cases such as the declining fall frozen-day frequency observed in the tundra. Future work should prioritize *in situ* validation of the D–R_{eco} relationship at additional tower sites spanning a broader range of biomes and climate regimes. Furthermore, investigating whether the magnitude of deep-winter D values predicts the intensity of spring thaw CO_2 bursts would establish the D index not merely as a monitor of cold-season dormancy, but as a predictive diagnostic tool for quantifying pulse carbon release during the critical freeze-to-thaw transition.

Funding

This work was supported by the Fonds de recherche du Quebec – Nature et technologies [grant number 330450, [Salmabadi, 2023]]; the Canadian Space Agency [grant number 19FAQCT B19]; the Natural Sciences and Engineering Research Council of Canada (NSERC).

Declaration of Competing Interest

The authors declare that they have no known competing financial interests or personal relationships that could have appeared to influence the work reported in this paper.

Supplementary Material

S1 Extended Results

S1.1 Feature Selection and Correlation Analysis

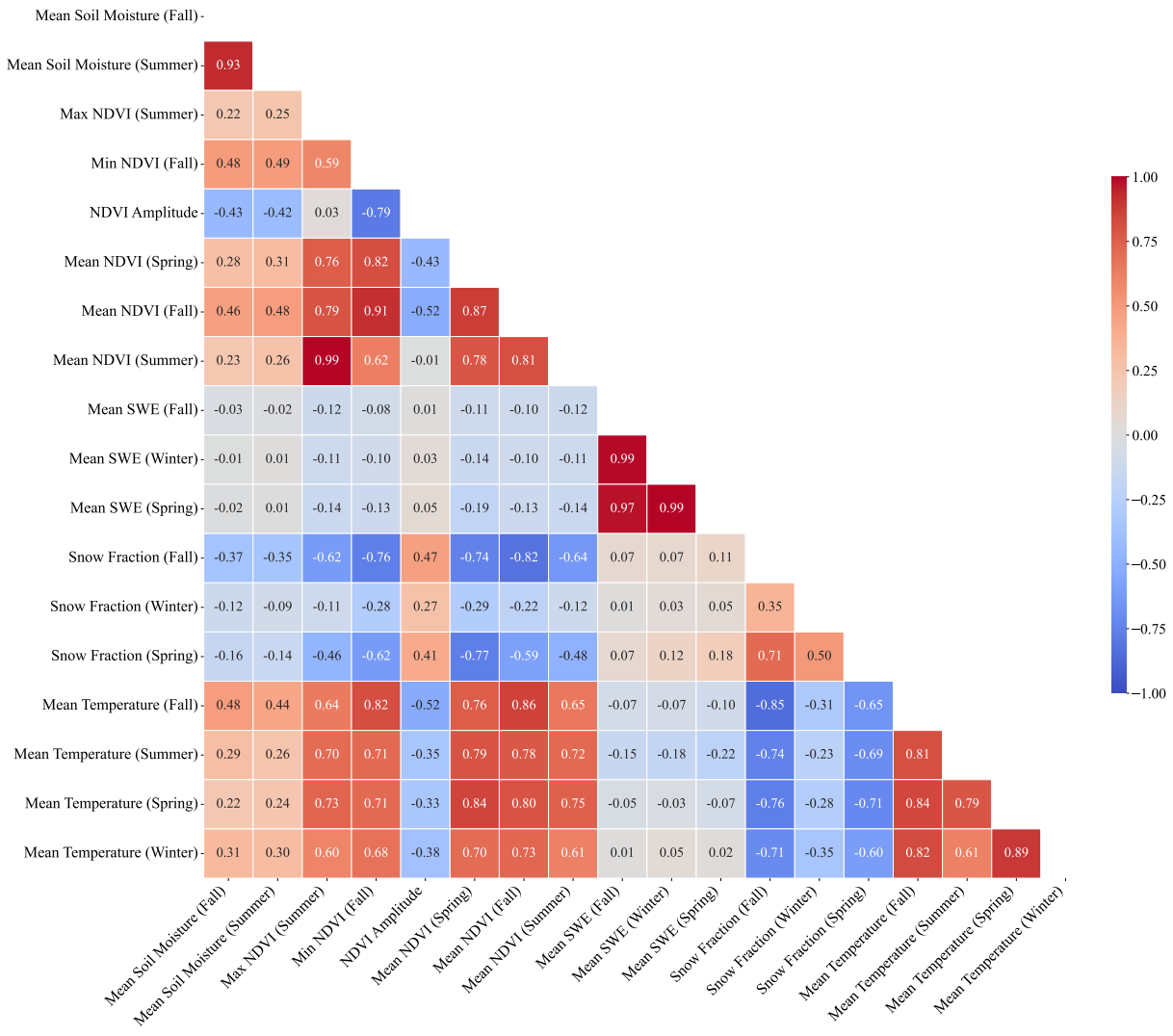


Figure S1: Pearson correlation matrix evaluating multicollinearity among the features. The analysis utilizes the balanced dataset across the targeted landcover classes. Note that the seasonal snow fraction predictors indicate the total number of days with snow cover per season, based on IMS data [Center, 2004]. Detailed descriptions of all remaining features and their original data sources are outlined in the methodology Sect. 4.3.5.

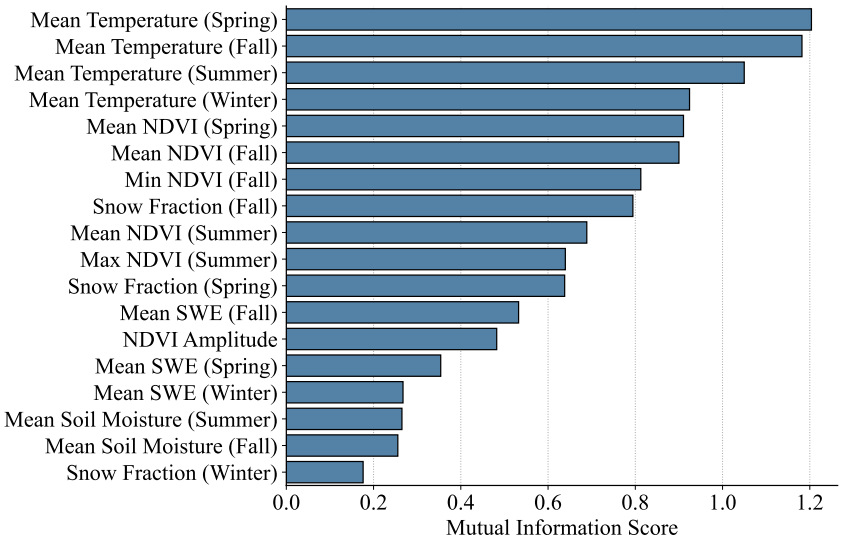


Figure S2: Mutual Information (MI) scores of the selected features relative to the target variable. The dataset was balanced across landcover classes to prevent class imbalance from skewing the information gain. The snow fraction variables represent the number of days per season with snow cover, derived from IMS data [Center, 2004]. Detailed descriptions of all remaining features and their original data sources are outlined in the methodology Sect. 4.3.5.

Table S1: Mean annual strictly frozen, zero-curtain, and total frozen ground days, alongside climatological freeze and thaw timing by biome, derived from the independent FT-SMOS product (2015–2024). Values in parentheses denote the number of zero-curtain days specifically occurring during the fall freeze-up phase. This table is provided as a corroboration of the primary FT-CUSTOM results (Table 4.1); the two products are algorithm-independent and differ in sensor, retrieval architecture, and spatial footprint, so absolute offsets are expected. Interannual directional agreement between the products is discussed in Sect. 3.3.

Region / Landcover	Strictly Frozen	Zero-curtain (Fall)	Total Frozen	EOS	SOS
Overall	162.8	15.4 (10.7)	178.2	Oct 29	Apr 28
Cropland	113.1	17.0 (11.2)	130.1	Nov 14	Mar 19
Mixed Forest	127.4	19.5 (12.8)	146.8	Nov 17	Apr 04
Boreal Forest	161.0	15.0 (10.4)	176.0	Nov 01	Apr 24
Boreal Tundra	203.7	10.2 (8.0)	213.9	Oct 15	May 15
Tundra	201.9	14.7 (11.0)	216.6	Oct 11	May 24

S1.2 Baseline Spatial Patterns of the Freeze–Thaw Regime

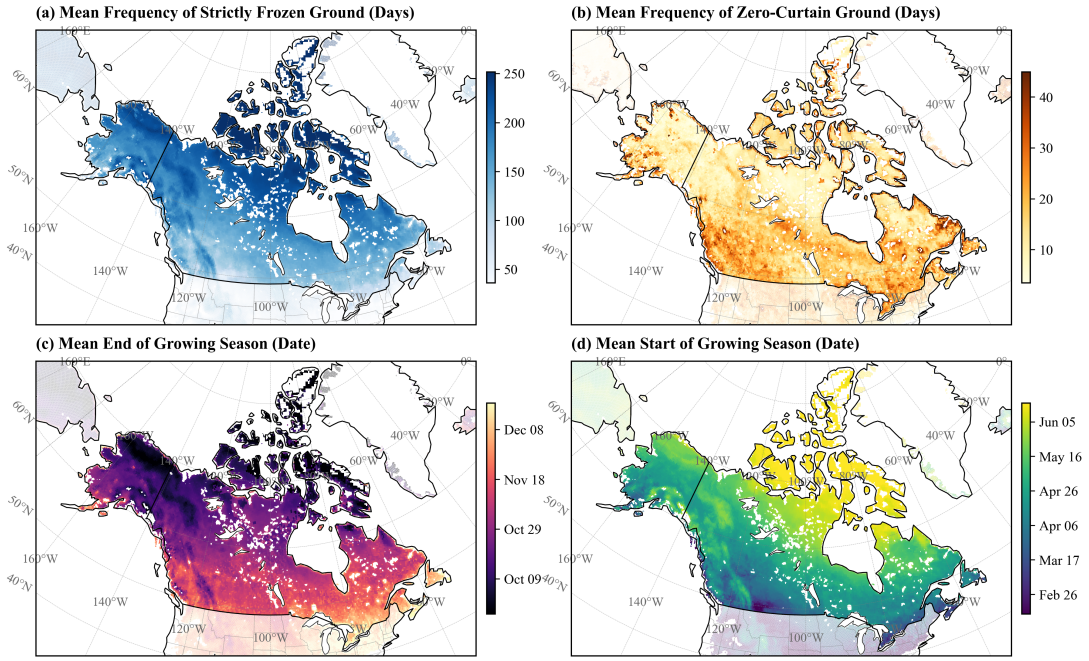


Figure S3: These maps present the mean spatial distribution of the freeze–thaw regime across North America (2015–2024) derived from the FT-SMOS product. They illustrate the multi-year mean accumulation of (a) strictly frozen days and (b) zero-curtain days. The lower panels display the corresponding mean phenological timing for the (c) end of growing season (EOS) and (d) start of growing season (SOS).

S1.3 Interannual Trends and Variability



Figure S4: Annual Mann-Kendall trends indicate the frozen, zero-curtain, and total frozen ground duration in days. Both products capture highly dynamic interannual fluctuations, with predominantly non-significant long-term linear trends across most land covers.

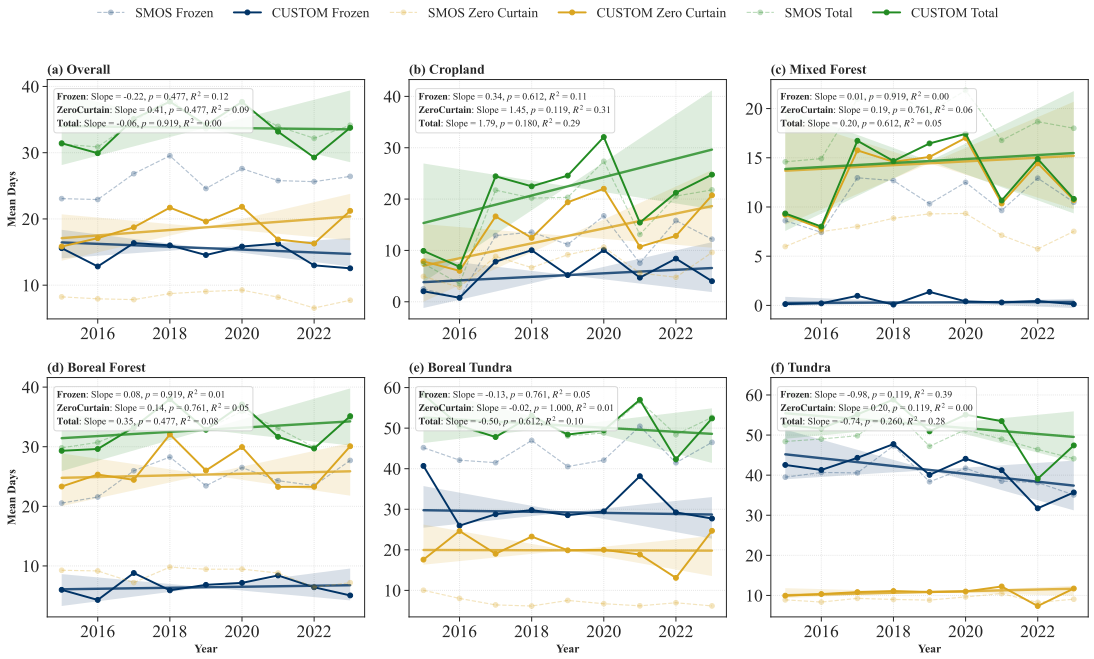


Figure S5: Fall season Mann-Kendall trends indicate the frozen, zero-curtain, and total frozen ground duration in days. The results demonstrate consistent tracking between the CUSTOM and SMOS products alongside high interannual variance. Tundra region exhibits a localized trend in frozen days.



Figure S6: Spring season Mann-Kendall trends replicate the analysis of Fig. S5 for the spring season. The data demonstrate consistent tracking between the CUSTOM and SMOS products alongside high interannual variance, with no significant trends observed.

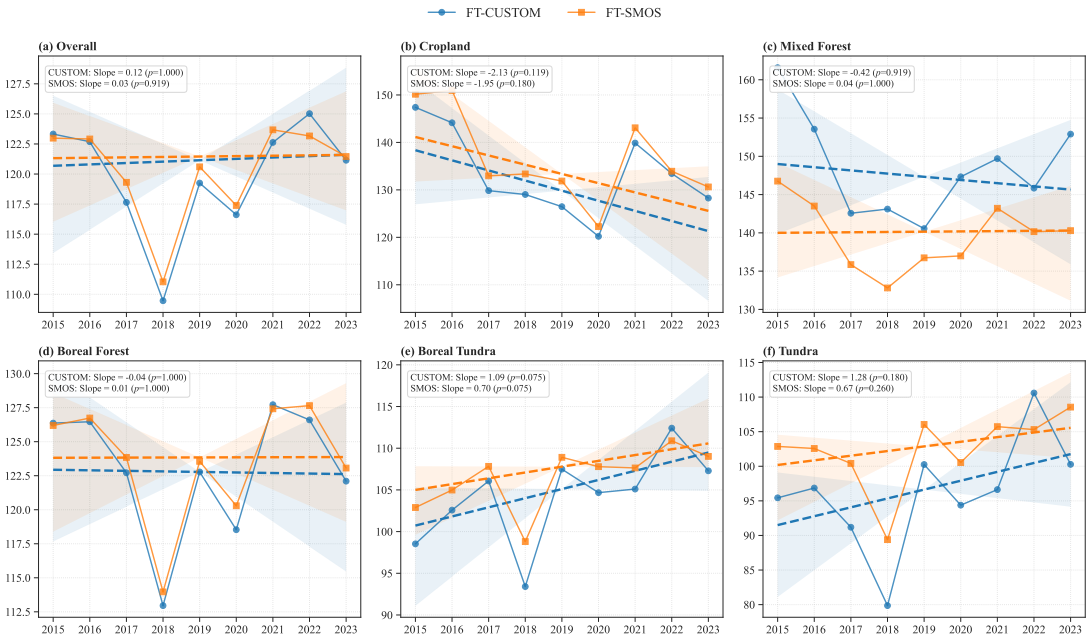


Figure S7: This plot illustrates the interannual variability in the EOS timing (2015–2023). The CUSTOM and SMOS trajectories show excellent agreement in capturing early versus late freeze years, with no significant trends observed.

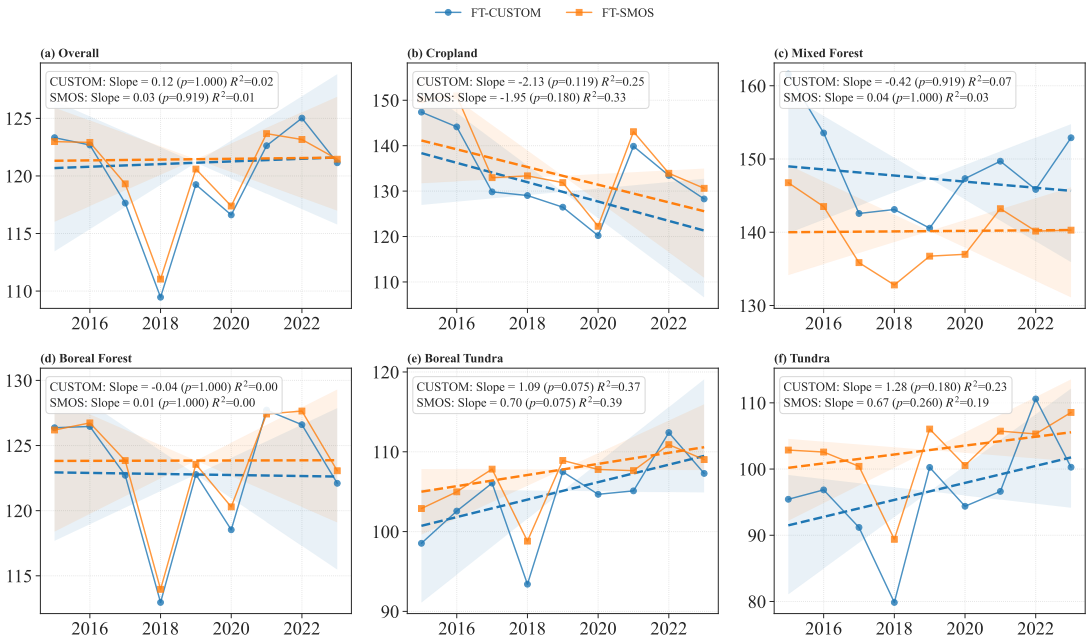


Figure S8: This plot illustrates the interannual variability in the SOS timing (2015–2023), mirroring Fig. S7. The timing of the spring thaw exhibits fluctuations with non-significant linear trends over the observational period. Both products track each other closely.

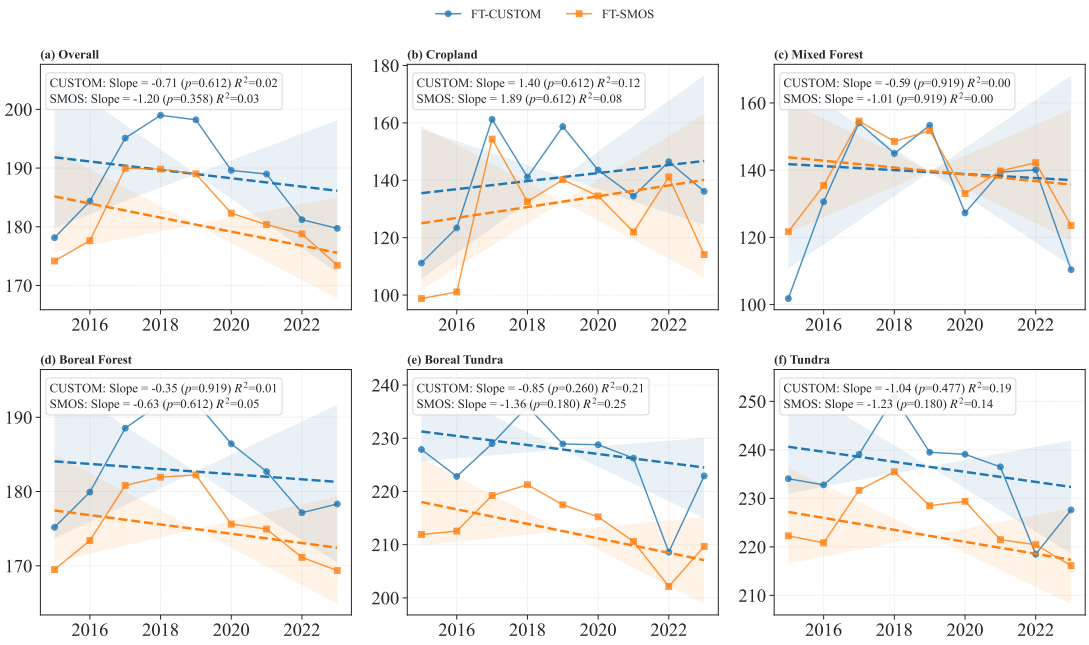


Figure S9: Interannual variability in the cold-season duration — defined here as the continuous phenological interval between the end of growing season (EOS) and the start of growing season (SOS) — from 2015 to 2023. Unlike the frequency metrics reported in Fig. S4–S6, which represent aggregate counts of daily soil-state labels, this metric capture the total elapsed time between the onset of sustained freezing and the onset of sustained thawing. Both products exhibit highly dynamic interannual variability with no statistically significant directional trend over the observational period.

S1.4 Within-Biome Pixel-Level Regression of Fall Zero-Curtain Duration

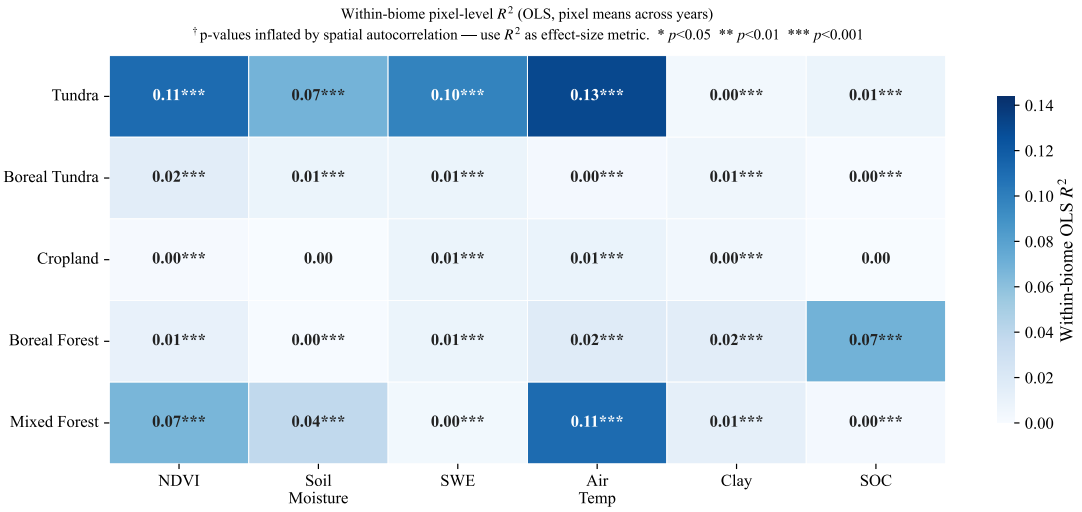


Figure S10: Within-biome coefficient of determination (R^2) for ordinary least-squares regressions of fall zero-curtain duration against six environmental predictors, computed independently for each of the five North American biomes using pixel-level observations averaged across the 2015–2024 record. Asterisks denote raw OLS significance (* $p < 0.05$, ** $p < 0.01$, *** $p < 0.001$), which should be interpreted cautiously given spatial autocorrelation between adjacent 9 km pixels. The uniformly low R^2 values across all predictor–biome combinations indicate that none of the seasonal variables employed here explains a meaningful fraction of spatial variance in zero-curtain duration within any individual biome.

S2 FT-SMOS product performance

Table S2: Cross-validated predictive performance of the XGBoost model trained on the independent FT-SMOS target, reported across global and biome-specific domains. R^2 and MAE values represent means ± standard deviation across leave-P-years-out cross-validation folds. This table is provided as a corroboration Table 4.2; near-equivalent performance across both targets indicates that the attribution results are not an artefact of the FT-CUSTOM retrieval.

Domain / Biome	R^2	MAE (days)
Global (Overall)	0.876 (±0.008)	11.83 (±0.14)
Tundra	0.901 (±0.019)	12.17 (±1.04)
Boreal Forest	0.745 (±0.041)	10.56 (±0.51)
Boreal Tundra	0.731 (±0.050)	9.06 (±0.37)
Mixed Forest	0.667 (±0.038)	13.89 (±0.91)
Croplands	0.573 (±0.050)	15.72 (±1.41)

4.3 References

K. A. Arndt, W. C. Oechel, J. P. Goodrich, B. A. Bailey, A. Kalhori, J. Hashemi, C. Sweeney, and D. Zona. Sensitivity of methane emissions to later soil freezing in arctic tundra ecosystems. *Journal of Geophysical Research: Biogeosciences*, 124(8):2595–2609, 2019. doi: 10.1029/2019JG005242.

M. Azizi-Rad, G. Guggenberger, Y. Ma, and C. A. Sierra. Sensitivity of soil respiration rate with respect to temperature, moisture and oxygen under freezing and thawing. *Soil Biology and Biochemistry*, 165:108488, 2022. doi: 10.1016/j.soilbio.2021.108488.

C3S. Era5 hourly data on single levels from 1940 to present, 2018.

U. N. I. Center. Ims daily northern hemisphere snow and ice analysis at 1 km, 4 km, and 24 km resolutions, version 1, 2004.

T. Chen and C. Guestrin. Xgboost. *Proceedings of the 22nd ACM SIGKDD International Conference on Knowledge Discovery and Data Mining*, pages 785–794, 2016. doi: 10.1145/2939672.2939785.

H. Cheng, G. Wang, H. Hu, and Y. Wang. The variation of soil temperature and water content of seasonal frozen soil with different vegetation coverage in the headwater region of the yellow river, china. *Environmental Geology*, 54(8):1755–1762, 2007. doi: 10.1007/s00254-007-0953-x.

K. Didan. Modis/terra vegetation indices monthly l3 global 0.05deg cmg v061, 2021.

E. Du, Z. Zhou, P. Li, L. Jiang, X. Hu, and J. Fang. Winter soil respiration during soil-freezing process in a boreal forest in northeast china. *Journal of Plant Ecology*, 6(5):349–357, 2013. doi: 10.1093/jpe/rtt012.

B. Elberling and K. K. Brandt. Uncoupling of microbial co2 production and release in frozen soil and its implications for field studies of arctic c cycling. *Soil Biology and Biochemistry*, 35(2):263–272, 2003. doi: 10.1016/S0038-0717(02)00258-4.

M. Friedl and D. Sulla-Menashe. Modis/terra+aqua land cover type yearly l3 global 0.05deg cmg v061, 2022.

M. Hayashi. The cold vadose zone: Hydrological and ecological significance of frozen-soil processes. *Vadose Zone Journal*, 12(4):1–8, 2013. doi: 10.2136/vzj2013.03.0064.

C. E. Johnston, S. A. Ewing, J. W. Harden, R. K. Varner, K. P. Wickland, J. C. Koch, C. C. Fuller, K. Manies, and M. T. Jorgenson. Effect of permafrost thaw on co ₂ and ch

₄ exchange in a western alaska peatland chronosequence. *Environmental Research Letters*, 9(8):085004, 2014. doi: 10.1088/1748-9326/9/8/085004.

C. Knoblauch, C. Beer, S. Liebner, M. N. Grigoriev, and E.-M. Pfeiffer. Methane production as key to the greenhouse gas budget of thawing permafrost. *Nature Climate Change*, 8(4): 309–312, 2018. doi: 10.1038/s41558-018-0095-z.

J. Kreyling, C. Beierkuhnlein, K. Pritsch, M. Schloter, and A. Jentsch. Recurrent soil freeze–thaw cycles enhance grassland productivity. *New Phytologist*, 177(4):938–945, 2007. doi: 10.1111/J.1469-8137.2007.02309.X.

G. Li, Y. Zhao, W. Zhang, and X. Xu. Influence of snow cover on temperature field of frozen ground. *Cold Regions Science and Technology*, 192:103402, 2021a. doi: 10.1016/j.coldregions.2021.103402.

T. Li, Y.-Z. Chen, L.-J. Han, L.-H. Cheng, Y.-H. Lv, B.-J. Fu, X.-M. Feng, and X. Wu. Shortened duration and reduced area of frozen soil in the northern hemisphere. *The Innovation*, 2(3): 100146, 2021b. doi: 10.1016/j.xinn.2021.100146.

S. Lundberg and S.-I. Lee. A unified approach to interpreting model predictions, 2017.

A. Mavrovic, O. Sonnentag, J. Lemmetyinen, C. Voigt, N. Rutter, P. Mann, J.-D. Sylvain, and A. Roy. Environmental controls of winter soil carbon dioxide fluxes in boreal and tundra environments. *Biogeosciences*, 20(24):5087–5108, 2023. doi: 10.5194/bg-20-5087-2023.

K. Migala, M. Wieczorek, M. Kasprzak, and A. Traczyk. Long-term trends of freeze-thaw cycles in the northern hemisphere. *Climatic Change*, 179(1), 2025. doi: 10.1007/s10584-025-04092-2.

C. J. Mikan, J. P. Schimel, and A. P. Doyle. Temperature controls of microbial respiration in arctic tundra soils above and below freezing. *Soil Biology and Biochemistry*, 34(11):1785–1795, 2002. doi: 10.1016/S0038-0717(02)00168-2.

P. ONeill, S. Chan, E. Njoku, T. Jackson, R. Bindlish, and J. Chaubell. Smap enhanced l3 radiometer global daily 9 km ease-grid soil moisture, version 4, 2020.

N. Panikov, P. Flanagan, W. Oechel, M. Mastepanov, and T. Christensen. Microbial activity in soils frozen to below -39 °c. *Soil Biology and Biochemistry*, 38(4):785–794, 2006. doi: 10.1016/j.soilbio.2005.07.004.

G. Pastorello, C. Trotta, E. Canfora, H. Chu, D. Christianson, Y.-W. Cheah, C. Poindexter, J. Chen, A. Elbashandy, M. Humphrey, P. Isaac, D. Polidori, M. Reichstein, A. Ribeca, C. van Ingen,

N. Vuichard, L. Zhang, B. Amiro, C. Ammann, M. A. Arain, J. Ardö, T. Arkebauer, S. K. Arndt, N. Arriga, M. Aubinet, M. Aurela, D. Baldocchi, A. Barr, E. Beamesderfer, L. B. Marchesini, O. Bergeron, J. Beringer, C. Bernhofer, D. Berveiller, D. Billesbach, T. A. Black, P. D. Blanken, G. Bohrer, J. Boike, P. V. Bolstad, D. Bonal, J.-M. Bonnefond, D. R. Bowling, R. Bracho, J. Brodeur, C. Brümmer, N. Buchmann, B. Burban, S. P. Burns, P. Buysse, P. Cale, M. Cavagna, P. Cellier, S. Chen, I. Chini, T. R. Christensen, J. Cleverly, A. Collalti, C. Consalvo, B. D. Cook, D. Cook, C. Coursolle, E. Cremonese, P. S. Curtis, E. D'Andrea, H. da Rocha, X. Dai, K. J. Davis, B. D. Cinti, A. d. Grandcourt, A. D. Ligne, R. C. De Oliveira, N. Delpierre, A. R. Desai, C. M. Di Bella, P. d. Tommasi, H. Dolman, F. Domingo, G. Dong, S. Dore, P. Duce, E. Dufrêne, A. Dunn, J. Dušek, D. Eamus, U. Eichelmann, H. A. M. ElKhidir, W. Eugster, C. M. Ewenz, B. Ewers, D. Famulari, S. Fares, I. Feigenwinter, A. Feitz, R. Fensholt, G. Filippa, M. Fischer, J. Frank, M. Galvagno, M. Gharun, D. Gianelle, B. Gielen, B. Gioli, A. Gitelson, I. Goded, M. Goeckede, A. H. Goldstein, C. M. Gough, M. L. Goulden, A. Graf, A. Griebel, C. Gruening, T. Grünwald, A. Hammerle, S. Han, X. Han, B. U. Hansen, C. Hanson, J. Hatakka, Y. He, M. Hehn, B. Heinesch, N. Hinko-Najera, L. Hörtnagl, L. Hutley, A. Ibrom, H. Ikawa, M. Jackowicz-Korczynski, D. Janouš, W. Jans, R. Jassal, S. Jiang, T. Kato, M. Khomik, J. Klatt, A. Knohl, S. Knox, H. Kobayashi, G. Koerber, O. Kolle, Y. Kosugi, A. Kotani, A. Kowalski, B. Kruijt, J. Kurbatova, W. L. Kutsch, H. Kwon, S. Launiainen, T. Laurila, B. Law, R. Leuning, Y. Li, M. Liddell, J.-M. Limousin, M. Lion, A. J. Liska, A. Lohila, A. López-Ballesteros, E. López-Blanco, B. Loubet, D. Loustau, A. Lucas-Moffat, J. Lüers, S. Ma, C. Macfarlane, V. Magliulo, R. Maier, I. Mammarella, G. Manca, B. Marcolla, H. A. Margolis, S. Marras, W. Massman, M. Mastepanov, R. Matamala, J. H. Matthes, F. Mazzenga, H. McCaughey, I. McHugh, A. M. S. McMillan, L. Merbold, W. Meyer, T. Meyers, S. D. Miller, S. Minerbi, U. Moderow, R. K. Monson, L. Montagnani, C. E. Moore, E. Moors, V. Moreaux, C. Moureaux, J. W. Munger, T. Nakai, J. Neirynck, Z. Nesic, G. Nicolini, A. Noormets, M. Northwood, M. Nosetto, Y. Nouvellon, K. Novick, W. Oechel, J. E. Olesen, J.-M. Ourcival, S. A. Papuga, F.-J. Parmentier, E. Paul-Limoges, M. Pavelka, M. Peichl, E. Pendall, R. P. Phillips, K. Pilegaard, N. Pirk, G. Posse, T. Powell, H. Prasse, S. M. Prober, S. Rambal, Ü. Rannik, N. Raz-Yaseef, C. Rebmann, D. Reed, V. R. d. Dios, N. Restrepo-Coupe, B. R. Reverter, M. Roland, S. Sabbatini, T. Sachs, S. R. Saleska, E. P. Sánchez-Cañete, Z. M. Sanchez-Mejia, H. P. Schmid, M. Schmidt, K. Schneider, F. Schrader, I. Schroder, R. L. Scott, P. Sedlák, P. Serrano-Ortíz, C. Shao, P. Shi, I. Shironya, L. Siebicke, L. Šigut, R. Silberstein, C. Sirca, D. Spano, R. Steinbrecher, R. M. Stevens, C. Sturtevant, A. Suyker, T. Tagesson, S. Takanashi, Y. Tang, N. Tapper, J. Thom, M. Tomassucci, J.-P. Tuovinen, S. Urbanski, R. Valentini, M. van der Molen, E. van Gorsel, K. van Huissteden, A. Varlagin, J. Verfaillie, T. Vesala, C. Vincke, D. Vitale, N. Vygodskaya, J. P. Walker, E. Walter-Shea, H. Wang, R. Weber, S. Westermann, C. Wille, S. Wofsy, G. Wohlfahrt,

S. Wolf, W. Woodgate, Y. Li, R. Zampedri, J. Zhang, G. Zhou, D. Zona, D. Agarwal, S. Biraud, M. Torn, and D. Papale. The fluxnet2015 dataset and the oneflux processing pipeline for eddy covariance data. *Scientific Data*, 7(1), 2020. doi: 10.1038/s41597-020-0534-3.

L. Poggio, L. M. de Sousa, N. H. Batjes, G. B. M. Heuvelink, B. Kempen, E. Ribeiro, and D. Rossiter. Soilgrids 2.0: producing soil information for the globe with quantified spatial uncertainty. *SOIL*, 7(1):217–240, 2021. doi: 10.5194/soil-7-217-2021.

K. Rautiainen, M. Holmberg, J. Cohen, A. Mialon, M. Schwank, J. Lemmetyinen, A. de la Fuente, and Y. Kerr. An operational smos soil freeze–thaw product. *Earth System Science Data*, 17 (10):5337–5353, 2025. doi: 10.5194/essd-17-5337-2025.

H. Salmabadi. Development of new microwave multi-sensor freeze/thaw products for improving growing season monitoring in north america, 2023. URL https://doi.org/10.69777/330450. Doctoral Research Scholarship.

N. V. Smith, S. S. Saatchi, and J. T. Randerson. Trends in high northern latitude soil freeze and thaw cycles from 1988 to 2002. *Journal of Geophysical Research: Atmospheres*, 109(D12), 2004. doi: 10.1029/2003JD004472.

S. A. Sokratov and R. G. Barry. Intraseasonal variation in the thermoinsulation effect of snow cover on soil temperatures and energy balance. *Journal of Geophysical Research: Atmospheres*, 107(D10), 2002. doi: 10.1029/2001JD000489.

B. Stenberg, M. Johansson, M. Pell, K. Sjödahl-Svensson, J. Stenström, and L. Torstensson. Microbial biomass and activities in soil as affected by frozen and cold storage. *Soil Biology and Biochemistry*, 30(3):393–402, 1998. doi: 10.1016/S0038-0717(97)00125-9.

G. W. Tefera, S. Gurau, B. Deegala, D. Wilson, K. Kularathna, S. Chaudhary, C. A. Igwenagu, B. Mengistie, and R. L. Ray. Dynamics and environmental thresholds of ecosystem respiration across the conterminous united states: Insights from ameriflux and remote sensing data. *Ecological Informatics*, 95:103738, 2026. doi: 10.1016/j.ecoinf.2026.103738.

J. Wang, Q. Wu, Z. Yuan, and H. Kang. Soil respiration of alpine meadow is controlled by freeze–thaw processes of active layer in the permafrost region of the qinghai–tibet plateau. *The Cryosphere*, 14(9):2835–2848, 2020. doi: 10.5194/tc-14-2835-2020.

Y. Yang, R.-S. Chen, Y.-J. Ding, H.-Y. Li, and Z.-W. Liu. Changes in global land surface frozen ground and freeze–thaw processes during 1950–2020 based on era5-land data. *Advances in Climate Change Research*, 15(2):265–274, 2024. doi: 10.1016/j.accre.2024.03.007.

Y. Yang, X. Wang, Z. Li, T. Wang, and T. Che. Shortened thawing and freezing intervals in the northern hemisphere since 1990 from sites observations and remote sensing. *Remote Sensing of Environment*, 328:114881, 2025. doi: 10.1016/j.rse.2025.114881.

J. Zhang, J. Hong, D. Wei, and X. Wang. Severe freezing increases soil respiration during the thawing period: A meta-analysis. *European Journal of Soil Science*, 73(1), 2021a. doi: 10.1111/ejss.13161.

T. Zhang. Influence of the seasonal snow cover on the ground thermal regime: An overview. *Reviews of Geophysics*, 43(4), 2005. doi: https://doi.org/10.1029/2004RG000157. URL https://agupubs.onlinelibrary.wiley.com/doi/abs/10.1029/2004RG000157.

W. Zhang, Y. Shen, X. Wang, S. Kang, A. Chen, W. Mao, and X. Zhong. Snow cover controls seasonally frozen ground regime on the southern edge of altai mountains. *Agricultural and Forest Meteorology*, 297:108271, 2021b. doi: 10.1016/j.agrformet.2020.108271.

G. Zheng, Y. Yang, D. Yang, B. Dafflon, Y. Yi, S. Zhang, D. Chen, B. Gao, T. Wang, R. Shi, and Q. Wu. Remote sensing spatiotemporal patterns of frozen soil and the environmental controls over the tibetan plateau during 2002–2016. *Remote Sensing of Environment*, 247:111927, 2020. doi: 10.1016/j.rse.2020.111927.

D. Zona, B. Gioli, R. Commane, J. Lindaas, S. C. Wofsy, C. E. Miller, S. J. Dinardo, S. Dengel, C. Sweeney, A. Karion, R. Y.-W. Chang, J. M. Henderson, P. C. Murphy, J. P. Goodrich, V. Moreaux, A. Liljedahl, J. D. Watts, J. S. Kimball, D. A. Lipson, and W. C. Oechel. Cold season emissions dominate the arctic tundra methane budget. *Proceedings of the National Academy of Sciences*, 113(1):40–45, 2015. doi: 10.1073/pnas.1516017113.

Chapter 5

General Discussion and Conclusion

5.1 Opening Synthesis

The overarching objective of this dissertation was to resolve a persistent and consequential misrepresentation in the science of seasonally frozen ground: the collapse of a physically complex, thermodynamically prolonged phase transition into a binary 0°C threshold. This binary framing permeates the field simultaneously at two scales. At the site scale, the conventional Soil Freezing Characteristic Curve (SFCC) framework requires converting bulk dielectric permittivity to liquid water content — a conversion that fails in the organic-rich, clay-heavy, and moisture-variable soils that dominate the boreal and tundra landscapes where the transitional state is most consequential. At the satellite scale, operational passive microwave algorithms enforce discrete frozen/unfrozen classifications that structurally erase the zero-curtain phase — the biogeochemically active period during which liquid water and ice coexist and microbial activity remains elevated despite subzero air temperatures. The three research chapters of this dissertation addressed these two challenges not in isolation but as a sequential, mutually reinforcing problem: reformulating the *in situ* framework first, then using that reformulation to build a physically grounded satellite retrieval, and finally deploying that retrieval to reveal how the transitional state is distributed across North American biomes and how it governs cold-season carbon flux. The result is an end-to-end framework that traces the freeze–thaw continuum from the needle of a dielectric soil sensor to a satellite 700 km above Earth, and links the cryospheric state of the soil directly to ecosystem functioning.

5.2 Bridging Observational Scales: From Soil Sensor to Satellite

What connects the three chapters of this dissertation is a consistent operational principle: that the gradual physics of soil freezing — long established in the cryosphere literature — can now be quantified rather than collapsed into a binary state, from the scale of an *in situ* dielectric sensor to the continental footprint of passive microwave satellites. This required a solution at the site scale before it could be meaningful at the satellite scale, because the *in situ* records used to train and validate satellite FT algorithms carry the same binary assumptions that distort the satellite products themselves.

Reformulating the SFCC directly in permittivity–temperature space removed the central obstacle to *in situ* non-binary monitoring. By fitting the phase-change model to the observable dielectric signal rather than to the derived liquid water content, the approach renders site-level characterisation of the transitional state tractable without soil-specific calibration — a requirement that is difficult to satisfy reliably across the diverse sensor platforms, soil textures, and organic contents represented in continental-scale monitoring networks. The Bayesian hierarchical partial-pooling framework extended this tractability further, allowing information to be shared across data-sparse sites and networks while preserving genuine spatial differences in freezing behaviour. The resulting biome-level parameters are not merely statistical summaries; they are physically interpretable quantities that reflect the dominant controls on soil freezing in each landscape. The low b values in prairie and western boreal networks reflect the broad matric suction distributions of clay-rich and low-moisture soils, while the high b values in eastern boreal and tundra networks reflect the abrupt phase transitions of wet, coarse-textured, or organic-saturated pore systems.

These parameters then directly enabled the satellite-scale advance. Rather than labelling training data with a universal 0 °C threshold — the standard practice that embeds binary assumptions into the training set itself — the second chapter used the biome-specific SFCC parameters to assign probabilistic ground-state labels, filtering out the ambiguous shoulder-season observations that otherwise contaminate the decision boundary and inflate classification errors during the zero-curtain period. This seemingly technical choice has a profound effect on the resulting product: by training the logistic regression model exclusively on high-confidence end-members, the transitional class is not a third category imposed on the model but an emergent radiometric zone between the frozen and unfrozen signatures — one that, as thermodynamic validation confirmed, physically anchors to the latent heat plateau of soil freezing across all five biomes tested. The continuous Frozenness Index D, derived as a standardised geometric distance from the biome-specific decision boundary, inherits this physical grounding: it is not a probabilistic confidence measure but a dielectric state variable that tracks the progressive

depletion of liquid water during the phase change.

The performance gradient observed across biomes — from near-perfect classification in open tundra (match rate 98.2%, Kappa 0.87) to degraded performance in dense mixed forests (match rate 78.8%, Kappa 0.44) — is itself a scientifically informative outcome. It is not a failure of the algorithm but a faithful reflection of a physical reality: passive microwave L-band and Ka/Ku-band signals are dominated by canopy emission in densely vegetated environments, decoupling the satellite observation from the soil dielectric state that the model was designed to track. Compounding this radiometric challenge, forests are also the environments where zero-curtain duration is longest, meaning the algorithm must correctly resolve a prolonged transitional state rather than the unambiguous hard-frozen signatures that dominate open environments. This limitation is not unique to the logistic framework; it affects all passive microwave FT algorithms equally, as benchmarking against *in situ* soil temperature networks confirmed. The biome-stratified coefficient structure of the model — where the polarisation ratio dominates in open croplands and the spectral gradient index dominates in forested biomes — represents a physically interpretable quantification of this canopy-driven regime shift.

5.3 Biogeochemical Coupling and Earth System Implications

The continental-scale application of the non-binary retrieval record revealed a distinctly non-latitudinal spatial pattern in zero-curtain duration. Zero-curtain duration peaks in mid-latitude mixed forests at 57.4 days, while both high-Arctic tundra (13.7 days) and lower-latitude croplands (23.9 days) show substantially shorter durations — a pattern that atmospheric temperature alone cannot explain. Biome-level co-variation analysis reveals that fall vegetation density (NDVI) shows the clearest and most monotonic correspondence with zero-curtain duration, increasing from sparse tundra to structurally complex mixed forest, consistent with the role of dense canopies in intercepting outgoing longwave radiation and sustaining the latent heat release that prolongs the near-0°C phase-change period; NDVI likely also acts as an integrated proxy for organic layer thickness, since productive ecosystems accumulate thicker near-surface organic horizons that buffer soil thermal dynamics. This co-variation is descriptive at the biome scale: within-biome pixel-level regressions against all predictors yielded uniformly low R^2 values (maximum 0.13), indicating that these coarse-resolution seasonal variables capture ecosystem-type differences at the continental scale but cannot explain pixel-scale variance in zero-curtain duration within any individual biome. The large zero-curtain accumulation in mixed forests may be partly inflated by passive microwave limitations in densely vegetated environments, where canopy scattering can blur the distinction between frozen and unfrozen phases. The XGBoost attribution framework provides the more rigorous quantitative characterisation of environmental controls: while spring

and fall atmospheric temperatures govern total frozen ground frequency globally (mean SHAP impacts of 17.5 and 12.1 days, respectively), dense forest canopies trigger a structural regime shift in which sub-canopy snowpack supersedes direct thermal forcing as the dominant driver of frozen ground duration, decoupling the soil from atmospheric forcing in forested environments.

The mechanistic linkage between the Frozenness Index and ecosystem respiration translates this physical characterisation into ecological consequence. Piecewise regression of AmeriFlux R_{eco} against D identifies a consistent metabolic breakpoint across biomes that aligns with the satellite-derived lower zero-curtain boundary D_{lower} — the point at which ice formation begins to restrict substrate diffusion and microbial access to liquid water. Above this threshold, ecosystem respiration is co-limited by multiple factors and exhibits high variance; below it, progressive ice formation imposes a thermodynamic ceiling on biological activity that the boundary line analysis quantifies as an exponential decay in maximum respiratory potential. This finding has a direct implication for carbon cycle modelling: the zero-curtain phase is not merely a thermal transition zone but the interval during which the dominant control on R_{eco} switches from temperature to liquid water content. Models that represent this transition as instantaneous — as all binary FT products implicitly do — systematically mistime this regime switch, generating errors in cold-season carbon flux estimates that compound over a season that contributes an estimated 39–50% of annual ecosystem CO_2 emissions.

Collectively, these findings reframe a question that has been approached primarily as a remote sensing retrieval problem — how to classify the soil state from satellite brightness temperatures — as a question with direct consequences for how the land surface carbon cycle is parameterised. The transitional state is not a radiometric artefact to be classified away; it is a physically and ecologically distinct phase of the soil system whose duration is determined by canopy density, organic layer depth, and snowpack insulation, and whose termination marks the critical tipping point at which cold-season respiration becomes liquid-water-limited rather than temperature-limited.

5.4 Limitations

The integrated framework advances the field, but it operates within boundaries that future work must address.

The spatial resolution of the passive microwave retrievals — 9 km on the EASE-Grid 2.0 projection — is the most consequential technical constraint. At this scale, a single pixel integrates radiometric signals from a heterogeneous mosaic of open water bodies, bare bedrock, wetlands, variable canopy densities, and differential snowdrift accumulation. Validating such a footprint against *in situ* point sensors is fundamentally limited: even a network of sensors within the pixel

cannot adequately characterise its spatial complexity if the landscape is heterogeneous, because sensors are placed near monitoring infrastructure and accessible terrain rather than distributed to represent the full range of sub-pixel land cover. This problem is most acute in mixed and boreal forest biomes, where within-pixel variability in canopy density, soil moisture, and organic layer depth is high — and it is reflected directly in the results: the low inter-product consensus ratio in mixed forests (56.7%) and the degraded Kappa values in forested biomes are not a deficiency of the logistic framework but the compounded expression of three physical and observational constraints shared by all existing passive microwave FT algorithms: canopy emission that decouples the satellite signal from the soil dielectric state, a prolonged zero-curtain period that demands correct resolution of an inherently ambiguous transitional state, and sub-pixel spatial heterogeneity that no point-sensor network can fully characterise.

The *in situ* SFCC construction rests on the assumption that total soil water content remains constant throughout a freezing cycle — an assumption that holds reasonably well during sustained autumn freeze-up but breaks down during thawing cycles, when snowmelt introduces continuous water influx that prevents the identification of a stable moisture baseline. This is why the SFCC analysis was restricted to freezing cycles and why thawing dynamics remain uncharacterised at the site level. It also means that the biome-specific SFCC parameters used for satellite training labels carry implicit assumptions about pre-freeze moisture conditions that may not hold uniformly across all sites within a biome.

The observational record of the satellite retrieval spans only nine years (2015–2024), which is insufficient to robustly detect long-term climatological trends in frozen ground phenology beyond specific regional signals such as the declining fall frozen-day frequency observed in the tundra. The cross-validated agreement between FT-CUSTOM and FT-SMOS in capturing interannual variability provides confidence in the year-to-year signal, but multi-decadal attribution of phenological shifts requires either an extended record or a bias-corrected fusion with the longer FT-ESDR archive.

Finally, both the SFCC parameterisation and the logistic regression model were developed and validated exclusively using North American monitoring networks and land cover. The biome-specific coefficients, SFCC parameters, and environmental driver relationships may not transfer directly to Eurasian boreal and tundra landscapes, which differ in soil organic matter depth, vegetation structure, and continental climate regime. This geographic constraint limits the immediate global generalisability of the framework and represents a clear priority for extension.

5.5 Broader Impacts and Future Directions

The integrated findings of this dissertation carry implications that extend well beyond the development of an improved FT satellite product. At the most immediate level, the framework is deployable within existing passive microwave data pipelines: both SMAP and AMSR2 are fully operational, the logistic model is computationally trivial, and the SFCC-based labelling methodology is compatible with any dielectric monitoring network that measures permittivity and temperature simultaneously. The vast existing archives of such networks — RISMA, SNOTEL, and the broader AmeriFlux and FLUXNET infrastructure — can adopt the permittivity–temperature SFCC methodology described in Chapter 2 to generate physically grounded, non-binary soil state labels without soil-specific liquid water content calibration, immediately expanding the geographic coverage of high-quality FT reference data available for satellite algorithm development.

At the land surface modelling level, the findings carry indirect but meaningful implications. The biome-level co-variation between fall vegetation density (NDVI) and zero-curtain duration, together with the XGBoost finding that sub-canopy snowpack supersedes direct thermal forcing in forested environments, suggests that models relying on atmospheric temperature as the sole driver of soil freezing onset may systematically underperform in forested biomes, where canopy structure and sub-canopy snowpack exert dominant thermodynamic control over the phase-change period. The carbon cycle results reinforce this concern from a different angle: the piecewise regression analysis identifies a regime shift in R_{eco}—from temperature-governed to liquid-water-governed—that aligns with the satellite-derived onset of the zero-curtain phase. Models that represent the soil as passing instantaneously through this transition necessarily mistime the point at which cold-season respiration becomes liquid-water-limited rather than temperature-limited. The importance of correctly simulating the zero-curtain duration is illustrated by Tao et al. (2021), who showed that improving the latent heat representation in the phase-change scheme of the ELMv1-ECA land surface model—which better reproduced zero-curtain duration and soil thermal conditions—reduced the mean absolute error in simulated cold-season CO_2 flux by approximately 70% and CH_4 emissions by approximately 72%. Taken together, these results motivate a clear priority for future work: benchmarking existing land surface model FT outputs against the non-binary satellite record and Frozenness Index D developed here, to quantify where and by how much binary FT schemes diverge from the observed zero-curtain climatology across North American biomes.

Looking further ahead, three directions stand out as priorities. The first is the extension of the SFCC parameterisation and logistic retrieval to Eurasian boreal and tundra networks, where distinct soil organic matter profiles, permafrost distributions, and continental climate regimes may alter the biome-specific coefficients sufficiently to warrant independent calibration. The

second direction concerns the use of Sentinel-1 C-band synthetic aperture radar (SAR) data. Since C-band backscatter tracks the dielectric state of the soil during freeze-up with classification accuracies of ~92% relative to near-surface soil temperature (Bartsch et al., 2025), pairing SAR backscatter with *in situ* temperature records could allow SFCC parameters to be constructed at sites where permittivity sensors are unavailable, substantially expanding the geographic coverage of physically grounded freeze–thaw training data beyond the sensor networks used in Chapter 2. The same SAR data also enable spatial benchmarking of the FT-CUSTOM product and Frozenness Index D: by classifying each 10 m Sentinel-1 pixel as frozen or unfrozen and computing the frozen fraction within each 9 km passive microwave grid cell, one can directly evaluate whether a given value of D corresponds to partial, patchy, or near-complete freezing across the footprint — a question that a single *in situ* soil sensor cannot answer. Bartsch et al. (2025) demonstrated this approach for SMAP and SMOS over tundra, revealing that coarse passive microwave frozen and partially frozen flags often misrepresent the actual spatial distribution of frozen ground within the pixel. Both SAR applications are currently limited to open tundra and non-forested biomes; extension to forested environments will require forthcoming L-band SAR missions such as NISAR, whose frequency is compatible with SMAP and SMOS. The third direction is whether the magnitude of deep-winter D values predicts the intensity of spring thaw CO_2 pulses: severe freeze events physically burst microbial cells and trap gases that are released as a pulse upon thaw, and because D tracks the progressive depletion of liquid water during freeze-up, it may serve not only as a monitor of cold-season dormancy but as a predictor of the pulse carbon release that punctuates the onset of each growing season.

Under ongoing Arctic amplification, the zero-curtain period is projected to lengthen and shift in timing as soils warm across the Northern Hemisphere — meaning that the fraction of the frozen season that binary monitoring frameworks are structurally incapable of characterising is itself increasing. Each additional day of zero-curtain conditions is a day during which ecosystem respiration is neither at its dormant-season minimum nor at its growing-season level, but governed by soil liquid water availability: binary products that label this period as frozen cause carbon cycle models to assign low flux, while those that label it as unfrozen cause models to apply full temperature-sensitive respiration — both systematically wrong in opposite directions. This dissertation provides the conceptual framework, the observational methodology, and the satellite data record needed to close this gap: to move the representation of seasonally frozen ground in Earth system science from a binary state transition to a continuum to be characterised.

Scientific Contributions

This section outlines the scientific contributions, including peer-reviewed journal articles, book chapters, conference proceedings, and presentations, completed during the course of this doctoral research.

Peer-Reviewed Journal Articles

Thesis-Related Publications

Published

- **Salmabadi, H.**, Pardo Lara, R., Berg, A., Mavrovic, A., Hanes, C., Montpetit, B., & Roy, A. (2026). *In situ* monitoring of seasonally frozen ground using soil freezing characteristic curve in permittivity–temperature space. *The Cryosphere*, 20(3), 1635–1654.

- Berg, A. A., Wicks, K., Ambadan, J. T., Roy, A., Magagi, W., . . . , **Salmabadi, H.**, et al. (2025). Soil Moisture Active/Passive Validation Experiment Within the Canadian Boreal Forest in 2022 (SMAPVEX22-Boreal). *IEEE Journal of Selected Topics in Applied Earth Observations and Remote Sensing*, 18, 11816–11834. https://doi.org/10.1109/JSTARS.2025.3564195
  Author Contribution: Participated in field data collection.

Submitted and In Preparation

- Gorrab, A., **Salmabadi, H.**, Maire, V., Houmma, I., Gelinas, A., Mavrovic, A., Berg, A., & Roy, A. (Submitted). Laboratory Calibration of TEROS Soil Moisture Sensors with Variable Organic Matter Content in Canadian Boreal Forest Soils. *Vadose Zone Journal*.

- Carreno-Luengo, H., Ruf, C. S., Bourgeau-Chavez, L., Roy, A., **Salmabadi, H.**, Hanes, C. C., Rogers, B. M., Jandt, R., York, A., & Majors, S. (Submitted). Monitoring freeze/thaw status to better predict Arctic-boreal wildfires. *Communications Earth & Environment*.

Other Peer-Reviewed Publications

Published

- Ziyad, J., Hamel Jomphe, E., Sghinolfi, A., **Salmabadi, H.**, Gorrab, A., Mavrovic, A., Roy, C., Gélinas, A., De Courville, D., Rouleau, M., Bado, Y. A. G., Ouandjagabou, I., & Roy, A. (2026). Using models and remote sensing to support a warning system: diagnosing climate and land use changes in Nahouri, Burkina Faso. *International Journal of Climate Change Strategies and Management*, 18(1), 191–215.

- **Salmabadi, H.**, Saeedi, M., Notaro, M., & Roy, A. (2025). Dust transport pathways from the Mesopotamian Marshes. *Aeolian Research*, 73, 100975.

- **Salmabadi, H.**, Saeedi, M., Roy, A., & Kaskaoutis, D. G. (2023). Quantifying the contribution of Middle Eastern dust sources to PM10 levels in Ahvaz, Southwest Iran. *Atmospheric Research*, 295, 106993.

Book Chapters and Major Reports

- Contributing Author. (Forthcoming). Chapter 6: Cryosphere Changes. In *Canada's Changing Climate Report (CCCR 2025)*.

Proceedings, Conferences, and Scientific Meetings

First-Authored Proceedings & Presentations

- **Salmabadi, H.**, Berg, A., & Roy, A. (2026). Capturing the Soil Zero-Curtain Effect from Multi-Frequency Passive Microwave Retrievals. *XXV ISPRS Congress*, Toronto, ON, Canada (July 4–11). **[Oral Presentation & Extended Abstract]**

- **Salmabadi, H.**, Berg, A., & Roy, A. (2026). A multi-sensor passive microwave model for soil freeze-thaw detection. *46e colloque annuel du Centre d'études nordiques (CEN)*, Université Laval, Québec, QC, Canada (February 12–13). **[Oral Presentation]**

- **Salmabadi, H.**, Berg, A., & Roy, A. (2024). *In Situ* Modeling of Freezing/Melting Point Depression Across Diverse Canadian Ecosystems: An Analysis of Soil Freezing Characteristics Using Permittivity and Temperature Measurements. *45th Canadian Symposium on Remote Sensing (CSRS)*, Dalhousie University, Halifax, NS, Canada (June 10–13). **[Oral Presentation & Extended Abstract]**

- **Salmabadi, H.** (2024). Soil freezing/melting point depression observed *in situ* over several Canadian ecosystems. *Soil Moisture Active Passive Validation Experiments Workshop*, University of Guelph, Guelph, ON, Canada (May 7–9). **[Oral Presentation]**

- **Salmabadi, H.**, Berg, A., Mavrovic, A., & Roy, A. (2023). Variability, correlation, and trend analysis of *in situ* soil freeze/thaw measurements in northern Quebec's boreal forest. *43e colloque annuel du Centre d'études nordiques (CEN)*, Université du Québec à Rimouski (UQAR), Rimouski, QC, Canada. **[Poster Presentation]**

Co-Authored Proceedings & Presentations

- Carreno-Luengo, H., Ruf, C. S., Bourgeau-Chavez, L., Roy, A., **Salmabadi, H.**, Hanes, C. C., Rogers, B. M., Jandt, R., York, A., & Majors, S. (2026). Enhancing Freeze/Thaw Monitoring with GNSS-R: Arctic-Boreal Zone Wildfire Prediction. *IGARSS 2026 - 2026 IEEE International Geoscience and Remote Sensing Symposium*. **[Oral Presentation]**

- Carreno-Luengo, H., Ruf, C. S., Bourgeau-Chavez, L., Roy, A., **Salmabadi, H.**, Hanes, C. C., Rogers, B. M., Jandt, R., York, A., & Majors, S. (2025). Freeze/Thaw Dynamics by GNSS-R: Climate Change Effects over the Arctic Boreal Zone. *IGARSS 2025 - 2025 IEEE International Geoscience and Remote Sensing Symposium*, 680–683.

- Carreno-Luengo, H., Ruf, C. S., Gleason, S., Russel, A., Roy, A., & **Salmabadi, H.** (2024). Freeze/Thaw Surface State Retrieval Over The Arctic Boreal Zone By SmallSat GNSS-Reflectometry. *AGU Fall Meeting Abstracts*, 2024(1777), A11L-1777.

- Carreno-Luengo, H., Ruf, C. S., Gleason, S., Russel, A., Roy, A., & **Salmabadi, H.** (2024). Novel gnss-r methods for freeze/thaw surface state retrieval. *IGARSS 2024 - 2024 IEEE International Geoscience and Remote Sensing Symposium*, 835–838.